The Evolution of Prestellar Cores

by

Robert J. Simpson

A thesis submitted to

Cardiff University

for the degree of

Doctor of Philosophy

February 2010

ProQuest LLC
789 East Eisenhower Parkway
P.O. Box 1346
Ann Arbor, MI 48106-1346

ACKNOWLEDGMENTS

First and foremost, I would like to thank my wife, Victoria. She has been incredibly supportive over these past three-and-a-half years. Whilst dealing with her own life, work, and even pregnancy, she has been eternally patient and kind. This thesis could not have been done without her and I dedicate it to her, and to our daughter, Avalon.

I thank Professor Derek Ward-Thompson for allowing me to take part in this research, and for his amazing help and support during the PhD. I have learned the lesson of GIGO, and I promise I really do know that 'data' is the plural of 'datum'! I also thank Dr. David Nutter, who sat behind me all the time and answered my endless questions — when he wasn't dragging me up a mountain.

To my parents, family and friends I am grateful for the advice, support and time that many of them have given to help me during my studies. Thanks also go to the students and staff of Cardiff University who have been friendly, helpful and fun over the years. The ever-changing star formation group have been wonderful comrades, and I would like to thank Dr. Jason Kirk and Sarah Stickler for their friendship and help during the PhD.

In 2007, whilst observing at the JCMT, I was taken ill with altitude sickness. During my unpleasant experience, with what turned out to be a pulmonary oedema, I was assisted by a great many kind people. Thus I'd like to thank the kitchen staff at Hale Pohaku, the support staff at the Joint Astronomy Center, my fellow student Sarah Sadavoy, and the JCMT's telescope operator that night, Ben Warrington. A special thank you to both James Di Francesco and Henry Matthews, who sat with me for hours in hospital and made sure I was ok. My family and I are very grateful for all your quick actions and assistance.

Finally I would like to thank the astronomy community of @twitter. Whatever the hour, they have answered questions and given advice. Without them, this thesis would have been so much harder to complete and a little less fun #omgthesis.

ABSTRACT

In this thesis I re-analyse the SCUBA archive data for the L1688 main cloud of Ophiuchus, incorporating all available scan-map and jiggle-map data. I create a new core mass function (CMF) for L1688 using updated values for the distance to this region, as well as new estimates for the temperatures and masses of the cores.

I show that the CMF for L1688 is consistent with a three part power-law, with slopes the same as those seen in the stellar IMF. The deeper maps allows the discovery of a turnover in the CMF at $0.7M_{\odot}$ which shows that the core mass function appears to mimic the stellar initial mass function. This concordance is indicative that the stellar IMF is determined at the prestellar core phase.

I also present HCO^+ (J=4→3) spectral line observations from HARP on the JCMT. Data are presented for 59 of the prestellar cores mapped using SCUBA. Using these data, I present a proposed evolutionary diagram for prestellar cores in the form of a radius-mass plot. I hypothesise that a core is formed in the low-mass, low-radius region of the plot. It then accretes quasi-statically, increasing in both mass and radius. When it crosses the limit of gravitational instability it begins to collapse, decreasing in radius, towards the region of the diagram where protostellar cores are seen. My predictions are borne out when I plot the collapsing cores on this diagram.

I outline an analytical model, created by Whitworth & Ward-Thompson (2001), describing the collapse of a starless core with a Plummer-like density profile. I describe my addition of a simple radiative transfer code, which allows simulated spectral line profiles to be created for such cores. The model is shown to be consistent with previous models, and with the observed physical properties of prestellar cores.

This model is applied to 20 of the spectral line profiles from the HCO^+ (J=4→3) data. These 20 modelled cores are placed onto the proposed evolutionary diagram. Their modelled physical states are found to be consistent with the proposed evolutionary track. In conjunction with the SCUBA and HARP data, these fits allow a potential timeline for the L1688 cloud to be established for the first time.

Contents

List of Figures

List of Tables

Chapter 1

An Overview of Star Formation

1.1 Introduction

Star formation is one of the most important processes at work in the cosmos. The atoms that make up our planet and ourselves were made in the centres of stars, billions of year ago. To study star formation is to begin to understand the origin and make-up of the Galaxy and the Universe at large.

The mass distribution of stars and the rate at which they are born determines the nature and evolution of galaxies, such as our own Milky Way Galaxy. To understand many aspects of galaxy evolution, planet formation and cosmology, an understanding of star formation is required. It is one of the most fundamental mechanisms at work in the Universe.

Massive stars live brief, energetic lives, changing their environment dramatically through stellar winds, ionising radiation and supernova explosions. The debris left in the wake of a dying supergiant star may go on to form new stars and

Figure 1.1: Spitzer MIPS/IRAC image of the Ophiuchus star-forming region. Source: http://www.spitzer.caltech.edu/Media/releases/ssc2008-03/release.shtml

planets or may collapse to form a black hole or neutron star.

Smaller, lower-mass stars exist for many billions of years, steadily fusing hydrogen into helium, illuminating the galaxy and interacting with other stars and with the interstellar medium (ISM). They account for the vast majority of stars and are the building blocks of galaxies as well as the hosts for planetary systems. In their death throws, they fuse new atoms and disperse material into the ISM, paving the way for future populations of stars and planets.

In this chapter I will discuss the current understanding of star formation. Section 1.2 outlines mechanisms and models for the collapse of molecular clouds. In Section 1.3 I discuss the properties of prestellar cores, the progenitors of protostars. In Section 1.4 protostars themselves are discussed, including their evolution. Section 1.5 discusses the Stellar Initial Mass Function.

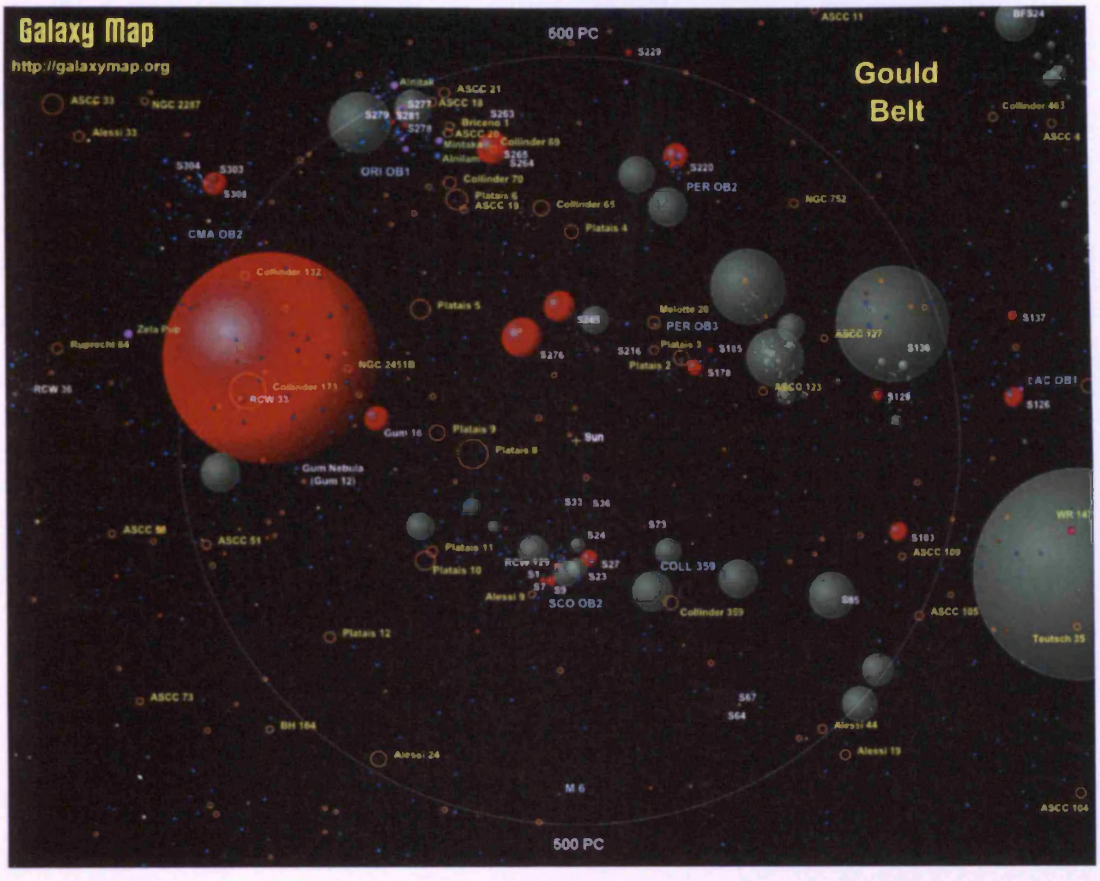

Figure 1.2: The area within 500 pc of the Solar System. Red spheres are nebulae, green spheres are molecular clouds, star clusters are shown as yellow circles and bright stars as blue dots. Source: http://www.galaxymap.org

1.2 Cloud Collapse

In this section I discuss how a molecular cloud can form prestellar and then protostellar cores. This section also outlines ways in which we can think about prestellar collapse and the methods used to model and understand it. Also discussed are the mechanisms for cloud support, in an effort to understand the rate of star formation in GMCs.

Giant Molecular Clouds (GMCs) are most likely formed by compression of gas in the Galaxy's spiral arms (Williams, Blitz, & McKee, 2000). Typical GMCs have

masses of 10^5 - 10^6 $M_\odot$, diameters of the order of 10–50pc and hydrogen number densities of around 10^2 cm^{-3} (Williams et al., 2000). The molecular clouds and nebulae within 500 pc of the Solar System are shown in Figure 1.2. The molecular clouds are shown in green. There are a great many of them in just this small part of the Milky Way and they also vary greatly in size (Williams et al., 2000).

High column densities shield molecular cloud interiors and prevent molecules being photodissociated by interstellar UV radiation. Cooling occurs by emission from molecules and dust grains and this, combined with the shielding, gives a typical interior temperature of 10-20K (Johnstone et al., 2001; Stamatellos, Whitworth, & Ward-Thompson, 2007). Such low temperatures mean that the cloud's thermal support is reduced and gravitational instabilities may form, in turn these may become stars.

1.2.1 Jeans Mass

Stars form in clumps in dense molecular clouds. Jeans (1929) outlined how this might happen through gravitational instability. In an isothermal medium there is a balance between self-gravity, internal pressure and external pressure. Clumps more massive than a critical mass will collapse, those less massive will expand. There is a balanced, equilibrium mass, where neither contraction due to gravity nor expansion due to internal pressure will occur. This is now known as the Jeans Mass, M_J, which is given by

$$M_J = 5.5\frac{c^3}{G^{3/2}\rho^{1/2}} \tag{1.1}$$

where c is the isothermal sound speed, ρ is the initial density and G is the universal gravitational constant.

Turbulent motion can create density perturbations with masses greater than M_J. Clumps that are much more massive than M_J will be dominated by their self-gravity and will collapse in approximate freefall. The freefall time is given to be

$$t_{ff} = \left(\frac{3\pi}{32G\rho}\right)^{1/2}. \tag{1.2}$$

1.2.2 Virial Mass

To determine if an object is gravitationally stable, we can use the virial theorem. If $\mathcal{T}$, $\mathcal{W}$ and $\mathcal{M}$ are, respectively, the total internal kinetic energy, the gravitational potential energy and the magnetic energy, then for a cloud or fragment in equilibrium,

$$2\mathcal{T} + \mathcal{W} + \mathcal{M} = 0. \tag{1.3}$$

If the total is greater than 0 then the cloud expands, if it is less than 0 the cloud contracts. $\mathcal{T}$ is determined by the thermal and non-thermal components of kinetic energy. It is generally determined from molecular line widths and defined as,

$$\mathcal{T} = \frac{3}{2}M\sigma^2, \tag{1.4}$$

where σ is the one-dimensional velocity dispersion and M is the mass of the core.

$\mathcal{W}$ is derived from the potential energy of a uniform density sphere,

$$\mathcal{W} = -\frac{3GM^2}{5R}. \tag{1.5}$$

where R is the radius of the core. $\mathcal{M}$ is derived as,

$$\mathcal{M} = \frac{B^2}{2\mu_0}V, \tag{1.6}$$

where B is the magnetic field strength, μ_0 is the permeability of free space and V is the volume of the core.

1.2.3 Turbulent Cloud Support

Myers (1983) observed non-thermal motions in molecular clouds. Broad molecular line profiles were deduced to be the result of hydrodynamic turbulence. This turbulence is expected to dissipate on the order of 10^6 years (Mac Low et al., 1998) so over a core's 10^7 year lifetime, the source of turbulence will have to be replenished.

Norman & Ferrara (1996) discussed possible sources of turbulence in the ISM. They categorised turbulence into three types, based on their origins: shocks from stellar energy input, gravitational sources of turbulence and turbulence created by global flows in the ISM.

Stellar energy inputs include supernovae and turbulence from stellar winds. HII regions and superbubbles also contribute turbulence, though more weakly.

Gravitational sources of turbulence include shocks from tidal interactions in the Galaxy as well as those from disk instabilities, spiral waves and bars. Galactic shear also injects energy into the ISM.

The ISM is also influenced by larger, global effects such as disk-halo interactions in the Galaxy or interactions with infalling objects such as Galactic satellites.

These multiple sources of turbulence, operating on different scales, will have varying effects on the process of star formation. In the large-scale case of cloud support it could be that Galactic shear and supernovae are at work. On smaller scales it is thought that stellar outflows could be the source of turbulence within star-forming complexes.

1.2.4 Magnetic Cloud Support

Mestel & Spitzer (1956) proposed that magnetic fields, permeating the ISM, could play a part in GMC evolution. Mouschovias (1976) showed that these magnetic fields could be capable of supporting a collapsing, thermally supercrtical cloud. Figure 1.3 shows a sketch of how the collapse might proceed.

Cosmic rays and ultraviolet radiation may partially ionise a cloud. Charged particles feel a resistance against crossing magnetic field lines in the ISM. Friction between the ions and the neutral particles slows down the gravitational contraction of the cloud in directions perpendicular to the field lines. In turn, the cloud begins to form a flattened structure (Mouschovias, 1976).

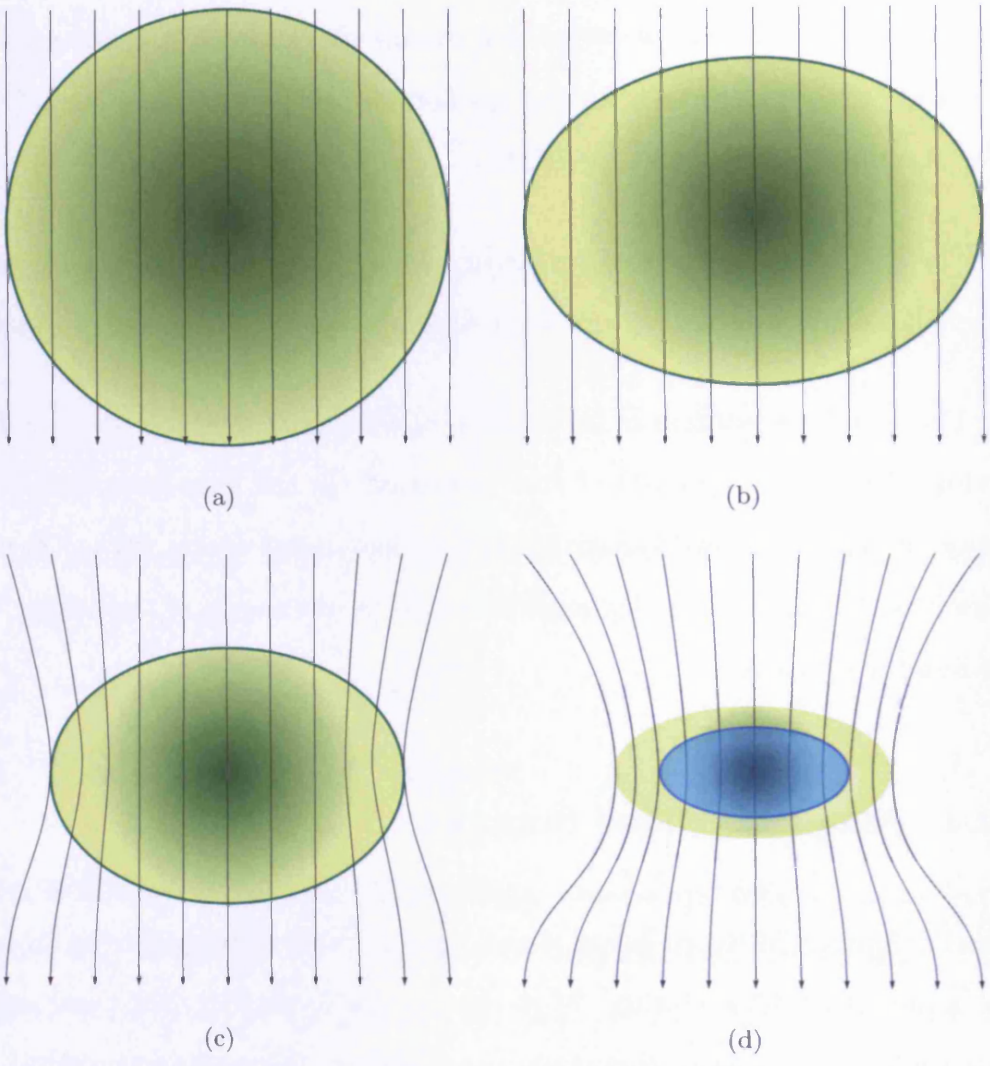

Figure 1.3: Schematic of cloud collapse under the influence of a magnetic field. (a) A cloud threaded by a weak magnetic field. (b) Charged particles in the cloud temporarily support it against collapse, perpendicular to the field, flattening its shape. (c) As gravitational collapse overcomes magnetic support, the magnetic field lines are dragged inward. (d) The neutral particles (shown in blue) move past the charged ions in a process called ambipolar diffusion. Eventually the mass within the blue region is large enough that the magnetic field can no longer support the cloud against collapse to form a protostar (after Mouschovias, 1976).

Assuming the magnetic field is initially weak compared to the gravitational field, the cloud may continue to contract, dragging the field lines along with it. This process can only continue as long as the force from the magnetic tension is less than that of the cloud's self-gravity. When the two are equal, the collapse cannot continue. In this equilibrium state, a cloud is said to be magnetically critical (Mouschovias & Ciolek, 1999).

In the case of a magnetically subcritical cloud, where gravity is not sufficient to continue the collapse, magnetic flux must be removed for the collapse to continue. This is achieved through a process called ambipolar diffusion, where the neutral particles flow past the ions (Mestel & Spitzer, 1956). A magnetically subcritical cloud evolves quasi-statically until it has built up enough mass to form a supercritcal core. At this point gravity overcomes the magnetic field and dynamical collapse can continue — see Figure 1.3.

The time-scale for the collapse of a supercritical core is modified from the freefall time by collisions between neutral and ionized particles (Mouschovias & Ciolek, 1999). As the cloud collapses, although the magnetic field may keep the more centrally condensed parts supported, the outer parts may still collapse. Eventually, as the cloud evolves, the field can no longer support the cloud.

1.3 Prestellar Cores

In this section I discuss the research and history of prestellar cores, the progenitors to protostars. Their discovery and known physical properties are outlined. Myers, Linke, & Benson (1983) selected 90 regions of high optical extinction from the Palomar Observatory Sky Survey. In each they observed extinction maxima in

^{13}CO and $C^{18}O$ with a 1.9 arcminute resolution. This study showed that within such dark, obscured regions, there are dense cores with masses 10–250$M_{\odot}$ and sizes 0.4–4pc. A follow-up survey in ammonia (Myers & Benson, 1983) found cores of mass 0.5 to 10$M_{\odot}$ and size 0.05 to 0.3pc. Some of these cores correlated with the positions of known T-Tauri stars.

Beichman et al. (1986) correlated the IRAS sky survey with the positions of the CO and NH_3 cores and found that half of them contained infrared point sources. Of these, one third were also optical T-Tauri stars. Those without infrared sources were named 'starless' cores.

Ward-Thompson et al. (1994) surveyed 21 of the closer starless cores in ^{13}CO on the JCMT on Mauna Kea. Peaks of column density were found for 17 of them. These were then observed using the JCMT (at 450μm, 850μm and 1.1mm) and IRAM (at 1.3mm). Each was found to have a mass at least comparable to its virial mass, indicating that some may be gravitationally bound. The virial mass is the mass required for the self-gravity of a core to match its turbulent and thermal pressures. Hence it is a useful quantity and is formally defined in Section 1.2.2 above.

The lack of an IRAS point source and the shape of the spectral energy distribution (SED) mean that there is no evidence for a central protostar in starless cores. The luminosity is consistent with thermal emission due to heating by the interstellar radiation field (Ward-Thompson, André, & Kirk, 2002).

Ward-Thompson et al. (1994) called the densest of the starless cores pre-protostellar cores. This name has subsequently been shortened to just 'prestellar' cores. They can be regarded as the subset of starless cores which are gravitationally

bound (Di Francesco et al., 2007; Ward-Thompson et al., 2007).

1.3.1 Density Profiles

Ward-Thompson et al. (1994) found that the density profiles of prestellar cores were more centrally condensed than constant density spheres but less so than those of an inverse square density profile. They suggested a flatter profile $\rho(r) \propto r^{-1.25}$ at the centre which steepens to $\rho(r) \propto r^{-2}$ beyond a radius of around 4000AU.

Subsequent maps at improved resolutions confirmed that the profile was flatter at the centre (André, Ward-Thompson, & Motte, 1996; Ward-Thompson, Motte, & André, 1999). Mid-infrared absorption studies also agreed (Bacmann et al., 2000) and showed that for some cores the profile was seen to steepen again at 10,000 AU or beyond to r^{-3} or r^{-4}.

When mapped at high enough resolution, prestellar cores show an inner, flattened dense region (Ward-Thompson et al., 1994; André et al., 1996; Ward-Thompson et al., 1999). Protostellar envelopes are generally centrally condensed (Motte, André, & Neri, 1998). Ward-Thompson et al. (1999) reasoned that this change in the density profile occurs at the end of the life of the prestellar core.

Ebert (1955) and Bonnor (1956) describe an isothermal sphere confined by external pressure and supported against self-gravity. The stability of such a sphere is determined by the ratio of the core radius to the radius exhibiting a flatter density profile. The stable equilibria of Bonnor-Ebert spheres are determined by the external pressure; they can be defined by this ratio. Barnard 68 (see Figure 1.4) is an isolated, low-mass core which according to Alves, Lada, & Lada (2001) is best described as a critically stable Bonner-Ebert sphere. Alves et al. (2001) used this

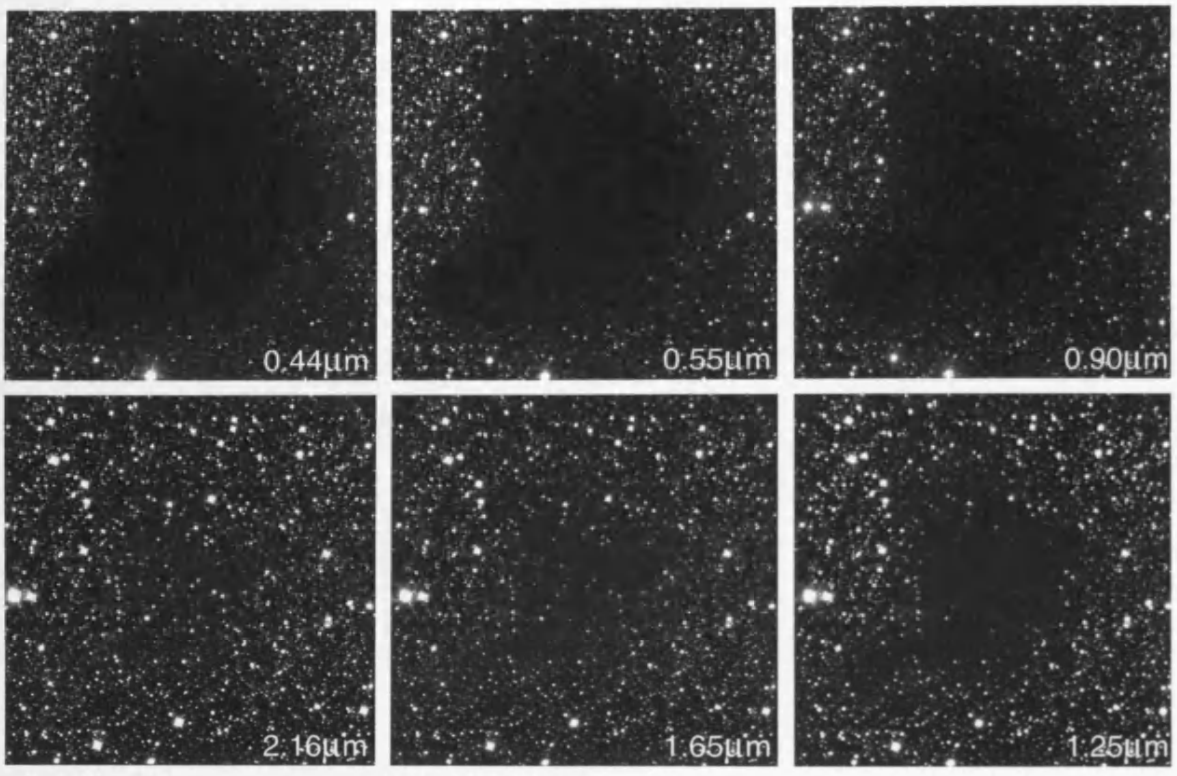

Figure 1.4: European Southern Observatory images of the dark cloud Barnard 68 at six different wavelengths.

to show that B68 was in equilibrium.

However, Bonnor-Ebert spheres are not the only possible description of the mass-radius relation of such cores. Ballesteros-Paredes, Klessen, & Vázquez-Semadeni (2003) ran simulations which suggested that many cores can resemble Bonner-Ebert spheres but still be far from equilibrium. Whitworth & Ward-Thompson (2001) modelled a prestellar core as a Plummer-like density profile, leading to a subsequent changing accretion rate with time. They found this to be consistent with the properties of core L1544.

1.3.2 Core Temperatures

The molecular cloud in which a prestellar core sits, shields it against much of the interstellar radiation field. Prestellar cores also have no internal heating source and thus are very cold. Ward-Thompson et al. (2002) used ISOPHOT data (at 90, 170 and 200μm) to analyse the far-infrared properties of 18 prestellar cores. All but one showed little or no emission at 90μm, indicating that such objects are very cold, with temperatures around T=10–20K. It was shown that on a scale comparable to the resolution of SCUBA, these cores were isothermal.

ISOCAM absorption data, from Bacmann et al. (2000), allowed Ward-Thompson et al. (2002) to calculate the energy balance for these prestellar cores. It was shown that they are externally heated by the interstellar radiation field. Using additional data from SCUBA (at 450 and 850μm) and IRAM (at 1.3mm), they were also able to create SEDs. These were used to fit modified blackbody functions of the form:

$$F_\nu = B_{\nu,T}(1 - e^{-\tau_\nu})\Omega, \tag{1.7}$$

where F_ν is the flux density at frequency ν, $B_{\nu,T}$ is the blackbody function at frequency ν and temperature T, τ_ν is the dust mass opacity at frequency ν, and Ω is the solid angle over which the flux is received. They found good fits to observations for T=10–15K.

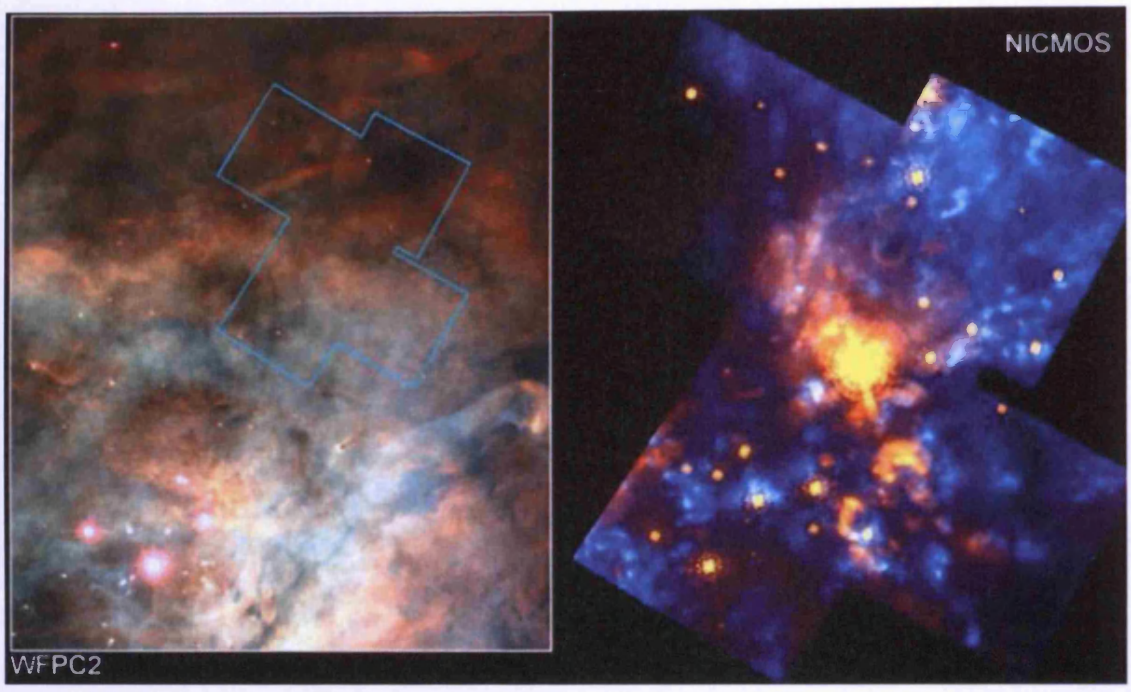

Figure 1.5: Hubble Wide Field Planetary Camera 2 (WFPC2) image of the giant Orion Molecular Cloud 1 (OMC-1). Protostars are revealed within the nebula, using Hubble's Near-Infrared Camera and Multi-Object Spectrometer (NICMOS). The footprint of the NICMOS image is shown as a blue outline on the WFPC2 image. Source: R. Thompson (U. Arizona) et al., NASA, http://antwrp.gsfc.nasa.gov/apod/ap000506.html

1.4 Protostars

Once a prestellar core has evolved and become a centrally condensed, hydrostatic object, it has formed a protostar. At this point it undergoes a fairly well understood evolution. This is discussed in this section, as well as an estimation of protostellar lifetimes.

1.4.1 Early Stages of Protostars

Once a protostar has formed, what remains of the core will accrete onto a circumstellar disk and eventually onto the star itself, or will be pushed outward from the

star by the emerging radiation pressure. Ultimately the star accretes most of the mass in the system from the envelope surrounding it (André, Ward-Thompson, & Barsony, 2000).

Protostars remain embedded within their progenitor molecular clouds after they have begun to form (Ambartsumian, 1958). As protostars accrete material and collapse, they produce bipolar molecular outflows (e.g. Bachiller, 1996). These are usually seen in CO. They are often coincident with Herbig-Haro (HH) objects and jets, which are the optical counterpart of the outflow. HH objects are seen by emission shocks in molecular hydrogen (Herbig & Jones, 1981). Protostars are also detected in centimetre emission, arising from free-free emission at shock fronts either on the protostar surface or at the edges of the outflow (Neufeld & Hollenbach, 1996).

The four classes of a protostar's life, denoted 0, I, II and III (André, Ward-Thompson, & Barsony, 1993; Lada, 1987), make up the evolutionary sequence of the protostar. Class III protostars subsequently move onto the Main Sequence and become a star. These classes are described in the following sections. Figure 1.8 gives a graphical representation of the changing shape of the SED during a protostar's evolution.

1.4.2 Class 0 Protostars

André et al. (1993) discovered the first Class 0 object in the ρ Ophiuchus molecular cloud complex. Class 0 objects are defined as having accreted less than half of their final main sequence mass, i.e. $M_\star < M_{env}$. They also have no detectable infrared counterpart. Class 0 protostars are distinguished from others by their large submm

luminosity (L_{smm}) compared to their bolometric luminosity (L_{bol}) — André et al. (1993). L_{smm} is defined as the luminosity longward of 350μm, and is proportional to the mass of the circumstellar envelope. André et al. (1993) used the equation,

$$L_{bol} = \frac{GM_*\dot{M}_{acc}}{R_*}, \tag{1.8}$$

to estimate M_* based on L_{bol}. M_* and R_* are respectively the mass and radius of the central object. $\dot{M}_{acc}$ is the accretion rate. G is the gravitational constant. It is possible to find L_{smm}/L_{bol} and thus infer M_{env}/M_*.

The circumstellar envelope around a protostar is centrally peaked and has a density profile of the form,

$$\rho(r) \propto r^{-p}, \tag{1.9}$$

where p~1.5-2 (Motte et al., 1998; Motte & André, 2001). This holds until the envelope merges into the ambient cloud at its outer edge.

The outer radius of the envelope is determined by the environment in which the protostar sits. For example, in the clustered ρ Oph star forming region the envelope can be < 5,000 AU (Motte et al., 1998). By comparison, in the Taurus isolated star formation region the protostars are more widely spaced and the envelope sizes are found to be around 10,000-15,000 AU (Motte & André, 2001).

Class 0 sources undergoing gravitational collapse display an asymmetry in their spectral line profiles due to their thick surrounding envelopes. We preferentially see material that is closer to us. Material on the near-side of a collapsing core is

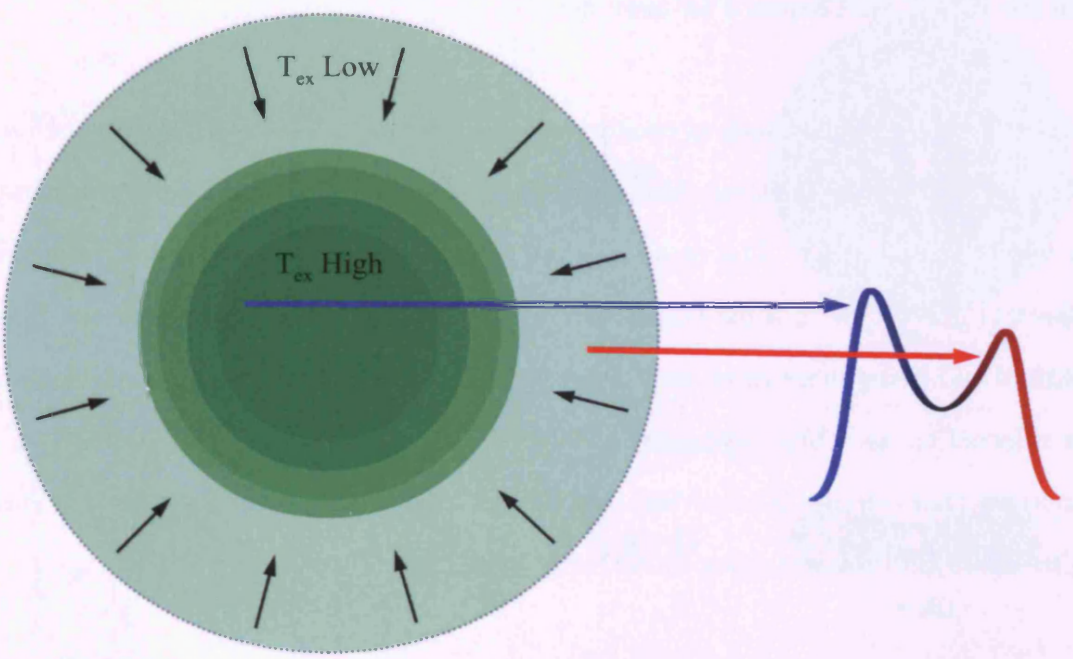

Figure 1.6: Illustration of the origin of the blue-asymmetric double peaked spectral line profile. An observer always preferentially sees material that is closer. For the relatively red-shifted material this means preferentially seeing the lower excitation temperature part of the core. For the relatively blue-shifted material, the higher excitation temperature region is preferentially seen. See text for details.

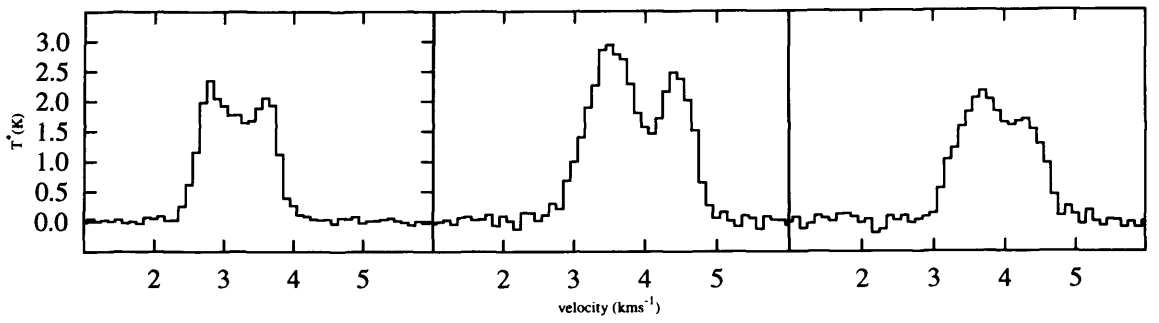

Figure 1.7: Three examples of blue-asymmetric double-peaked profiles taken using HARP on the JCMT. See Chapter 4 for more details.

therefore preferentially seen as cooler than material on the far side (see Figure 1.6). This means that the relatively blue-shifted material is seen to the observer as having a higher temperature. The result is that collapsing cores display an asymmetric spectral line profile in some transitions, with the peak from material at the blue-shifted end being more prominent than the red-shifted peak. Such a profile shape is referred to as a blue-asymmetric double-peaked profile and can be used as a signpost that collapse is occurring (see Figure 1.7). This is an indication that such Class 0 objects may be going on to form stars.

1.4.3 Protostellar Evolution, SEDs and Classes

Classes I, II and III were defined from the Lada & Wilking (1984) ρ Oph survey. These classifications are defined by the spectral slope α_{IR} of the SED between 10 and 25μm. α_{IR} is defined as

$$\alpha_{IR} = \frac{dlog(\lambda F_\lambda)}{dlog(\lambda)} \tag{1.10}$$

The wavelength range over which α_{IR} is measured was subsequently changed to

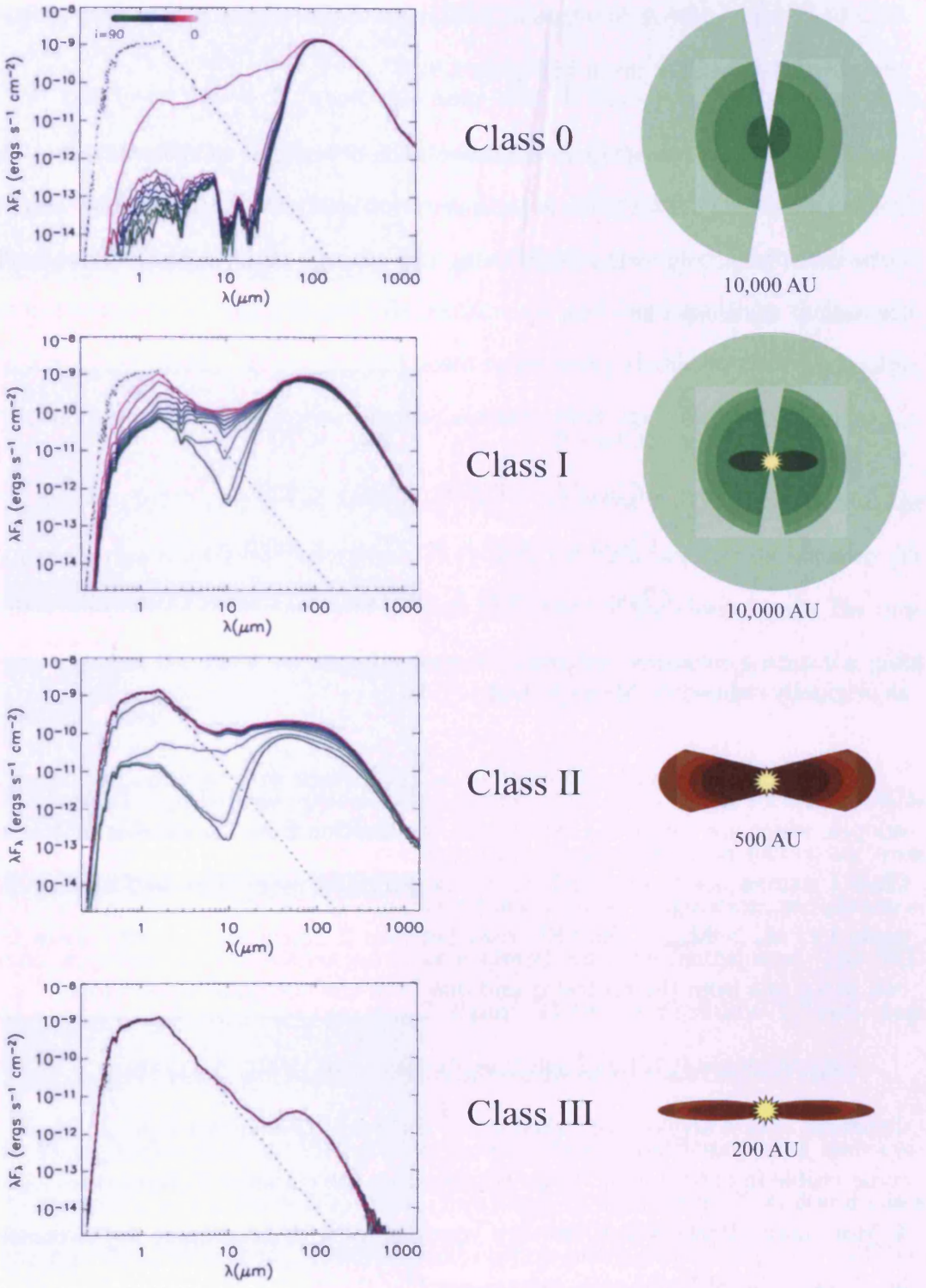

Figure 1.8: Illustration showing the evolving SED of a protostar through Classes 0, I, II and III from Whitney et al. (2003). The approximate physical size in AU and a simple schematic of the structure are also shown.

be 2 to 25μm (André & Montmerle, 1994). Examples of the SEDs of the different protostellar classes are given in Figure 1.8.

An alternative evolutionary indicator is the bolometric temperature, T_{bol} (Myers & Ladd, 1993). This is the temperature a blackbody would have if it had the same mean frequency as the SED. Using this concept, the range of values for T_{bol} for each of the classes is:

$$\begin{array}{lrll} Class\ 0 & & T_{bol} & < 70\ K \\ Class\ I & 70\ K < & T_{bol} & < 650\ K \\ Class\ II & 650\ K < & T_{bol} & < 2880\ K \\ Class\ III & 2880\ K < & T_{bol} & \end{array} \tag{1.11}$$

as originally defined by Myers & Ladd (1993).

Class I objects can be thought of as protostars with surrounding large envelopes, which are still in the main phase of accretion from the envelope. However, Class I sources are those which have now accreted more than half of their final mass, i.e. $M_* > M_{env}$. The SED rises between 2–25μm and broadly arises from two parts, one from the protostar and one from the surrounding envelope.

Class II objects are those where the envelope mass has either been accreted or dispersed. These are no longer sheilded by their protostellar envelopes and have become visible in optical light. Class II protostars are classical T-Tauri stars (André & Montmerle, 1994), which are very young stars with accompanying circumstellar disks. The SEDs of such sources are like those of a blackbody but with an additional large, infrared excess generated by the optically thick dust around the protostar. The slope of the SED has now flattened between 2–25μm, or possibly

become negative.

It has been known for many decades that T-Tauri stars are younger than main sequence stars. These very young stars were discovered by Joy (1945) and are named after the prototypical object in Taurus. They are characterised by their irregular variability; strong Hα emission and lithium absorption; their excesses in the ultraviolet (UV) and infrared (IR) continuum; and importantly by their association with nebulosity. T-Tauris are known to be young thanks to their association with short-lived O-associations (Ambartsumian, 1958, and references therein).

Herbig (1977) and Jones & Herbig (1979) surveyed the T-Tauri stars in the Taurus-Auriga dark cloud complex. They found a tight association between the proper motions of these very young stars and those of the cloud itself. The conclusion is that the stars, so recently formed, came into existence within the giant molecular cloud.

Class III objects have optically thin circumstellar disks and as such their SEDs are just reddened blackbody functions. The circumstellar disk has either been swept up by forming planets or diminished due to dust coagulation into planetesimals; dispersed by the stellar wind; or accreted onto the central star. The SED has a steep, negative slope between 2–25μm. These are weak-line T-Tauri stars (André & Montmerle, 1994) and will subsequently join the main sequence.

Young stellar objects (YSOs) drive powerful bipolar outflows during their evolution into stars (e.g. Bachiller, 1996). In a study of outflows in Class 0 and Class I sources, Bontemps et al. (1996) showed outflow momentum flux (F_{CO}) in Class 0 sources is ten times the level seen in Class I sources, given a linear relation in L_{bol}. F_{CO} is also shown in this study to be correlated with the envelope mass

M_{env}. This suggests that as protostars evolve, their outflows weaken. Accretion is thought to be responsible for powering outflows and so it was hypothesised in this study that accretion may be slowing during evolution.

1.4.4 Protostellar Lifetimes

Jessop & Ward-Thompson (2000) used IRAS data (at 60 and 100μm) to compile a catalogue of molecular cloud cores. Those cores with associated IRAS point sources were seen to be forming stars, but this was a fairly small fraction of the total. The study compared a sample derived from the IRAS catalogue with other samples and deduced a relationship between core lifetime, t_p, and central density $n(H_2)$,

$$t_p \propto n(H_2)^{-0.85\pm0.15}. \tag{1.12}$$

Wilking et al. (1989) used relative number counts of objects in Ophiuchus to establish lifetimes. They estimated the age of the Class II sources in the region to be roughly 0.4 Myr by calculating the Kelvin-Helmholtz contraction time since the end of the accretion phase (Thomson, 1892). They also found approximately equal numbers of Class I and Class II sources, suggesting equal lifetimes. Greene et al. (1994) found from one quarter to three quarters as many Class I sources as Class II in Ophiuchus, suggesting that the Class II phase is longer than Class I.

Kenyon & Hartmann (1995) showed that the situation in the Taurus region was completely different. They found roughly 10 times as many Class II and Class III sources as Class I. By comparison to evolutionary tracks, they suggested Class

II plus Class III lifetimes to be of the order of 2 Myr. This is consistent with recent studies by Cieza et al. (2007) and Spezzi et al. (2008).

However, relative population counting is not an ideal approach. It assumes that star formation in the counted region has been continuous and steady for as long as the oldest members of the population. It assumes that other variables are not relevant, such as the available mass or the local conditions (e.g. turbulence). It is most problematic when there are low numbers of objects available. Nevertheless, it remains the best tool for estimating the relative lifetimes of protostellar phases.

The earliest estimates for the lifetime of Class 0 objects — 0.01 Myr — were based on the very small number of objects in Ophiuchus (André et al., 1993). These first Class 0 discoveries had powerful collimated outflows and thus suggested a rapid accretion rate (André et al., 2000). The Class 0 phase appears to be a relatively short, energetic phase following the formation of the central hydrostatic object. More than half the mass of the final object is accreted during this part of the protostar's life.

Most of these estimates were based on samples of 50-100 objects and are fairly cloud-specific. The c2d Spitzer Legacy project (Evans et al., 2009) used images and photometry from the IRAC and MIPS instruments to measure the properties of over 1000 YSO sources in five large, nearby molecular clouds (Serpens, Perseus, Ophiuchus, Lupus and Chamaeleon).

Evans et al. (2009) derive updated lifetimes for the prestellar and protostellar phases by averaging across all the clouds — although it should be noted that stark cloud-to-cloud differences exist. Notably the cores in Ophiuchus appear to live shortened lives by a factor of 2–3. These lifetimes are shown in Table 1.1.

Table 1.1: Table of lifetimes (in Myrs) of the different phases of prestellar and protostellar evolution based on Evans et al. (2009)

Prestellar	Class 0	Class I	Class II	Class III
0.61	0.16	0.38	1.4	0.29

1.5 The Stellar IMF

The distribution of stellar masses at the moment they join the main sequence is referred to as the initial mass function (IMF). The IMF has dramatic consequences for the evolution of the parent cloud, the ISM and the whole galaxy. The mass-to-light ratio of distant galaxies also depends on the IMF. Thus the IMF is an important topic in many areas of astronomy and cosmology.

1.5.1 History of the IMF

The first measure of the IMF was by Salpeter (1955). He found that in the solar neighbourhood, between 0.4 $M_\odot$ and 10 $M_\odot$, the IMF is a power law of the form

$$M\frac{dN}{dM} \propto M^{-1.35}. \tag{1.13}$$

For high mass stars (>10 $M_\odot$), the IMF is consistent with Salpeter up to 120 $M_\odot$ (Massey, 1998). The scatter of the slopes observed is larger here; this could be actual variation or simply the accuracy of the methods used. For example, surveys are often employed to find distant stars that do not account for the binary fraction.

For low mass stars (0.08 $M_\odot$ to 0.5 $M_\odot$) the IMF slope is -0.3 ± 0.5 (Kroupa, 2001). For very low mass stars (<0.08 $M_\odot$) the slope appears to turn over to be about +0.5 (Martín et al., 2000; Chabrier, 2003). At these lower masses, IMF studies generally use much more nearby stars and so the binary fraction is accounted for. A sketch of the IMF is shown in Figure 1.9.

1.5.2 Origin of the IMF

The IMF seems to be universal, meaning that it is observed to have approximately the same form in most regions in which it is observed. This universality is at odds

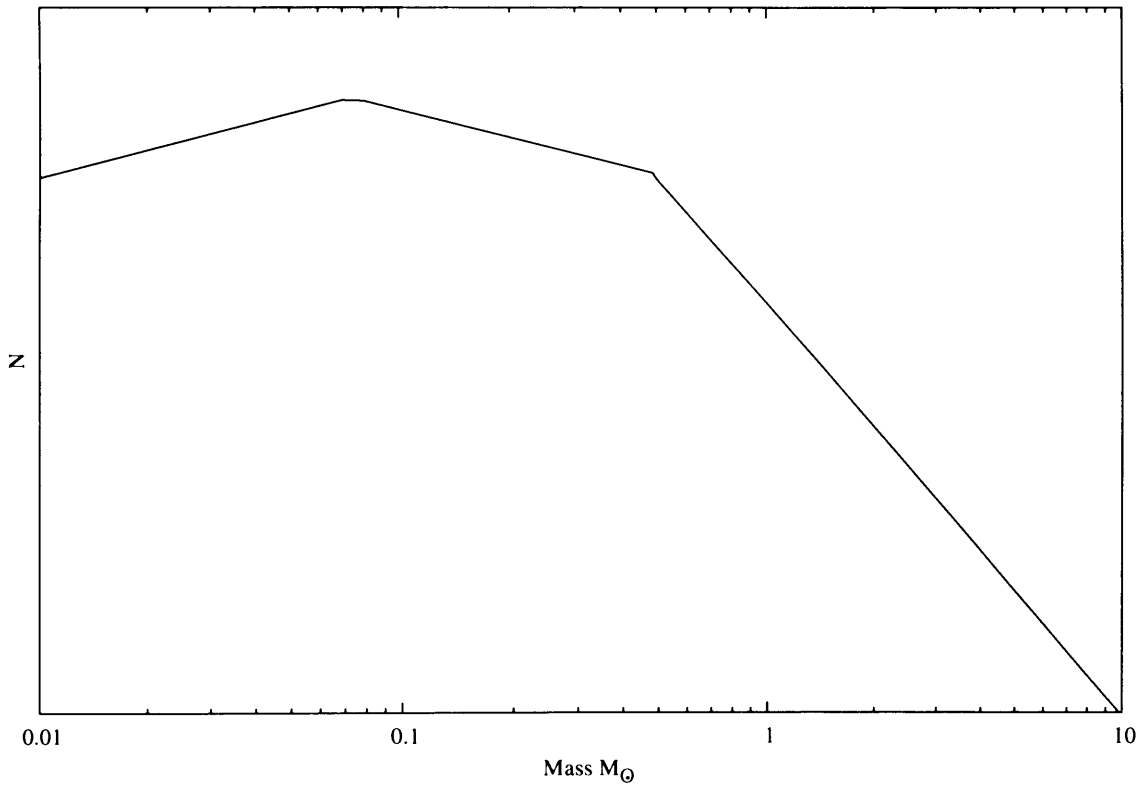

Figure 1.9: Diagram showing the piecewise power-law form of the stellar Initial Mass Function (IMF) between 0.1 and 10 $M_\odot$. This three-part power law form of the IMF is made up of slopes (from the right) from Salpeter (1955), Kroupa (2001) and Chabrier (2003). See text for more details.

with models that suggest the IMF should vary with the pressure and temperature of the region where the stars are forming (Larson, 1998; Kroupa, 2001). Whilst it is true that some exotic galaxies — e.g. NGC 3603 (Eisenhauer et al., 1998) — do have different IMFs, these are usually in extreme and difficult-to-measure situations. On the whole the IMF does appear to remain constant regardless of location, although some variations are seen (e.g. Eisenhauer et al., 1998).

Chabrier (2001) reasoned that the origin of the IMF must be inherent in the properties of the original cloud fragments. Bonnell et al. (2001) suggested that the IMF is determined by dynamical effects such as competitive accretion. Bacmann et al. (2000) used mid-infrared data to show that some prestellar cores appear to be decoupled from their parent clouds, meaning they have only finite reservoirs of mass for subsequent star formation. This would in turn affect the IMF.

Motte et al. (1998) surveyed prestellar cores in ρ Oph and found a core mass function (CMF). Their CMF showed the same slope as the Salpeter IMF but shifted in mass. This has led many to suggest that the IMF is actually determined at the prestellar core stage (Ward-Thompson et al., 2007).

Further work on this was performed by Nutter & Ward-Thompson (2007), who found not only that the CMF for the Orion region showed a similar shift along the mass-axis, but also that a turnover in the form of the CMF — similar to that in the IMF — was also observed. This further adds to the notion that the IMF originates in the prestellar core phase. The relationship between the Stellar IMF and the CMF has not yet been fully explained, although there are a number of theories that have been proposed (e.g. Hennebelle & Chabrier, 2008).

1.6 Summary and Thesis Overview

In this chapter I have discussed our current understanding of the star formation process. The measured physical properties of molecular clouds, prestellar cores and protostars have been outlined. I have explained the basics of current models of cloud collapse and support. The universal stellar IMF and observed CMFs have been discussed, along with the possible relationship between them.

The outline of the rest of the thesis is as follows: Chapter 2 describes the methods and instrumentation used to obtain the data in this thesis. The telescope used was the James Clerk Maxwell Telescope in Hawaii. The instruments used were the SCUBA submillimetre continuum array camera and the HARP spectral imaging instrument.

In Chapter 3, 850 μm archive SCUBA data of the L1688 dark cloud in the Ophiuchus region are presented. The prestellar and protostellar cores are identified and their radii and masses are measured and calculated. This includes the identification of several new prestellar cores. These data are used to produce a core mass function. This is compared to other work in the literature, and to the stellar IMF.

Chapter 4 presents HARP spectral line maps of the same region, L1688, and analyses the line profile shapes to determine the nature of the previously identified SCUBA cores.

In Chapter 5, I present a simple model of molecular cloud collapse. This model is used to estimate some of the physical properties of the cores in L1688 and compared to the observations in Chapters 3 and 4.

In Chapter 6, I discuss the implications of the results and draw conclusions related to the evolution of prestellar cores. Chapter 7 presents a summary of the thesis and outlines future work.

Chapter 2

Observations and Data Reduction

In this chapter I discuss the methods, instruments and facilities used to obtain the submillimetre data analysed in Chapters 3 and 4. I also outline the data reduction software and techniques used to produce useful maps from the raw data.

2.1 Instrumentation

2.1.1 The James Clerk Maxwell Telescope

At submillimetre wavelengths, where the data used in this thesis were obtained, the sky is opaque due to water vapour in the atmosphere. At very high, dry locations the transmission of such radiation through the atmosphere can improve to as much as 80% and submillimetre observations can be made. One such location that is ideal for submillimetre astronomy, is Mauna Kea, a 4200-m high volcano on the Big Island of Hawaii.

Figure 2.1: The James Clerk Maxwell Telescope (JCMT) on Mauna Kea, Hawaii. The JCMT is the largest single-dish telescope dedicated to submillimetre astronomy in the world.

The James Clerk Maxwell Telescope (JCMT) is one of the world's largest submillimetre astronomy facilities (see Figure 2.1). It operates between 200 μm and 2 mm and sits above 97% of the atmosphere's water vapour for much of the time. The JCMT's 15-m primary mirror means that at the principal operating wavelengths of 450 μm and 850 μm it has a resolution of 8″ and 14″ respectively.

The JCMT is a Cassegrain/Nasmyth design with an alt-az mount. A rotating tertiary mirror allows the beam to be directed to any one of a variety of instruments. These fall into two types: heterodyne receivers (e.g. HARP) measuring molecular spectral line emission; and the Submillimetre Common-User Bolometer Array (SCUBA), which measures continuum emission. The JCMT is run by the Joint Astronomy Centre (JAC), in Hilo, Hawaii. The project is funded by the UK (55%), Canada (25%) and the Netherlands (20%).

2.1.2 SCUBA

SCUBA is a dual-camera system utilising 91 short-wavelength pixels and 37 long-wavelength bolometer pixels in two separate hexagonal arrays. Both of these arrays have a field of view of 2.3 arcmin in diameter and can be used simultaneously. Additionally the long-wavelength array has single pixels at 1.1, 1.35 and 2.0 mm which can be used for photometry. The SCUBA bolometers on the JCMT were cooled to 100 mK (Holland et al., 1999).

Bolometers are made using absorbers of known specific heat capacity, C, thermally connected to a fixed-temperature heat sink. Incident energy, E (in this case submillimetre photons), causes the temperature of the absorber to rise by some small, but predictable temperature, δT. This change in temperature alters the

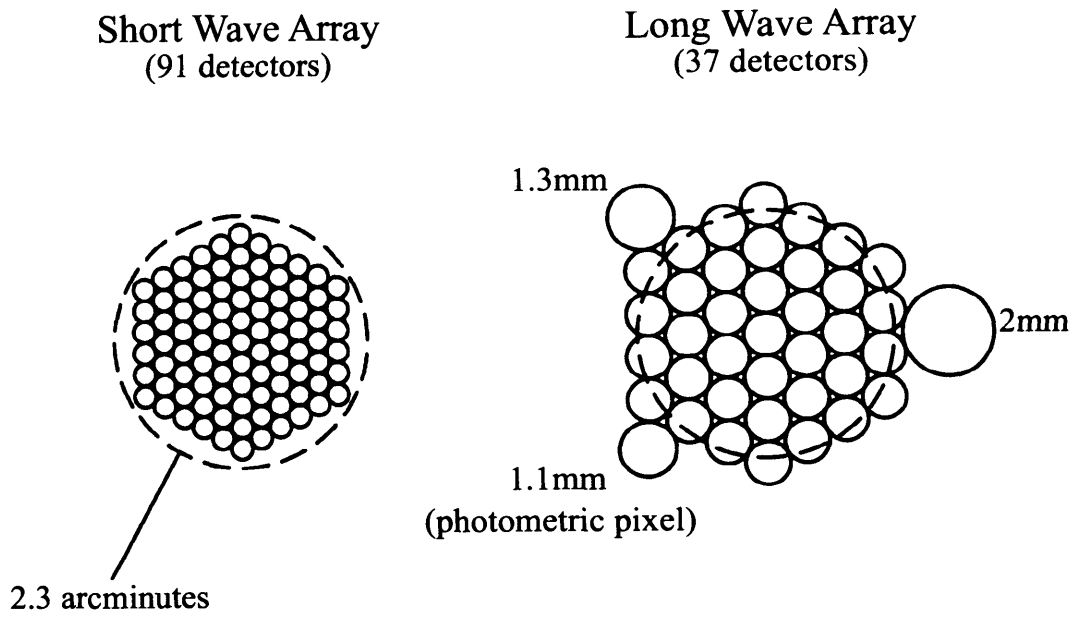

Figure 2.2: Schematic of the SCUBA short- and long-wave bolometer arrays from Holland et al. (1999).

resistance, R, and therefore the voltage, V, across the device. Hence

$$\delta V \propto \delta R \propto \delta T = \frac{E}{C}. \tag{2.1}$$

The submillimetre beam is coupled to the detectors by conical feedhorns, optimised for use at 450 μm and 850 μm (see Figure 2.2). In order to fully sample the beam, the detector array must be moved relative to the incoming radiation. There are two ways to do this: one is to 'jiggle' the secondary mirror to fill in the gaps in the focal plane; the other is to raster the array across the sky. These are discussed in the following section.

SCUBA was mounted on the left-hand Nasmyth platform of the JCMT from

1996 to 2005. The operation and design of the instrument is explained in detail by Holland et al. (1999). A public data archive exists at the Canadian Astrophysics Data Centre (CADC), containing all of the observations that SCUBA made. A complete, standardised re-reduction was made to create the SCUBA Legacy Catalogue, which is also available at the CADC (Di Francesco et al., 2008).

SCUBA was particularly good at detecting the thermal emission from cold dust (3 to 30 K) in the Universe. SCUBA detected a range of high-redshift galaxies (e.g. Ivison et al., 1998; Cimatti et al., 1998), revealed the population of galaxies responsible for at least part of the far-infrared background (e.g. Smail, Ivison, & Blain, 1997; Barger et al., 1998; Hughes et al., 1998; Eales et al., 1999), discovered potential protoplanetary systems (e.g. Holland et al., 1998; Greaves et al., 1998), mapped a great number of molecular cloud complexes and outflow regions (e.g. Davis et al., 1999; Johnstone et al., 2000; Nutter & Ward-Thompson, 2007), and, most importantly for this thesis, enabled the discovery and exploration of new populations of Class 0 protostars and of prestellar cores (e.g. Ward-Thompson et al., 2000; Motte et al., 2001; Kirk, Ward-Thompson, & André, 2005).

The era of SCUBA was a golden age in submillimetre astronomy. SCUBA offered mapping capabilities some 10,000 times greater than that of UKT14, its immediate predecessor, as well as an extensive wavelength range and field of view. The science that it facilitated was ground-breaking, as shown above. Since 2005, the community has been waiting for SCUBA-2, the faster, more efficient successor to SCUBA, which at time of writing has had first light and taken test data. SCUBA-2 is expected to begin scientific operation in 2010, some five years after SCUBA was removed from the telescope.

2.1.3 HARP

HARP (Heterodyne Array-Receiver Program) is a heterodyne focal-plane array receiver designed and built for operation on the JCMT (Smith et al., 2003, 2008; Buckle et al., 2009). It works with the ACSIS backend — Auto-Correlation Spectral Imaging System (Dent et al., 2000; Hovey et al., 2000; Buckle et al., 2009) — correlator to achieve high spectral, and hence velocity, resolution (0.026 km s^{-1}). It has the same spatial resolution as SCUBA at 850μm (Holland et al., 2006). HARP was installed on the right-hand Nasmyth platform of the JCMT and achieved first light in 2005.

HARP provides a 3-dimensional imaging capability in the 325 – 375 GHz range, meaning that it is capable of observing the energy transitions of some of the most abundant molecules in the ISM. The HARP imaging array consists of 16 SIS detectors arranged in a 4x4 grid, separated by 30 arcsec between adjacent pixels. The beam size is 14 arcsec at 345 GHz, which means this array arrangement under-samples the focal plane with respect to Nyquist sampling and further data points must be taken in between the nominal on-sky positions to produce a fully-sampled map.

HARP works in single sideband mode, with typical receiver noise temperatures under 150 K (Buckle et al., 2009). The K-mirror rotates the array with respect to the plane of the sky to maximise the observing efficiency, allowing large scan-maps to be made with the array oriented at an angle to the scan direction. ACSIS provides either wide-band (up to 1.9 GHz wide) or high-resolution spectra (up to 31 kHz channels). HARP also allows simultaneous imaging of two close-together transitions by splitting the frequency range into two sub-bands.

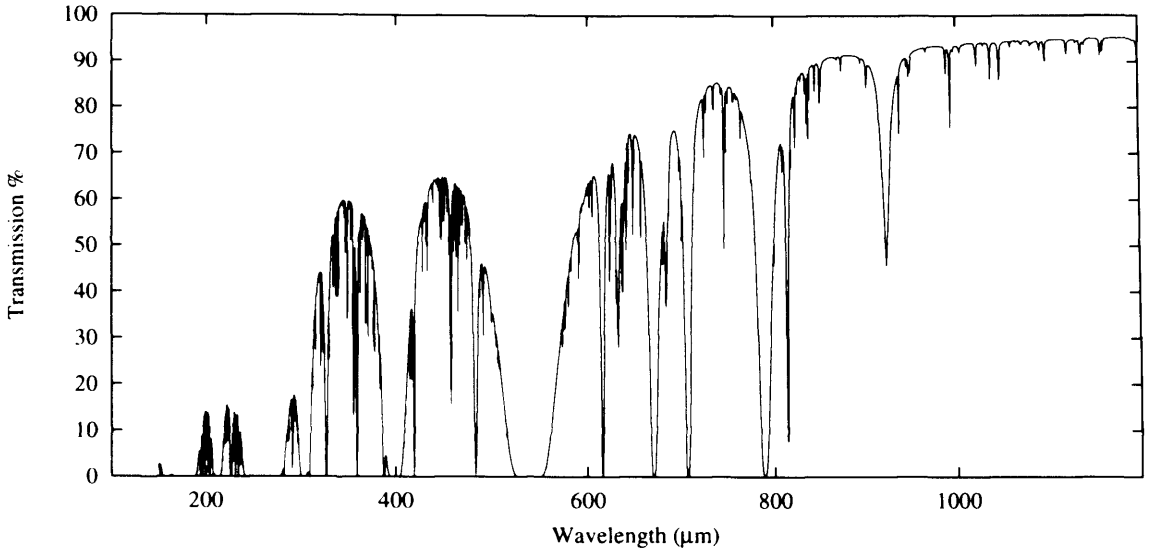

Figure 2.3: Atmospheric transmission on Mauna Kea through 0.3 mm of water vapour.

2.2 Continuum Observing Methods

2.2.1 Chopping and Nodding

The summit of Mauna Kea is very high and dry but still not all submillimetre radiation can pass through it. The JCMT's 15-m primary mirror can only take advantage of certain atmospheric transmission 'windows' (see Figure 2.3). As well as attenuating submillimetre radiation, the atmosphere is always emitting it too. This sky emissions is generally many orders of magnitude more intense than any astronomical signal and as such needs to be removed from observations, even at the JCMT. The standard method for removing sky emission in the submillimetre and infrared is to 'chop' and 'nod' the telescope (Glass, 1972; Papoular, 1983).

Chopping is the process by which the array is alternately shown the target and a blank piece of sky by oscillating the secondary mirror. The sky beam can then be subtracted from the target beam, thus removing the sky emission. To make

this process most efficient, the distance between the two beams — known as the chop throw — should be as small as possible, whilst ensuring that the sky beam is truly off source. A typical chop throw would be 120 arcsec. Choosing the right chop throw can be particularly tricky when observing targets within molecular clouds, where extended emission surrounds the desired signal. Ideally, chopping should occur on a timescale shorter than the typical atmospheric variation, though this is often impossible and a compromise must be made. The standard chopping frequency is approximately 7.8 Hz (Holland et al., 1999).

Nodding is achieved by moving the primary mirror just enough to place the source at the former location of the sky beam, and to thus provide a new sky beam on the opposite side of the source. This removes asymmetries between the two beams and any linear gradients in sky emission. The primary is nodded at a rate of 0.1 Hz.

Chopping and nodding combine to provide the best method of sky noise removal. Although it is not perfect, this method removes the majority of problems and the resultant data can be used to produce excellent maps through post-observation processing.

2.2.2 Jiggle-mapping

For extended sources that are smaller than the field of view of the SCUBA arrays, jiggle-mapping is the preferred observing mode. The SCUBA bolometers are arranged such that the sky is under-sampled in any instantaneous observation. 16 offset positions are required to created a fully-sampled map (see Figure 2.4). If using both of SCUBA's hexagonal arrays, a 64-point jiggle pattern

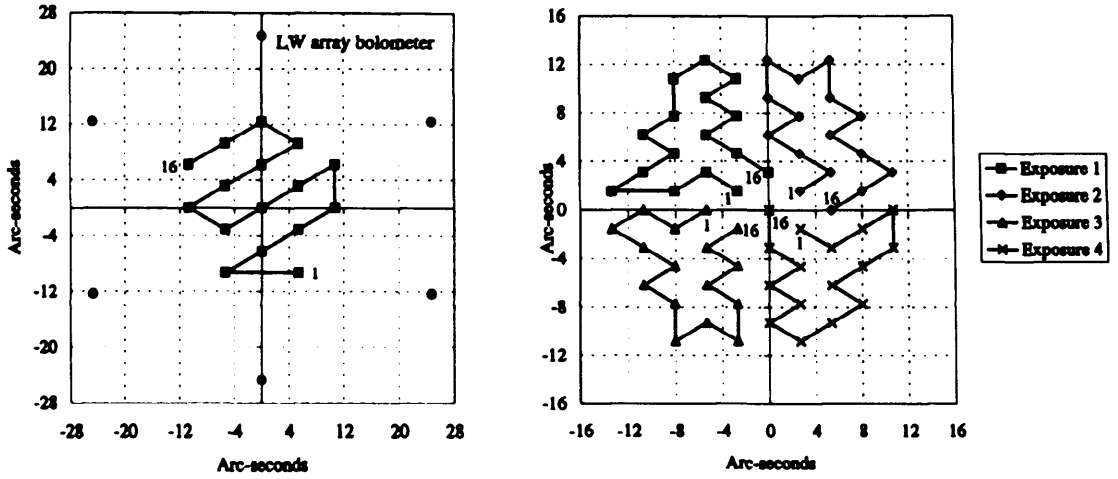

Figure 2.4: SCUBA jiggle-map patterns from Holland et al. (1999).

is required because of the difference in spacing between the short-wavelength and long-wavelength bolometer arrays (see Figure 2.2).

Each position in the jiggle pattern is given one second of integration time, half of which is off-source because of the chopping. The telescope is also nodded, meaning that the point is repeated again, with the new off-source position. As such, the single-array, 16 point jiggle pattern takes 32 seconds to complete and the dual-array mode takes 128 seconds.

2.2.3 Scan-mapping

Scan-mapping is used to map regions that are larger than the field of view of the SCUBA arrays. The telescope is scanned across a region, whilst chopping, to produce a differential map of the source that is up to several arcmin long, but only the width of the array. Additional strips can be added in a raster pattern to produce a larger map of a region.

The telescope is scanned at a rate of 24 arcsec/s with a chop frequency of 7.8 Hz, giving roughly 3-arcsec sampling along a scan length. An overlap of half an array-width between adjacent rows is usually adopted to create the best map. The SCUBA arrays have to be scanned at an angle of $15.5° + N \times 60°$ to the array to produce a fully sampled map, where $N = 0 \rightarrow 5$. This is because of the hexagonal shape of the array and the separation of the bolometers.

The best scan-mapping method is that described by Emerson (1995). Maps of the same region are taken with several chop throws and in several directions — usually three chop throws, chopping in both RA and Dec. (Holland et al., 1999). The individual maps are Fourier transformed and co-added. Each map is weighted according to the sensitivity of the chop, and then the co-added map is inverse transformed to give the final image.

Jenness, Lightfoot, & Holland (1998) showed that using this 'Emerson II' technique gave a significant improvement over previous scan-mapping methods. Generally six maps are made, three of which are made whilst chopping in R.A. and three in Dec. Chop throws of 20″, 30″ and 65″ are usually used.

2.3 Spectral Line Observing Methods

2.3.1 Position Switching

This is the method whereby the telescope observes alternately the source and a nearby reference position. Using this pair of spectra, the software can obtain a calibrated result with most instrumental and atmospheric effects removed. The integration time spent on a single signal or reference position is a compromise

between observing efficiency and the rate at which conditions change (Matthews, Leech, & Friberg, 2004). It is typically 30 seconds or less.

2.3.2 Beam Switching

In this technique, the secondary mirror is usually chopped at about 1 Hz in the azimuth direction (although chopping in any direction is possible) with the source in one beam. At a slower rate, typically every 10–30 seconds, the telescope is moved by an amount equal to the chop throw, to bring the source into the other beam. This produces both a negative signal (when the source is in the reference beam) and a positive signal (when it is in the signal beam). This technique is effective for sources smaller than the beam throw (Matthews et al., 2004).

2.3.3 Frequency Switching

In frequency switching mode the telescope remains at a fixed position and data are continuously accumulated. The centre of the receiver passband is switched between the signal and an offset frequency separated by a small amount (e.g. 10–20 MHz). If the frequency shift is small enough, the spectral line will appear in both the signal and reference spectra. The spectrum can be 'folded' to obtain a $\sqrt{2}$ improvement in signal-to-noise.

This observing method is ideal for narrow-line (less than a few MHz in width) spatially-extended objects (Matthews et al., 2004). Telescope motion is no longer part of the observing process, thus this method speeds up observations. The primary drawback of frequency switching is that the spectral baselines are generally

not as good as with position or beam switching.

2.3.4 Point-by-Point Mapping

Extended sources can also be mapped by combining multiple observations made using the above methods. The most convenient way to make such observations is by setting up a grid of positions (Matthews et al., 2004). Any number of grids may be combined to make the map. If position-switching is used, the reference position is defined with respect to the map centre and remains unchanged throughout the map, unless changed by the observer.

2.3.5 Raster Mapping

For extended fields with relatively bright line emission, raster mapping is the best observing method. In this mode the telescope is scanned along a line of constant RA with the system continuously integrating incoming signals, forming the average once every few seconds and saving the result. The on-source observing efficiency is up to 75%, compared with about 30% for point-by-point grid maps. Maps can be continuously observed for up to an hour at longer wavelengths when the sky is stable, and a data rate approaching 1000 spectra per hour can be achieved using this technique. Raster mapping runs only in the position-switched mode, with an integration at a user-supplied reference position once at the end of every row.

2.4 SCUBA Data Reduction

SCUBA data are best reduced using the SCUBA Users Reduction Facility (SURF — Jenness & Lightfoot, 2003). This package can be used for both jiggle- and scan-map observations, although some slight difference in the reduction of the two types of data exist. Removal of correlated sky-noise and removal of baselines are the two main regions where the data reduction methods are different. In the following section I will outline the way that SCUBA data are reduced. In the following section, the reduction of HARP data is outlined.

2.4.1 Reduce Switch and Flatfield

The SURF routine REDUCE_SWITCH subtracts the 'sky' beam from the 'source' beam and eliminates most of the sky emission. In the case jiggle-maps this should leave behind only residual sky noise. Since the 'sky' beam for a jiggle-map observation should have no astronomical flux, this routine should also leave jiggle-map entirely positive.

For scan-maps the process is slightly different because the two beams are scanned across the target region. This means that each astronomical object gives rise to both a positive and negative image. For most of the data reduction process, scan-map data remain in the form of a time-series for each bolometer.

The SURF command FLATFIELD is carried out regardless of whether the data is a jiggle- or scan-map. This removes fixed differences between different bolometers.

2.4.2 Atmospheric Extinction

Radiation observed from the Earth's surface is partially absorbed by the atmosphere. Bouguer's Law describes the attenuation of radiation as it passes through a medium — in our case the Earth's atmosphere (Bouguer, 1729):

$$I = I_0 e^{-\tau secz}, \tag{2.2}$$

where I is the measured intensity, I_0 is the intensity at the top of the atmosphere, τ is the optical depth of the atmosphere, and z is the zenith distance. If the atmosphere at the zenith were stable enough, then τ could be measured by following a source as it moved through different zenith distances and plotting $\ln I$ against $secz$. However this is not the case and so instead skydips are used.

Skydips estimate the optical depth at the zenith by measuring the emission from the sky as a function of elevation. Defining the observed brightness of the sky as an equivalent blackbody brightness, J_{obs}, and assuming that the only contributions to this brightness come from the atmosphere, J_{atm}, and the telescope itself, J_{tel}, we can say that,

$$J_{obs} = (1 - \eta)J_{tel} + \eta J_{atm}(1 - e^{-\tau secz}), \tag{2.3}$$

where η is the efficiency of the telescope (Hazell, 1991). This is complicated by that fact that τ is not constant across the observing filter's passband and requires the addition of a 'bandwidth' factor, b, where $1 - b$ is the fraction of the filter bandwidth that is opaque due to atmospheric absorption. Hence equation 2.3

becomes,

$$J_{obs} = (1 - \eta)J_{tel} + \eta J_{atm}(1 - be^{-\tau secz}). \quad (2.4)$$

Fitting observations to equation 2.4 allows τ to be calculated.

The Caltech Submillimetre Observatory (CSO), which is located adjacent to the JCMT on Mauna Kea, has a tipping radiometer that takes skydips every ten minutes at 225 GHz (1.25 mm). Since regular skydips at the JCMT are not time-efficient, we can use the empirical relationships between τ_{225}, τ_{450} and τ_{850} to know the approximate 450μm or 850μm sky opacity for most observations when the JCMT is unable to take them (Archibald et al., 2002). Years of historical records have been used to show that the CSO skydip data fit the JCMT skydip data over long timescales.

Skydips are the primary source of sky opacity data for the data reduced for this thesis. Since these data were taken, the JCMT installed its own radiometer that collects data every 6 seconds along the line-of-sight of the main beam of the telescope. This allows the stability of the atmosphere to be measured even more precisely.

When sky opacity data are available, the SURF command EXTINCTION can be used to correct the flatfielded data so that it represents the flux density received above the atmosphere.

2.4.3 Spikes and Noisy Bolometers

Some bolometers in the SCUBA array are more noisy than others. Despite the fact that weighting by standard deviation will remove the influence of such bolometers in any final map, it is best to remove them completely. The SURF command CHANGE_QUALITY is used to designate these bolometers as 'BAD'. When the time-series for such bolometers are removed, the change in dynamic range often allows the user to see further problems or other bad bolometers that they were previously unaware of.

As well as bad bolometers, the time-series data must have any spikes removed. Spikes that occur on a faster timescale than the 128 Hz data acquisition rate, are removed by the SCUBA transputers at the time of observation. Other, longer spikes are left to be removed by the user. The SURF package contains several despiking tools. These are outlined below:

SIGCLIP is a routine for clipping data that is further from the mean that n-sigma, where n is defined by the user. Statistics are calculated from the entire observation and thus the data tend to be clipped for the much noisier bolometers. SCUCLIP is a routine much like SIGCLIP only it calculates the statistics for each bolometer in turn. It is better for use with data of weak sources. Both routines iterate over the data again when a spike is removed and both may try to remove actual sources. These can be manually blanked out when clipping jiggle-map data. Neither routine can be used for scan-map data.

DESPIKE is a routine that regrids the data onto a grid representing the sky and then partitions it into cells. Despiking then occurs on data that are more than n-sigma from the mean within a cell. This routine is better on regions near bright

sources and the source itself is less likely to be clipped.

DESPIKE2 can be used to remove spikes from scan-map data. Time-series data are compared point-by-point to neighbouring data and flagged for despiking when they are more than n-sigma from the mean value. The data are then smoothed along the scan direction and the flagged points are rechecked. Genuine spikes will not smooth in the same way as real sources and so the spikes can be more confidently removed.

2.4.4 Baselines

For scan-map data there is the additional problem of removing baselines. The Emerson II scan-mapping technique (Emerson, 1995) uses a chopping system in celestial coordinates. This means that the 'sky' and 'source' beams see different airmasses, and thus there is likely to be some difference in sky emission between them. Also, individual scans do not necessarily have a mean of zero, since a bright source may only appear in one beam. Hence subtraction of the mean does not always account for the offset.

Baselines are removed using the SURF command SCAN_RLB, which itself can use several different methods. These are outline below and shown in Figure 2.5.

MEAN

The mean value for points along each scan are used to define a flat baseline across each scan. This method is starkly affected by spikes, where a scan containing a spike will have its baseline artificially raised above the others.

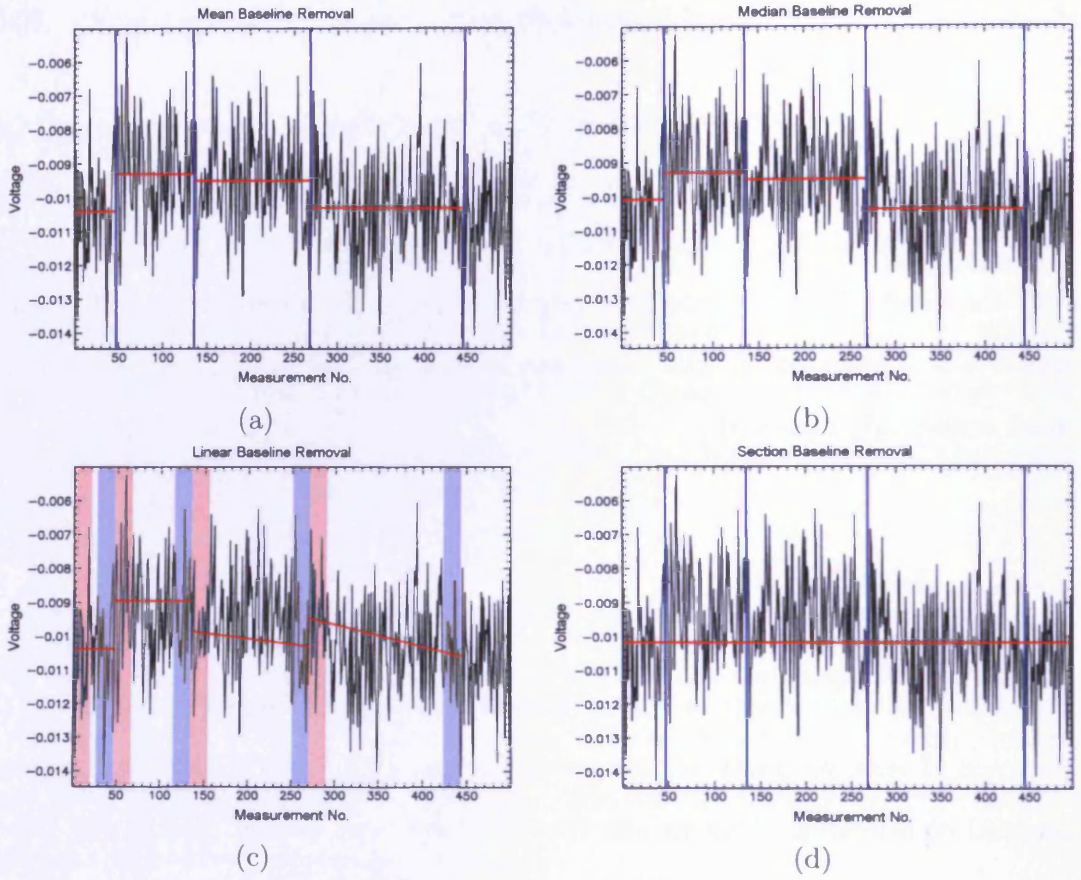

Figure 2.5: (a) – (d). The first 500 measurements taken with a single bolometer. The baselines calculated using the (a) MEAN, (b) MEDIAN, (c) LINEAR, and (d) SECTION methods are shown as red horizontal lines. The ends of each scan are shown with blue vertical lines. In (c), the measurements used to calculate the beginning and end of each linear baseline are shaded red and blue respectively.

MEDIAN

Very similar to the MEAN method, however the median value of points along a scan are used and this avoids the problem of spikes. Both of these methods are very simple but only account much for some of the variation that may occur within a scan length.

LINEAR

This method is excellent at removing sloping baselines. The median value of points at either end of a scan are taken and an interpolation between them is used to define the baseline. This produces a sloped baseline for each scan which means that when there is a significant change in signal between one end of a scan and the other, this method can account for it. However this method only works well when the source is small, as each end of the scans needs to be off source for the baselines to be drawn correctly.

SECTION

This method measures the median value of the data for a specific section of the scan to produce a baseline. In this way, the user can select some portion(s) of the scan known to be off-source, and thus create a more accurate set of baselines. The more specific the user is with each scan, the better the final result will be.

2.4.5 Correlated Sky Noise

Chopping and nodding cannot remove all of the effects of atmospheric emission because the 'sky' and 'source' beams take different paths through the atmosphere. This variation in emission is correlated across the array, because all bolometers sample similar atmospheric paths. This is usually referred to as correlated sky noise. Thus if any one of the bolometers are off-source and can sample the atmospheric variability then this variation can be characterised and removed from all of the bolometers.

Scan-mapping means that no bolometer is entirely off-source for the whole map. Each bolometer therefore sees a time-varying signal as a result of scanning across the source as well as from the atmospheric fluctuations. It is thus not easy to remove the correlated sky noise for data taken in scan-mapping mode.

The solution lies in the fact that in scan-mapping mode almost all parts of the final map are scanned more than once (the edges are the only places where this is not true). In any one observation, each position is scanned twice due to the half-array offset between scans. Observations are also taken in multiple chop configurations (six altogether in the Emerson II technique). This provides the information required by the SURF command CALCSKY to remove the majority of residual sky emission.

CALCSKY bins the data into quarter beam-width bins and uses the median value of each bin to construct a model of the source. The more data that are included here, the better the model becomes. The model of the source is then subtracted from each observation and the correlated sky noise is determined from the mean of all the bolometers from each measurement in the time-series. This can then be subtracted from the original data to produce a final set of time-series data.

2.4.6 Regridding and Mosaicing

The SURF command REBIN is used to transform the time-series data into a rectangular grid. REBIN allows the user to define the pixel scale, grid size and coordinate system. REBIN can also apply various weighting functions to combine measurements from the same position.

When co-adding multiple scan-maps, edge effects can be problematic. The edges of the maps are only covered by one of the two beams during the scan-mapping process and these create edge effects when they are deconvolved from the time-series. When two maps are co-added these edges are quite obvious. The REBIN routine can be used to co-add data with the same chop configuration. Fortunately most of the more recent data in the archive have the same configuration — that of the Emerson II technique.

The power in the final reconstructed map is not a measured quantity. Each source in the map appears in both the 'sky' and 'source' beams and so the mean value in the dual beam is zero. The mean value is not changed by the Fourier deconvolution, so the areas of low flux density in the map will be negative after the deconvolution.

Therefore the best approximation of 'zero' in the map is found using the off-source regions. All the flux density values in the map must be taken relative to this background level, and the background level itself will change from one scan-map to another.

The final stage in scan-map reduction is to remove the differential nature of the data. The standard way to do this is to use the Emerson II method discussed in Section 2.2.3. This is done using the SURF routine REMDBM.

2.4.7 Calibration

Bolometer measurements (see Section 2.1.2) must be calibrated by observing objects of known brightness. The primary calibrator sources used at the JCMT are Uranus and Mars. Planets have predictable and well-understood brightnesses,

which make them good calibrator sources. Jupiter and Saturn are too large in the JCMT beam to be useful for this task.

When Mars and Uranus are not available, a selection of secondary sources can be used. These have been calibrated using the primary sources and despite some having extended emission (Sandell, 1994), and some being variable, they are well understood thanks to a large number of observations (Jenness et al., 2002). Secondary calibrators include protostars (e.g. IRAS 16293-2422 and NGC 2071IR) and protoplanetary nebulae (e.g. IRC+10216 and CRL618).

Calibration is carried out at least twice per shift, allowing linear interpolation between two calibrators over the night. The advantage of more observations of calibrators must be weighed against the increased overhead costs in making additional measurements.

The JCMT primary mirror is segmented, allowing for an optimal surface shape to be used for observations. However this shape will always deviate from a perfect parabola and as such the mirror has an associated error beam. The JCMT error beam can be approximated to a broad Gaussian that is convolved with the mean beam. This error beam must be accounted for differently, depending on the calibration method used.

The calibration methods for maps containing point sources and extended sources are different. These are outlined below.

Point Sources

For point sources, calibration is done in Jy/aperture (Sandell, Jenness, & Jessop, 2001). Voltage is measured in equally sized apertures on both the source and calibrator. The flux density of the source (S_{source}) is given by,

$$S_{source} = V_{source}\frac{S_{tot}}{V_{cal}} \tag{2.5}$$

where V_{source} and V_{cal} are the integrated voltage within the source and calibrator apertures respectively, and S_{tot} is the total flux density of the calibrator.

The program FLUXES can be used to obtain S_{tot} for primary calibrators. It calculates the positions of planets and hence the flux density received.

For secondary calibrators, the flux density has been determined using a large number of observations (Jenness et al., 2002) made over a number of years. The values of the peak and integrated flux densities within a 40″ aperture are given by Sandell (2002). The fraction $\frac{S_{tot}}{V_{cal}}$ is known as the flux conversion factor (FCF) and changes with aperture size.

This calibration method is not affected by the JCMT error beam because the same fraction of radiation is scattered from the primary beam to the error beam for equal sized apertures. This calibration method only works if the angular size of the calibrator source is small compared with the aperture size used.

Extended Sources

For extended sources, calibration is done in Jy/beam (Sandell et al., 2001). This method requires the flux density received from the calibrator. The fraction of this flux density that couples with the telescope beam gives a coupling constant, K. The coupling of the flux density with the telescope beam is given by,

$$S_{beam} = \frac{S_{tot}}{K}, \tag{2.6}$$

where K is given by,

$$K = \frac{x^2}{1 - e^{-x^2}}, \tag{2.7}$$

and

$$x = \frac{D}{1.2\theta_A}. \tag{2.8}$$

D is the dish diameter (15 m), θ_A is the FWHM of the primary beam and can be measured from the map of the calibrator. If a primary calibrator is used, its angular size must be deconvolved from the measured FWHM (θ_M):

$$\theta_A = \left(\theta_M^2 - \frac{ln2}{2}D^2\right)^{0.5} \tag{2.9}$$

The FCF can then be calculated by,

$$\mathrm{FCF} = \frac{\mathrm{S_{beam}}}{\mathrm{V_{peak}}}, \tag{2.10}$$

where V_{peak} is the peak voltage in the calibrator map. Multiplying the source map by the FCF will calibrate the map in Jy/beam.

For secondary calibrator sources, S_{beam} is quoted directly (Sandell et al., 2001). Thus the FCF can be calculated by dividing the quoted value by the peak flux density from the secondary calibrator map.

When measuring the flux density in an aperture from a map calibrated in Jy/beam, the measured value must be divided by the beam integral for a Gaussian, which is equal to $1.134\theta_A^2$. A correction must also be made for the error beam in this method. This can be calculated by multiplying the calibrator map by the FCF, and measuring the flux density in an aperture placed over the calibrator. A larger aperture will increase the measured flux density. The flux density of the source, measured using a given aperture, must be divided by the error beam correction factor for that aperture.

2.5 HARP Data Reduction

The process of reducing HARP data has been greatly streamlined compared with the SCUBA data reduction process. The steps described here cover the recommended procedures for removing baselines, bad receptors and spikes. In most cases HARP data needs only to be run through the SMURF package MAKECUBE (Jenness et al., 2008). The steps below could be considered more advanced techniques.

Raw HARP data are reduced using a variety of tools from the Starlink collection [1]. The SMURF package contains the tools to create data cubes (Jenness et al., 2008). GAIA (Draper et al., 2009) can be used to view the data cube, and SPLAT (Draper & Taylor, 2009) can be used to view individual spectra. The KAPPA (Currie & Berry, 2010) and CUPID (Berry, 2009) packages also contain useful tools for spectral-line data reduction, as described in the following sections.

2.5.1 Preparing a Data Cube

As with SCUBA data, there may be bad receptors causing problems in raw HARP data. These can be removed using the CHPIX command in KAPPA. For most HARP observations this step is sufficient to produce a working cube. In some cases there may be interference spikes in the raw data that cause further problems. For best results, these should be removed before converting the data into a cube (see Section 2.5.2). Once the time series has been cleaned, the SMURF command MAKECUBE is used to convert it into a data cube.

The baselines in a cube can be fitted to and removed using the MFITTREND command in KAPPA. This can also be done within GAIA, in an interactive manner. An example of baseline removal in HARP data is shown in Figure 2.6. The MFITTREND routine fits a polynomial (up to 15^{th} order) to all lines of data along a chosen axis. The fits can be restricted to selected regions so that lines of emission or absorption can be avoided. Fits are then extrapolated and interpolated across the whole spectral region in the cube. The resultant baselines can then be removed from the input cube.

[1] http://starlink.jach.hawaii.edu/starlink

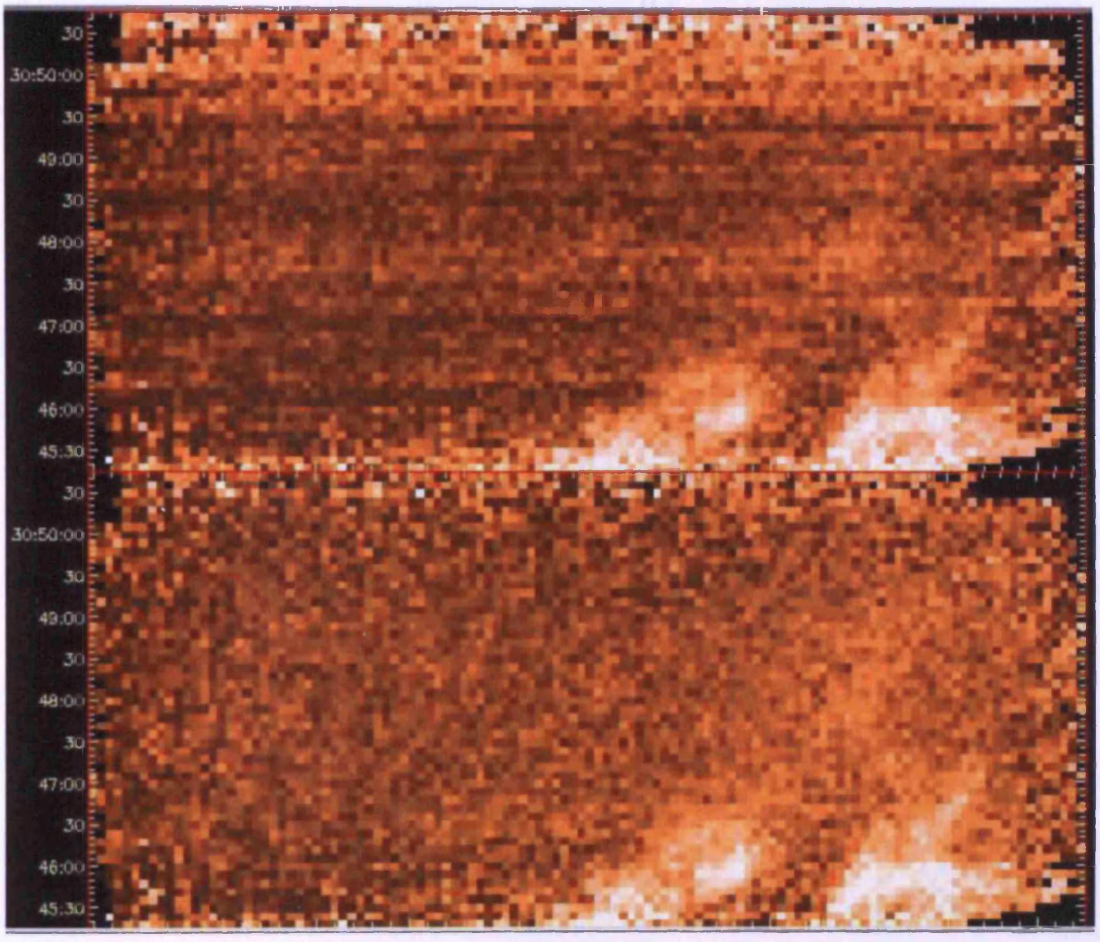

Figure 2.6: A 'before-and-after' example of baseline removal in HARP data. The top image shows data before baseline removal. Source: http://www.jach.hawaii.edu/JCMT/spectral_line/data_reduction/acsisdr/first-steps.html

2.5.2 Despiking HARP Data

Interference spikes can appear in HARP data. Spikes in the data cube occur at the same frequency throughout the observed cube and at almost uniform intensity. When spikes are found, the COLLAPSE command can be used to help remove them. The time series is initially collapsed into a single, spectral dimension to give an average spectrum. This will need to be done twice, once for each axis. To accentuate the presence of spikes over the data, COLLAPSE should use the RMS estimator method (see Figure 2.7).

Now that spikes in the data can be identified, they need to be removed. This is initially done using the CUPID commands THRESH and FINDBACK. THRESH masks out any large values that may have been generated at the edges of the spectrum by the COLLAPSE routine. FINDBACK traces the background signal, avoiding the spikes (see Figure 2.8a).

The KAPPA command SUB can be used to subtract the background from the spectrum. Then the FFCLEAN command masks and removes the spikes (see Figure 2.8b).

The final part of the despiking procedure is to extrapolate the 1D mask into a 3D mask. This can be done using the WCSALIGN command, using the initial time series cube as a reference for the dimensionality of the resultant cube. COPYBAD is then used to copy the location of the bad pixels (i.e. those containing the spurious values) onto the original time-series data. MAKECUBE can now be run to continue the reduction process, as in Section 2.5.1.

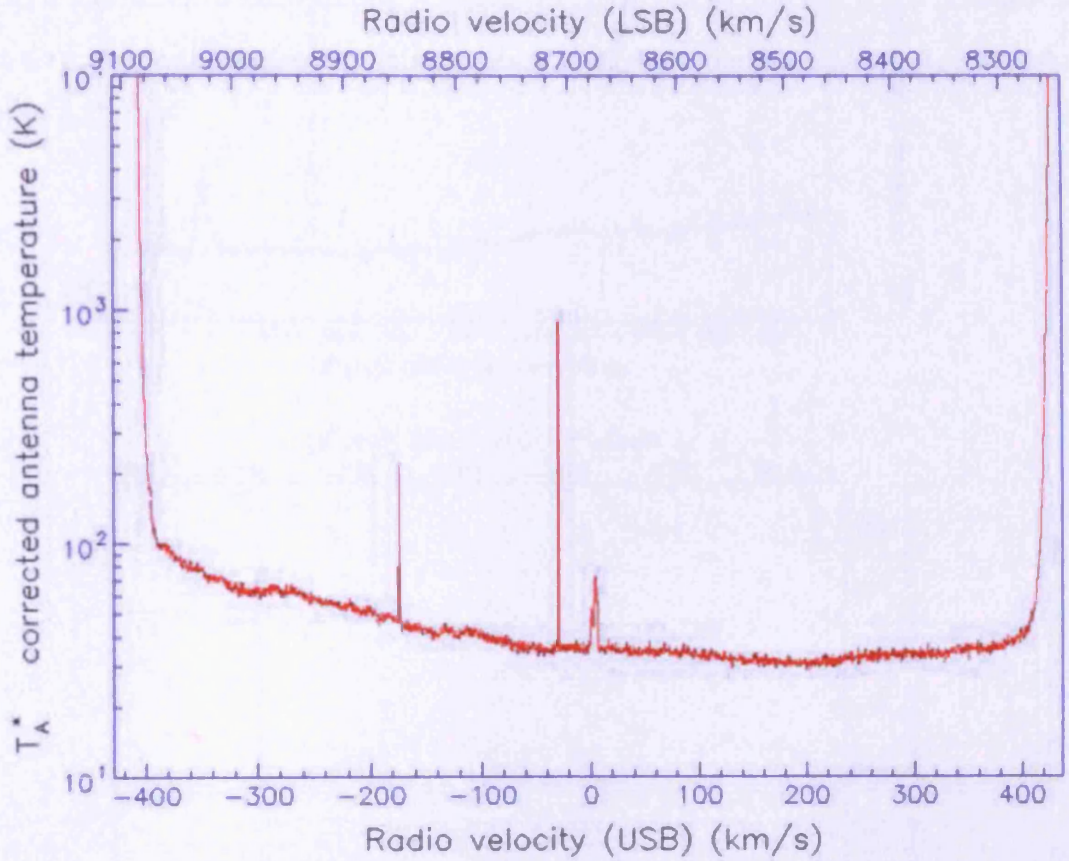

Figure 2.7: Example spectrum, showing the effect of using the method 'estimator=rms' on collapsing a data cube. Two spikes are seen in this cube. The spikes are clearly seen, accentuated over the real signal in the data. The science signal is seen at around 0 km s^{-1}. Source: http://www.jach.hawaii.edu/JCMT/spectral_line/data_reduction/acsisdr/advanced.html

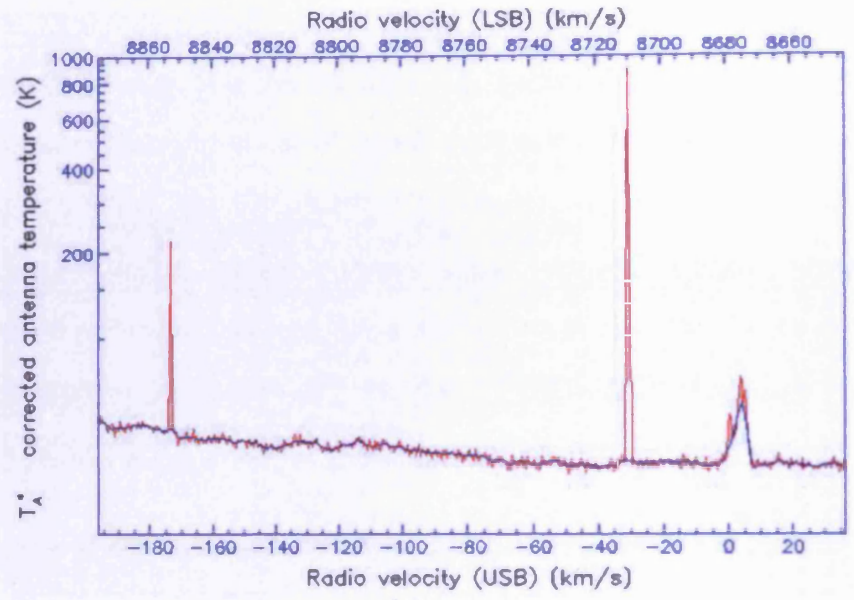

(a)

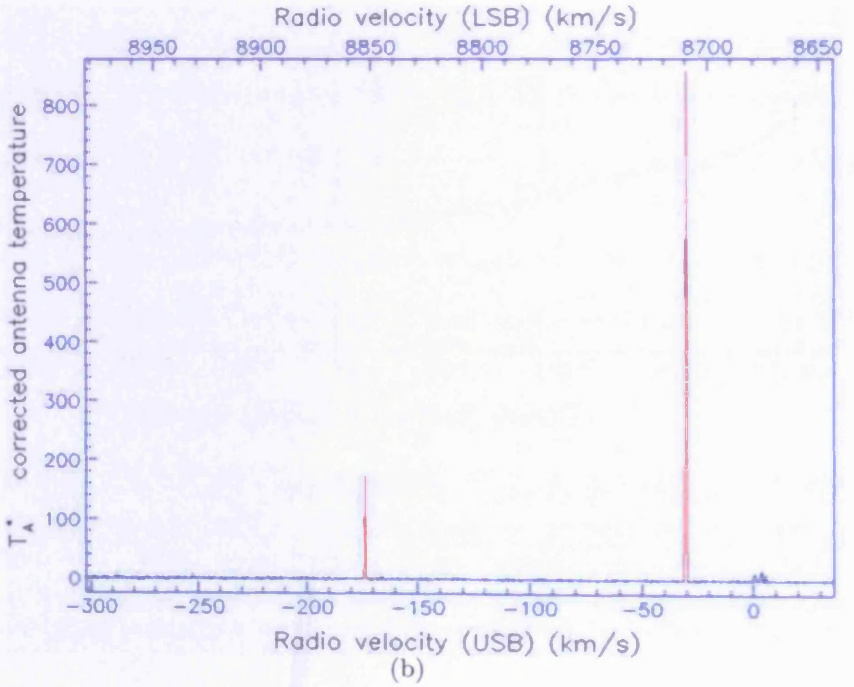

(b)

Figure 2.8: Close up on spikes in the spectrum from Figure 2.7. (a) shows the background, traced by FINDBACK, in blue. (b) shows the effect of the FFCLEAN command. The blue spectrum is what remains after the spikes are masked and removed. Source: http://www.jach.hawaii.edu/JCMT/spectral_line/data_reduction/acsisdr/advanced.html

2.6 Summary

In this chapter I have reviewed the telescope and instruments used to obtain the data described in the following chapters. The techniques and tools used to reduce those data have been outlined in detail for both HARP and SCUBA. The atmosphere at the telescope, and the strategies used to minimise its effect, were also discussed.

Chapter 3

SCUBA Observations of L1688 — Producing a Core Mass Function

3.1 Introduction

A number of observations have shown that the core mass function (CMF) of prestellar cores appears to mimic (Motte Andre & Neri 1998, hereafter MAN98, Testi & Sargent, 1998; Motte et al., 2001; Johnstone et al., 2001; Kroupa, 2002; Onishi et al., 2002; Johnstone, Matthews, & Mitchell, 2006) the stellar initial mass function (IMF; Salpeter, 1955).

However, the comparison between the core mass function and stellar IMF has not often been accurately probed at lower masses. It is more difficult to study this part of the mass domain, but recent results have shown that the CMF exhibits a turnover at lower masses in a manner similar to the IMF (Nutter & Ward-Thompson, 2007).

In this chapter, I describe how I re-reduced all of the SCUBA wide-field scan-map data and narrow-field jiggle-map data taken of L1688 to produce the deepest submillimetre map of this cloud ever made. Of the original regions covered at 1.3mm by MAN98 (Oph-A, -B, -C, -D, -E and -F) only one, Oph-D, is not included here as it is not part of the central region of L1688. A newly discovered region, which I named Oph-H, is discussed. I produce a core mass function (CMF) and investigate the low-mass end of the CMF of the cloud. Finally, I compare this with previous findings in Ophiuchus and also with the Orion molecular cloud (Nutter & Ward-Thompson, 2007).

3.2 Ophiuchus

The Ophiuchus star-forming region is located at a distance of 139 pc (Mamajek, 2008) and is a site of low-mass star formation (Wilking & Lada, 1983). The region consists of two main clouds, L1688 and L1689 which both have extended streamers leading out to lengths of around 10 pc (Loren, 1989). Specifically, it is the more massive of the two clouds, L1688, which is studied in this thesis, and which is generally known as the Ophiuchus main cloud. Very high star formation rates have been measured here with 14-40% of the molecular gas being converted into stars (Vrba, 1977; Evans et al., 2009).

The star-forming region in Ophiuchus has been observed in many wavelengths from the visible to the submilimetre (e.g. MAN98, Montmerle et al., 1983; Wilking, Lada, & Young, 1989; André et al., 1992; Greene & Young, 1992; Barsony et al., 1997; Jessop & Ward-Thompson, 2001). Because of this, the properties of Ophiuchus are very well known and it is therefore a good place to probe low-mass

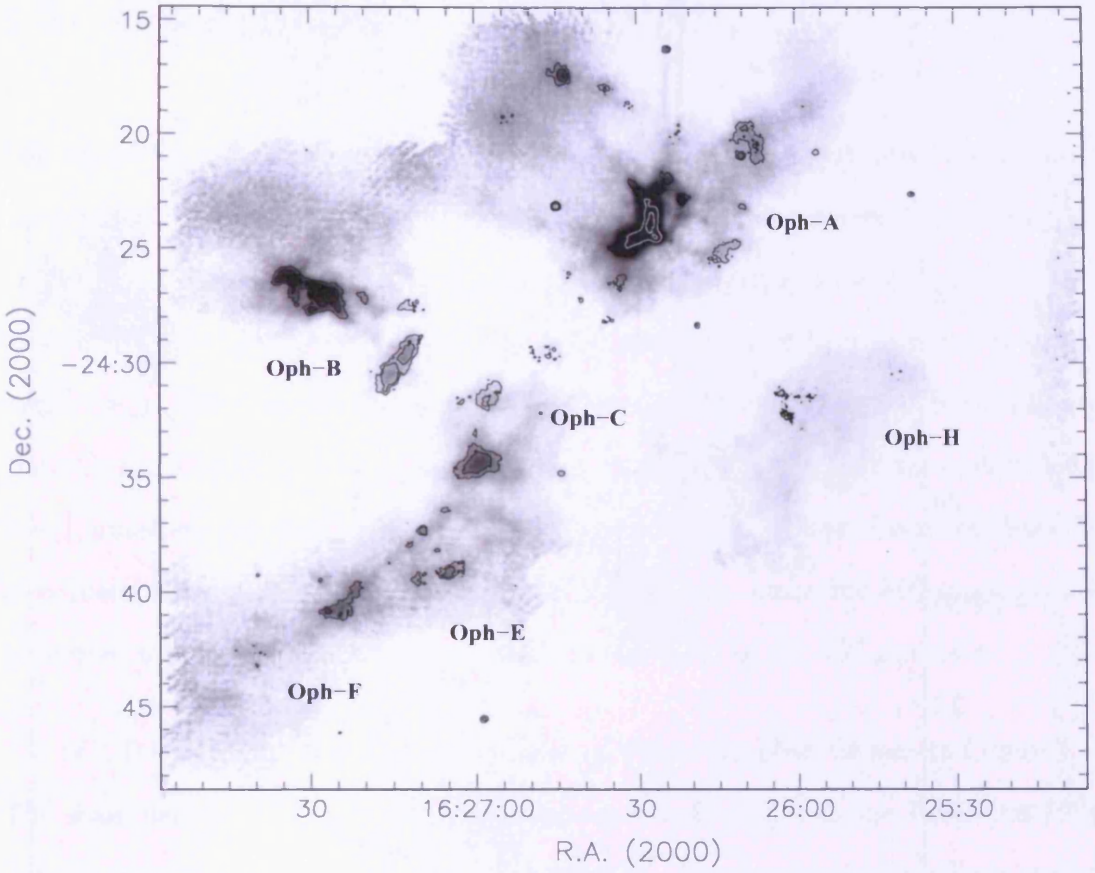

Figure 3.1: Greyscale image and isophotal contour map of the SCUBA 850μm continuum scan-map data of the Ophiuchus main cloud L1688. Signal-to-noise contours at 5σ and 10σ are shown in black; 25σ and 100σ contours shown in white. 1σ noise levels vary from 15 to 40 mJy/beam, with a mean value of 29 mJy/beam (see text for details).

star formation.

Ophiuchus is the nearest example of 'clustered' star formation (MAN98). This is important to study because most stars form in clustered environments (Zinnecker, McCaughrean, & Wilking, 1993). Ophiuchus may also be the nearest example of triggered star formation in action (Loren, 1989; Nutter, Ward-Thompson, & André, 2006), making it a prime candidate for study.

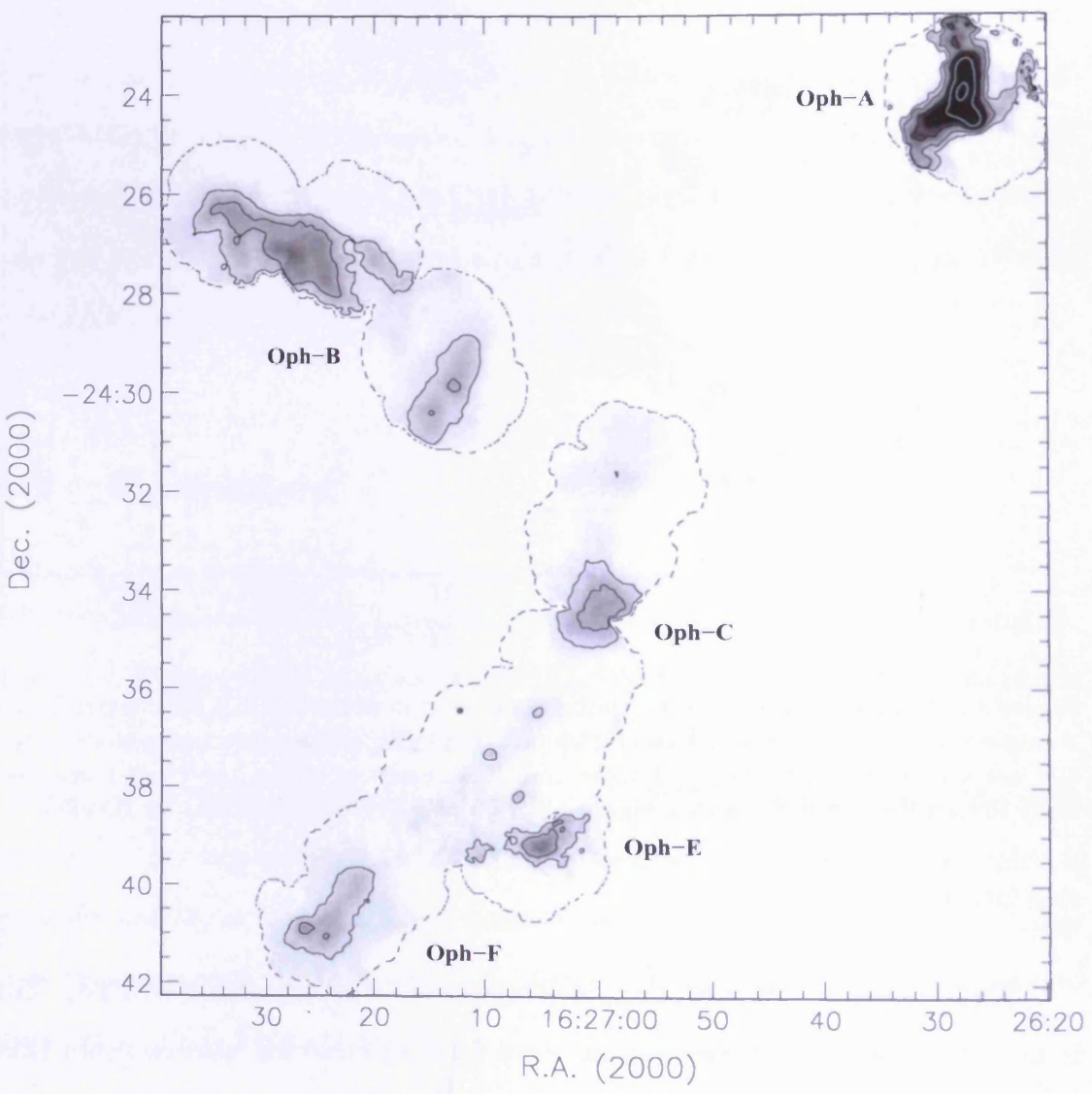

Figure 3.2: Greyscale image and isophotal contour map of the SCUBA 850μm continuum jiggle map data of the Ophiuchus dark cloud L1688. Contours at 0.25, 0.5 and 1.0 Jy/beam are shown in black; 2.0 and 4.0 Jy/beam contours shown in white. 1σ noise levels vary from 10 to 180 mJy/beam, with a mean value of 60 mJy/beam.

3.3 Observations

The submillimetre data presented in this chapter were obtained using the Submillimetre Common User Bolometer Array (SCUBA) on the James Clerk Maxwell Telescope (JCMT). SCUBA used a dichroic beam-splitter to simultaneously observe at 850-μm and 450-μm wavelengths at resolutions of 14 arcsec and 8 arcsec respectively. The data presented here were acquired from the Canadian Astronomy Data Center's JCMT data archive (Tilanus et al., 1997). Some of these data have been published previously (Johnstone et al., 2000) but all have been consistently re-reduced here using a single method for this thesis. Only the 850-μm data are presented due to the much lower signal-to-noise ratio of the 450-μm data.

SCUBA was used in scan-map mode to produce the observations in Figure 3.1. The scan-map data consist of 76 observations over 3 nights at the JCMT on 1998 July 11 and 12, and 1999 March 4 (see Table 3.1). The sky opacity at 850 μm varied from 0.10 to 0.29 with a mean value of 0.17, as determined by the 'skydip' method (Archibald et al., 2002). The data were reduced using the SCUBA User Reduction Facility (Jenness et al., 2000) and calibrated using observations of Uranus (Griffin & Orton, 1993), Mars (Griffin & Orton, 1993) or the secondary calibrator CRL618 (Sandell, 1994).

The scan-map observation mode results in differential maps which must be reconstructed. This is done in fourier space using the Emerson-2 method (Emerson & Payne, 1995). Baseline offsets were removed using the SURF command SCAN_RLB with the 'median' method (Jenness et al., 2000). The time-series data were checked for each observation and noisy bolometers were removed by eye. I estimate that the calibration uncertainty is $\pm$10% based on the variation in the calibration factors from Uranus and Mars across all the datasets (see Tables 3.6

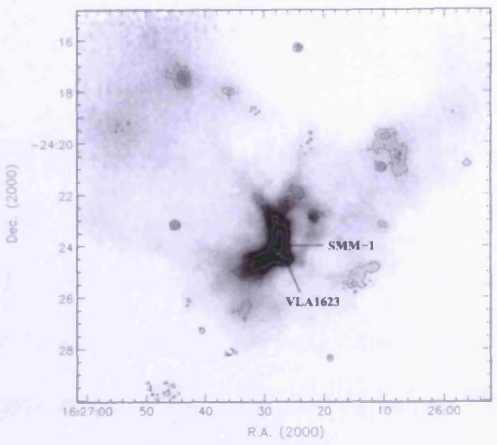

(a) Region Oph-A.

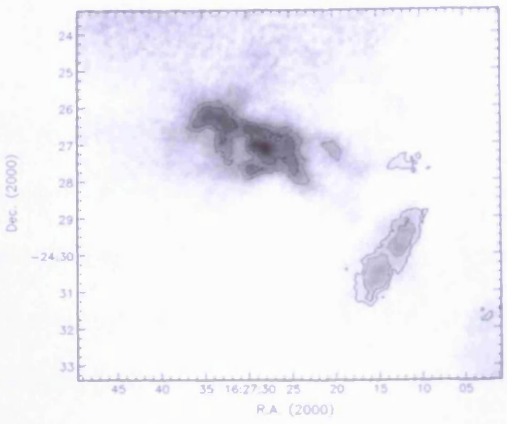

(b) Region Oph-B.

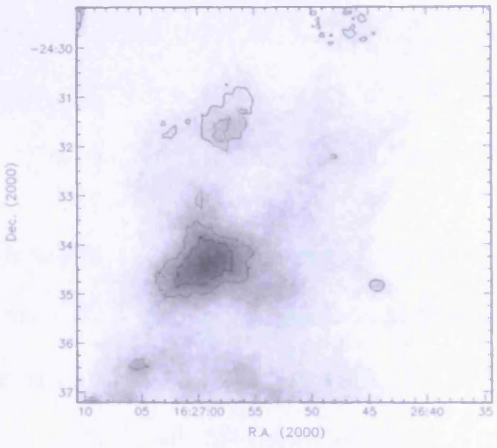

(c) Region Oph-C.

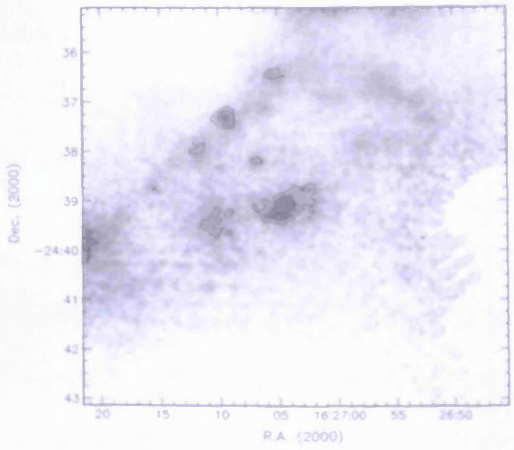

(d) Region Oph-E.

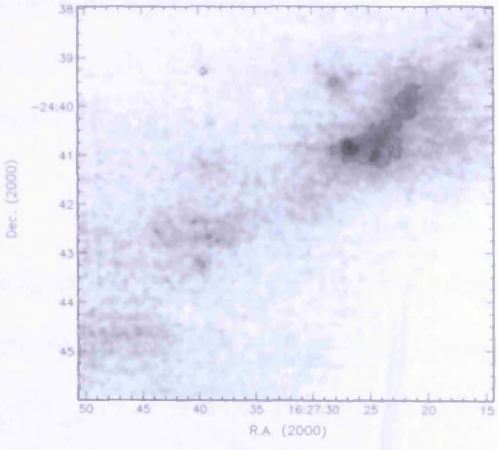

(e) Region Oph-F.

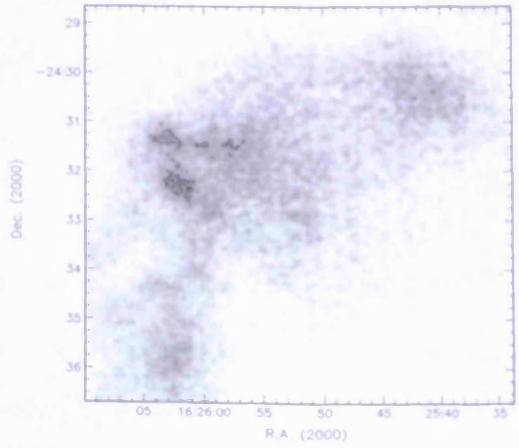

(f) Region Oph-H.

Figure 3.3: 850-μm continuum maps of regions Oph-A, B, C, E, F and new region H. Signal-to-noise contours at 5σ and 10σ are shown in black; 25σ and 100σ contours are shown in white. 1σ noise levels vary from 15 to 40 mJy/beam, with a mean value, for the whole map, of 29 mJy/beam. Median noise values for Oph-A, B , C, E, F and H are 25, 20, 25, 35, 35 and 25 mJy/beam respectively.

and 3.7).

The data make up one map which is split into 7 regions, following the naming methodology in MAN98. Figure 3.1 shows the whole map with the individual regions named. Johnstone et al. (2000) first published some of the 850-μm scan-map data used in this study. They found consistency with the results of MAN98.

SCUBA was used in jiggle-map mode for the observations in Figure 3.2. The jiggle-map data consist of 42 observations over 19 nights at the JCMT between 1997 August 7 and 2004 March 29 (see Table 3.1). The sky opacity at 850 μm varied from 0.21 to 0.52 with a mean value of 0.30, as determined by the 'skydip' method. The jiggle-map data were also reduced using the SCUBA User Reduction Facility and again calibrated using observations of Uranus, Mars, or the secondary calibrator CRL618. These data are shown in Figure 3.2. A close-up of each of the main regions is shown in Figure 3.3.

3.4 Results

The final map was created from data taken over a range of dates and weather conditions at the JCMT. To produce a final map, with quantified noise levels, I use the technique from Nutter & Ward-Thompson (2007).

In this technique the bright sources are masked before smoothing the map to remove the large-scale structure. This is then subtracted from the original data. The resultant map is then used to create a noise map by measuring the standard deviation of the pixel values in a series of 50 arcsec apertures. The gaps from the bright sources are filled in by simple interpolation between the edge values.

Table 3.1: Details of SCUBA archive observations for L1688.

Date	Mode	$\overline{\tau}_{850}$	No. of Datasets
1997 Aug 07	Jiggle Map	0.285	1
1997 Aug 08	Jiggle Map	0.282	1
1997 Aug 09	Jiggle Map	0.280	5
1997 Aug 10	Jiggle Map	0.220	1
1997 Aug 11	Jiggle Map	0.103	1
1997 Aug 25	Jiggle Map	0.206	2
1997 Aug 26	Jiggle Map	0.183	2
1997 Sep 09	Jiggle Map	0.108	6
1998 Jun 26	Jiggle Map	0.278	2
1998 Jul 11	Scan Map	0.103	27
1998 Jul 12	Scan Map	0.148	24
1998 Aug 11	Jiggle Map	0.211	2
1998 Aug 25	Jiggle Map	0.314	2
1999 Mar 04	Scan Map	0.205	25
1999 Mar 13	Jiggle Map	0.208	2
1999 Aug 20	Jiggle Map	0.279	2
2000 Aug 08	Jiggle Map	0.208	1
2001 Jul 31	Jiggle Map	0.310	3
2003 Feb 04	Jiggle Map	0.260	8
2004 Mar 29	Jiggle Map	0.255	1

Table 3.2: Source names, peak positions, 850-μm peak flux densities and signal-to-noise ratios of the cores in regions Ophiuchus-A and -B. The flux densities $S_{1.3mm}^{peak}$ and S_{850}^{peak} refer to the MAN98 peak flux density and the peak flux density in our dataset respectively.

Source	MAN98 Position		SCUBA Position		Flux Densities			
Name	RA (2000)	Dec. (2000)	RA (2000)	Dec (2000)	$S_{1.3mm}^{peak}$ (mJy/beam)	S_{850}^{peak} (mJy/beam)	S/N (σ)	IR assn
A-MM1	$16^h26^m22.44^s$	$-24°23'40.26''$	$16^h26^m23.00^s$	$-24°23'34.46''$	50 ± 15	380 ± 15	23	
A-MM2/3	—	—	$16^h26^m23.80^s$	$-24°24'09.95''$	—	660 ± 25	24	
A-MM4	$16^h26^m24.40^s$	$-24°21'52.13''$	$16^h26^m24.14^s$	$-24°21'59.30''$	80 ± 15	930 ± 20	42	
A-MM5	$16^h26^m26.42^s$	$-24°22'27.00''$	$16^h26^m26.66^s$	$-24°22'28.60''$	100 ± 20	1590 ± 20	71	
A-MM6	$16^h26^m28.43^s$	$-24°22'52.86''$	$16^h26^m28.21^s$	$-24°23'00.10''$	200 ± 25	4050 ± 30	138	
A-MM7	$16^h26^m29.42^s$	$-24°22'33.80''$	$16^h26^m29.45^s$	$-24°22'33.01''$	110 ± 30	1770 ± 30	60	
A-MM8	$16^h26^m33.48^s$	$-24°25'00.53''$	$16^h26^m31.80^s$	$-24°24'50.00''$	80 ± 25	6110 ± 25	245	
A-MM9	—	—	$16^h26^m45.18^s$	$-24°23'10.02''$	—	490 ± 30	16	Y
A-MM10	—	—	$16^h26^m21.83^s$	$-24°22'51.96''$	—	1640 ± 25	66	Y
A-MM11	—	—	$16^h26^m32.74^s$	$-24°26'14.40''$	—	1240 ± 25	50	
A-MM12	—	—	$16^h26^m14.24^s$	$-24°25'04.33''$	—	870 ± 25	35	
A-MM15	—	—	$16^h26^m40.50^s$	$-24°27'16.28''$	—	20 ± 30	1	Y
A-MM16	—	—	$16^h26^m36.26^s$	$-24°28'12.84''$	—	60 ± 20	3	
A-MM17	—	—	$16^h26^m34.77^s$	$-24°28'08.10''$	—	60 ± 20	3	
A-MM18	—	—	$16^h26^m43.73^s$	$-24°17'25.74''$	—	1680 ± 30	56	
A-MM19	—	—	$16^h26^m24.30^s$	$-24°16'16.11''$	—	430 ± 40	11	Y

Table 3.2: Source names, peak positions, 850-μm peak flux densities and signal-to-noise ratios of the cores in regions Ophiuchus-A and -B. The flux densities $S_{1.3mm}^{peak}$ and S_{850}^{peak} refer to the MAN98 peak flux density and the peak flux density in our dataset respectively.

Source	MAN98 Position		SCUBA Position		Flux Densities			
Name	RA (2000)	Dec. (2000)	RA (2000)	Dec (2000)	$S_{1.3mm}^{peak}$ (mJy/beam)	S_{850}^{peak} (mJy/beam)	S/N (σ)	IR assn
A-MM20	—	—	$16^h26^m36.18^s$	$-24°17'56.34''$	—	240 ± 30	8	
A-MM21	—	—	$16^h26^m31.64^s$	$-24°18'38.05''$	—	410 ± 35	12	
A-MM22	—	—	$16^h26^m31.45^s$	$-24°18'52.05''$	—	210 ± 35	6	
A-MM23	—	—	$16^h26^m07.89^s$	$-24°20'30.50''$	—	2370 ± 25	95	
A-MM24	—	—	$16^h26^m10.50^s$	$-24°20'56.83''$	—	760 ± 25	30	Y
A-MM25	—	—	$16^h25^m55.96^s$	$-24°20'49.47''$	—	140 ± 30	5	Y
A-MM26	—	—	$16^h26^m15.40^s$	$-24°25'32.50''$	—	820 ± 25	33	
A-MM27	—	—	$16^h26^m13.85^s$	$-24°25'25.16''$	—	650 ± 25	26	
A-MM28	—	—	$16^h26^m54.75^s$	$-24°19'16.55''$	—	410 ± 40	10	
A-MM29	—	—	$16^h26^m53.36^s$	$-24°19'28.08''$	—	350 ± 40	9	
A-MM30	—	—	$16^h26^m09.63^s$	$-24°19'43.25''$	—	2460 ± 20	123	
A2-MM1	$16^h26^m11.45^s$	$-24°24'40.00''$	$16^h26^m11.73^s$	$-24°24'54.16''$	60 ± 10	640 ± 20	32	
A3-MM1	$16^h26^m09.41^s$	$-23°24'06.13''$	$16^h26^m10.07^s$	$-24°23'11.00''$	90 ± 10	640 ± 30	21	
A-N	$16^h26^m21.35^s$	$-24°19'40.33''$	$16^h26^m22.74^s$	$-24°20'00.00''$	60 ± 10	410 ± 30	14	
A-S	—	—	$16^h26^m42.69^s$	$-24°26'08.05''$	85 ± 10	10 ± 35	0	
SM1	$16^h26^m27.45^s$	$-24°23'55.93''$	$16^h26^m27.73^s$	$-24°23'58.17''$	1300 ± 20	14140 ± 25	571	
SM1N	$16^h26^m27.44^s$	$-24°23'27.93''$	$16^h26^m27.46^s$	$-24°23'32.71''$	790 ± 25	5600 ± 15	359	
SM2	$16^h26^m29.46^s$	$-24°24'25.91''$	$16^h26^m29.41^s$	$-24°24'26.69''$	450 ± 30	11490 ± 15	690	
VLA1623	—	—	$16^h26^m26.74^s$	$-24°24'30.00''$	—	5630 ± 30	188	

Table 3.2: Source names, peak positions, 850-μm peak flux densities and signal-to-noise ratios of the cores in regions Ophiuchus-A and -B. The flux densities $S_{1.3mm}^{peak}$ and S_{850}^{peak} refer to the MAN98 peak flux density and the peak flux density in our dataset respectively.

Source	MAN98 Position		SCUBA Position		Flux Densities			
Name	RA (2000)	Dec. (2000)	RA (2000)	Dec (2000)	$S_{1.3mm}^{peak}$ (mJy/beam)	S_{850}^{peak} (mJy/beam)	S/N (σ)	IR assn
B1-MM1	$16^h27^m08.57^s$	$-24°27'50.19''$	$16^h27^m09.32^s$	$-24°27'43.73''$	50 ± 5	50 ± 30	2	
B1-MM2	$16^h27^m11.60^s$	$-24°29'17.99''$	$16^h27^m12.23^s$	$-24°29'23.65''$	45 ± 10	2140 ± 10	230	
B1-MM3	$16^h27^m12.62^s$	$-24°29'57.92''$	$16^h27^m12.60^s$	$-24°29'49.89''$	65 ± 10	4140 ± 10	446	
B1-MM4	$16^h27^m15.64^s$	$-24°30'41.72''$	$16^h27^m15.32^s$	$-24°30'36.82''$	60 ± 15	3330 ± 10	372	
B1-MM5	—	—	$16^h27^m16.05^s$	$-24°31'09.30''$	—	650 ± 25	26	Y
B1-MM6	—	—	$16^h27^m10.58^s$	$-24°28'54.69''$	—	350 ± 30	12	
B1-MM7	—	—	$16^h27^m18.72^s$	$-24°30'24.64''$	—	180 ± 30	6	
B1B2-MM1	$16^h27^m11.57^s$	$-24°27'38.99''$	$16^h27^m12.44^s$	$-24°27'30.31''$	40 ± 5	350 ± 35	10	
B1B2-MM2	$16^h27^m17.60^s$	$-24°28'47.59''$	$16^h27^m17.77^s$	$-24°28'59.75''$	45 ± 10	490 ± 10	51	Y
B2-MM2	$16^h27^m20.56^s$	$-24°27'08.39''$	$16^h27^m19.82^s$	$-24°27'13.87''$	85 ± 10	1390 ± 20	79	
B2-MM4	$16^h27^m24.58^s$	$-24°27'45.12''$	$16^h27^m24.50^s$	$-24°27'46.30''$	90 ± 15	1520 ± 20	86	
B2-MM5	$16^h27^m24.57^s$	$-24°27'26.12''$	$16^h27^m24.74^s$	$-24°27'29.29''$	100 ± 15	1810 ± 20	102	
B2-MM6	$16^h27^m25.57^s$	$-24°27'00.05''$	$16^h27^m25.57^s$	$-24°26'58.19''$	150 ± 15	2570 ± 20	134	
B2-MM7	$16^h27^m27.58^s$	$-24°27'38.92''$	$16^h27^m27.70^s$	$-24°27'38.86''$	100 ± 20	990 ± 25	39	
B2-MM8	$16^h27^m27.57^s$	$-24°27'06.92''$	$16^h27^m27.96^s$	$-24°27'06.85''$	215 ± 20	3140 ± 20	178	
B2-MM9	$16^h27^m28.56^s$	$-24°26'36.85''$	$16^h27^m28.82^s$	$-24°26'38.59''$	110 ± 15	2170 ± 20	113	
B2-MM10	$16^h27^m29.58^s$	$-24°27'41.78''$	$16^h27^m29.53^s$	$-24°27'40.85''$	160 ± 10	1020 ± 25	41	Y
B2-MM13	$16^h27^m32.55^s$	$-24°26'06.58''$	$16^h27^m32.95^s$	$-24°26'03.16''$	75 ± 15	780 ± 30	26	
B2-MM14	$16^h27^m32.56^s$	$-24°26'28.58''$	$16^h27^m32.58^s$	$-24°26'27.46''$	130 ± 15	1990 ± 15	128	
B2-MM15	$16^h27^m32.57^s$	$-24°27'02.58''$	$16^h27^m32.87^s$	$-24°26'59.16''$	90 ± 15	990 ± 30	33	
B2-MM16	$16^h27^m34.56^s$	$-24°26'12.45''$	$16^h27^m34.62^s$	$-24°26'16.39''$	100 ± 15	2090 ± 15	134	

Table 3.3: Source names, peak positions, 1.3mm and 850-μm peak flux densities and signal-to-noise ratios of the cores in regions Ophiuchus-C, -E, -F and -H.

Source	MAN98 Position		SCUBA Position		Flux Densities			
Name	RA (2000)	Dec. (2000)	RA (2000)	Dec (2000)	$S^{peak}_{1.3mm}$ (mJy/beam)	S^{peak}_{850} (mJy/beam)	S/N (σ)	IR assn
C-MM2	$16^h26^m58.69^s$	$-24°33'52.85''$	$16^h26^m59.75^s$	$-24°33'56.95''$	45 ± 10	1760 ± 25	70	
C-MM3	$16^h26^m58.70^s$	$-24°34'21.85''$	$16^h26^m58.80^s$	$-24°34'23.40''$	55 ± 25	2260 ± 20	106	
C-MM5	$16^h26^m59.70^s$	$-24°34'26.79''$	$16^h26^m59.61^s$	$-24°34'26.81''$	50 ± 25	1970 ± 20	93	
C-MM6	$16^h27^m01.71^s$	$-24°34'36.65''$	$16^h27^m01.58^s$	$-24°34'44.62''$	60 ± 20	1670 ± 20	79	
C-MM8	—	—	$16^h26^m49.09^s$	$-24°29'45.15''$	—	240 ± 35	7	
C-MM9	—	—	$16^h26^m48.10^s$	$-24°32'12.50''$	—	90 ± 30	3	
C-MM10	—	—	$16^h27^m02.26^s$	$-24°31'42.56''$	—	580 ± 25	23	
C-MM11	—	—	$16^h26^m44.27^s$	$-24°34'50.43''$	—	110 ± 30	4	Y
C-MM12	—	—	$16^h26^m59.80^s$	$-24°33'08.75''$	—	150 ± 30	5	
C-N	$16^h26^m57.64^s$	$-24°31'38.92''$	$16^h26^m58.11^s$	$-24°31'46.32''$	60 ± 10	2540 ± 25	105	
E-MM2a	$16^h27^m01.59^s$	$-24°38'28.66''$	$16^h27^m02.89^s$	$-24°38'46.47''$	50 ± 15	200 ± 40	5	
E-MM2b	$16^h27^m01.80^s$	$-24°38'51.65''$	$16^h27^m02.19^s$	$-24°39'11.49''$	60 ± 15	250 ± 40	6	
E-MM2d	$16^h27^m04.81^s$	$-24°39'15.45''$	$16^h27^m04.64^s$	$-24°39'15.63''$	110 ± 20	660 ± 40	17	
E-MM4	$16^h27^m10.82^s$	$-24°39'30.05''$	$16^h27^m10.67^s$	$-24°39'25.28''$	50 ± 10	490 ± 40	13	
E-MM5	$16^h27^m11.79^s$	$-24°37'56.98''$	$16^h27^m11.67^s$	$-24°37'57.46''$	55 ± 10	440 ± 30	14	
E-MM6	—	—	$16^h27^m09.46^s$	$-24°37'20.92''$	—	310 ± 35	9	Y
E-MM7	—	—	$16^h27^m05.45^s$	$-24°36'27.02''$	—	200 ± 30	7	Y
E-MM8	—	—	$16^h27^m04.19^s$	$-24°39'02.59''$	—	300 ± 30	10	
E-MM9	—	—	$16^h27^m06.84^s$	$-24°38'11.38''$	—	140 ± 30	5	Y
E-MM10	—	—	$16^h27^m15.55^s$	$-24°38'45.95''$	—	100 ± 40	3	Y

Table 3.4: Source names, peak positions, 1.3mm and 850-μm peak flux densities and signal-to-noise ratios of the cores in regions Ophiuchus-C, -E, -F and -H.

Source	MAN98 Position		SCUBA Position		Flux Densities			
Name	RA (2000)	Dec. (2000)	RA (2000)	Dec (2000)	$S^{peak}_{1.3mm}$ (mJy/beam)	S^{peak}_{850} (mJy/beam)	S/N (σ)	IR assn
F-MM1	$16^h27^m21.84^s$	$-24°39'59.31''$	$16^h27^m21.49^s$	$-24°39'54.38''$	65 ± 20	1660 ± 20	74	
F-MM2a	$16^h27^m23.86^s$	$-24°40'35.18''$	$16^h27^m24.43^s$	$-24°40'34.79''$	—	1760 ± 25	69	
F-MM2b	$16^h27^m23.86^s$	$-24°40'35.18''$	$16^h27^m24.69^s$	$-24°41'04.03''$	—	1220 ± 25	48	Y
F-MM3	—	—	$16^h27^m26.69^s$	$-24°40'51.71''$	—	1080 ± 35	31	Y
F-MM4	—	—	$16^h27^m28.20^s$	$-24°39'30.17''$	—	310 ± 35	9	Y
F-MM5	—	—	$16^h27^m39.62^s$	$-24°39'15.26''$	—	130 ± 35	4	Y
F-MM6	—	—	$16^h27^m43.73^s$	$-24°42'34.59''$	—	150 ± 40	4	
F-MM7	—	—	$16^h27^m39.81^s$	$-24°43'12.25''$	—	190 ± 40	5	Y
F-MM8	—	—	$16^h27^m39.22^s$	$-24°42'39.77''$	—	330 ± 40	8	
F-MM9	—	—	$16^h27^m40.46^s$	$-24°42'20.22''$	—	150 ± 40	4	
H-MM1	—	—	$16^h26^m19.12^s$	$-24°28'20.14''$	—	60 ± 15	4	Y
H-MM2	—	—	$16^h26^m02.17^s$	$-24°32'25.49''$	—	670 ± 25	27	
H-MM3	—	—	$16^h26^m03.45^s$	$-24°31'20.50''$	—	550 ± 25	22	
H-MM4	—	—	$16^h25^m59.95^s$	$-24°31'29.82''$	—	280 ± 20	14	
H-MM5	—	—	$16^h25^m40.64^s$	$-24°30'22.68''$	—	250 ± 20	13	
H-MM6	—	—	$16^h25^m42.25^s$	$-24°30'29.70''$	—	120 ± 25	5	
H-MM7	—	—	$16^h25^m38.39^s$	$-24°22'37.82''$	—	100 ± 35	3	

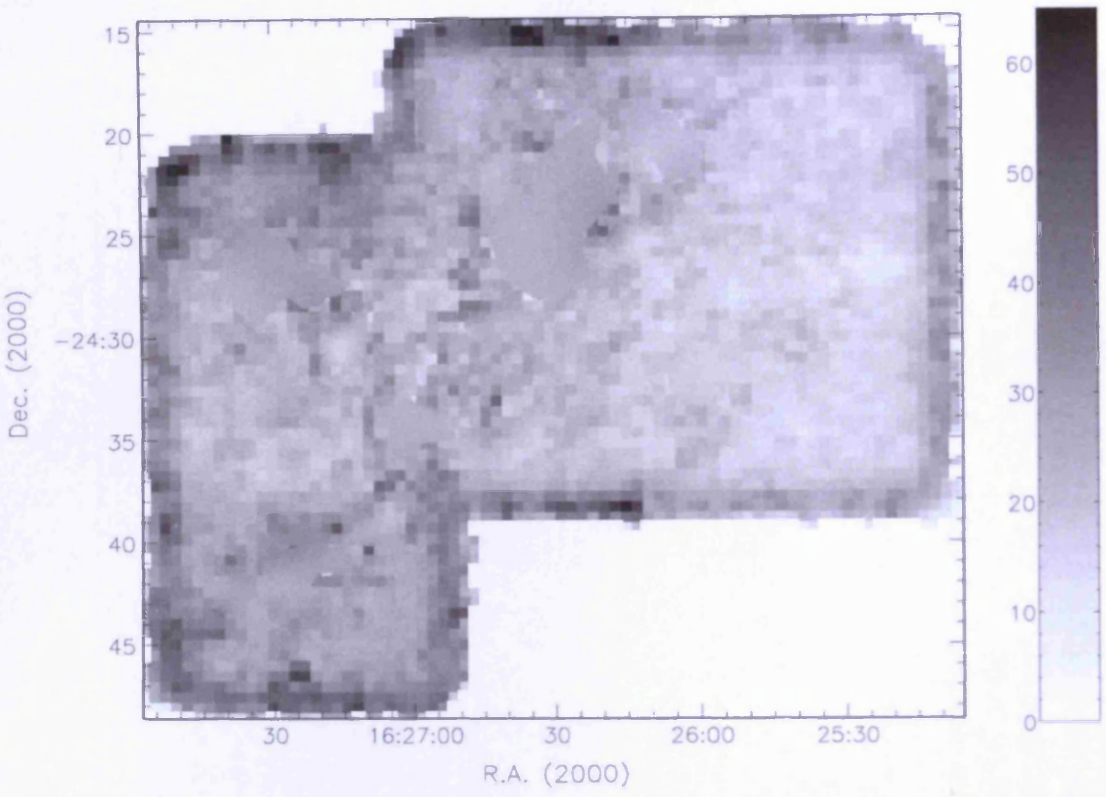

Figure 3.4: The 850-μm noise map for Ophiuchus main cloud L1688. The scale bar shown is in units of mJy/beam.

The resultant noise map is shown in Figure 3.4. It can be seen that the south and north-east corners of the map have a higher level of noise. These are the two regions containing the least number of observations. The noise in the whole map ranges from 15 to 40 mJy beam^{-1} with a median value of 25 mJy beam^{-1}.

A signal-to-noise map was created by dividing the data map by the noise map. Sources were identified with the method from Nutter & Ward-Thompson (2007), in which the signal-to-noise map is used along with the following set of criteria. Any sources with a peak flux density of 5σ or more were taken to be real. A dip of at least 3σ was required between two adjacent peaks for those two peaks to be identified as two separate sources.

The 3σ contour from the signal-to-noise map was used to draw an elliptical

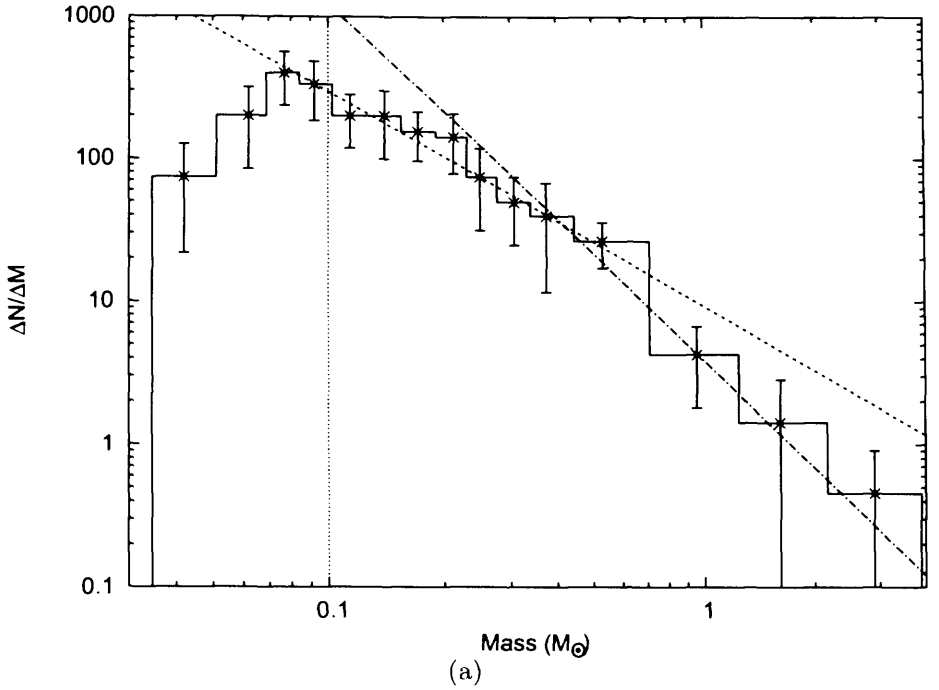

(a)

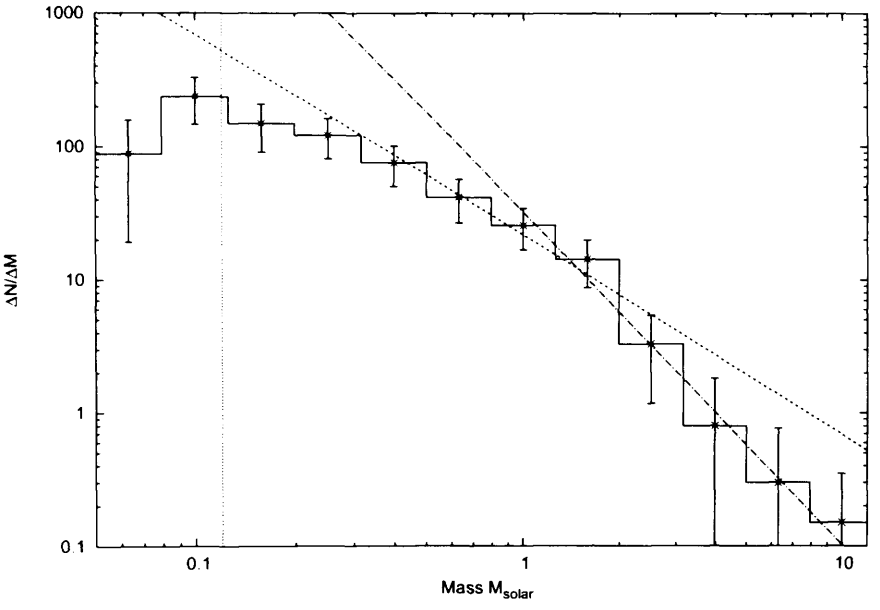

(b)

Figure 3.5: Comparison of 1.3-mm and 850-μm datasets. (a) Graph of $\Delta N/\Delta M$ against mass for L1688, recreated from MAN98 1.3-mm data for comparison with data from this study. The quantity $\Delta N/\Delta M$ is the number of cores per unit mass, counted in each mass bin. (b) Equivalent graph using SCUBA 850-μm data from JCMT archive. In each plot, the vertical dashed line shows the completeness limit of the study. The two dot-dashed lines on each plot show fits of the two power law slopes from the higher-mass end of the IMF (see text). Error bars correspond to $\sqrt{N}$ counting statistics. There are additional sources of uncertainty (e.g. errors in mass from noise in the map) however it is not clear how these should be included.

aperture around each identified source on the data. The flux density for any given source was then derived using this 3σ aperture and a 'sky' aperture of the same size placed on a nearby area in the map containing no significant emission. The locations of each core from each region are given in Tables 3.3 and 3.4. Also given in these tables are the equivalent flux densities from MAN98.

The only places on the map where this method for characterising cores does not apply is when the cores lie on, or adjacent to, bright emission. In these cases, such as cores next to SM1 in Rho Oph-A (Ward-Thompson et al., 1989), apertures were drawn following contours on the data map corresponding to the true 3σ value and the flux density divided in proportion to the peak flux densities of the cores within areas of bright emission. 93 cores were found, 20 of which had an IRAS or 2MASS infrared source associated with them. These latter cores were discounted in the subsequent analysis as not being prestellar.

Figures 3.6 and 3.7 show a comparison the Nutter & Ward-Thompson (2007) core extraction technique with a simple measure of the full-width at half-maximum (FWHM) for each core. Figures 3.6 and 3.7 show the core mass functions derived in each case. The plots are consistent, reflecting the fact that the overall variation in core masses across the region only differ by a small amount between the two techniques. I adopt the Nutter & Ward-Thompson (2007) method because it allows a direct comparison to be made to that study. This is discussed in Section 3.6.4.

The completeness limit, for prestellar cores, can be estimated using the measured sensitivity of the map, together with the average size of the detected cores. The latter because more mass can be hidden in the noise if the source is larger. In practice this can be done by scaling the integrated flux density from a number of well detected objects, down to the level where the sources would be just undetected,

taking into account the selection criteria. For more details of this technique, see Nutter & Ward-Thompson (2007). The completeness limit, for typical prestellar cores in Ophiuchus, was found to be 0.1 $M_{\odot}$.

3.5 Core Masses

If we adopt a representative spherical dust grain with radius a_D and internal density ρ_D, then the mass of a dust grain, M_D, is given by,

$$M_D = \frac{4\pi a_D^3 \rho_D}{3}, \tag{3.1}$$

and the number of dust grains, N_D, is therefore

$$N_D = \frac{3M_D}{4\pi a_D^3 \rho_D}. \tag{3.2}$$

Similarly, the monochromatic luminosity of a dust grain, L_ν, is given by,

$$L_\nu = 4\pi a_D^3 Q_\nu \pi B(\nu, T_D), \tag{3.3}$$

where Q_ν is the emissivity of the dust cloud, T is the temperature and $B(\nu, T_D)$ is the blackbody function. Provided the dust is optically thin at frequency ν, the monochromatic flux, F_ν, is given by,

$$F_\nu = \frac{N_D L_\nu}{4\pi D^2}. \tag{3.4}$$

This equation can be rearranged to give us the mass of the dust in the cloud:

$$M_D = \frac{4 a_D \rho_D D^2 F_\nu}{3 Q_\nu B(\nu, T_D)}. \tag{3.5}$$

At a given frequency, ν, the dust mass opacity can be defined (Hildebrand, 1983) by the equation ,

$$\frac{1}{\kappa_\nu} = \frac{4}{3}\frac{a\rho}{Q(\nu)}. \tag{3.6}$$

We can use this definition to simplify equation 3.5 to be

$$M_D = \frac{F(\nu) D^2}{B(\nu, T)} \frac{1}{\kappa_\nu}. \tag{3.7}$$

This equation means that we can determine the mass of a submillimetre dust cloud from observations if we know its distance, dust mass opacity and temperature. Temperatures for each of the regions in the cloud are given in Table 3.5. I calculate the masses using the revised temperatures given by Stamatellos et al. (2007), hereafter SWW07.

MAN98 assumed a value for dust mass opacity of $\kappa_{1.3mm} = 0.005$ cm^2 g^{-1} for prestellar clumps and cores (Preibisch et al., 1993; André et al., 1996). This is extrapolated to 850μm using the wavelength dependence factor, β, which is

Table 3.5: Assumed dust temperatures (T_{dust}) in Kelvin of the regions in the Ophiuchus cloud from MAN98 and SWW07.

Region	MAN98	SWW07
Oph-A	20	11
Oph-B	12	10
Oph-C	12	10
Oph-E	15	10
Oph-F	15	10
Oph-H	—	10

assumed have a value of 2 in the submillimetre (Hildebrand, 1983). Therefore I use a dust opacity value of $\kappa_{850} = 0.01$ cm^2 g^{-1}.

SWW07 estimated the dust temperatures of clumps in Ophiuchus. They found that in regions where prestellar cores are observed, temperatures of 10-11K are to be expected. Specifically they suggest a dust temperature of 10K for all the main regions identified by this study. The exception to this value is Oph-A, containing SM1 (see Table 3.5).

For this study I assume a distance of 139±6 pc to Ophiuchus (Mamajek, 2008). This value was determined using Hipparcos data and reddening studies (Chini, 1981; de Geus, de Zeeuw, & Lub, 1989; Knude & Hog, 1998). Using these new parameters for distance and temperature a new CMF for the region has been created.

3.6 Core Mass Function

In this section I describe CMFs constructed from the above data. First I compare these with previous work, and then see what can be learnt from this new analysis.

3.6.1 Comparison with Previous Work

MAN98

Figure 3.5 shows my data plotted in the same way as the mass spectrum from MAN98, which has been recreated for comparison. Good agreement is seen. Below about 2 $M_{\odot}$ in my data, the slope in the power law decreases from -1.35 to -0.3 (see section 3.6.2). The MAN98 results also place this 'knee' in the high-mass end of the spectrum, at approximately $0.5M_{\odot}$.

My mass spectrum also shows another decline in the slope at lower masses in the mass range up to approximately $0.7M_{\odot}$ (Figure 3.5). This effect is seen here, seven times above the completeness limit, and represents a power-law equivalent to the low-mass slope of the stellar IMF.

Johnstone et al. 2000

Johnstone et al. (2000) produced a cumulative CMF for L1688 using some of the same scan-map data (see their Figure 7). Once again, good agreement is seen. Their CMF shows similarities with the two higher-mass slopes of the stellar IMF, in agreement with this study. This earlier study's completeness limit of approximately $0.4M_{\odot}$ prevents comparison at lower masses.

The CMF produced by Johnstone et al. (2000) shows a 'knee' at around $0.8M_{\odot}$. This feature is seen in a similar location in my data when an adjustment is made for the different temperature assumptions of the two studies.

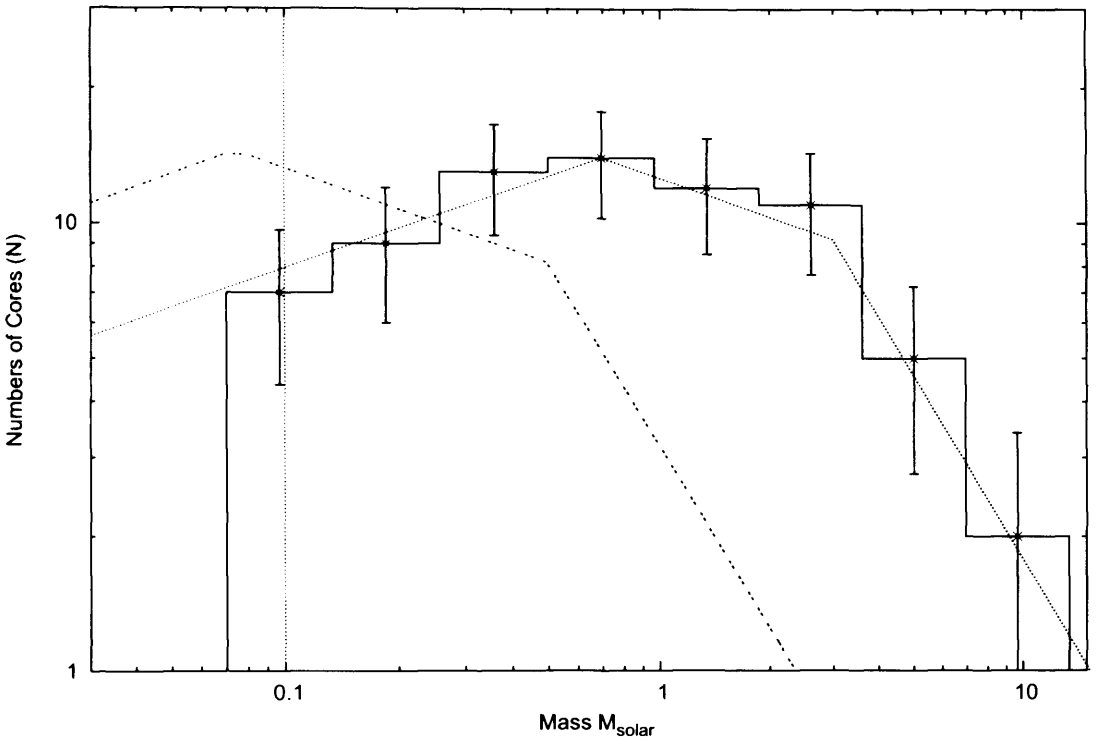

Figure 3.6: CMF for the Ophiuchus dark cloud shown as a plot of number of cores, N, against mass of cores in Solar masses. The completeness limit is shown at a dotted vertical line at $0.1M_{\odot}$. A three-part stellar IMF (see text), normalised to the peak in N of the CMF, is overlaid as a dotted line. The three power-law slopes of the IMF are also shown fitted to the data as solid black lines. Error bars correspond to $\sqrt{N}$ counting statistics. There are additional sources of uncertainty (e.g. errors in mass from noise in the map) however it is not clear how these should be included.

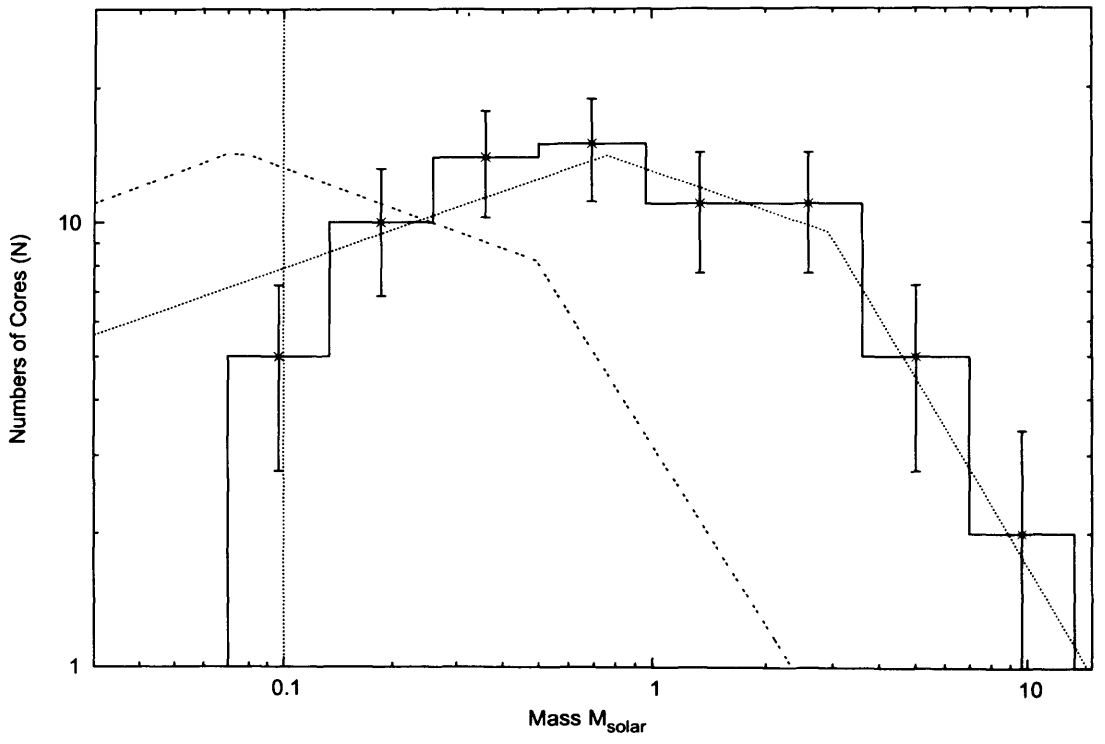

Figure 3.7: Same as Figure 3.6 but this time using the FWHM core extraction method. See text for details.

Stanke et al. 2006

Stanke et al. (2006) mapped the L1688 region at 1.2mm using IRAM. They produced a mass spectrum with a similar form to that produced in Figure 3.5b above. Stanke et al. (2006) survey 111 starless cores. Although this outnumbers the cores identified in this study, many of these are extended, low surface brightness objects that may not be gravitationally bound. They conclude that regardless of the details, the CMF resembles the shape of the IMF with three power-law slopes presented in their CMF plot.

Stanke et al. (2006) also show the 'knee' and a tentative turnover in their CMF. The positions of these features are not well constrained but their locations at 0.5-1.0$M_\odot$ and 0.1-0.3$M_\odot$, respectively, are consistent with my data.

3.6.2 My Data

The 73 cores in my data with no infrared association are used to plot the CMF in Figure 3.6. The dashed vertical line is the 5σ completeness limit of $0.1M_\odot$, for prestellar cores in the map. This is an improvement over the MAN98 completeness limit, which is mainly due to the better resolution and sensitivity of 850 μm provided by the complete SCUBA data.

Figure 3.6 shows my CMF. Cores noted to have a 2MASS or IRAS infrared source associated with their position in Tables 3.3 and 3.4, are not included. Compared with Figure 3.5, this representation of the data uses a simple number count of cores as opposed to a count divided by the bin size. Figure 3.6 demonstrates that the data are consistent with the three power-laws in the Stellar IMF.

This is the first time that the turnover in the CMF has been seen in Ophiuchus. Here it is seen at $0.7M_{\odot}$. The only other cloud for which this turnover has been detected is Orion (Nutter & Ward-Thompson, 2007). To compare the CMF to the stellar IMF we use a stellar IMF with a power law of the following form:

$$M\frac{dN}{dM} \propto M^{-x}, \tag{3.8}$$

where x takes on different values in different mass regimes. For the stellar IMF we assume the following exponents:

$$\begin{aligned} x &= 1.35, \quad 0.5M_{\odot} < M, \\ x &= 0.3, \quad 0.08M_{\odot} < M < 0.5M_{\odot}, \\ x &= -0.3, \quad 0.01M_{\odot} < M < 0.08M_{\odot}. \end{aligned} \tag{3.9}$$

The higher mass end values for x are taken from Kroupa (2002). Below $0.08M_{\odot}$ the IMF is based on fits to young cluster populations used by Chabrier (2003). In this study values between 0.2 and 0.4 are found, so an average of 0.3 is used here.

3.6.3 Star Formation Efficiency

The striking similarity between the CMF and the stellar IMF that is seen in the Ophiuchus L1688 cloud, once again gives a strong indication that the form of the IMF is determined at the prestellar core stage. Furthermore, I have traced this similarity to lower masses than was previously possible. This has allowed me to determine the turnover mass in the core mass function.

Table 3.6: Masses and Sizes for cores in Oph-A and Oph-B regions of the Ophiuchus L1688 core. Error in mass for each core is derived from the noise in the map. Error in radius is assumed as a human error of ±10% in the measurement of the radii of cores.

Core Name	Mass ($M_\odot$)	Mass Error ($M_\odot$)	Size (AU x AU)
A-MM1	0.09	0.004	Unresolved
A-MM2/3	0.16	0.004	2800 x 1900
A-MM4	0.48	0.012	2100 x 2100
A-MM5	0.82	0.012	2800 x 2500
A-MM6	2.10	0.015	3600 x 2500
A-MM7	0.92	0.015	3300 x 2200
A-MM8	3.18	0.013	2200 x 1900
A-MM11	0.64	0.013	5600 x 1900
A-MM12	0.45	0.013	Unresolved
A-MM16	0.03	0.010	Unresolved
A-MM17	0.03	0.010	1900 x 1900
A-MM18	0.87	0.016	4200 x 2800
A-MM20	0.12	0.016	Unresolved
A-MM21	0.21	0.018	Unresolved
A-MM22	0.11	0.018	2800 x 2200
A-MM23	1.50	0.016	4900 x 2100
A-MM26	0.43	0.013	3100 x 1900
A-MM27	0.34	0.013	4200 x 1900
A-MM28	0.18	0.021	2500 x 1900
A-MM29	0.16	0.021	Unresolved
A-MM30	1.28	0.010	4400 x 1900
A2-MM1	0.33	0.010	3300 x 1900
A3-MM1	0.33	0.016	2500 x 2200
A-N	0.21	0.016	Unresolved
A-S	0.01	0.018	2100 x 1900
SM1	7.35	0.013	6100 x 1900
SM1N	2.91	0.008	2500 x 1900
SM2	5.97	0.009	5100 x 3600
VLA1623	2.93	0.016	4200 x 2500

Table 3.6: Masses and Sizes for cores in Oph-A and Oph-B regions of the Ophiuchus L1688 core. Error in mass for each core is derived from the noise in the map. Error in radius is assumed as a human error of ±10% in the measurement of the radii of cores.

Core Name	Mass ($M_\odot$)	Mass Error ($M_\odot$)	Size (AU x AU)
B1-MM1	0.02	0.016	Unresolved
B1-MM2	0.63	0.006	3100 x 1900
B1-MM3	2.61	0.006	2800 x 2500
B1-MM4	2.10	0.006	5000 x 3200
B1-MM6	0.22	0.019	2500 x 1900
B1-MM7	0.11	0.019	1900 x 1900
B1B2-MM1	0.22	0.022	5600 x 2200
B2-MM2	0.88	0.011	3300 x 2200
B2-MM4	0.96	0.011	Unresolved
B2-MM5	1.14	0.011	3600 x 2500
B2-MM6	1.62	0.012	5000 x 4200
B2-MM7	0.62	0.016	4200 x 2800
B2-MM8	1.63	0.009	2800 x 2500
B2-MM9	1.37	0.012	3900 x 1900
B2-MM13	0.49	0.019	3100 x 2800
B2-MM14	1.26	0.010	4400 x 2100
B2-MM15	0.62	0.019	Unresolved
B2-MM16	1.31	0.010	2500 x 2200

Table 3.7: Masses and Sizes for cores in Oph-C, Oph-E, Oph-F and Oph-H regions of the Ophiuchus L1688 core. Error in mass for each core is derived from the noise in the map. Error in radius is assumed as a human error of ±10% in the measurement of the radii of cores.

Core Name	Mass ($M_\odot$)	Mass Error ($M_\odot$)	Size (AU x AU)
C-MM2	1.11	0.016	Unresolved
C-MM3	1.42	0.013	4200 x 3300
C-MM5	1.24	0.013	Unresolved
C-MM6	1.05	0.013	6700 x 3300
C-MM8	0.15	0.022	Unresolved
C-MM9	0.06	0.019	2200 x 2100
C-MM10	0.37	0.016	2400 x 1900
C-MM12	0.09	0.019	4400 x 2400
C-N	1.60	0.015	4700 x 3800
E-MM4	0.31	0.025	3600 x 3100
E-MM2a	0.12	0.025	1900 x 1900
E-MM2b	0.16	0.025	3100 x 2500
E-MM2d	0.41	0.025	Unresolved
E-MM5	0.28	0.020	2800 x 2100
E-MM8	0.19	0.019	3100 x 1900
F-MM1	1.05	0.014	4200 x 2400
F-MM2a	1.11	0.016	4400 x 3800
F-MM6	0.10	0.025	Unresolved
F-MM8	0.21	0.025	Unresolved
F-MM9	0.10	0.025	Unresolved
H-MM2	0.42	0.016	4700 x 3200
H-MM3	0.34	0.016	3900 x 2500
H-MM4	0.17	0.013	Unresolved
H-MM5	0.16	0.013	Unresolved
H-MM6	0.07	0.016	Unresolved
H-MM7	0.06	0.022	Unresolved

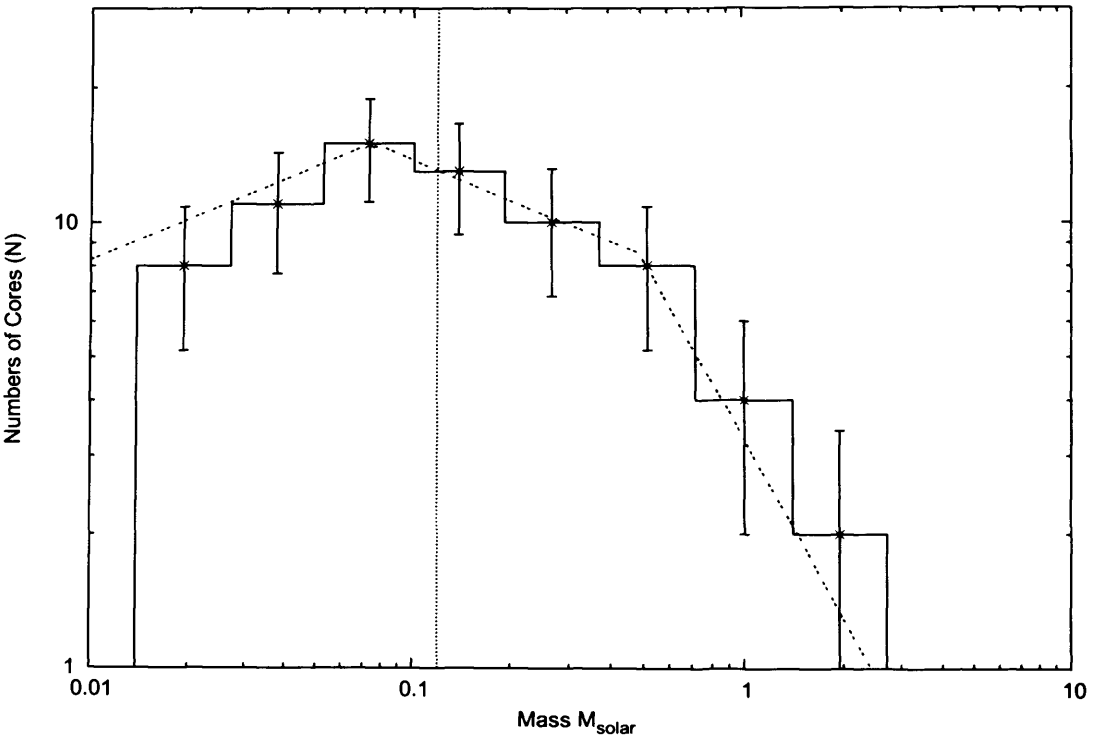

Figure 3.8: CMF for the Ophiuchus L1688 cloud multiplied by a star formation efficiency factor of 0.3, assuming each core forms a single star. A three part stellar IMF, normalised to the peak in N of the CMF, is overlaid as a dotted line (see text for details). Error bars correspond to $\sqrt{N}$ counting statistics.

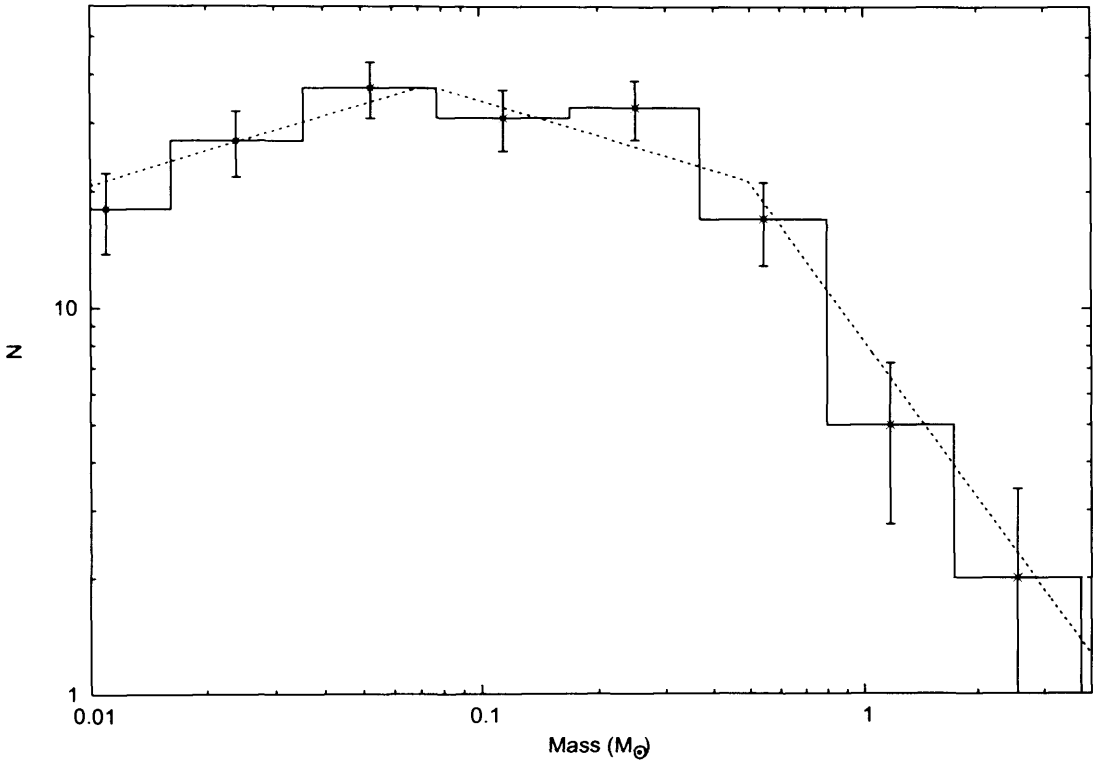

Figure 3.9: Potential stellar IMF for the Ophiuchus cloud, modelled using the 'fully multiple star model' from Goodwin et al. (2008) shown as a histogram. The real stellar IMF is shown as a dotted line. See text for details. Error bars correspond to $\sqrt{N}$ counting statistics.

If it is assumed that each core will form a single star with a fixed star formation efficiency (ϵ) for all cores, then the CMF can be used to predict an output IMF. In this case the best fit is obtained with $\epsilon = 0.2$ (see Figure 3.8). This is a simplistic model, and the shape of the CMF does not change as a function of ϵ.

A more sophisticated approach than 'one core, one star' would be to model the transformation between core masses and stellar masses in a way that produces multiple stars from each core. Goodwin et al. (2008) discuss what they call the 'fully multiple star model'. This model assumes that cores with masses lower than a certain mass, M_{CRIT}, will form binary systems and larger cores will form binary or multiple systems. $M_{CRIT} = \epsilon M_{KNEE}$, where M_{KNEE} is the location of the 'knee' in Figure 3.6 — Goodwin, Whitworth, & Ward-Thompson (2004). Thus for this study I use $M_{CRIT} = 2\epsilon M_{\odot}$.

Using the 'fully multiple star model' it is possible to transform the CMF in Figure 3.6 to produce a potential, future stellar IMF for L1688 – see Figure 3.9. This plot shows very good agreement with the real stellar IMF. The best fit model requires $\epsilon = 0.4$.

It is important to remember that this is the star formation efficiency within gravitationally bound cores, and so a high value is to be expected. The total mass of prestellar cores in L1688 is $29.3 M_{\odot}$. The total mass of the L1688 cloud complex is $1447 M_{\odot}$ (Loren, 1989). Coupling this to our value of $\epsilon = 0.4$ for the prestellar cores gives a value for the absolute star formation efficiency of the L1688 cloud of about 2%.

3.6.4 Comparison with Orion

Nutter & Ward-Thompson (2007) used the SCUBA data archive to produce a CMF for the Orion molecular cloud and found a turnover in the CMF at $1.3M_{\odot}$. This is over 2 times higher than the CMF turnover seen here at $0.5M_{\odot}$ in the L1688 cloud. The instrumentation and methodology for deriving the properties of cores is the same in both studies. However the two regions are clearly quite different.

Both regions can be modelled using the method described in the previous section (Goodwin et al., 2008), but only by using very different values for the SFE. These results suggest that the position of the turnover in the CMF varies with the environment in which the cores reside.

3.7 Summary

In this chapter I have re-analysed the SCUBA archive data for L1688, incorporating all available scan-map and jiggle-map data. An updated form of the CMF in the L1688 cloud complex has been presented using updated values for the distance to this region as well as new estimates for the temperatures of the cores.

I have shown that the CMF for L1688 is consistent with a three part power-law with slopes the same as seen in the stellar IMF. The higher-mass end of the CMF declines as a power law which is consistent with other studies of L1688 (MAN98; Johnstone et al., 2000; Stanke et al., 2006) as well as studies of Orion (Nutter & Ward-Thompson, 2007; Motte et al., 2001; Johnstone et al., 2001, 2006).

The results are mostly in agreement with those found in earlier studies. But

these deeper maps have allowed the discovery of a turnover in the CMF at $0.5M_{\odot}$ which shows that the core mass function appears to mimic the stellar initial mass function. This concordance is indicative that the stellar IMF is determined at the prestellar core stage.

It has been shown that the relationship between the CMF and IMF is not necessarily a simple 1:1 translation in the mass axis. Consistency can also be achieved using a fully multiple star model.

Chapter 4

HARP Observations of L1688

4.1 Introduction

In this Chapter I outline HCO^+ (J=4→3) spectral line data taken using HARP on the James Clerk Maxwell Telescope (JCMT). I present observations of a subset of the cores mapped in Chapter 3. I analyse 59 HCO^+ (J=4→3) spectral line profiles from prestellar cores in the L1688 region of the Ophiuchus star-forming complex.

HARP is a spectral-imaging receiver for the JCMT, operating at submillimetre wavelengths (Smith et al., 2003, 2008, see Section 2.1.3). It works in conjunction with ACSIS – Auto-Correlation Spectral Imaging System (Dent et al., 2000) – a back-end correlator. It provides a spectral resolution of 0.026 km s^{-1}, and a spatial resolution of 14 arcseconds — equivalent to SCUBA at 850 μm.

Table 4.1: Table of regions showing date of observation, position (in Right Ascension, Declination), size (in arcseconds), and position angle of observed HARP maps in this investigation. Right Ascension and Declination of map off positions are also shown. All dates of observations are from 2009.

Map	Dates of Observations	R.A. (2000)	Declination (2000)	Width (″)	Height (″)	PA (°)	Off Pos. R.A. (2000)	Off Pos. Declination (2000)
Oph-A	25-26 Apr, 01 May	$16^h26^m24.03^s$	$-24°23'43.0''$	690	349	45	$16^h25^m52.99^s$	$-24°25'23.0''$
Oph-AN	12,20 Jun	$16^h26^m44.07^s$	$-24°18'53.7''$	420	348	50	$16^h27^m05.03^s$	$-24°24'58.3''$
Oph-B	15,17,22 May, 02 Jun	$16^h27^m22.93^s$	$-24°28'17.9''$	550	348	150	$16^h27^m05.03^s$	$-24°24'58.3''$
Oph-C	08,10-11 Jun	$16^h26^m55.78^s$	$-24°34'16.5''$	420	348	50	$16^h27^m05.03^s$	$-24°24'58.3''$
Oph-E,F	03,04,06-08 Jun	$16^h27^m15.76^s$	$-24°39'52.4''$	600	348	40	$16^h27^m07.82^s$	$-24°44'14.3''$

4.2 Observations

The observations in this chapter consist of 40 hours of data taken on multiple nights from April to June 2009. Five fields in L1688 were mapped, and these are outlined in Table 4.1. The maps were taken in raster position-switch mode. In this mode spectra are taken on the fly, with the telescope scanning in a direction parallel to the sides of the map. At the end of each scan row, the array is displaced by one array-width perpendicular to the scan direction. Another map is created by scanning in a perpendicular direction to the first. These can be combined in a 'basket-weave' pattern to create a map with minimal striping due to differences in receptor noise. Separate fixed off-positions were used for each region. These are given in Table 4.1. These positions were selected as having no 850μm emission (Simpson, Nutter, & Ward-Thompson, 2008). They were also checked for HCO^+ (J=4$\rightarrow$3) emission using a 60-second position-switched 'stare' observation.

The data were reduced using the Starlink [1] project software KAPPA (Currie et al., 2008, and references therein) and SMURF (Jenness et al., 2008) routines. It was found that in order to produce the optimal map from the input data, the worst quality data had to be discarded before the map was reconstructed. This was done by measuring the root-mean-square (RMS) noise value of each of the spectra in the input data and masking those with the highest RMS before generating the map. An iterative method was used to determine the optimal RMS value to apply as a mask. In each step of the iteration, the data were masked using a different limiting RMS before being reconstructed into a map using the MAKECUBE routine (Jenness et al., 2008). The RMS in the reconstructed map was then measured. The limiting RMS was varied to produce a reconstructed map with the lowest RMS. This map

[1] http://starlink.jach.hawaii.edu/starlink

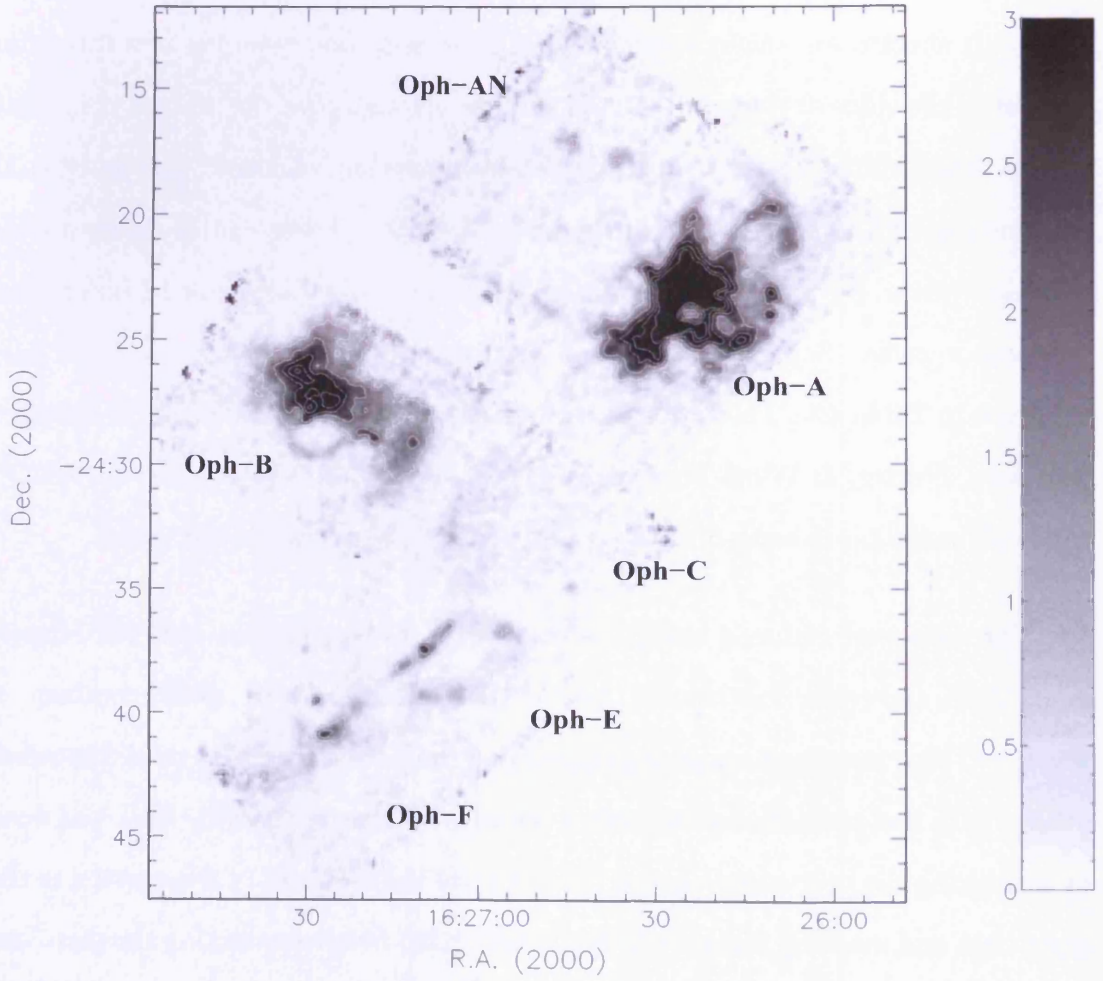

Figure 4.1: Integrated intensity map of HCO^+ (J=4→3) toward L1688. Contours at 1.0, 2.0, 3.0, 4.0 and 5.0 K km s^{-1}. The scale bar shows integrated intensity in K km s^{-1}

was taken to be the optimal map.

4.3 Results

4.3.1 Maps

Figure 4.1 shows the integrated intensity map towards L1688 in HCO^+ (J=4→3). A number of sources are seen in the map and the correlation between this integrated HCO^+ (J=4→3) map and the submillimetre continuum map shown in Chapter 3 is good. The main regions of the cloud are labelled according to their usual names (Motte et al., 1998).

The RMS noise map for the HCO^+ (J=4→3) data is shown in Figure 4.2. Excellent weather conditions gave a very low RMS noise of less than 0.15 K in antenna temperature, T_A^*, for maps of Oph-A, E and F. The noise in Oph-B increases to around 0.2 K toward the edges but most cores are still within the 0.15 K contours. Poorer weather during mapping of Oph-C resulted in a more mixed final map, with some portions mapped to 0.15 K and others to 0.2 K. The lower integration times on Oph-AN mean that the RMS noise level is higher in this region.

Figure 4.3 shows the same region as Figure 4.1 but with a narrower range of velocities. This figure has been split into red (4.0–5.0 km s^{-1}), green (3.0–4.0 km s^{-1}) and blue (2.0–3.0 km s^{-1}) velocity channels, centred around the systemic velocity of L1688 (Loren, 1989). On this version of the map it is clearly seen that Oph-A is moving toward us relative to the rest of L1688. Both Oph-A and B show evidence for HCO^+ (J=4→3) outflows and a wide range of velocities are seen in both regions. Oph-E and F appear much redder and are moving away from

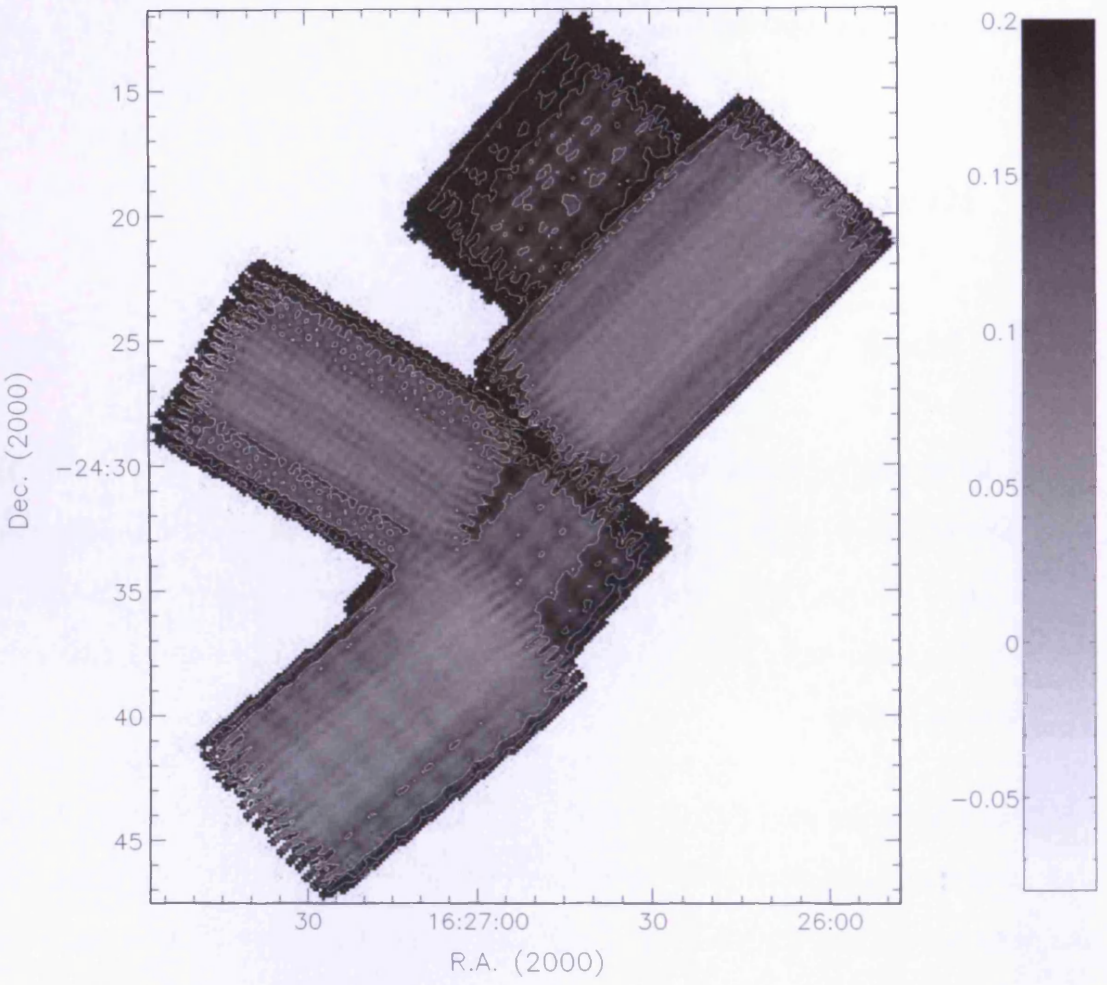

Figure 4.2: HCO^+ (J=4→3) noise map for L1688. Contours at 0.15, 0.20 and 0.25 K. The scale bar shown is also in units of K.

us relative to the other regions. Figure 4.4 shows the same data as Figure 4.3 displayed as three separate images.

Emission is dominated in the integrated intensity map by the bright Oph-A region (Francesco, André, & Myers, 2004), containing SM1 (Ward-Thompson et al., 1989) and VLA1623 (André et al., 1993). Both of these sources are highlighted by tightly packed contours in Figure 4.1. A great deal of structure can be made out in Oph-A. An arch of material is seen traced out just northwest of the brightest part of the region – the northern part of which is moving toward us relative to the

southern part. Just south of this arch, a line of sources make up a partial loop that curves around the western edge of the Oph-A region stretching through all the velocity channels.

The Oph-B region (Friesen et al., 2005) is also very active and a distinct semi-circular loop can be seen on its south side. Both this loop and those in Oph-A have approximate radii of curvature of 0.1pc and have kinematic velocities of the order of 1-2 km s^{-1}. The northern part of Oph-B is seen moving toward us relative to the rest of the region.

Oph-C appears to be faint in the maps. The weak SCUBA sources measured here (see Chapter 3) seem to have little HCO^+ (J=4→3) associated with them. A large, ring-like structure is seen, in the red channel, making up the Oph-E region and this in turn leads into a filament that moves into the green channel as it joins the Oph-F region. Only the northern-most part of the Oph-F region is seen in these maps.

4.3.2 Spectral Line Profiles

Prestellar cores undergoing collapse, will have excitation temperature profiles that increase toward their centre. In addition, we preferentially see material that is closer to us. Material on the near-side of a collapsing core is therefore preferentially seen as cooler than material on the far side. This means that the relatively blue-shifted material is seen to the observer as having a higher temperature. The result is that collapsing cores display an asymmetric spectral line profile, with the peak from material at the blue-shifted end being more prominent than the red-shifted peak. Such a profile shape is referred to as a blue-asymmetric double-peaked profile

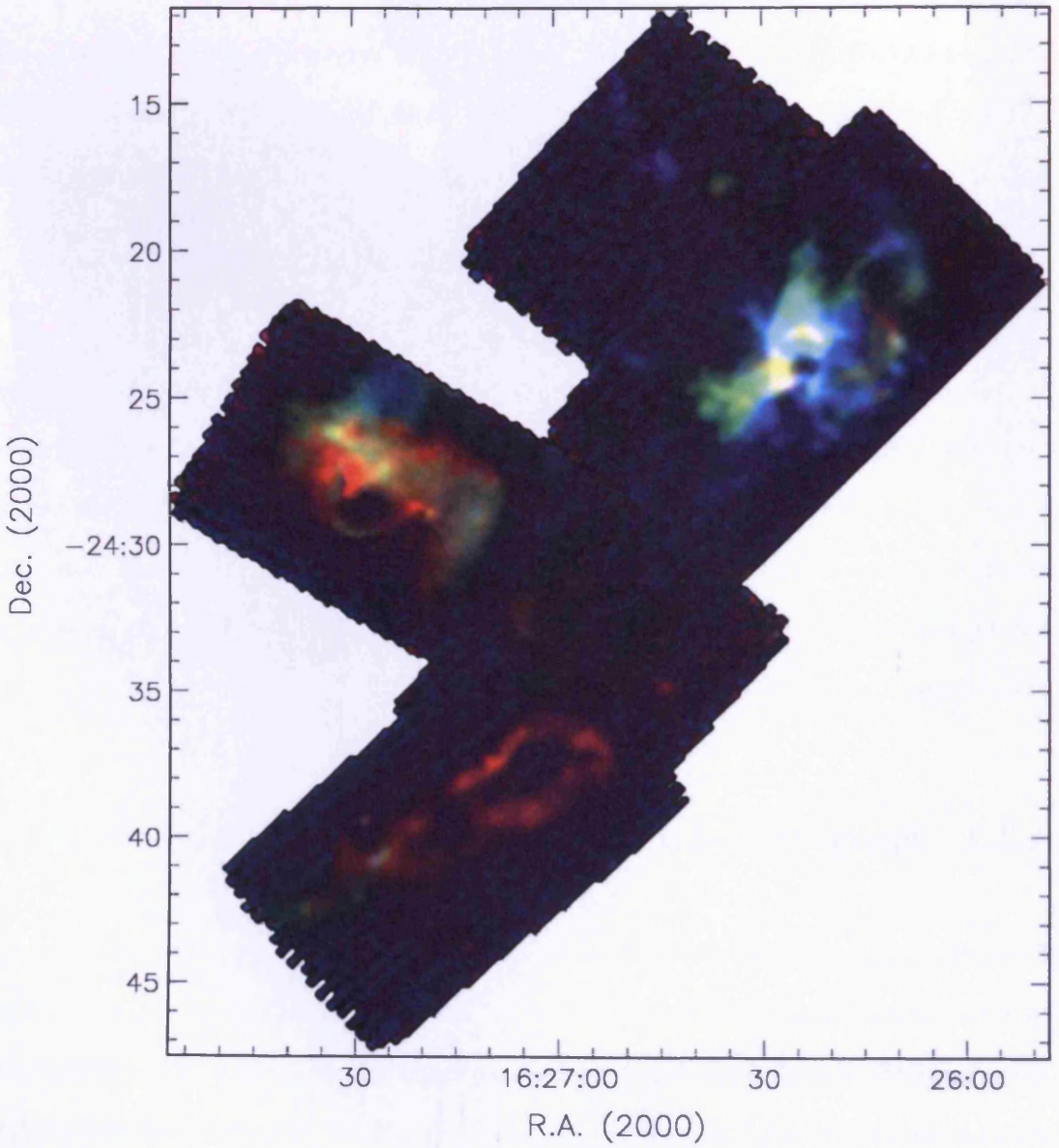

Figure 4.3: RGB false-colour image of HCO^+ (J=4→3) toward L1688 in red (4.0–5.0 km s^{-1}), green (3.0–4.0 km s^{-1}) and blue (2.0–3.0 km s^{-1}) velocity channels.

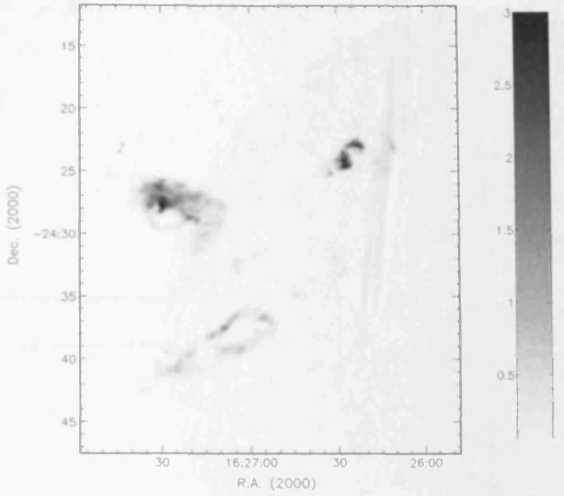

(a) 4.0–5.0 km s^{-1}

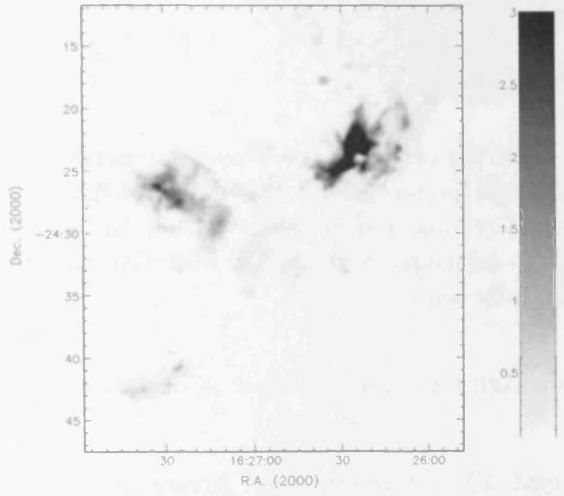

(b) 3.0–4.0 km s^{-1}

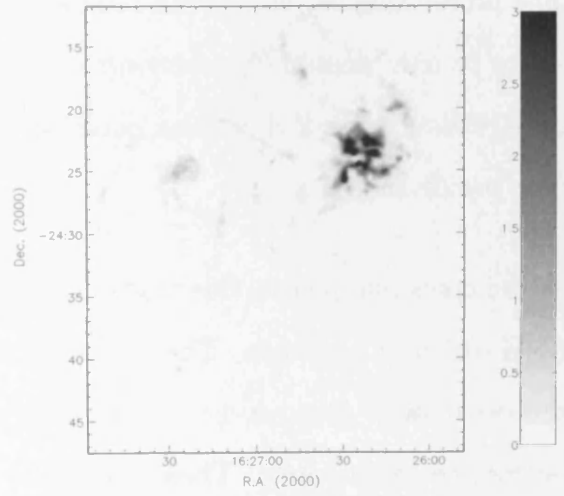

(c) 2.0–3.0 km s^{-1}

Figure 4.4: Integrated intensity maps of HCO^+(4–3) toward L1688 in red (4.0-5.0 km s^{-1}), green (3.0-4.0 km s^{-1}) and blue (2.0-3.0 km s^{-1}) velocity channels.

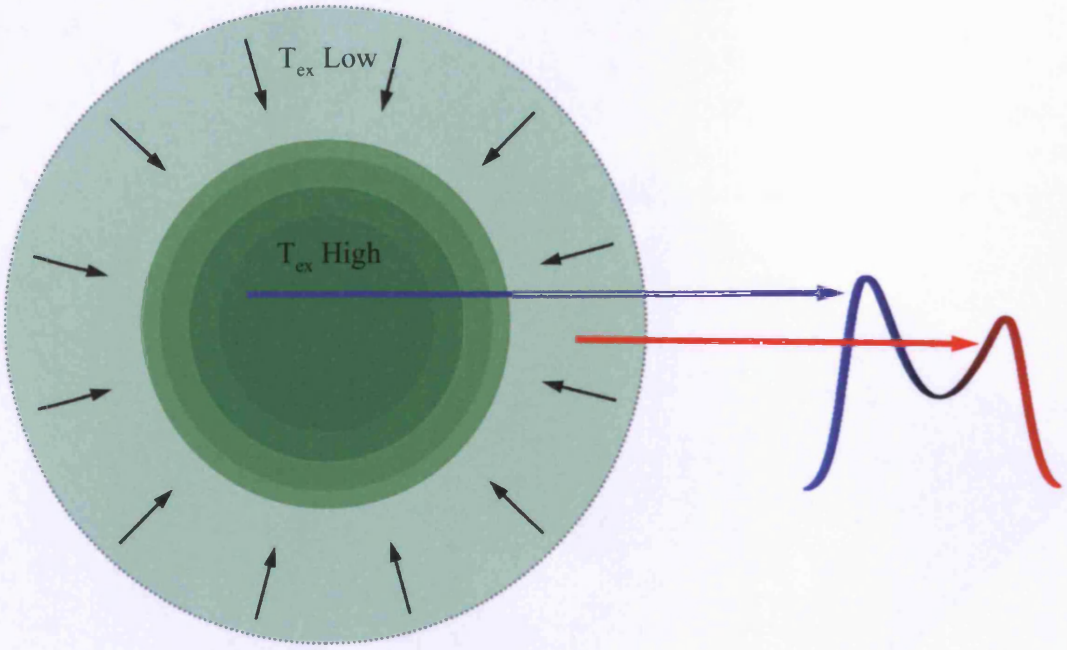

Figure 4.5: Illustration of the origin of the blue-asymmetric double peaked spectral line profile. An observer always preferentially sees material that is closer. For the relatively red-shifted material this means preferentially seeing the lower excitation temperature part of the core. For the relatively blue-shifted material, the higher excitation temperature region is preferentially seen.

and can be used as a signpost that collapse is occurring (See Figure 4.5).

I have categorised all of the observed prestellar cores based on their HCO^+ (J=4→3) spectral line profile shapes: cores with blue-asymmetric double-peaked profiles; cores with faint or only possible blue-asymmetric double-peaked profiles; cores with red-asymmetric double-peaked profiles; cores with single-peaked profiles and cores with unclear profile shapes.

Table 4.2 shows the cores mapped in this study, grouped into regions, along with their HCO^+ (J=4→3) profile shapes. The masses and radii for these cores from Chapter 3 are also shown. Figures 4.6 – 4.63 show the HCO^+ (J=4→3) spectral line profiles for the same cores. These plots also show the N_2H^+ line centres from André et al. (2007) as vertical dashed lines. These data are not

available for all cores.

Table 4.2: Table showing the Oph cores from Chapter 3, mapped using HARP. For each core, the radius (rounded to the nearest 100 AU) and mass from Chapter 3 are given along with the spectral profile shape from my HARP data. Blue-asymmetric and red-asymmetric double-peaked profiles are listed as BAD and RAD respectively.

Core ID	R.A. (2000)	Declination (2000)	Radius (AU)	Mass ($M_\odot$)	Profile Shape
A-MM1	$16^h26^m23.00^s$	-24°23′34.46″	1000	0.09	Single
A-MM2-3	$16^h26^m23.80^s$	-24°24′09.95″	1200	0.16	BAD (Possible)
A-MM4	$16^h26^m23.03^s$	-24°21′59.81″	1000	0.48	BAD
A-MM5	$16^h26^m26.66^s$	-24°22′28.60″	1300	0.82	RAD
A-MM6	$16^h26^m28.21^s$	-24°23′00.10″	1500	2.10	RAD
A-MM7	$16^h26^m30.05^s$	-24°22′17.93″	1400	0.92	BAD
A-MM8	$16^h26^m31.80^s$	-24°24′50.00″	1000	3.18	Single
A-MM11	$16^h26^m32.74^s$	-24°26′14.40″	1600	0.64	Single
A-MM16	$16^h26^m36.26^s$	-24°28′12.84″	1000	0.03	Single
A-MM17	$16^h26^m34.77^s$	-24°28′08.10″	1000	0.03	Single
A-MM18	$16^h26^m43.73^s$	-24°17′25.74″	1700	0.87	Single
A-MM21	$16^h26^m31.64^s$	-24°18′38.05″	1000	0.21	Single
A-MM22	$16^h26^m31.45^s$	-24°18′52.05″	1200	0.11	Unclear
A-MM23	$16^h26^m07.89^s$	-24°20′30.50″	1600	1.50	BAD
A-MM26	$16^h26^m15.40^s$	-24°25′32.50″	1200	0.43	BAD (Possible)
A-MM27	$16^h26^m13.85^s$	-24°25′25.16″	1400	0.34	BAD (Possible)
A-MM30	$16^h26^m09.63^s$	-24°19′43.25″	1500	1.28	Unclear
A2-MM1	$16^h26^m11.73^s$	-24°24′54.16″	1300	0.33	BAD (Possible)
A3-MM1	$16^h26^m10.07^s$	-24°23′11.00″	1200	0.33	Single
A-N	$16^h26^m22.74^s$	-24°20′00.00″	1000	0.21	Single
A-S	$16^h26^m42.69^s$	-24°26′08.05″	1000	0.01	Single
SM1	$16^h26^m27.73^s$	-24°23′58.17″	1700	7.35	RAD
SM1N	$16^h26^m27.93^s$	-24°23′31.67″	1100	2.91	Symmetric
SM2	$16^h26^m29.41^s$	-24°24′26.69″	2200	5.97	RAD
VLA1623	$16^h26^m26.74^s$	-24°24′30.00″	1600	2.93	RAD
B1-MM1	$16^h27^m09.32^s$	-24°27′43.73″	1100	0.02	Unclear
B1-MM2	$16^h27^m12.14^s$	-24°29′34.42″	1200	0.63	BAD
B1-MM3	$16^h27^m12.68^s$	-24°29′38.67″	1300	2.61	BAD
B1-MM4	$16^h27^m15.32^s$	-24°30′36.82″	2000	2.10	Unclear
B1-MM7	$16^h27^m18.72^s$	-24°30′24.64″	1000	0.11	Unclear
B1B2-MM1	$16^h27^m12.44^s$	-24°27′30.31″	1800	0.22	Unclear

Table 4.2: Table showing the Oph cores from Chapter 3, mapped using HARP. For each core, the radius (rounded to the nearest 100 AU) and mass from Chapter 3 are given along with the spectral profile shape from my HARP data. Blue-asymmetric and red-asymmetric double-peaked profiles are listed as BAD and RAD respectively.

Core ID	R.A. (2000)	Declination (2000)	Radius (AU)	Mass ($M_\odot$)	Profile Shape
B2-MM2	$16^h27^m19.97^s$	-24°27′23.45″	1400	0.88	BAD (Possible)
B2-MM4	$16^h27^m24.50^s$	-24°27′46.30″	1000	0.96	BAD
B2-MM5	$16^h27^m24.74^s$	-24°27′29.29″	1500	1.14	BAD
B2-MM6	$16^h27^m25.27^s$	-24°26′50.48″	2300	1.62	Single
B2-MM7	$16^h27^m26.66^s$	-24°27′39.72″	1700	0.62	BAD (Possible)
B2-MM8	$16^h27^m27.96^s$	-24°27′06.85″	1300	1.63	Unclear
B2-MM9	$16^h27^m28.74^s$	-24°26′40.65″	1400	1.37	BAD
B2-MM13	$16^h27^m32.95^s$	-24°26′03.16″	1500	0.49	BAD (Possible)
B2-MM14	$16^h27^m32.53^s$	-24°26′27.78″	1500	1.26	BAD
B2-MM16	$16^h27^m34.49^s$	-24°26′11.90″	1200	1.31	BAD
C-MM2	$16^h26^m59.10^s$	-24°33′50.15″	1000	1.11	BAD
C-MM3	$16^h26^m58.80^s$	-24°34′23.40″	1900	1.42	Unclear
C-MM5	$16^h26^m59.77^s$	-24°34′13.87″	1100	1.24	BAD
C-MM6	$16^h27^m01.58^s$	-24°34′44.62″	2400	1.05	BAD (Possible)
C-MM8	$16^h26^m49.09^s$	-24°29′45.15″	1000	0.15	Unclear
C-MM9	$16^h26^m48.10^s$	-24°32′12.50″	1100	0.06	Single
C-MM10	$16^h27^m02.26^s$	-24°31′42.56″	1100	0.37	Unclear
C-MM12	$16^h26^m59.80^s$	-24°33′08.75″	1600	0.09	Unclear
C-N	$16^h26^m58.11^s$	-24°31′46.32″	2100	1.60	RAD
E-MM2a	$16^h27^m02.89^s$	-24°38′46.47″	1000	0.12	Single
E-MM2b	$16^h27^m02.19^s$	-24°39′11.49″	1400	0.16	Single
E-MM2d	$16^h27^m04.53^s$	-24°39′06.42″	1000	0.41	BAD
E-MM4	$16^h27^m10.67^s$	-24°39′25.28″	1700	0.31	Unclear
E-MM5	$16^h27^m11.67^s$	-24°37′57.46″	1200	0.28	Single
E-MM8	$16^h27^m04.19^s$	-24°39′02.59″	1200	0.19	BAD (Possible)
F-MM1	$16^h27^m21.76^s$	-24°39′48.05″	1600	1.05	BAD
F-MM2a	$16^h27^m24.43^s$	-24°40′34.79″	2000	1.11	BAD (Possible)

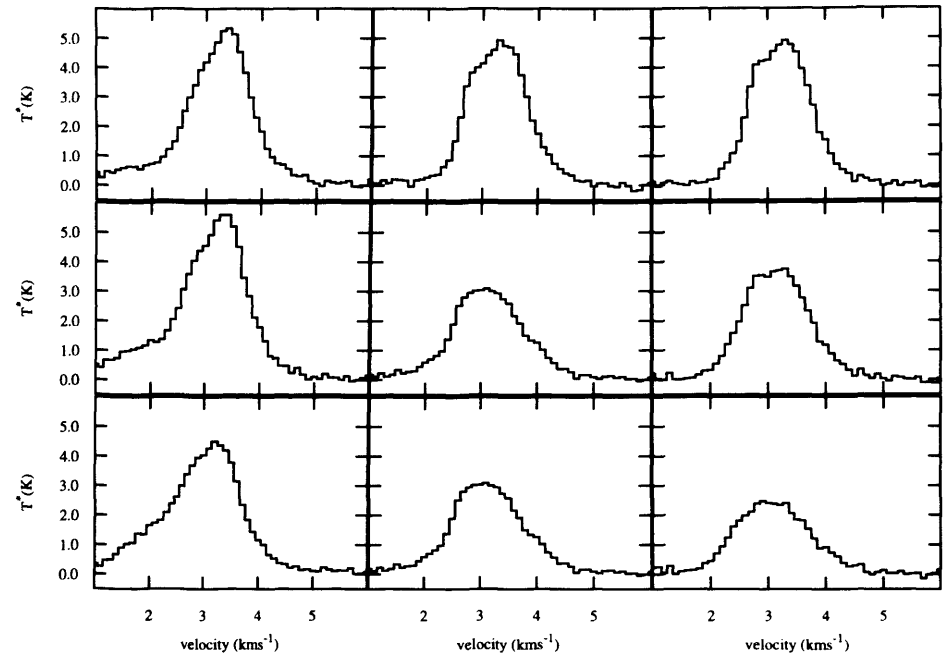

Figure 4.6: Map of HCO^+ (J=4→3) spectra in the core A-MM1. The central grid of 3×3 HARP pixels is shown here.

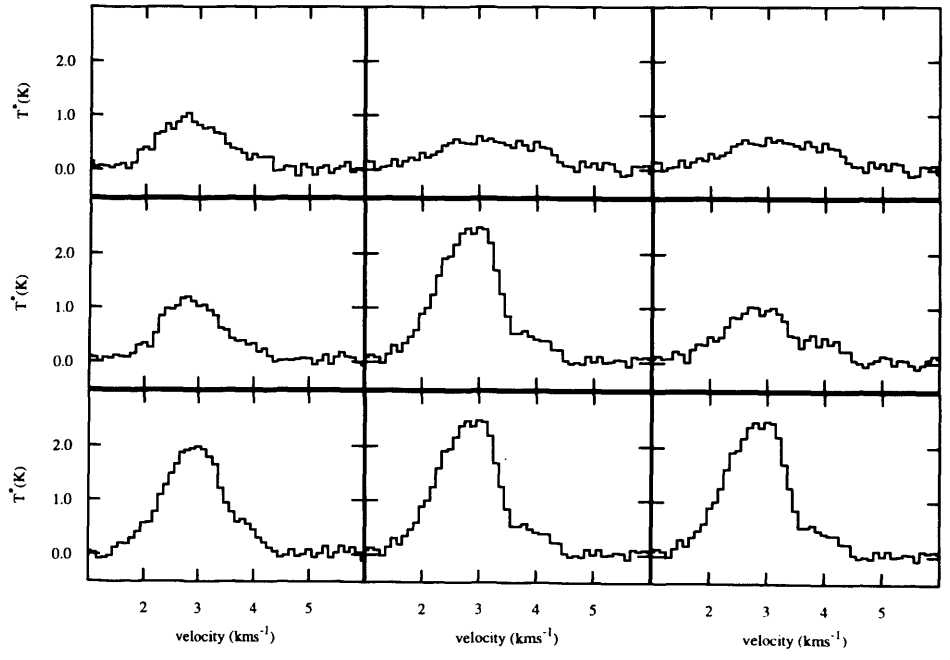

Figure 4.7: Map of HCO^+ (J=4→3) spectra in the core A-MM2-3. The central grid of 3×3 HARP pixels is shown here.

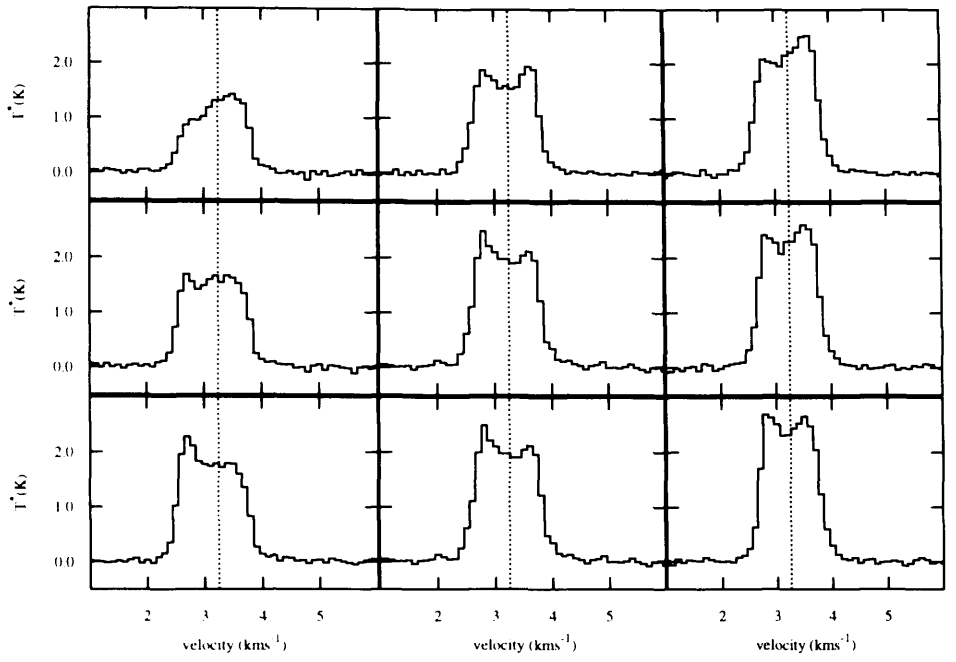

Figure 4.8: Map of HCO^+ (J=4→3) spectra in the core A-MM4. The central grid of 3×3 HARP pixels is shown here.

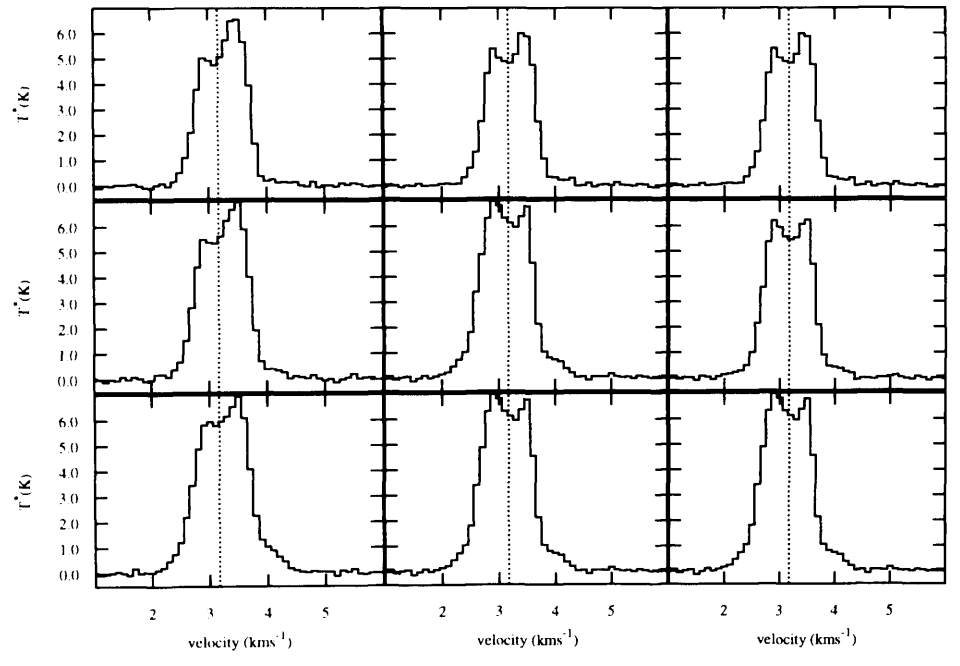

Figure 4.9: Map of HCO^+ (J=4→3) spectra in the core A-MM5. The central grid of 3×3 HARP pixels is shown here.

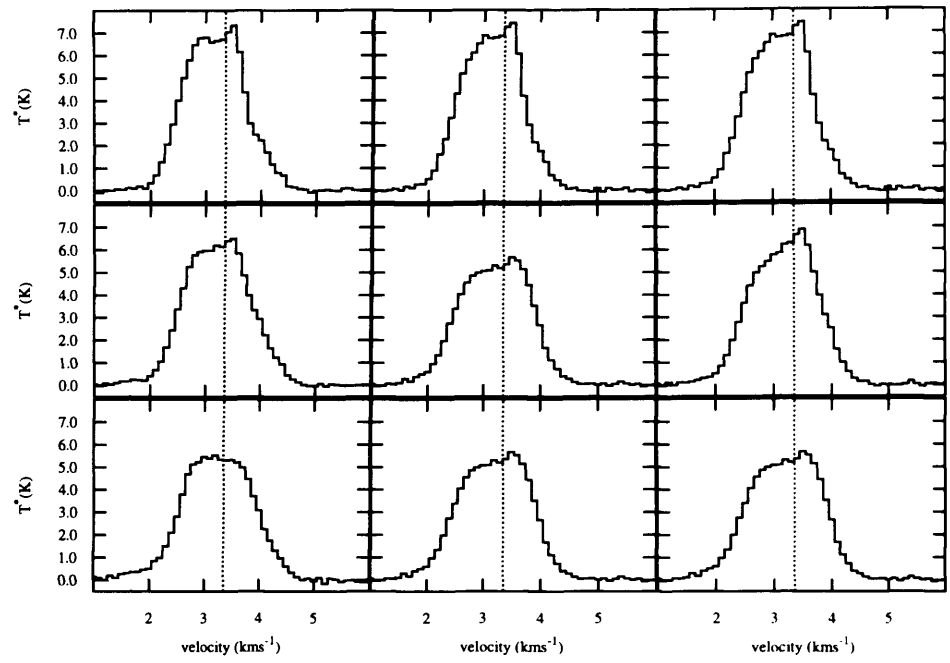

Figure 4.10: Map of HCO^+ (J=4→3) spectra in the core A-MM6. The central grid of 3×3 HARP pixels is shown here.

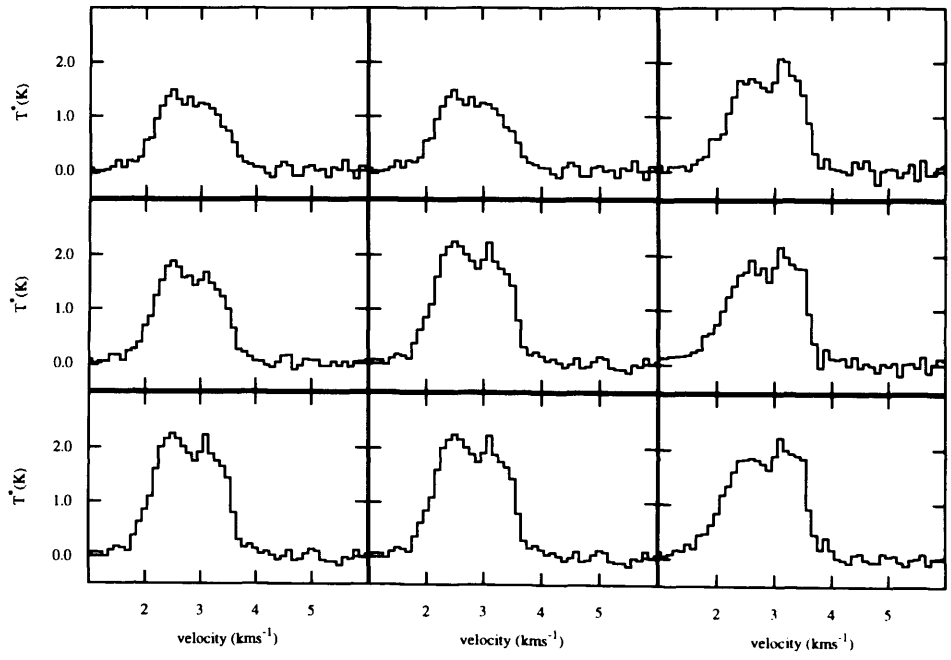

Figure 4.11: Map of HCO^+ (J=4→3) spectra in the core A-MM7. The central grid of 3×3 HARP pixels is shown here.

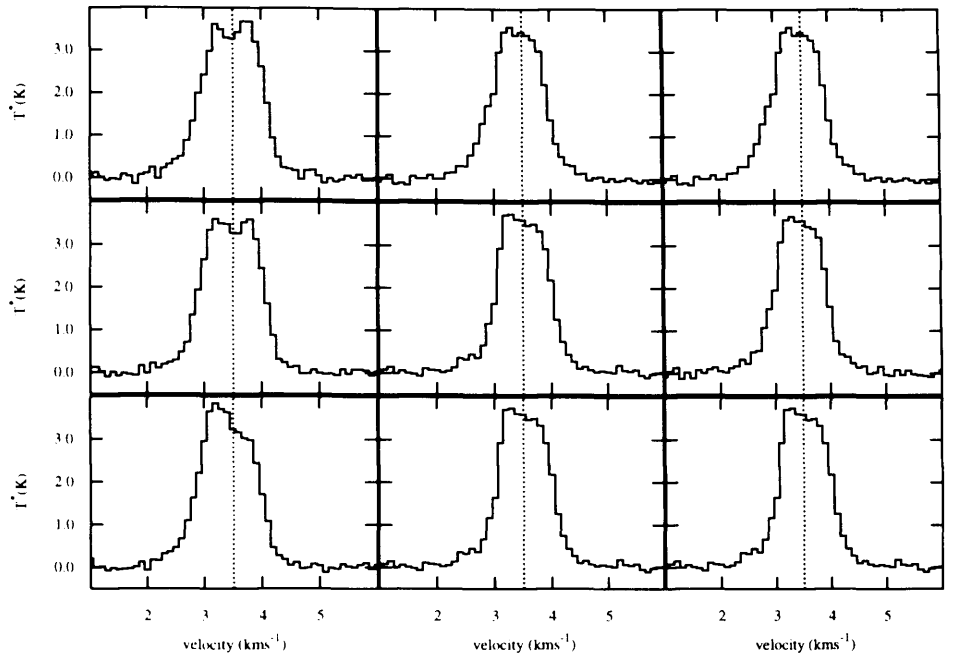

Figure 4.12: Map of HCO^+ (J=4→3) spectra in the core A-MM8. The central grid of 3×3 HARP pixels is shown here.

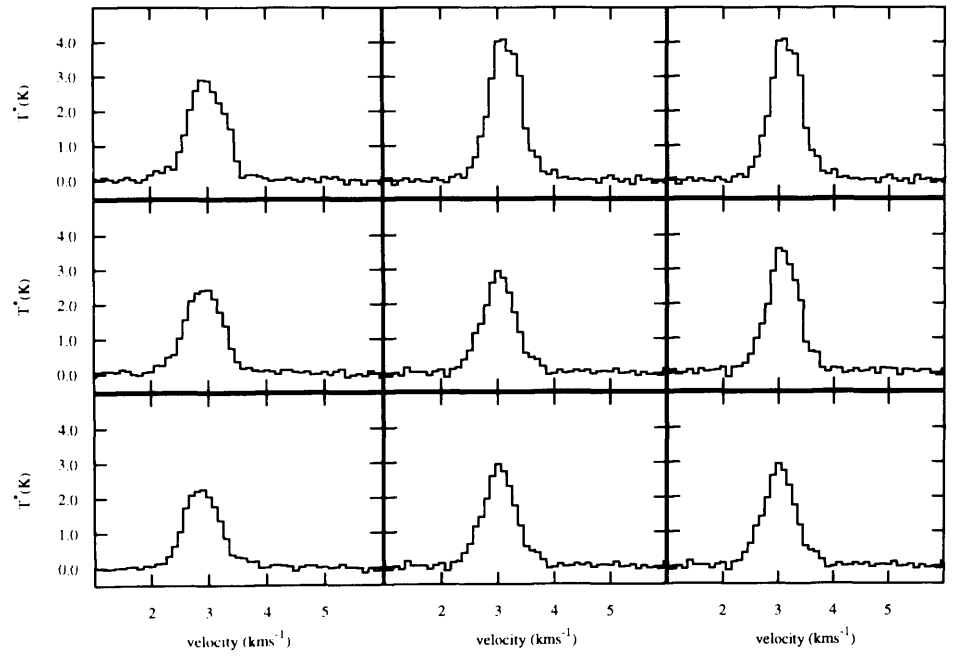

Figure 4.13: Map of HCO^+ (J=4→3) spectra in the core A-MM11. The central grid of 3×3 HARP pixels is shown here.

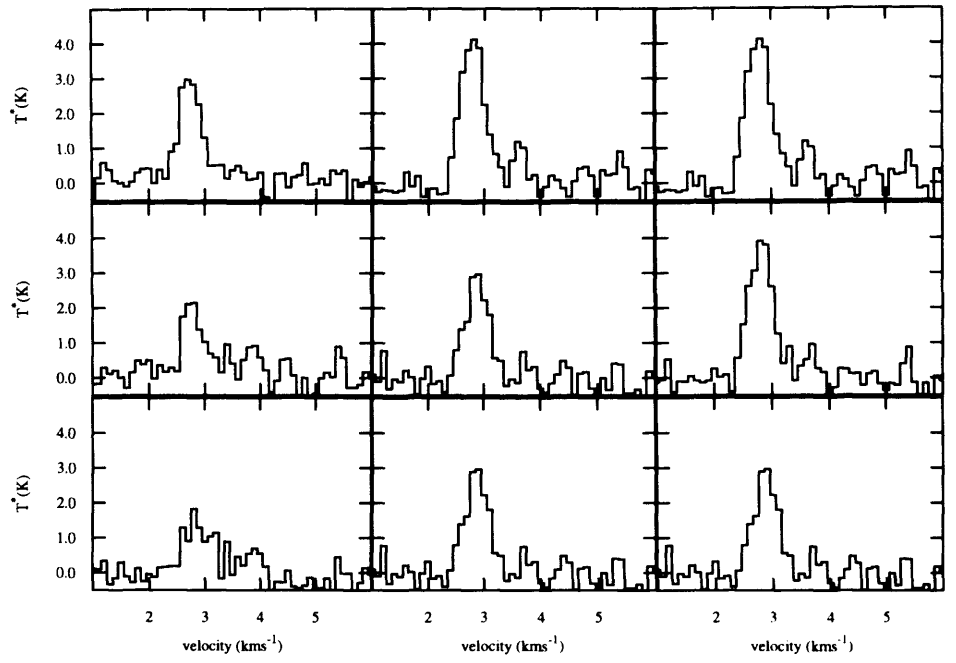

Figure 4.14: Map of HCO^+ (J=4→3) spectra in the core A-MM16. The central grid of 3×3 HARP pixels is shown here.

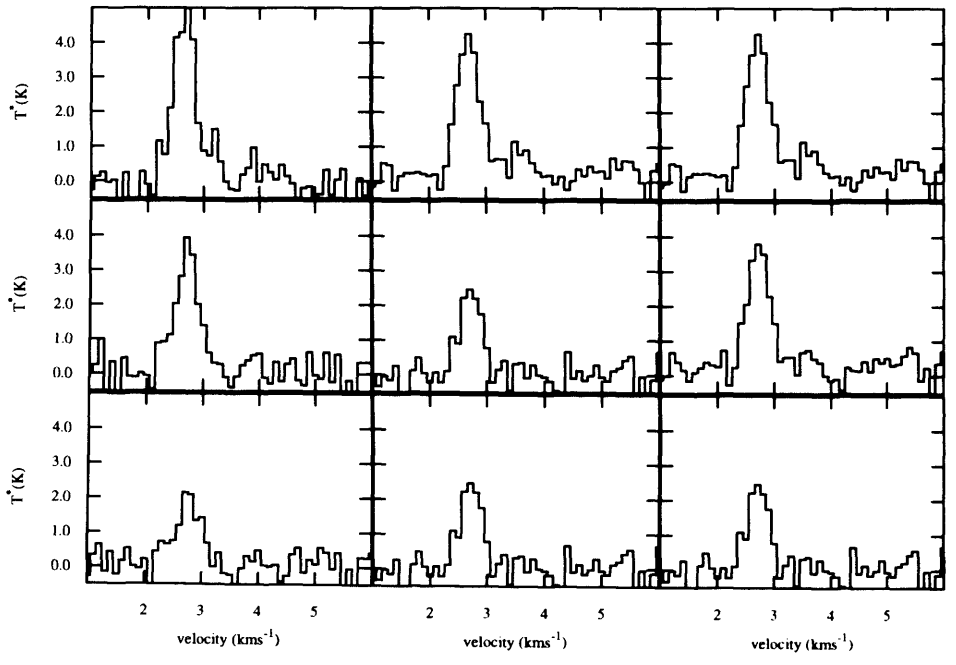

Figure 4.15: Map of HCO^+ (J=4→3) spectra in the core A-MM17. The central grid of 3×3 HARP pixels is shown here.

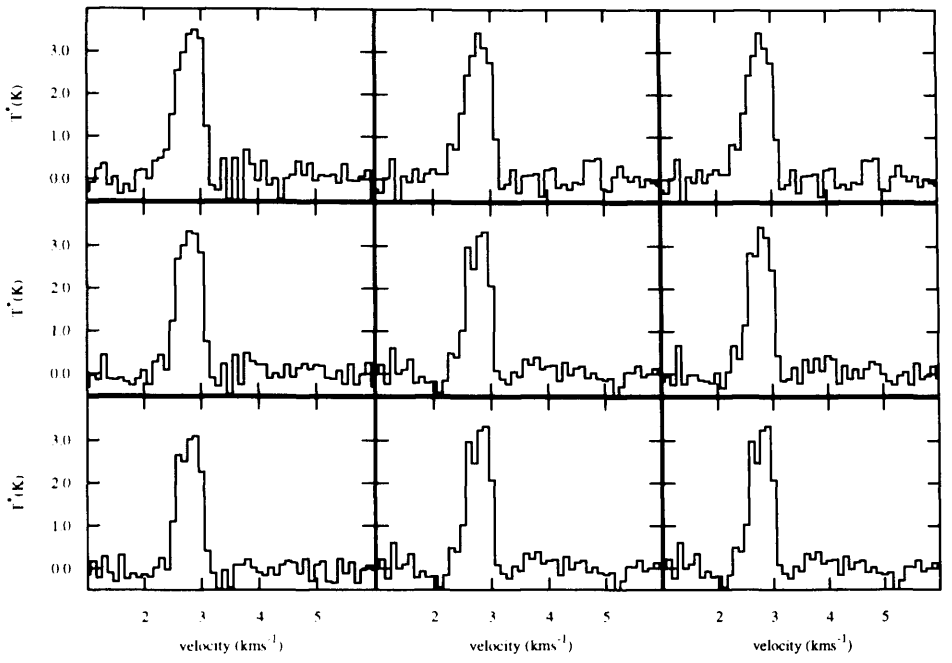

Figure 4.16: Map of HCO^+ (J=4→3) spectra in the core A-MM18. The central grid of 3×3 HARP pixels is shown here.

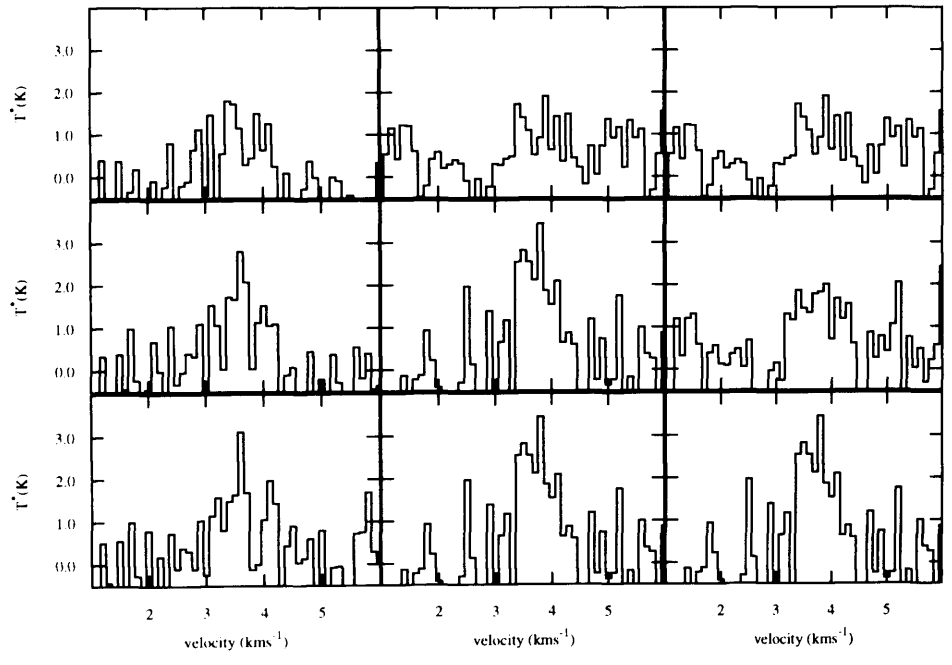

Figure 4.17: Map of HCO^+ (J=4→3) spectra in the core A-MM21. The central grid of 3×3 HARP pixels is shown here.

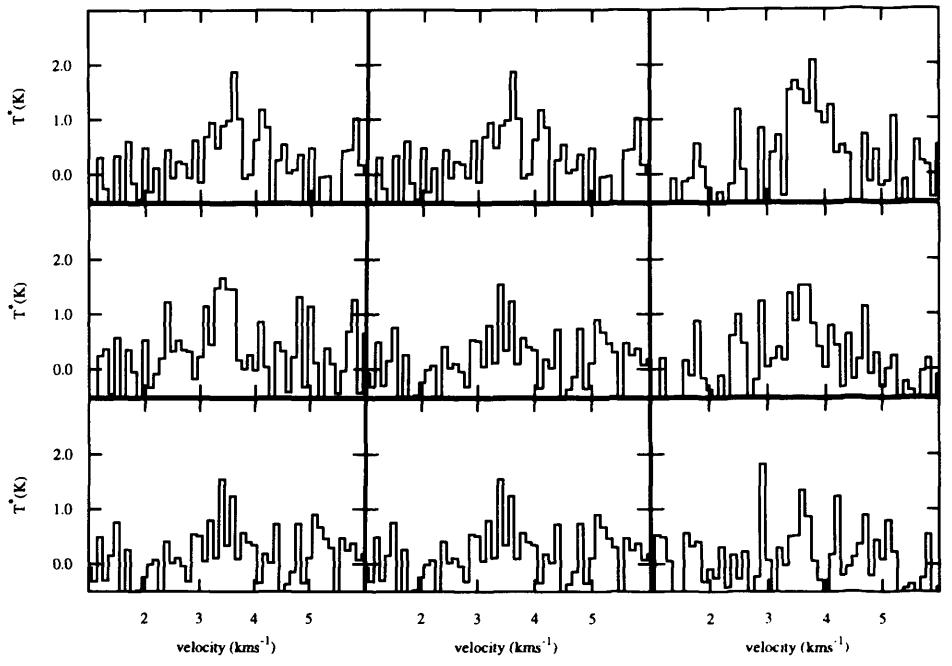

Figure 4.18: Map of HCO^+ (J=4→3) spectra in the core A-MM22. The central grid of 3×3 HARP pixels is shown here.

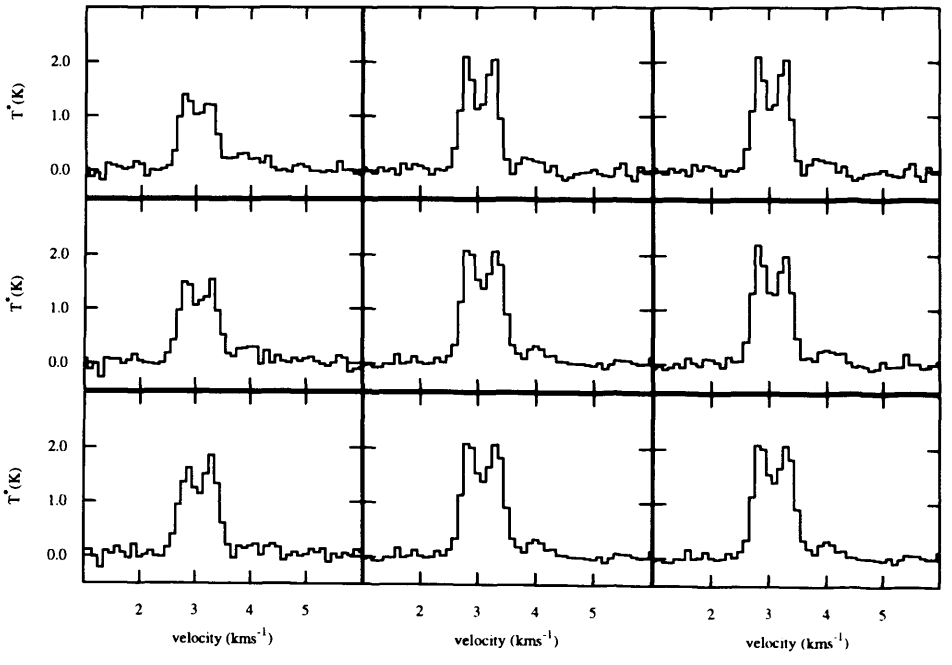

Figure 4.19: Map of HCO^+ (J=4→3) spectra in the core A-MM23. The central grid of 3×3 HARP pixels is shown here.

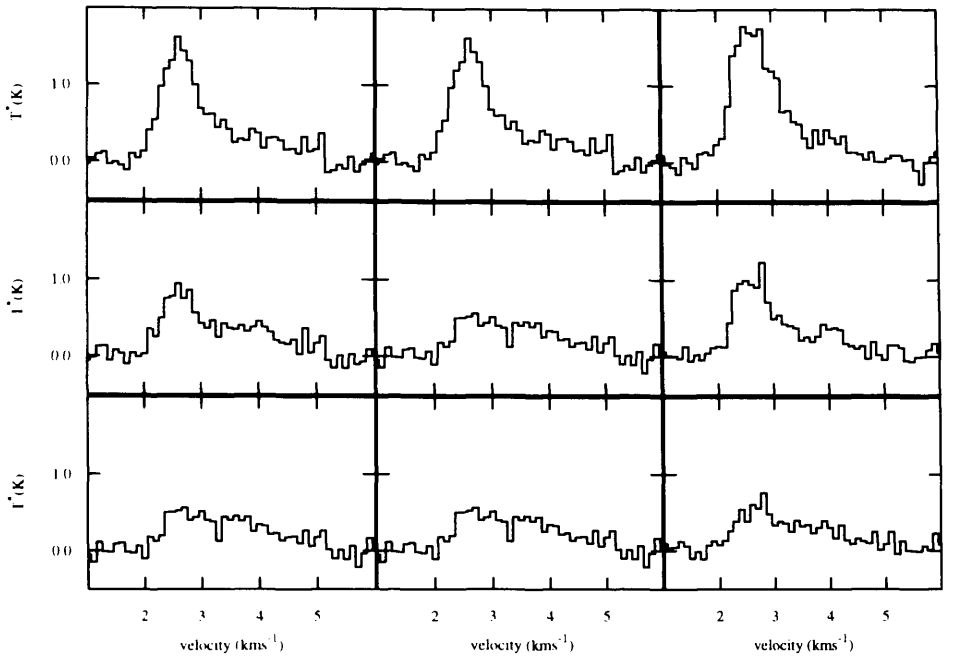

Figure 4.20: Map of HCO^+ (J=4→3) spectra in the core A-MM26. The central grid of 3×3 HARP pixels is shown here.

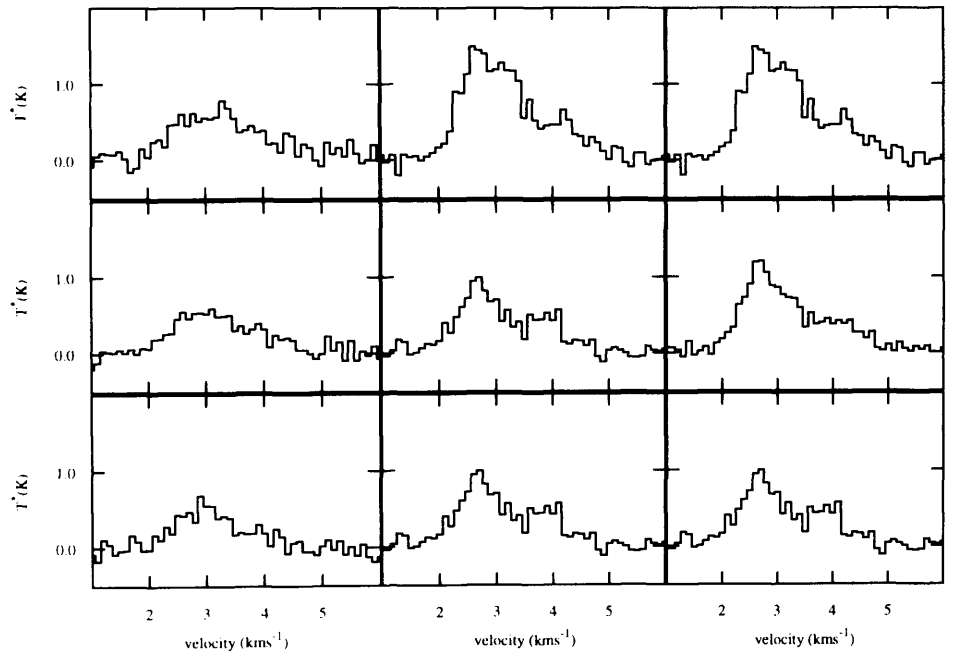

Figure 4.21: Map of HCO^+ (J=4→3) spectra in the core A-MM27. The central grid of 3×3 HARP pixels is shown here.

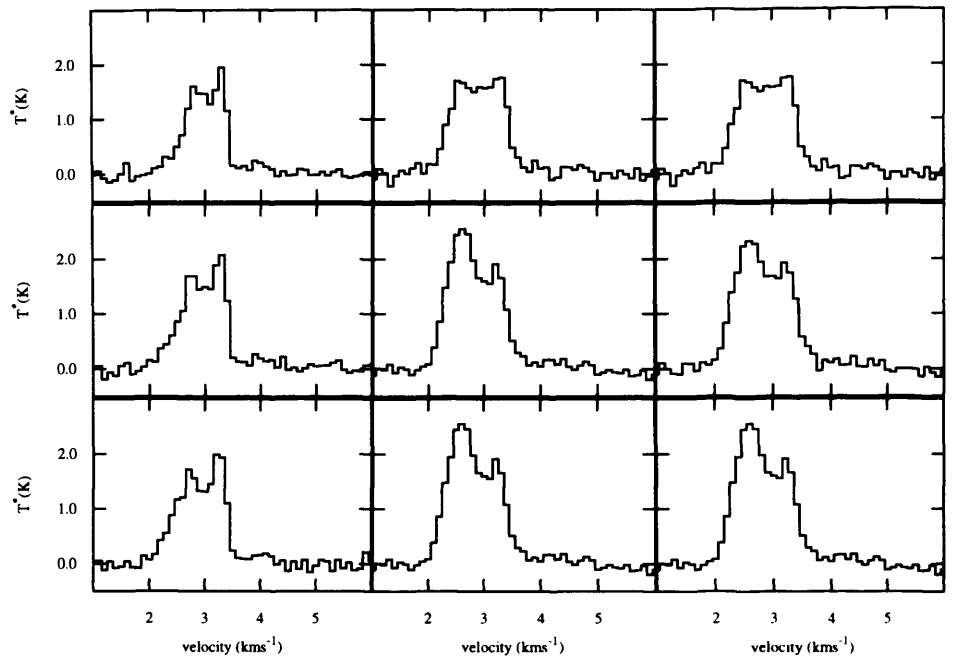

Figure 4.22: Map of HCO^+ (J=4→3) spectra in the core A-MM30. The central grid of 3×3 HARP pixels is shown here.

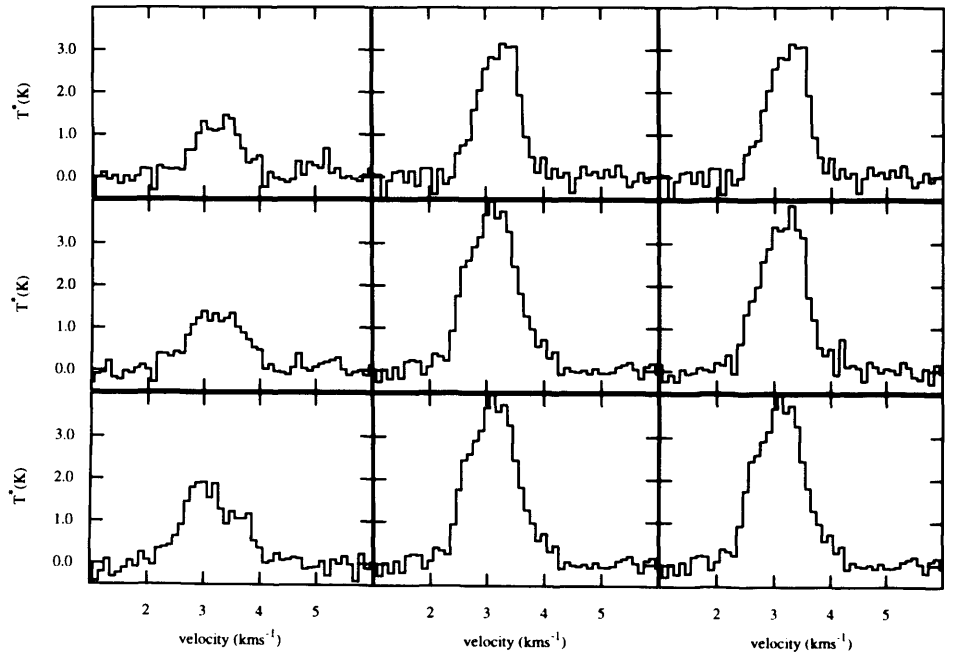

Figure 4.23: Map of HCO^+ (J=4→3) spectra in the core A-N. The central grid of 3×3 HARP pixels is shown here.

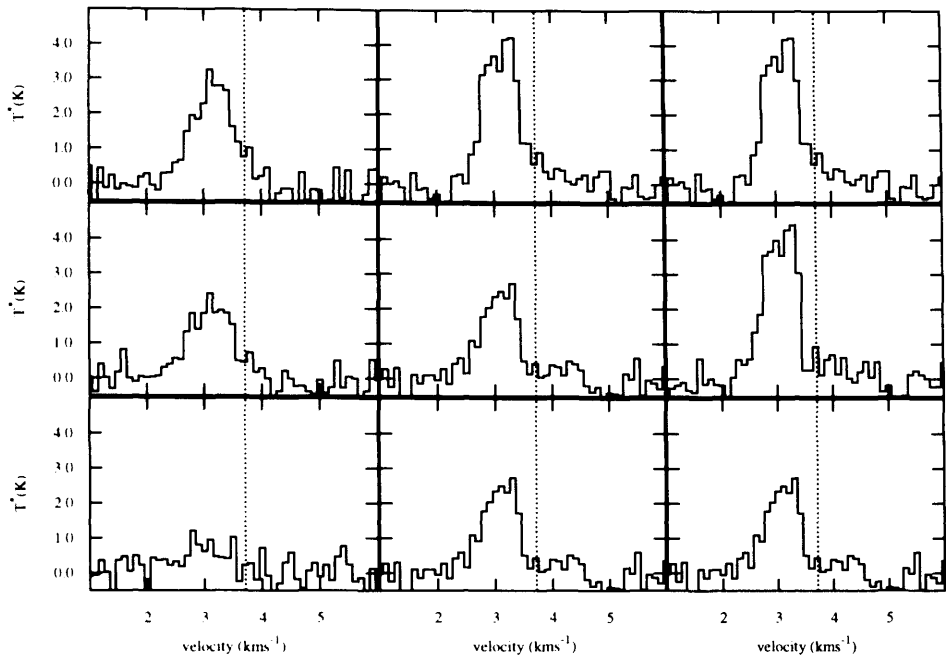

Figure 4.24: Map of HCO^+ (J=4→3) spectra in the core A-S. The central grid of 3×3 HARP pixels is shown here.

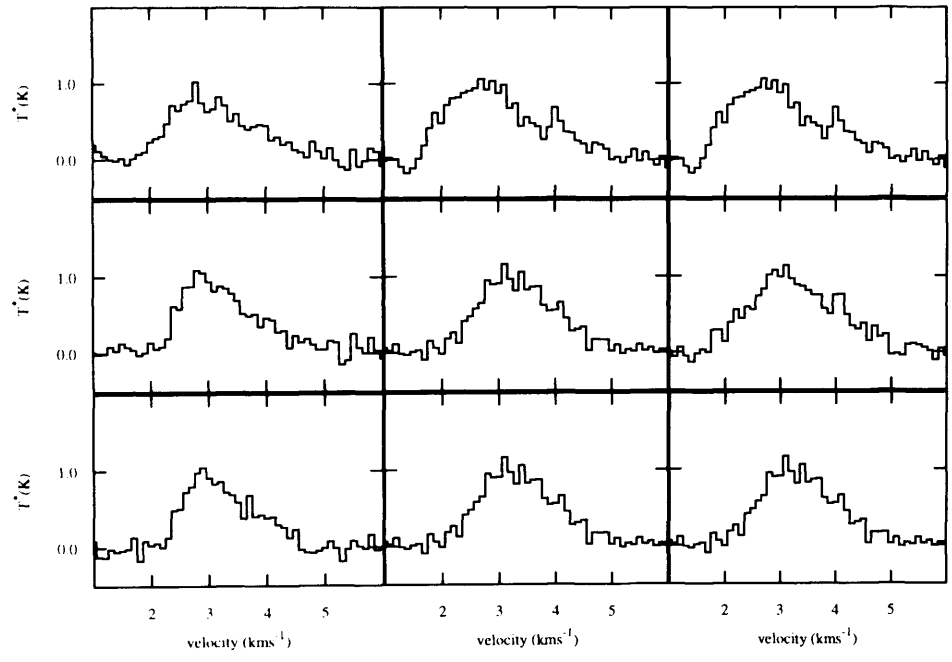

Figure 4.25: Map of HCO^+ (J=4→3) spectra in the core A2-MM1. The central grid of 3×3 HARP pixels is shown here.

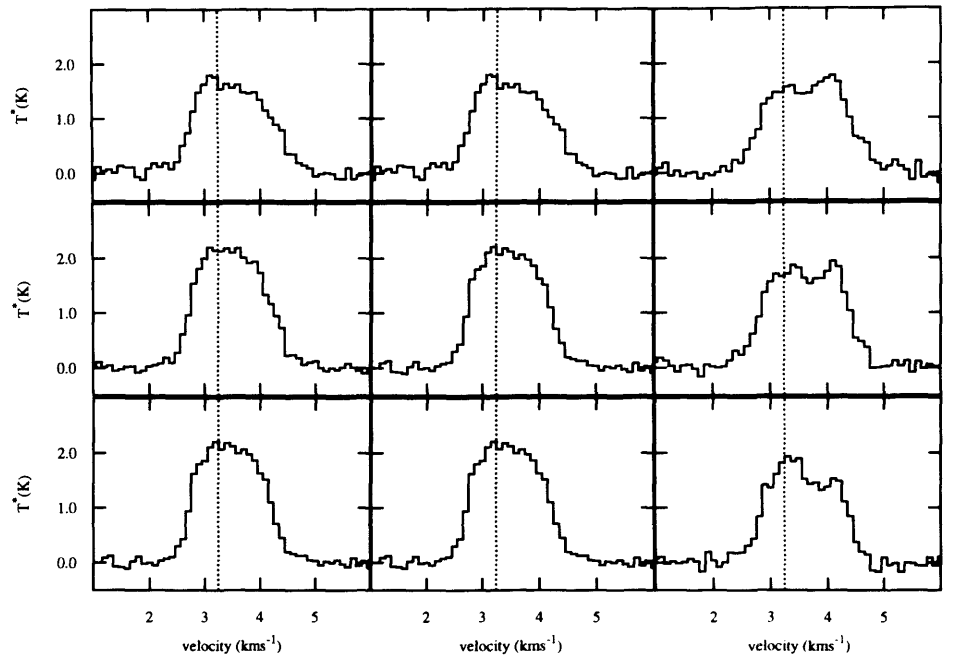

Figure 4.26: Map of HCO^+ (J=4→3) spectra in the core A3-MM1. The central grid of 3×3 HARP pixels is shown here.

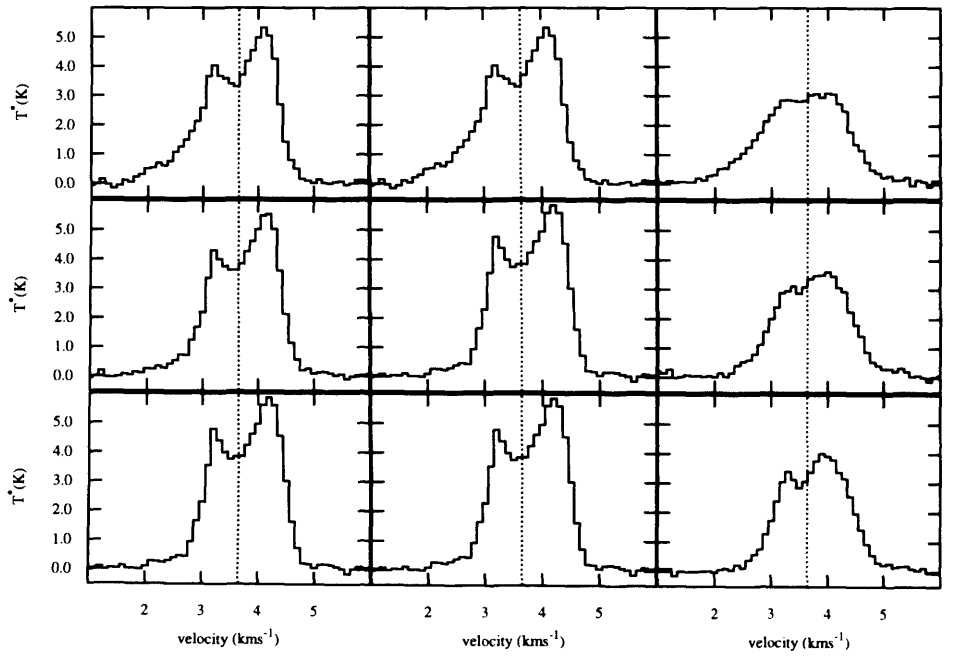

Figure 4.27: Map of HCO^+ (J=4→3) spectra in the core SM1. The central grid of 3×3 HARP pixels is shown here.

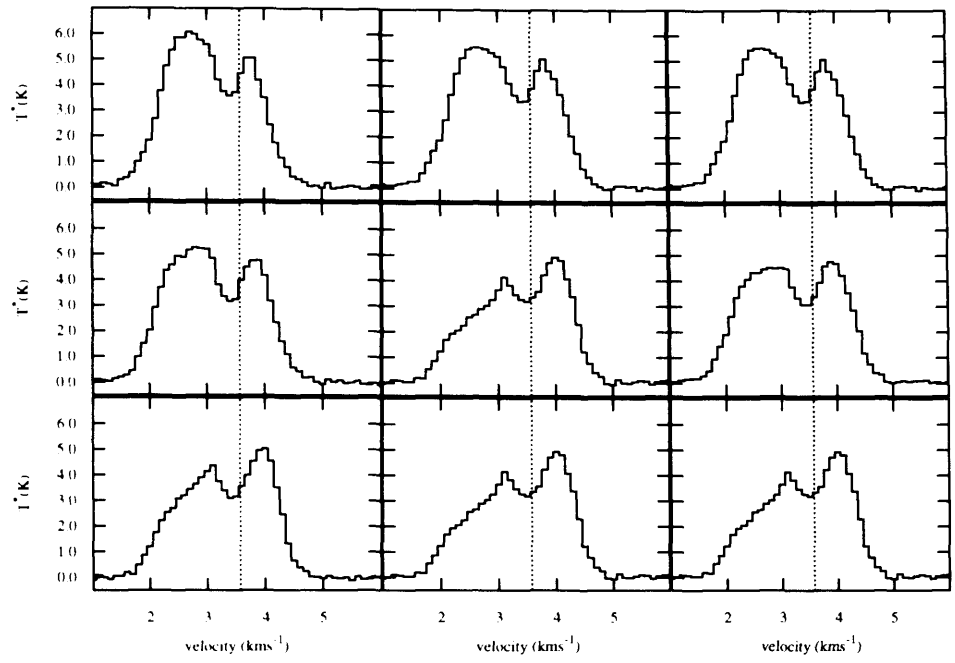

Figure 4.28: Map of HCO^+ (J=4→3) spectra in the core SM1N. The central grid of 3×3 HARP pixels is shown here.

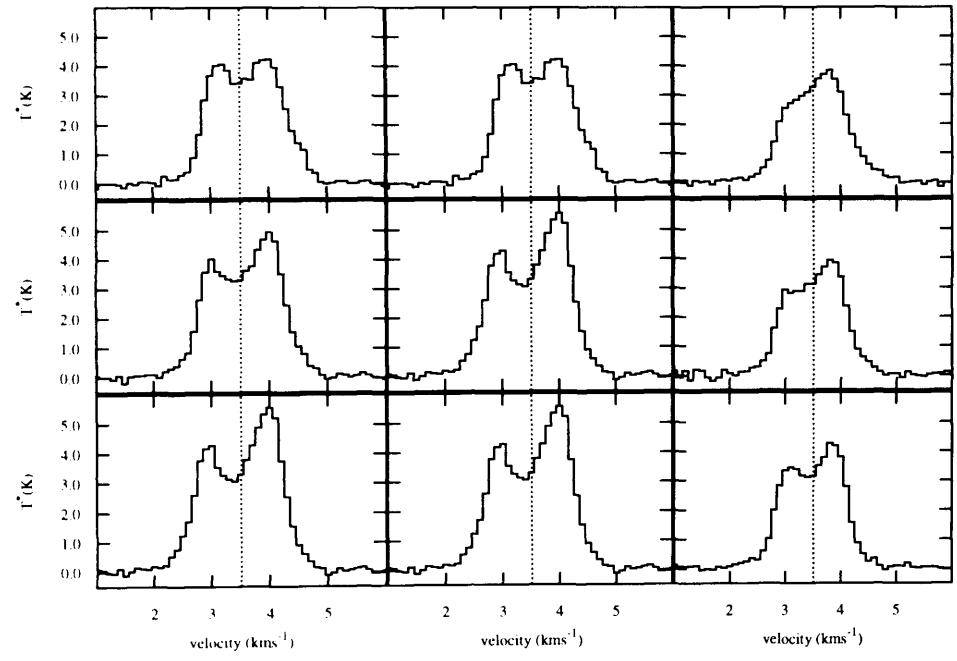

Figure 4.29: Map of HCO^+ (J=4→3) spectra in the core SM2. The central grid of 3×3 HARP pixels is shown here.

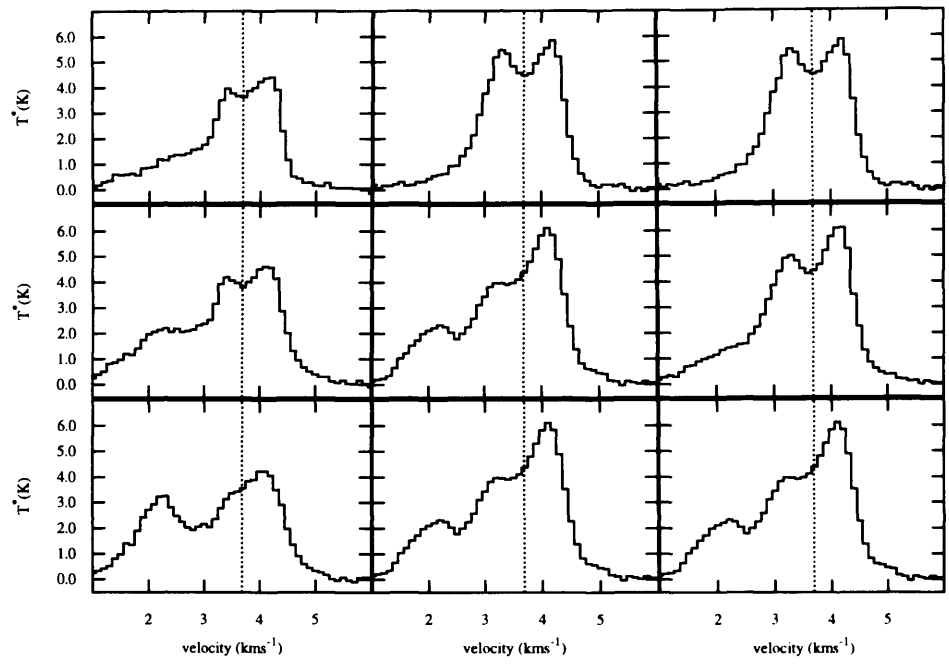

Figure 4.30: Map of HCO^+ (J=4→3) spectra in the core VLA1623. The central grid of 3×3 HARP pixels is shown here.

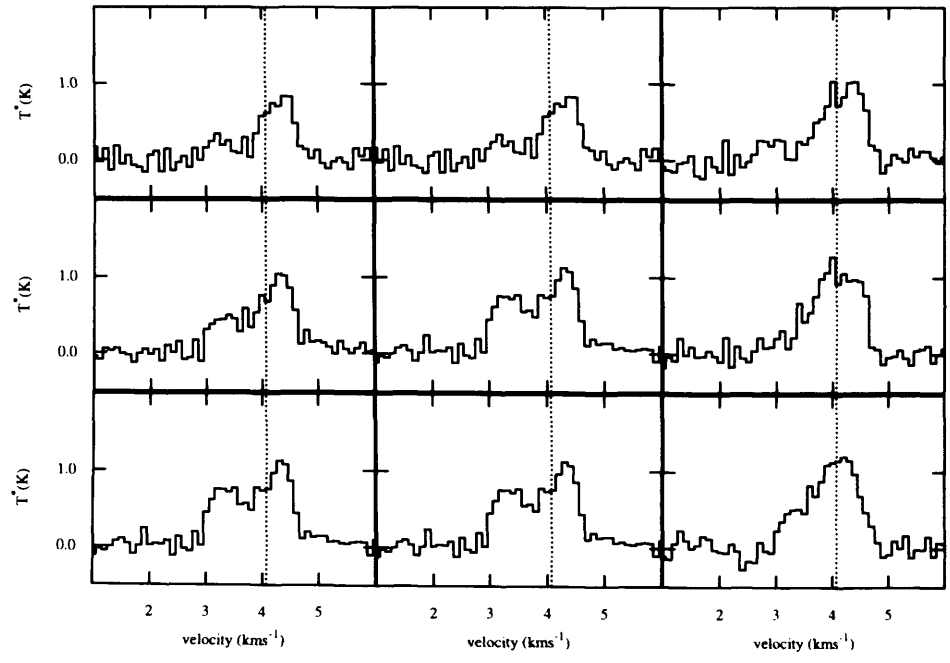

Figure 4.31: Map of HCO^+ (J=4→3) spectra in the core B1-MM1. The central grid of 3×3 HARP pixels is shown here.

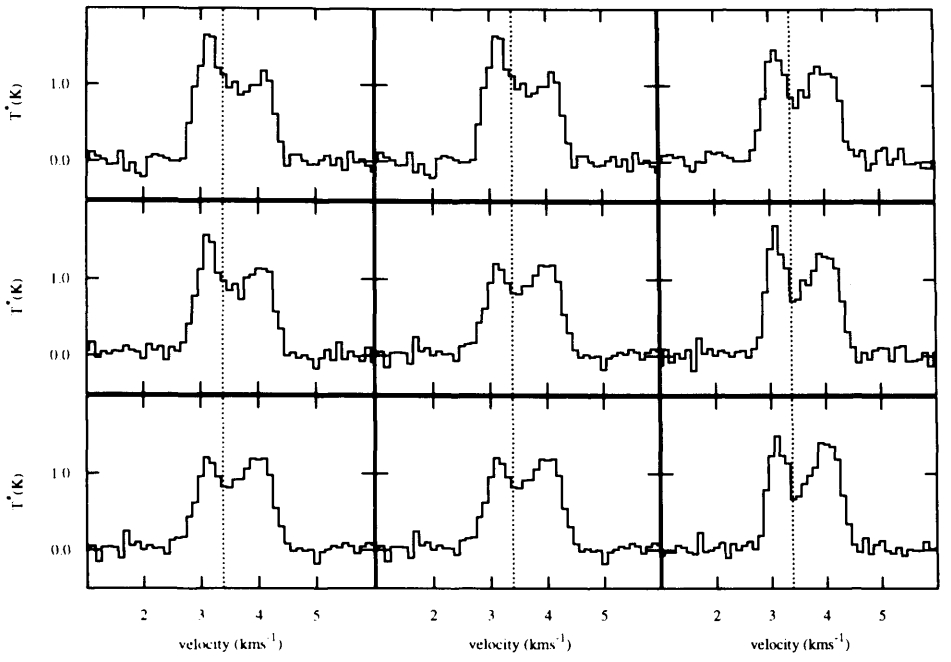

Figure 4.32: Map of HCO^+ (J=4→3) spectra in the core B1-MM2. The central grid of 3×3 HARP pixels is shown here.

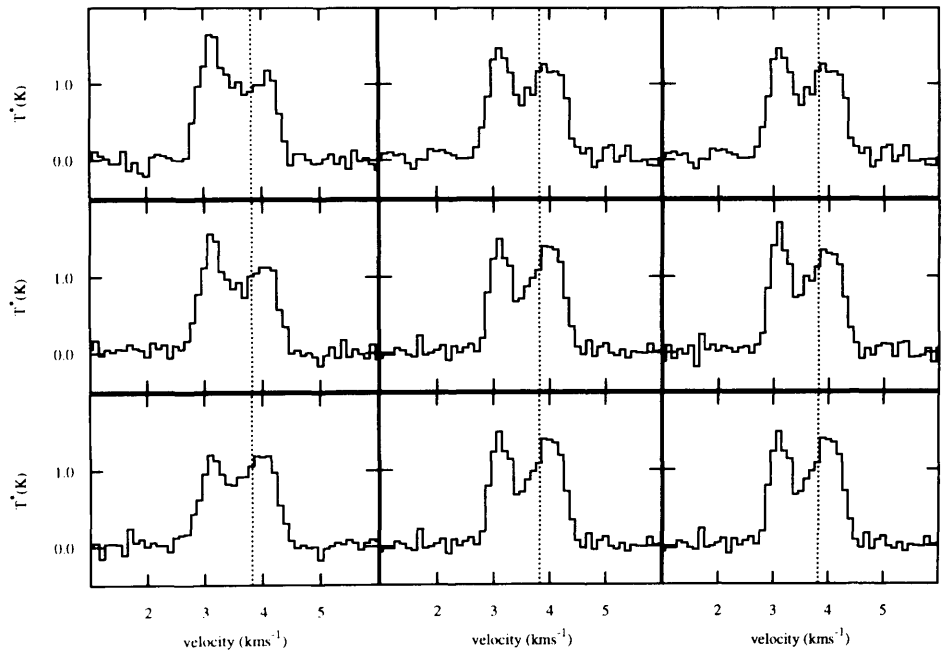

Figure 4.33: Map of HCO^+ (J=4→3) spectra in the core B1-MM3. The central grid of 3×3 HARP pixels is shown here.

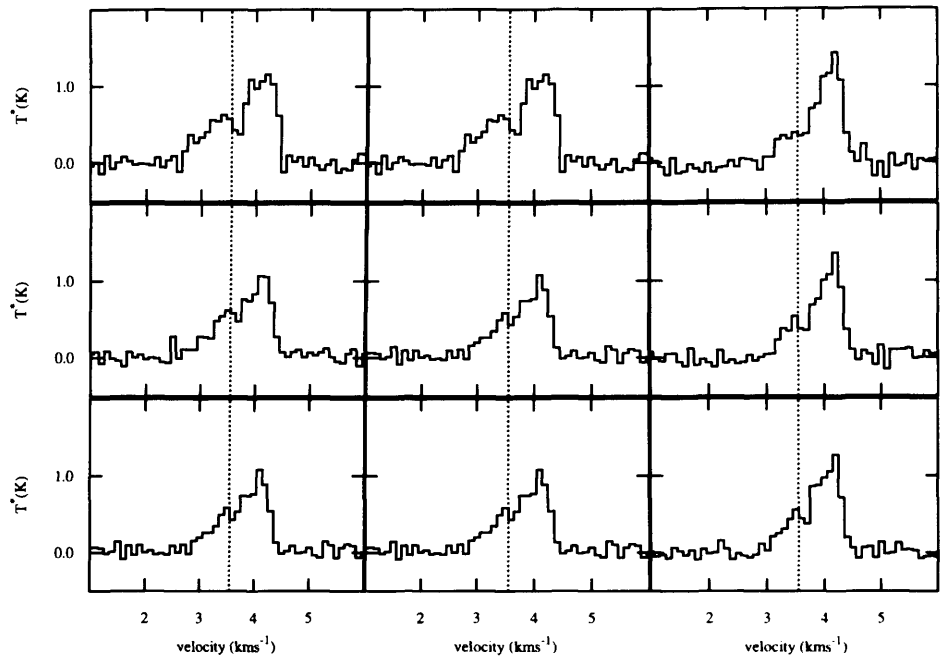

Figure 4.34: Map of HCO^+ (J=4→3) spectra in the core B1-MM4. The central grid of 3×3 HARP pixels is shown here.

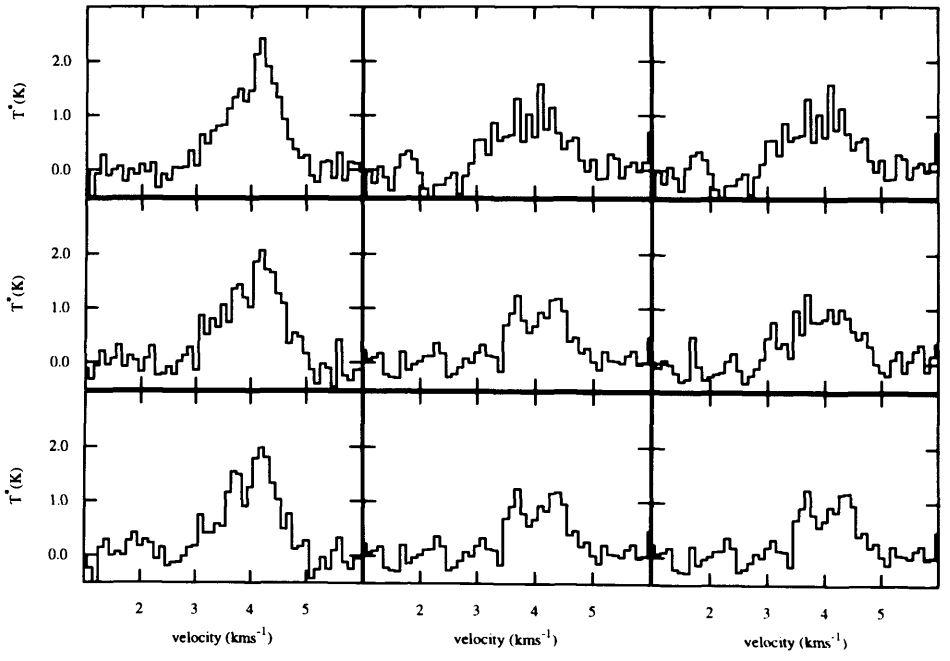

Figure 4.35: Map of HCO^+ (J=4→3) spectra in the core B1-MM7. The central grid of 3×3 HARP pixels is shown here.

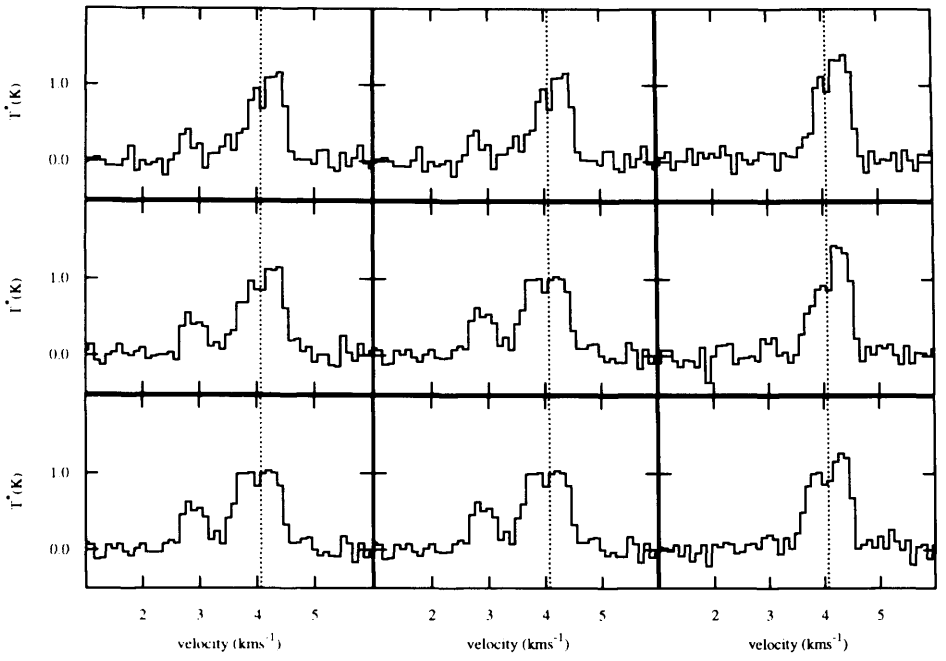

Figure 4.36: Map of HCO^+ (J=4→3) spectra in the core B1B2-MM1. The central grid of 3×3 HARP pixels is shown here.

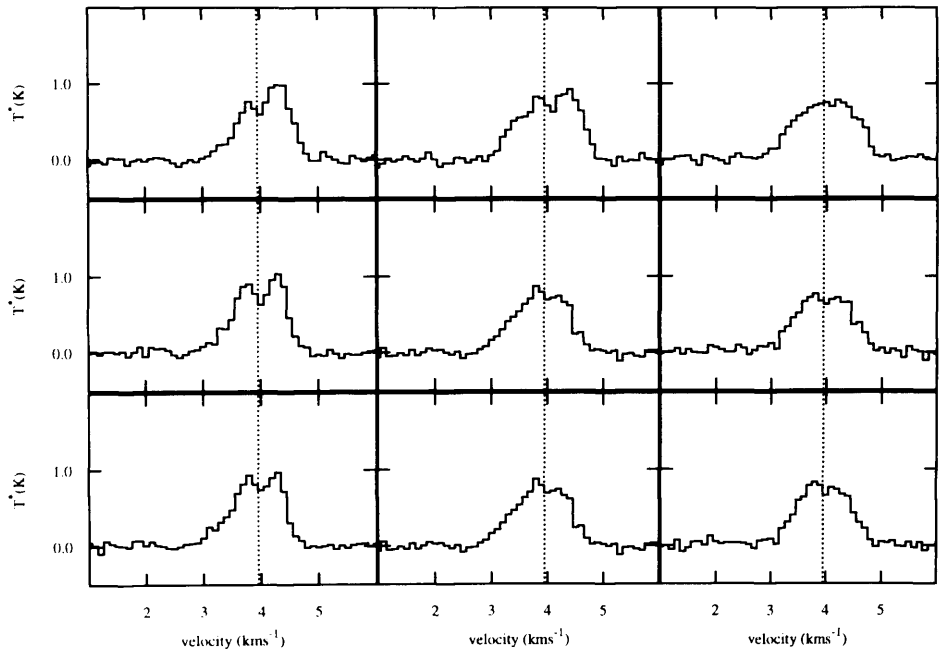

Figure 4.37: Map of HCO^+ (J=4→3) spectra in the core B2-MM2. The central grid of 3×3 HARP pixels is shown here.

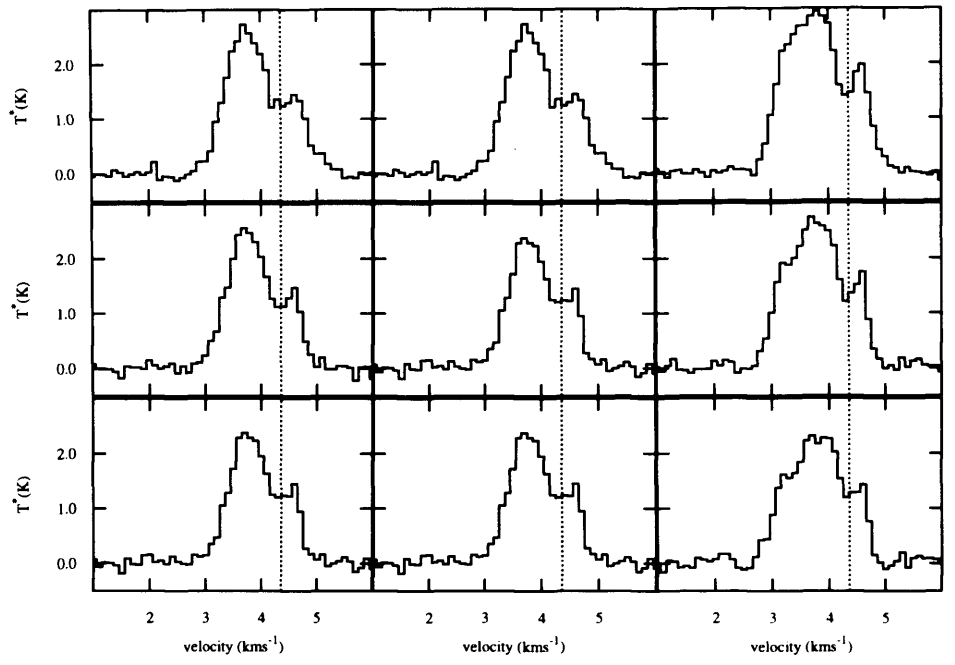

Figure 4.38: Map of HCO^+ (J=4→3) spectra in the core B2-MM4. The central grid of 3×3 HARP pixels is shown here.

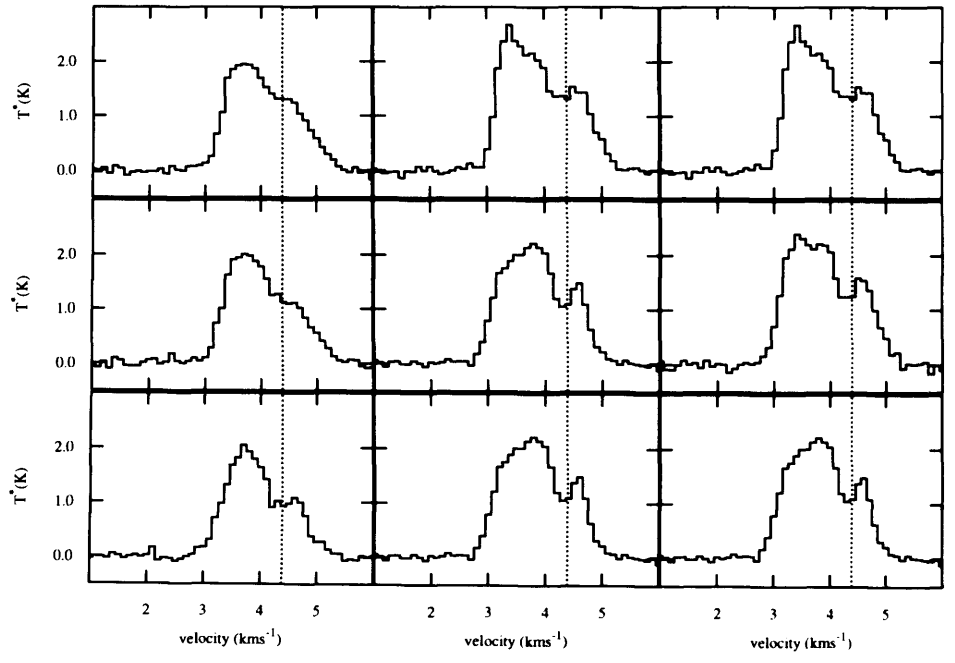

Figure 4.39: Map of HCO^+ (J=4→3) spectra in the core B2-MM5. The central grid of 3×3 HARP pixels is shown here.

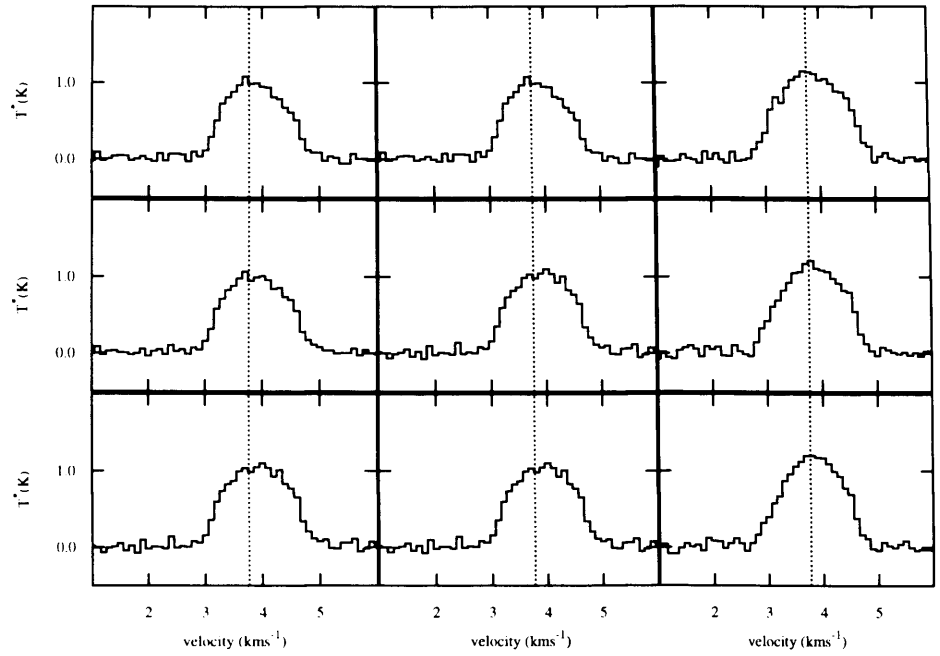

Figure 4.40: Map of HCO^+ (J=4→3) spectra in the core B2-MM6. The central grid of 3×3 HARP pixels is shown here.

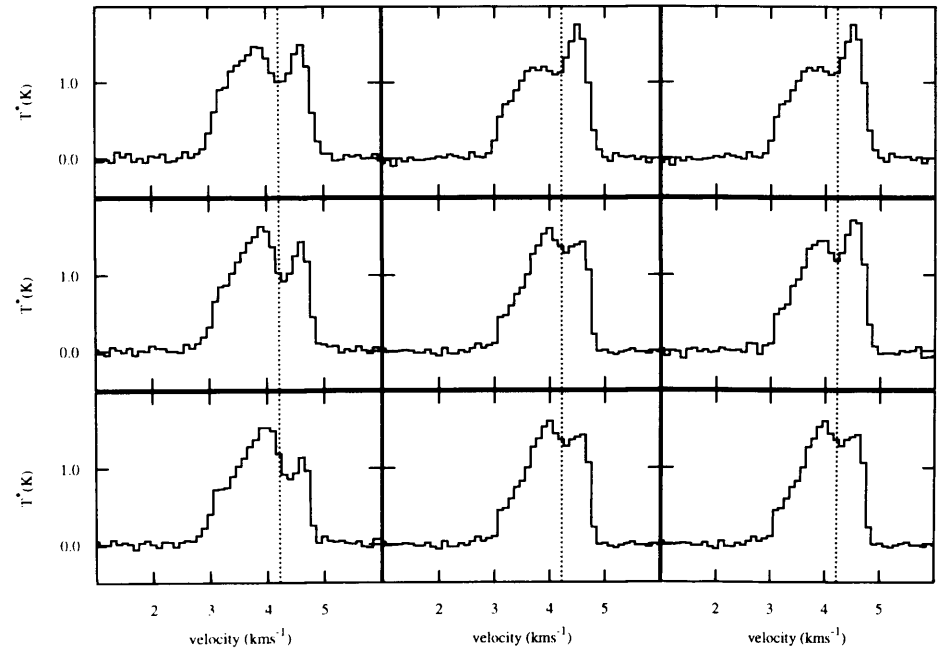

Figure 4.41: Map of HCO^+ (J=4→3) spectra in the core B2-MM7. The central grid of 3×3 HARP pixels is shown here.

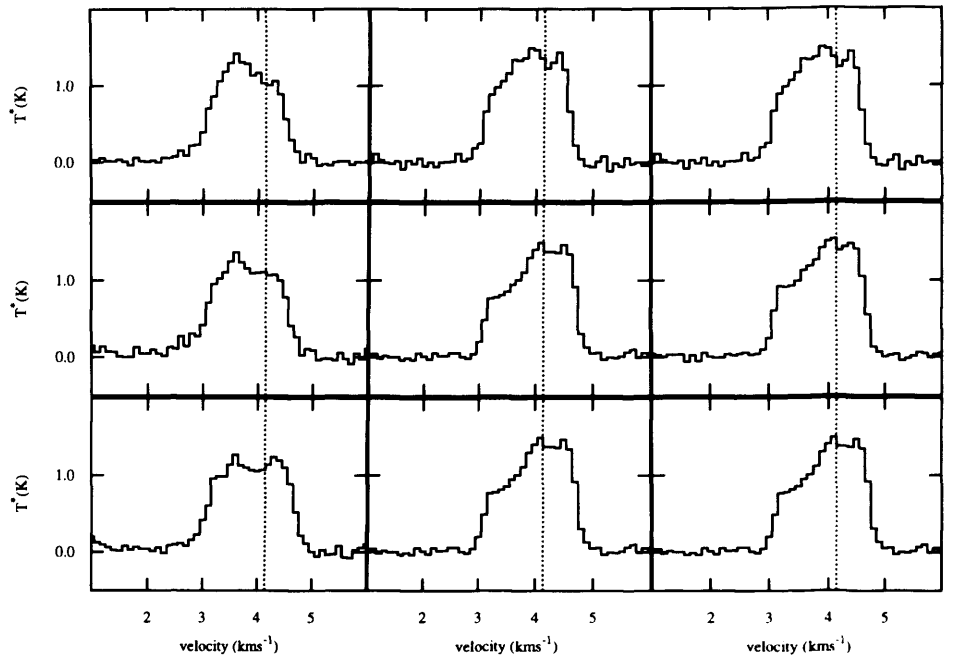

Figure 4.42: Map of HCO^+ (J=4→3) spectra in the core B2-MM8. The central grid of 3×3 HARP pixels is shown here.

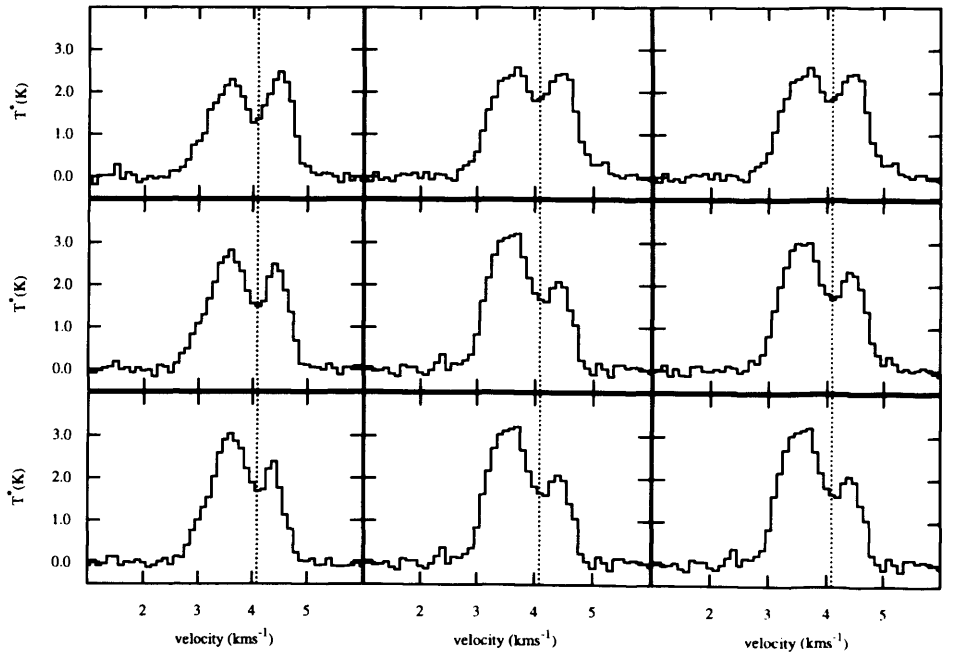

Figure 4.43: Map of HCO^+ (J=4→3) spectra in the core B2-MM9. The central grid of 3×3 HARP pixels is shown here.

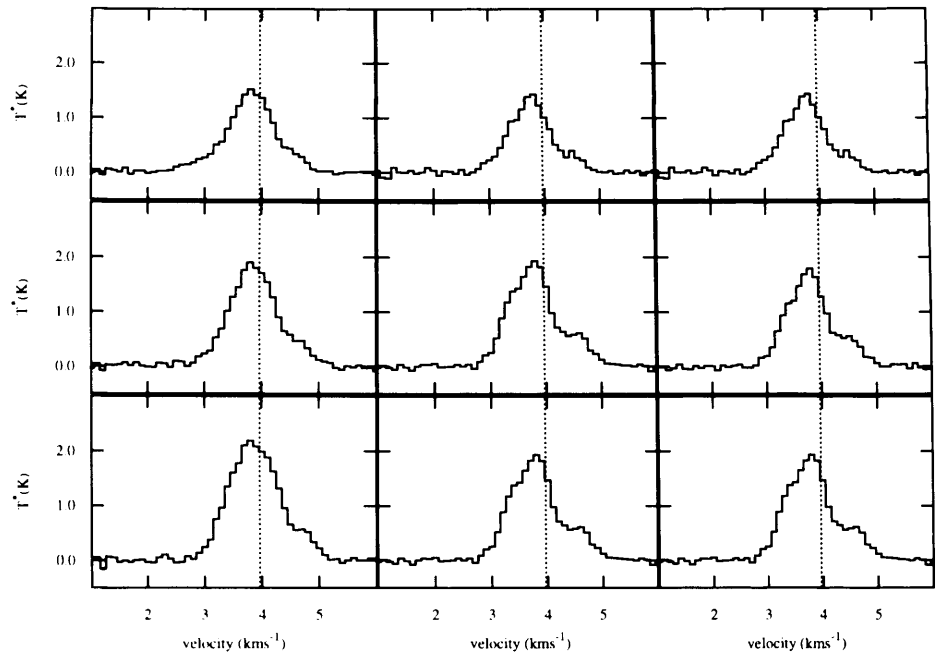

Figure 4.44: Map of HCO^+ (J=4→3) spectra in the core B2-MM13. The central grid of 3×3 HARP pixels is shown here.

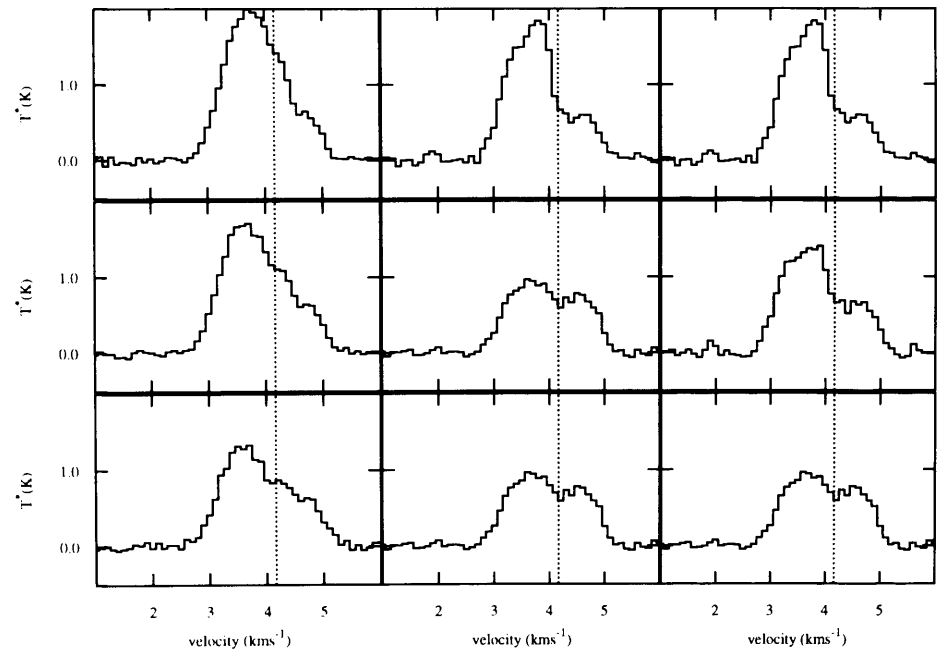

Figure 4.45: Map of HCO^+ (J=4→3) spectra in the core B2-MM14. The central grid of 3×3 HARP pixels is shown here.

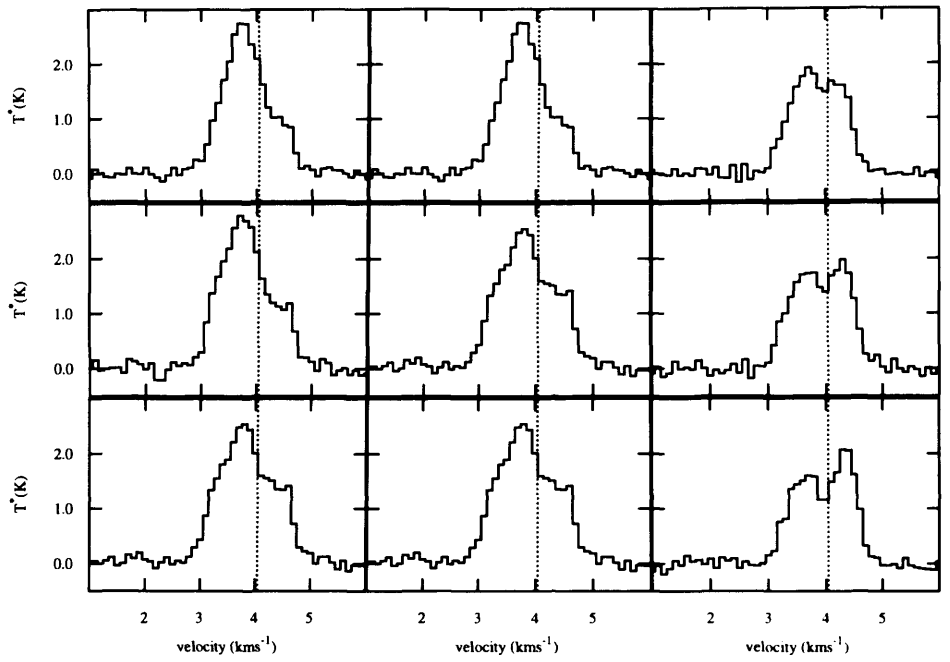

Figure 4.46: Map of HCO^+ (J=4→3) spectra in the core B2-MM16. The central grid of 3×3 HARP pixels is shown here.

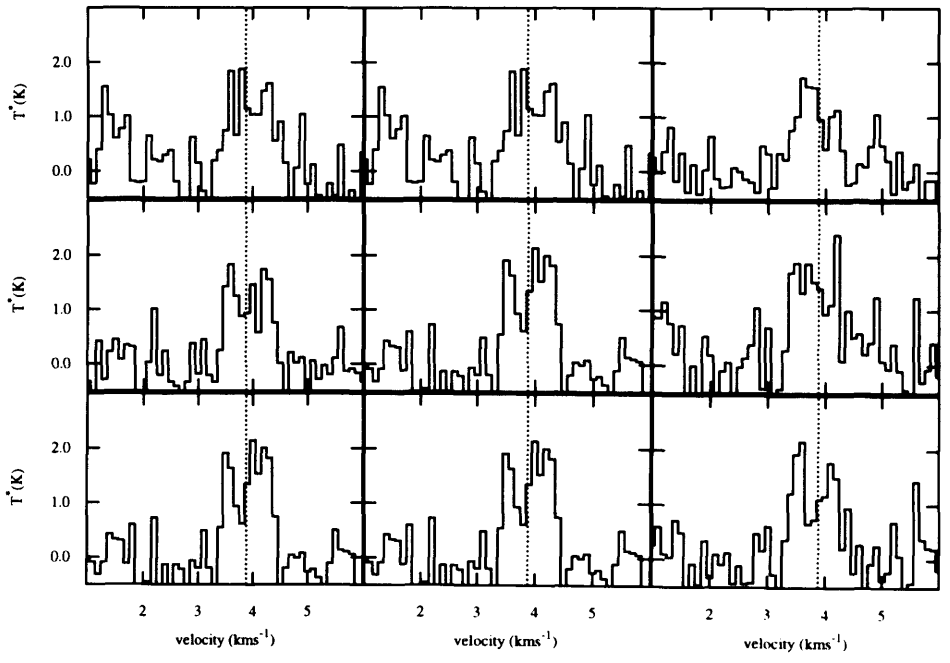

Figure 4.47: Map of HCO^+ (J=4→3) spectra in the core C-MM2. The central grid of 3×3 HARP pixels is shown here.

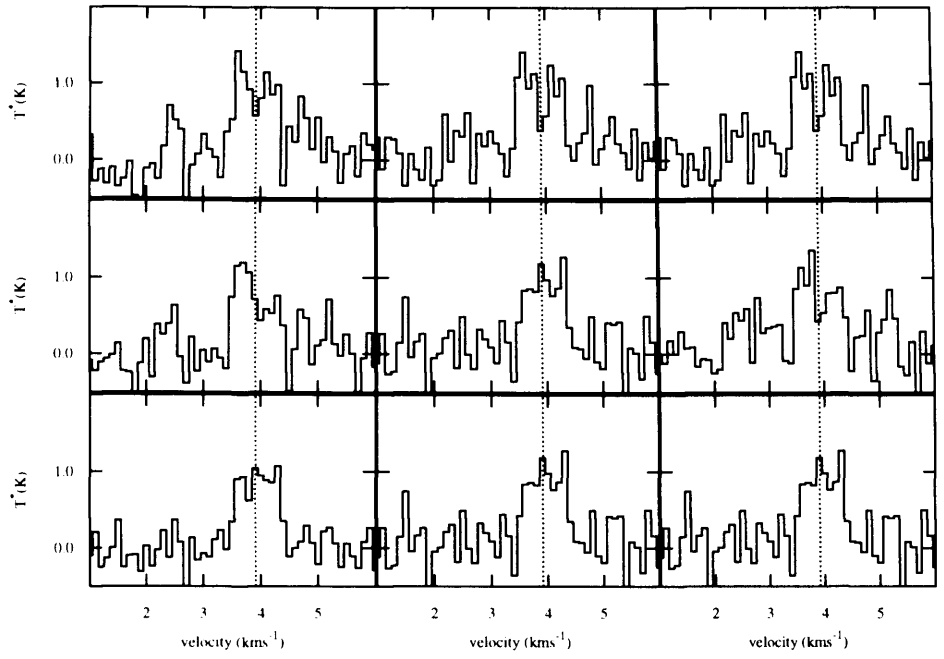

Figure 4.48: Map of HCO^+ (J=4→3) spectra in the core C-MM3. The central grid of 3×3 HARP pixels is shown here.

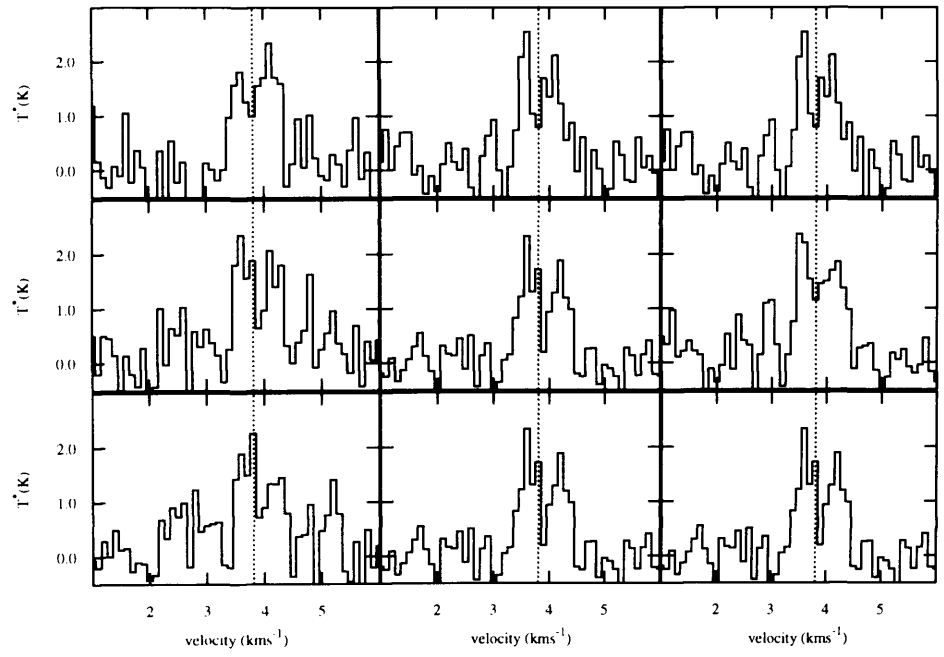

Figure 4.49: Map of HCO^+ (J=4→3) spectra in the core C-MM5. The central grid of 3×3 HARP pixels is shown here.

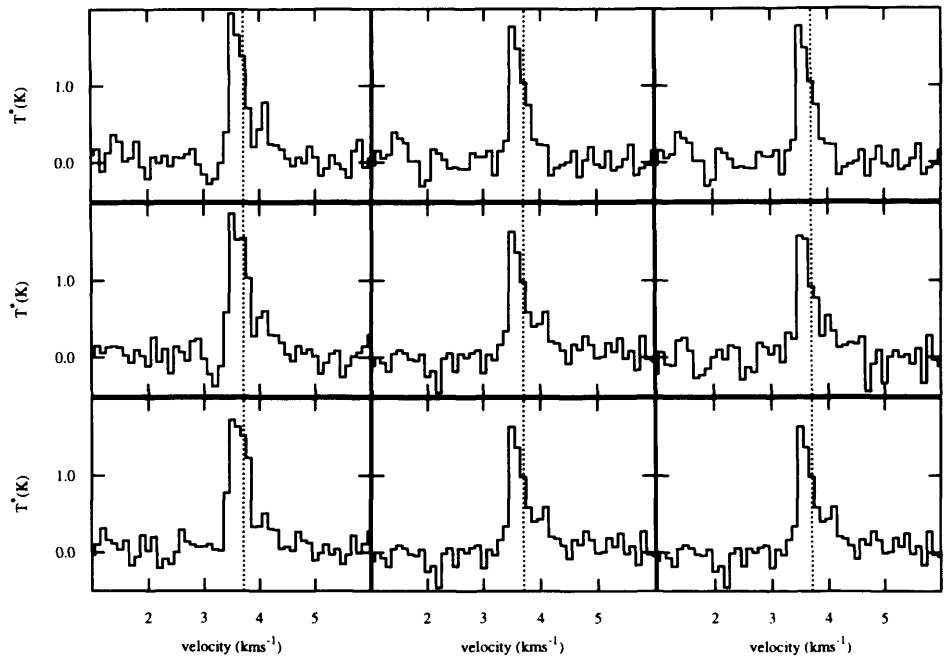

Figure 4.50: Map of HCO^+ (J=4→3) spectra in the core C-MM6. The central grid of 3×3 HARP pixels is shown here.

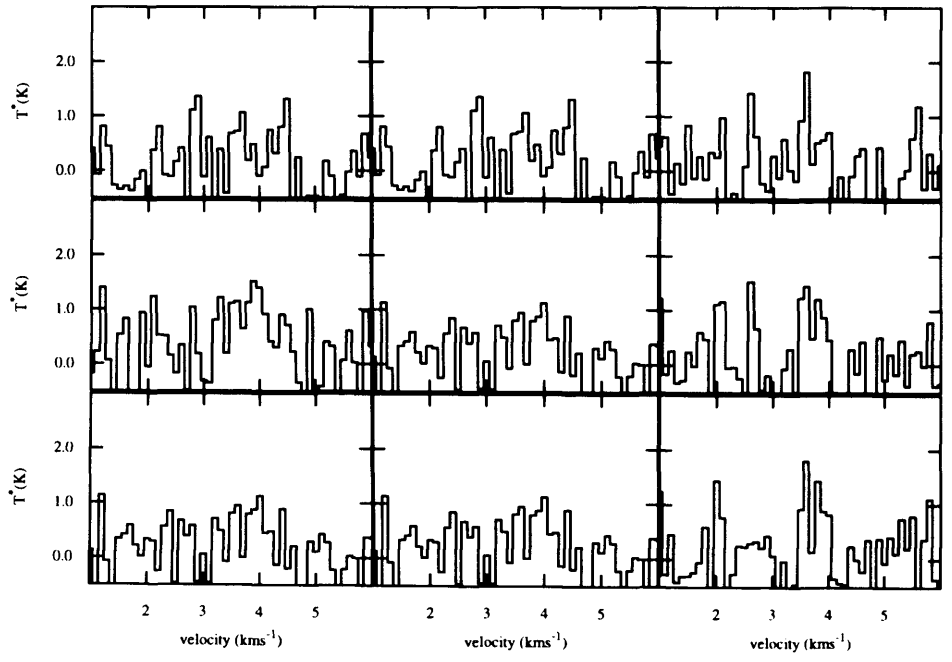

Figure 4.51: Map of HCO^+ (J=4→3) spectra in the core C-MM8. The central grid of 3×3 HARP pixels is shown here.

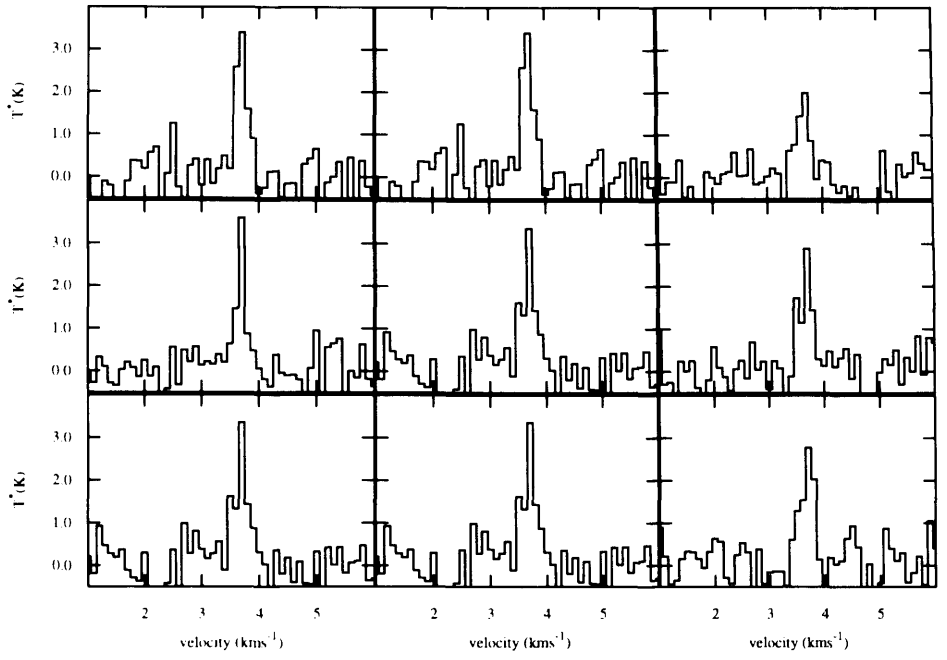

Figure 4.52: Map of HCO^+ (J=4→3) spectra in the core C-MM9. The central grid of 3×3 HARP pixels is shown here.

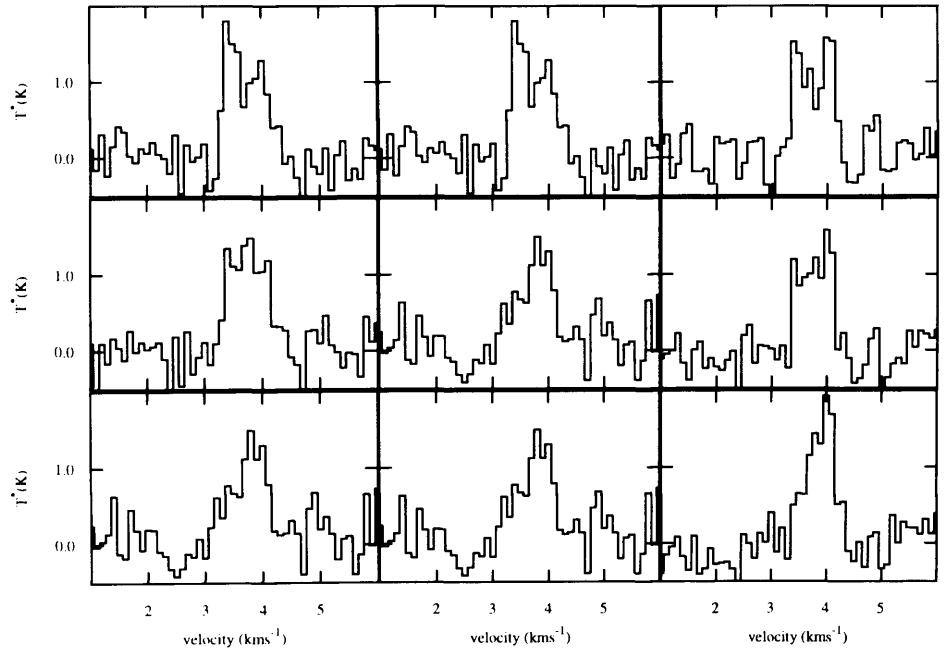

Figure 4.53: Map of HCO^+ (J=4→3) spectra in the core C-MM10. The central grid of 3×3 HARP pixels is shown here.

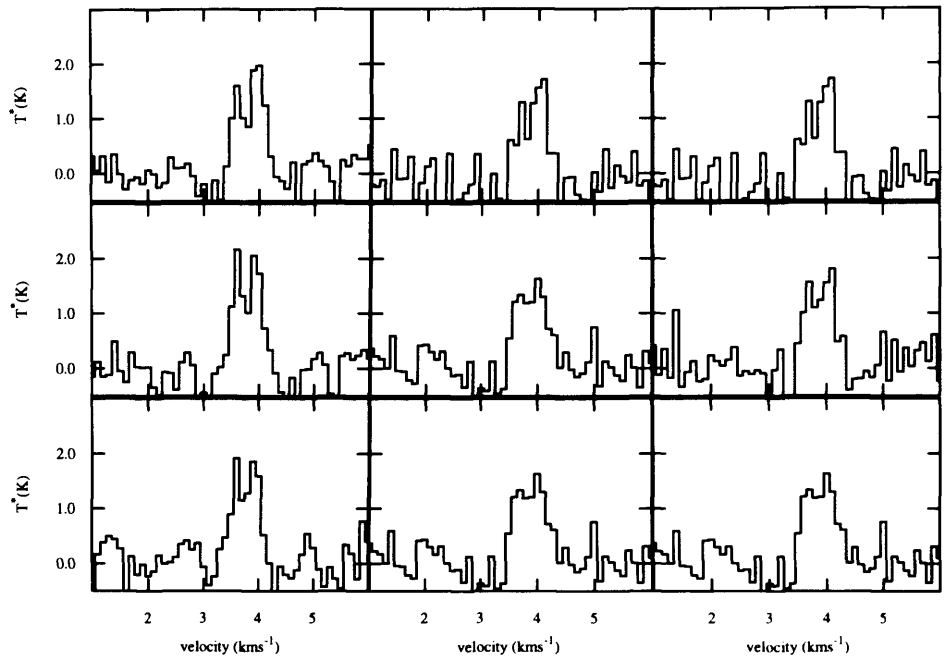

Figure 4.54: Map of HCO^+ (J=4→3) spectra in the core C-MM12. The central grid of 3×3 HARP pixels is shown here.

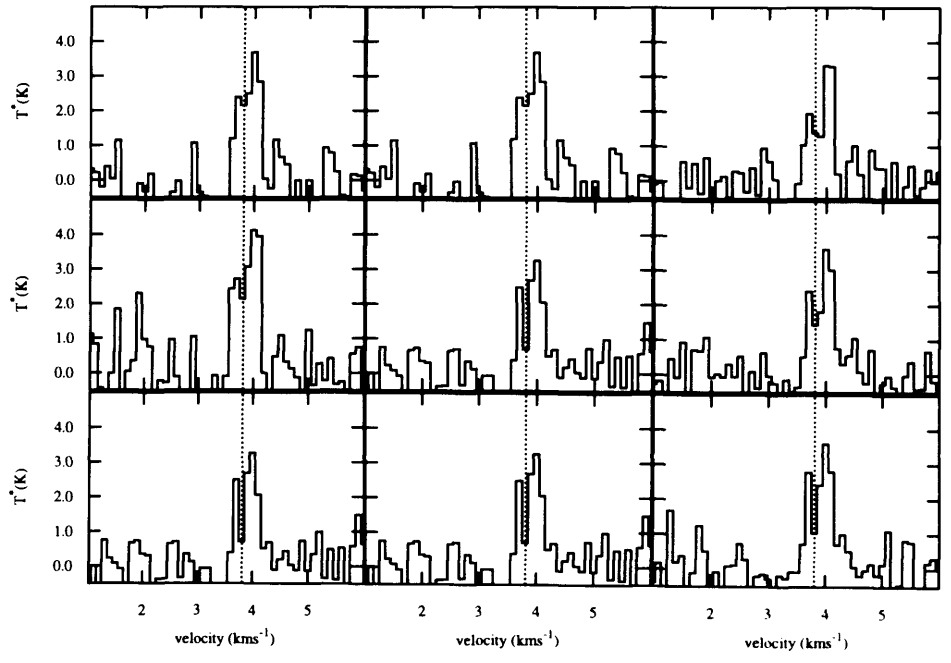

Figure 4.55: Map of HCO^+ (J=4→3) spectra in the core C-N. The central grid of 3×3 HARP pixels is shown here.

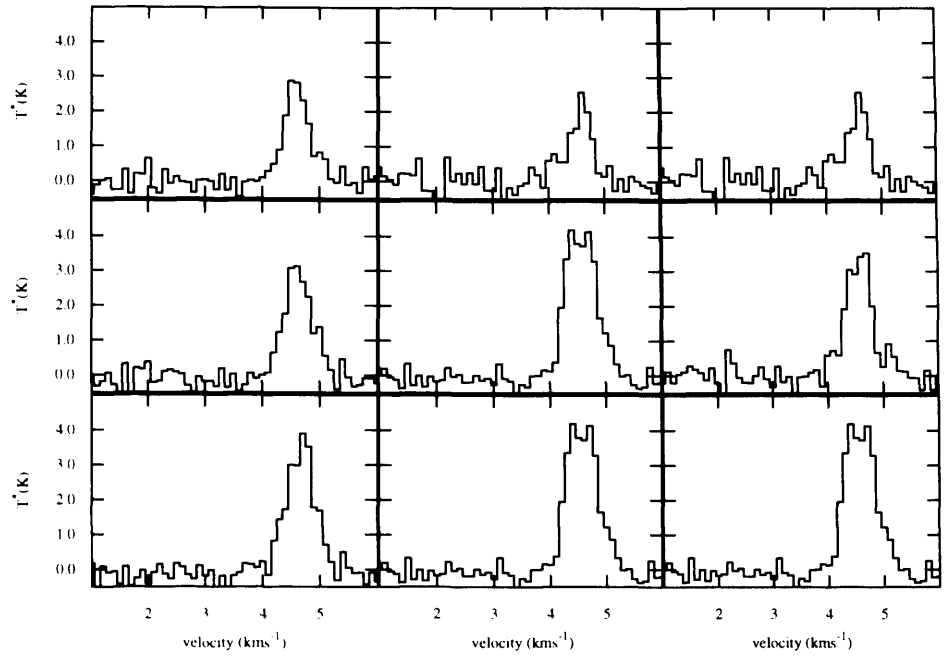

Figure 4.56: Map of HCO^+ (J=4→3) spectra in the core E-MM2a. The central grid of 3×3 HARP pixels is shown here.

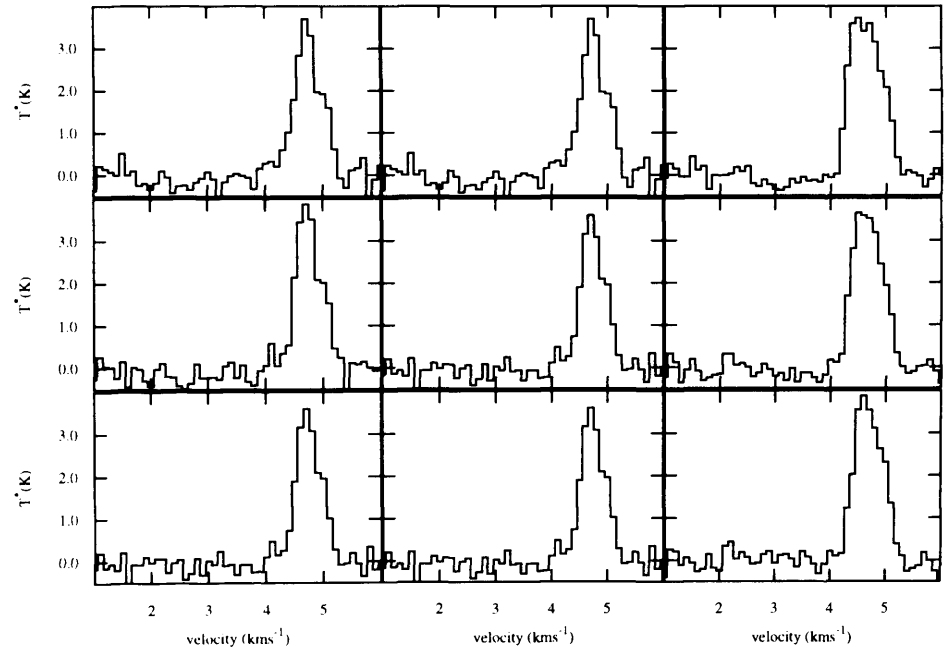

Figure 4.57: Map of HCO^+ (J=4→3) spectra in the core E-MM2b. The central grid of 3×3 HARP pixels is shown here.

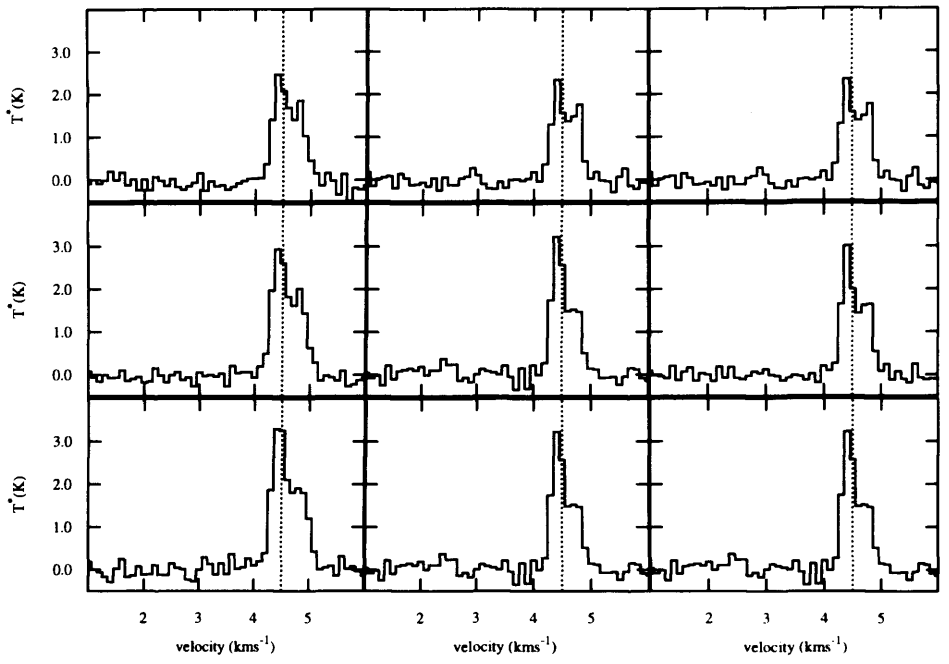

Figure 4.58: Map of HCO^+ (J=4→3) spectra in the core E-MM2d. The central grid of 3×3 HARP pixels is shown here.

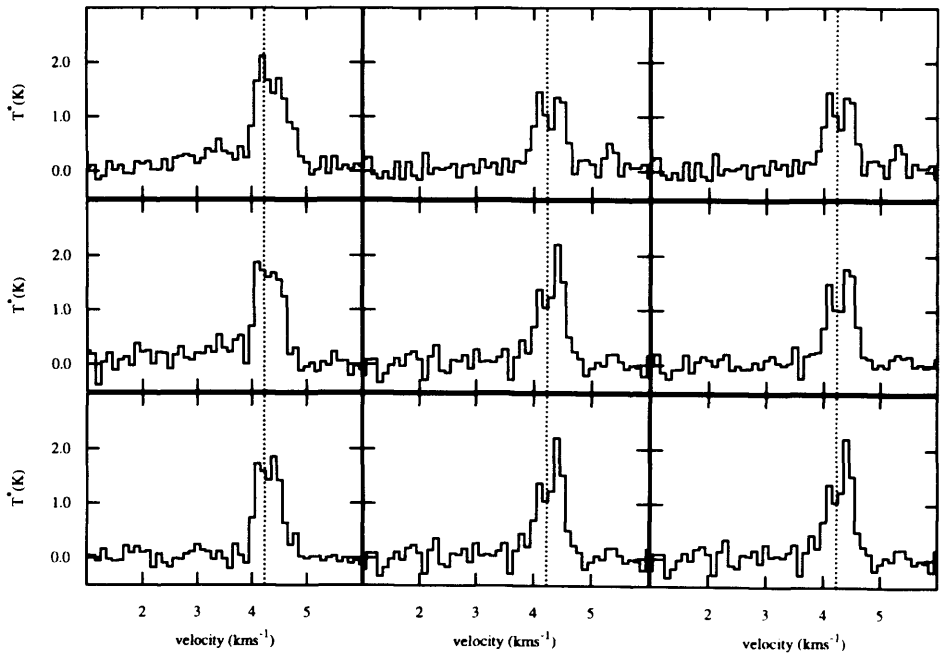

Figure 4.59: Map of HCO^+ (J=4→3) spectra in the core E-MM4. The central grid of 3×3 HARP pixels is shown here.

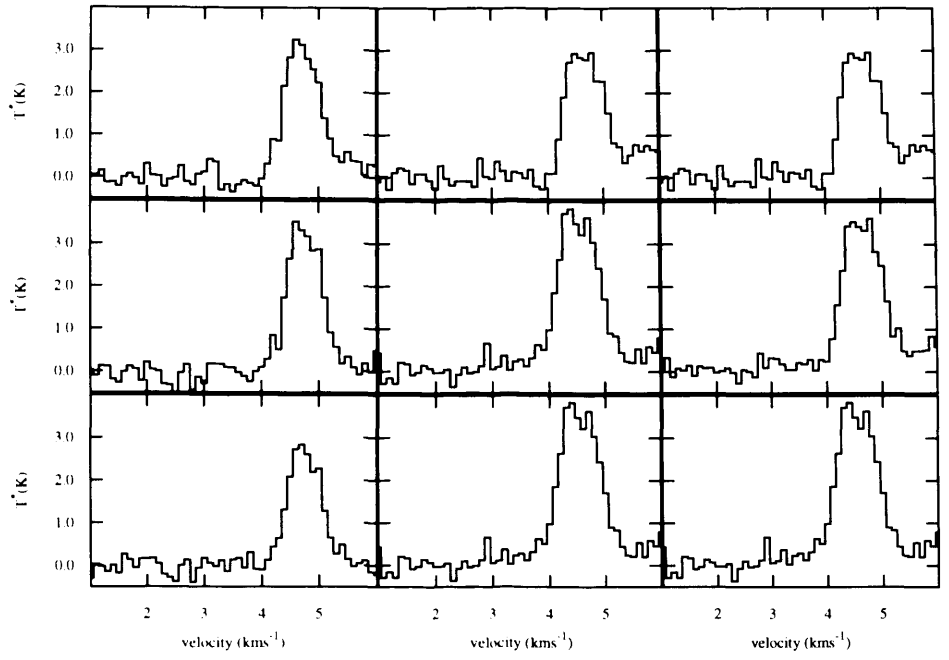

Figure 4.60: Map of HCO^+ (J=4→3) spectra in the core E-MM5. The central grid of 3×3 HARP pixels is shown here.

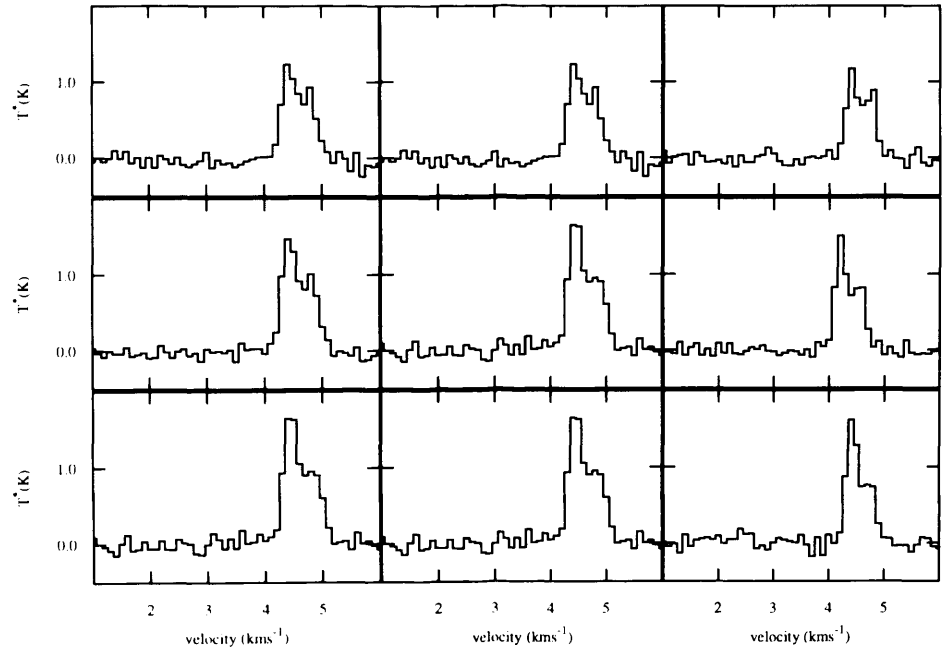

Figure 4.61: Map of HCO^+ (J=4→3) spectra in the core E-MM8. The central grid of 3×3 HARP pixels is shown here.

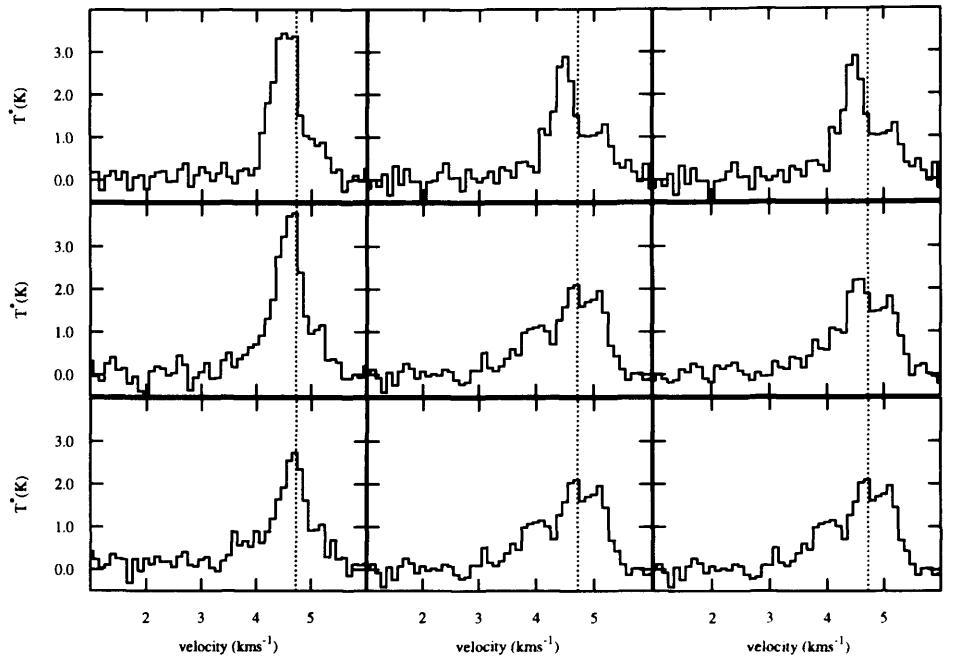

Figure 4.62: Map of HCO^+ (J=4→3) spectra in the core F-MM1. The central grid of 3×3 HARP pixels is shown here.

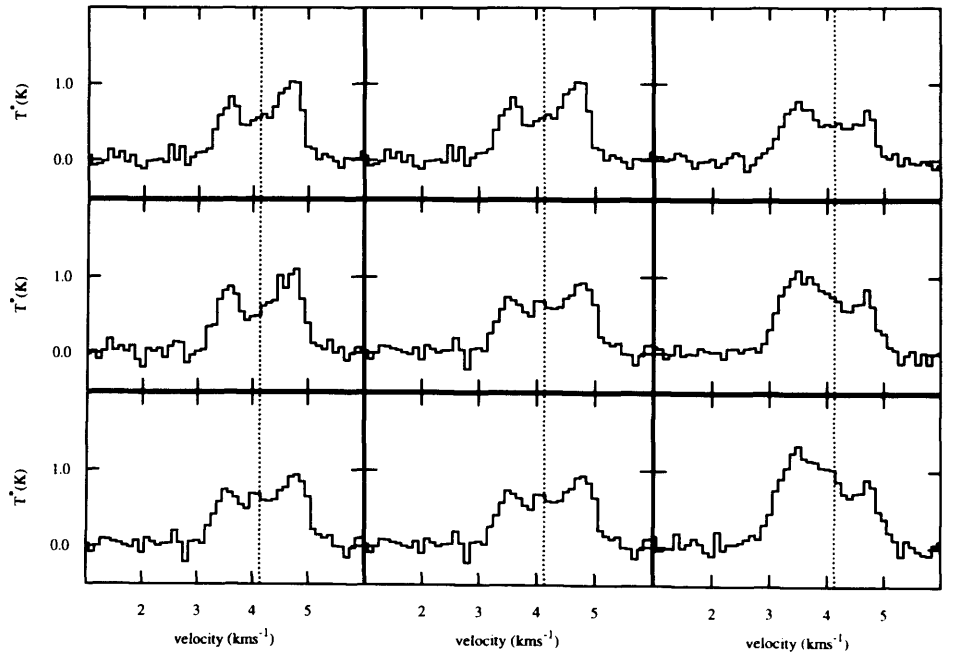

Figure 4.63: Map of HCO^+ (J=4→3) spectra in the core F-MM2a. The central grid of 3×3 HARP pixels is shown here.

4.4 Summary

I have presented HCO^+ (J=4→3) spectral line observations from HARP on the JCMT. Data are presented for 59 of the prestellar cores mapped in Chapter 3. These cores have been categorised according to their spectral line profile shapes.

In Chapter 6, I discuss the results of putting together the data from this chapter and those from Chapter 3.

Chapter 5

Simulating Spectral Line Profiles for Collapsing Cores

5.1 Introduction

The prestellar phase represents the initial conditions of protostellar collapse. The gas envelopes surrounding prestellar cores are under suitable conditions to excite many rotational molecular transitions, such as the HCO^+ (J=4$\rightarrow$3) transition observed in the previous chapter. These submillimetre line profiles contain information about the motion of the gas envelope, and can be observed to reveal the properties of cores on the verge of forming stars.

The characteristics of protostellar infall have been outlined by many authors (e.g. Zhou et al., 1993; Ward-Thompson et al., 1996). Infall in prestellar cores has also been explored (e.g. Tafalla et al., 1998; Lee, Myers, & Tafalla, 1999). Lee et al. (1999) observed CS spectral lines for 163 gravitationally bound cores and

detected a large fraction with self-absorbed double-peaked profiles. Moreover the study found an over-abundance of these peaks were blue-shifted, indicating infall motions, compared to red-shifted ones. It is this blue-shifted asymmetric double peak (BAD peak) that shows a core is infalling. In non-contracting cores there is no infall and so no asymmetric peak is seen. This is the signpost that infall, and hence star formation, may be occurring.

In this chapter I model the collapse of such cores under gravity. The model accounts for radiation transfer through the cloud. Hence I am able to create model spectral line profiles for collapsing cores of various densities, sizes and temperatures, and over various timescales. Using this model I explore how changes in the physical properties of such cores affect their observed line profiles. These trends allow me to estimate the initial properties of real cores, by comparison with observed measurements of their spectral line profiles. In this way we can understand observed objects in the present epoch in the context of their history.

5.2 The Model Profile

Many radiation-transfer models have been published previously, exploring the molecular line profiles produced as cores collapse (e.g. Rawlings et al., 1992; Ward-Thompson & Buckley, 2001; Tsamis et al., 2008). Whitworth & Ward-Thompson (2001, hereafter WW01) outline an analytic model describing the evolution of a young star from a self-gravitating gas cloud. They set out to build a model fitting observational data. Invoking a Plummer-like density profile (Plummer, 1911), they assume a non-magnetic model and this allows them to form a reasonably simple, analytic model for a core's collapse.

A Plummer-like density profile has the form

$$\rho(r, t = 0) = \rho_{flat} \left[\frac{r_{flat}}{(r_{flat}^2 + r^2)^{\frac{1}{2}}} \right]^{\eta}. \tag{5.1}$$

This gives a density profile like that shown approximately in Figure 5.1. It has a flat, central region, which steepens towards the edge. In equation 5.1, it is r_{flat} that determines the size of the flat region, and ρ_{flat} gives the density of that region. r_{bdry} is the point beyond which we cease to model the profile. It is essentially the outer edge of the core, where the density profile has dropped significantly, as shown in Figure 5.1. WW01 chose this model for the density of the initial cloud because it gives the fewest free parameters, whilst still leaving the main observed properties of prestellar cores intact.

For a true Plummer Sphere, $\eta = 5$. However, the $\eta = 4$ case gives the best fit to observational data, which is why they are described as Plummer-like spheres. In the model, a core with this density profile is left to free-fall under its own self-gravity starting at time $t = 0$.

5.2.1 Outline of the Analytic Model

The model uses the independent variables of mass and time. This may not seem as intuitive as using radius and time, but it is more practical. The change is made using a Lagrangian formulation. Thus by integrating equation 5.1, an initial mass profile is found, which has the form

$$M(r, t = 0) = \int_{r'=0}^{r'=r} \rho(r', t = 0) 4\pi r'^2 dr'. \tag{5.2}$$

From this one can find the initial radius of a shell enclosing mass M by inverting the equation to get $r(M, t = 0)$. Thus radius is now defined in terms of mass.

WW01 derived an equation to give the density profile at any time, t. The location of a shell of any mass, M, needs to be found in terms of time since collapse began (at $t = 0$). The freefall time for a shell of mass M is

$$t_{ff}(M) = \frac{\pi}{2}\left[\frac{r^3(M,0)}{2GM}\right]^{\frac{1}{2}}. \tag{5.3}$$

Hence the equation for the rate of infall of mass M onto the central protostar is

$$\dot{M}(M) = \left[\frac{dt_{ff}}{dM}(M)\right]^{-1} = \frac{64GM^2\rho(M,0)t_{ff}(M)}{\pi[3M - 4\pi r^3(M,0)\rho(M,0)]}. \tag{5.4}$$

To find the density profile, consider a time $t = t_1$ and examine the free-fall times of all the shells originally in the cloud at $t = 0$. Shells with $t_{ff} < t_1$ are obviously now in the condensed object at the centre of the core. For all shells with $t_{ff} > t_1$, the instantaneous radius $r(M, t)$ is given by a rearrangement of

$$\frac{t}{t_{ff}(M)} = \frac{2}{\pi}cos^{-1}\left(\left[\frac{r(M,t)}{r(M,0)}\right]^{\frac{1}{2}}\right)$$

$$+\frac{2}{\pi}\left[\frac{r(M,t)}{r(M,0)}\right]^{\frac{1}{2}} + \frac{2}{\pi}\left[1 - \frac{r(M,t)}{r(M,0)}\right]^{\frac{1}{2}} \tag{5.5}$$

It is now possible, using $r(M, t)$ to calculate the density profile of the core at any chosen time, t, which has the form

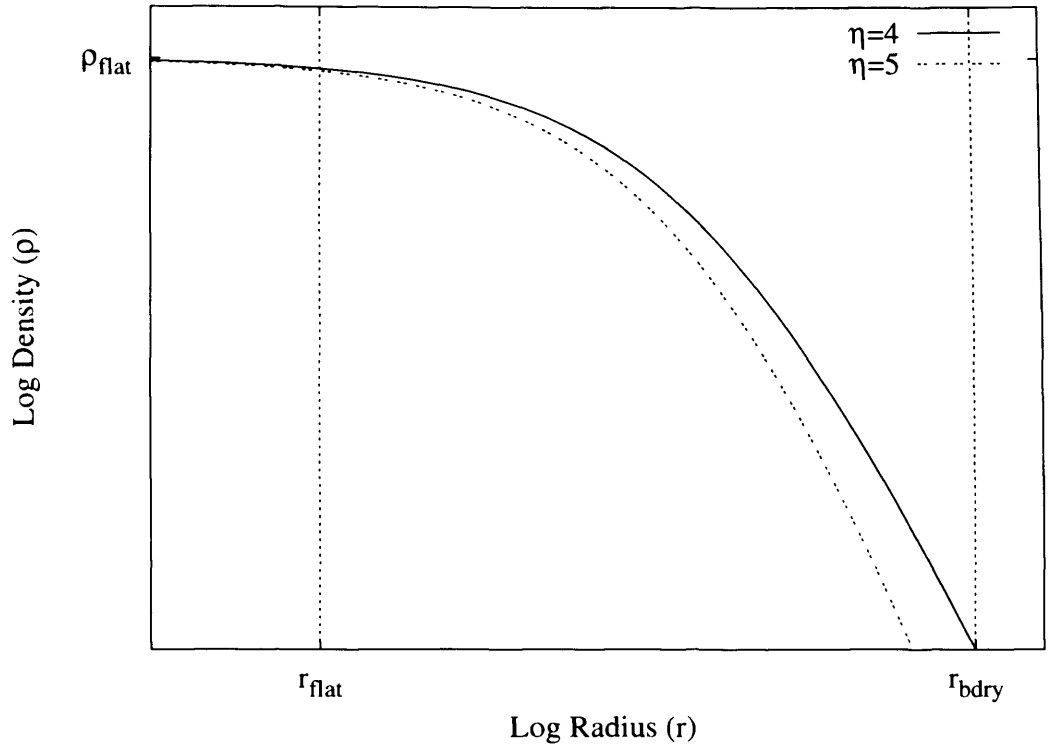

Figure 5.1: Variation of log density, ρ, with radius, for a Plummer-like ($\eta = 4$) and a Plummer ($\eta = 5$) profile, as described in Equation 5.1. See text for more details.

$$\rho(M,t) = \left\{ 4\pi r^2(M,t) \left. \frac{\delta r}{\delta M} \right|_t \right\}. \tag{5.6}$$

This now allows one to operate a radiative transfer code on the analytic profile.

5.3 Radiation Transport

The dust and gas inside a cloud alter the radiation passing through it by a combination of absorption and emission. The analytic model proposed in WW01 allows one to calculate nearly all the parameters needed to perform radiation transport calculations through the cloud. In other words, given a value for the radiation

incident on the back of a cloud (e.g. the CMB), it should be possible to calculate what kind of spectral line profile emerges from the front of the collapsing cloud.

Any absorbing medium (e.g. the ISM) has a characteristic absorption coefficient, κ_ν, for any given frequency, ν. Similarly it has an emission coefficient, j_ν. I assume a simple temperature profile of the form $T(r) = T_0 r^{-0.4}$ (Ward-Thompson & Buckley, 2001).

Together these define the amount of radiation the gas or dust absorbs and emits at a given frequency. Using the terms introduced above, the equation of radiation transfer becomes

$$\frac{dI_\nu}{dr}(r, T(r)) = -\kappa_\nu(r, T(r))I_\nu(r) + j_\nu(r, T(r)), \tag{5.7}$$

where j_ν, gives the spontaneous emission from molecules in the gas cloud. Stimulated emission is accounted for by the absorption coefficient, κ_ν, being the net absorption coefficient (i.e. true absorption less the stimulated emission). κ_ν is given by

$$\kappa_\nu = [n_i \sigma_i(\nu)] = [n_i \sigma_0 \phi(\nu - \nu_0)]\,. \tag{5.8}$$

Here n_i is the number density of absorbing particles, $\sigma_i(\nu)$ is the cross section presented by one absorbing particle to photons of frequency ν. σ_0 is the integrated cross-section of the transition. ϕ is the profile function, and ν_0 is the central line frequency. The profile function, incorporating the random thermal and turbulent motions of particles, is described by the equation

$$\phi(\nu - \nu_0) = \frac{1}{(2\pi)^{\frac{1}{2}}\Delta\nu_D(r)} exp\left\{\frac{-(\nu - \nu_0(r))^2}{2\Delta\nu_D^2(r)}\right\}. \tag{5.9}$$

$\Delta\nu_D$ is the change in ν at radius r due to Doppler broadening, and has the form

$$\Delta\nu_D(r) = \frac{\nu_0(r)}{c}\left[\frac{k_B T(r)}{m_x} + \Delta U_{turb}^2(r)\right]^{\frac{1}{2}}, \tag{5.10}$$

where U_{turb} is the random motion contribution due to turbulence.

Using all of the above, it now becomes possible to derive a spectral line profile for almost any impact parameter through the cloud, at any time during its evolution.

To explore the results of this analysis, a code has been written, which produces a spectral line profile for given initial conditions. The code requires the initial ρ_{flat}, r_{flat}, r_{bdry} and the desired viewing time. The output and results of this code are described in the following section.

The foregoing holds true for any diagnostic spectral line. The code has been constructed to allow the properties of any molecular transition to be input, using, for example, data from the Cologne Database for Molecular Spectroscopy (Müller et al., 2001, 2005). However the molecular line tracer that is most commonly used to study infall is HCO^+ and the observational data used here are all from the HCO^+ (J=4→3) or HCO^+ (J=3→2) transition.

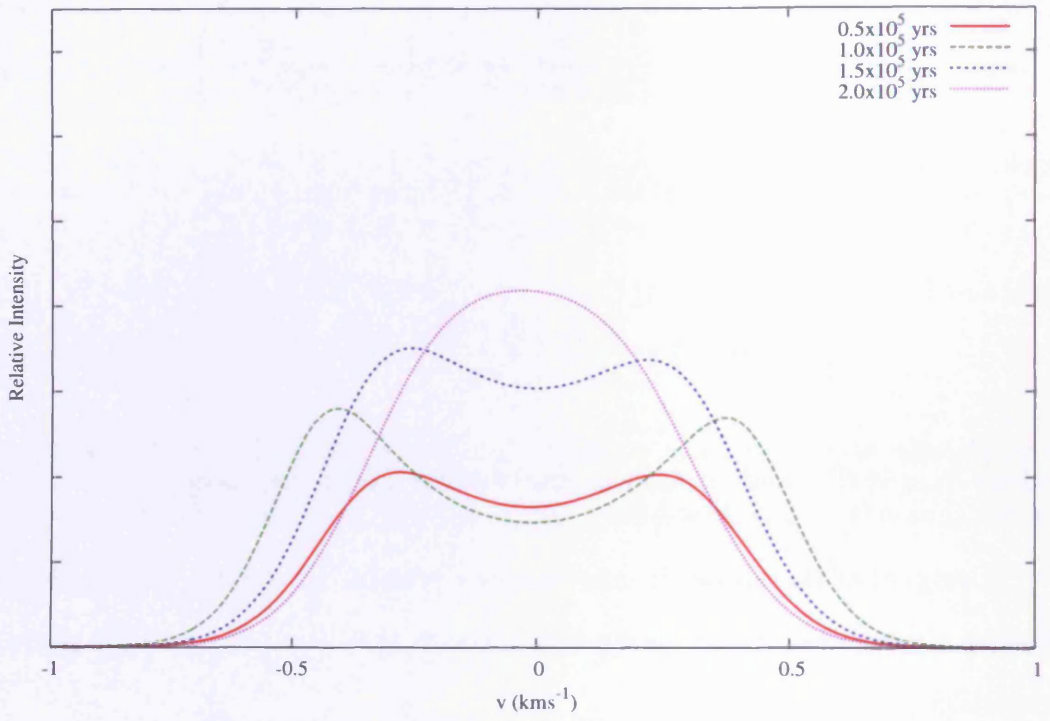

(a) $\rho_{flat} = 10^5$ cm^{-3}

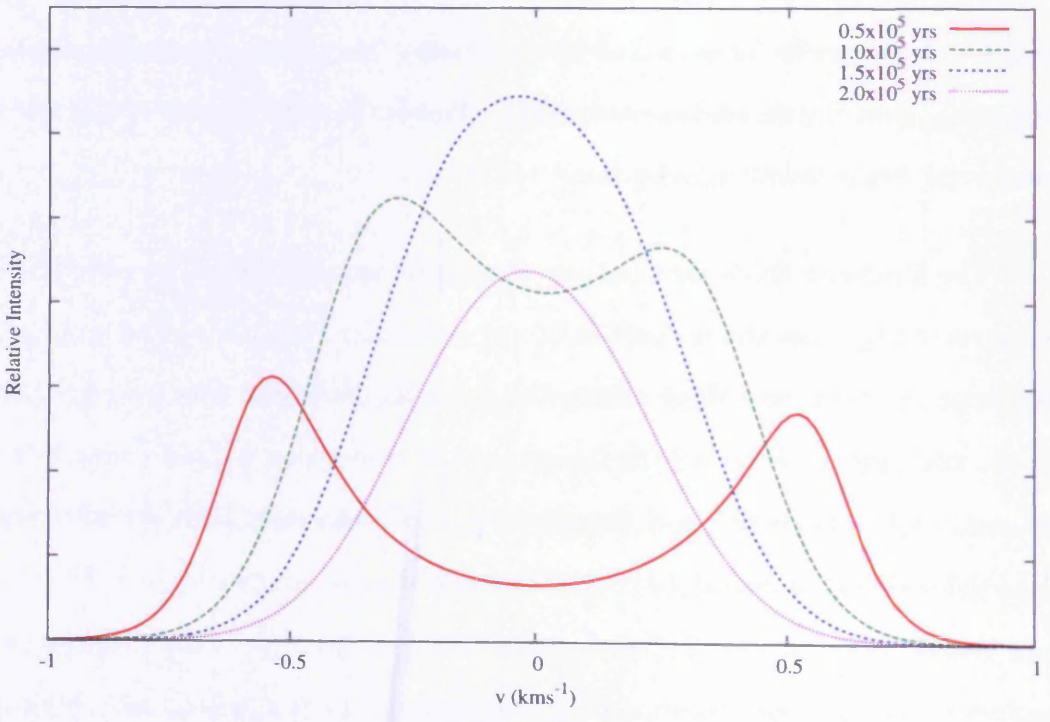

(b) $\rho_{flat} = 5 \times 10^5$ cm^{-3}

Figure 5.2: Spectral line profiles for model cores of central density 1×10^5 and 5×10^5 cm^{-3}, viewed at 0.5×10^5, 1×10^5, 1.5×10^5 and 2×10^5 years since collapse began.

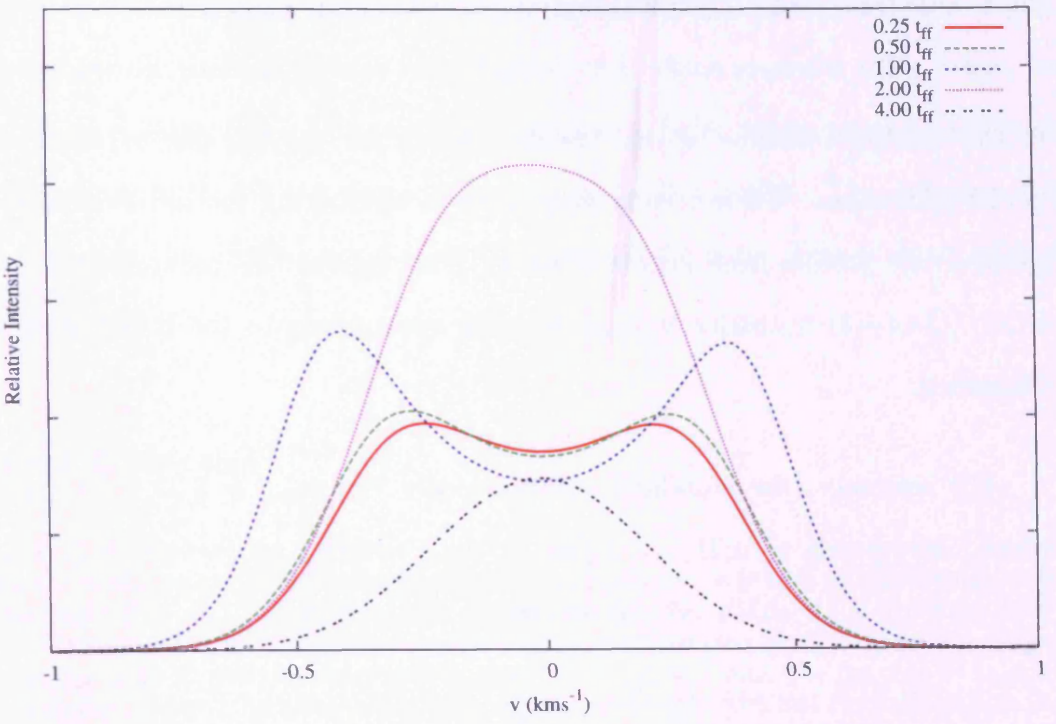

(a) $\rho_{flat} = 10^5$ cm^{-3}

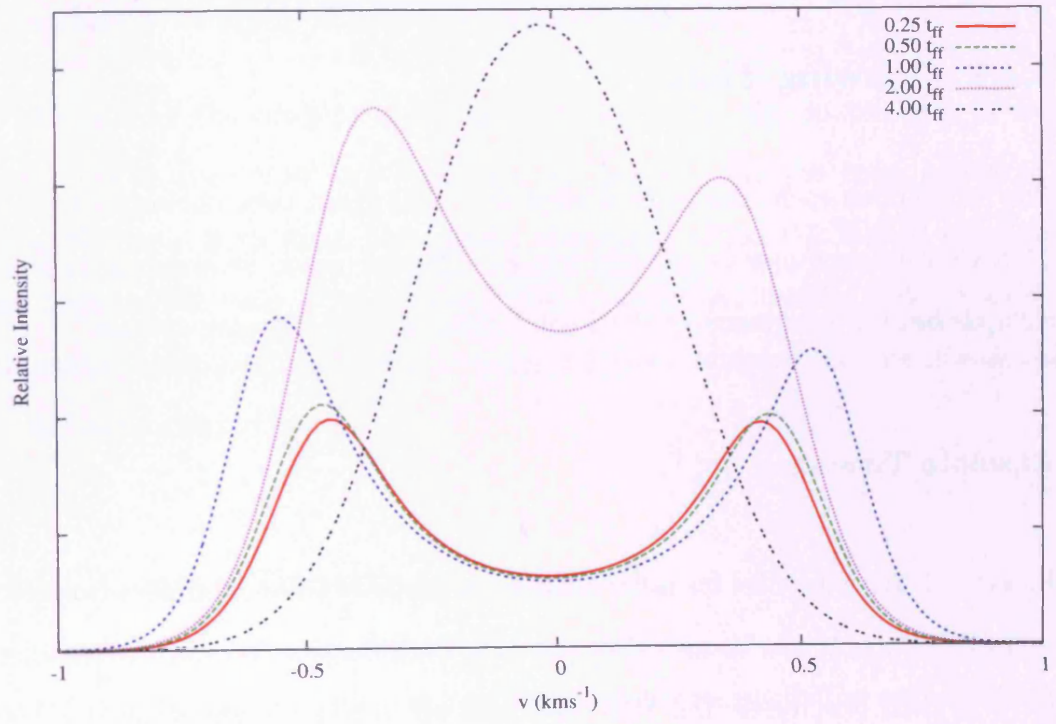

(b) $\rho_{flat} = 5{\times}10^5$ cm^{-3}

Figure 5.3: Spectral line profiles for model cores of central density 10^5 cm^{-3} and 5×10^5 cm^{-3}, viewed at 0.25×, 0.50×, 1.00×, 2.00× and 4.00×t_{ff}. t_{ff} equivalent to 96,133 years and 42,992 years for (a) and (b) respectively.

5.4 Parameter Study

In this section I outline several trends, seen when varying one or more of the model parameters. These trends assist later in identifying the nature of observed spectral line profiles from prestellar cores. Throughout this parameter study the HCO^+ (J=4→3) transition is used, to allow comparison to the HARP data from Chapter 4.

For reference, the standard canonical core has $\rho_{flat} = 3.32 \times 10^{-19}$gcm^{-3}, which corresponds to n(H_2) = 10^5cm^{-3}, r_{flat} = 0.002 pc ($\approx$ 400 AU), r_{bdry} = 0.01 pc ($\approx 2 \times 10^3$ AU), central excitation temperature, T_0 = 10K, turbulence, Δv_{turb} = 0.1 km s^{-1} and $t = t_{ff}$. For each of the cores shown in this section, the parameters have these values, unless otherwise stated.

5.4.1 Viewing Time

The code allows each core to be viewed at a user-given time during its evolution. This viewing time can be defined in two different ways, as absolute time since collapse began, or in terms of the freefall time of the collapsing system.

Absolute Timescale

Figure 5.2 shows profiles for different density cores as time progresses from 5×10^4 to 2×10^5 years. It can be seen that low- and high-density cores evolve in different ways as time progresses, but that they end up in roughly the same place. The 5×10^5 cm^{-3} core shows dramatic rises, falls and asymmetries in its peaks compared to the 10^5 cm^{-3}equivalent. The increased central density effectively speeds up the

system by increasing the gravitational force exerted by the centre of the object. Simultaneously, there is greater mass further out, which means it takes longer for the core to collapse fully. The two effects appear to balance out, as by 2×10^5 years the two cores both show a very similar, single-peaked profile. The differences in the shapes of the profiles are due to the mass of the core. This is dealt with in Section 5.4.2.

Freefall Timescale

Figure 5.3 shows profiles for cores as time progresses in terms of the freefall time of the system. Figure 5.3 gives us a different perspective from Figure 5.2. Upon the collapse of our Plummer-like cores, the mass within the flat density region will all reach the central point simultaneously, creating a protostar. This timescale is defined here as being the freefall time of the system.

Apart from the effect of increased mass (i.e. that the double peak is more pronounced in the 5×10^5 cm^{-3} model), we can see that the cores evolve in a similar fashion. Both reach the highest intensity around 1–2 freefall times and then begin to fall away after 4 freefall times. The lower density core appears to have almost completely collapsed by 4 freefall times, whereas the more dense core still has some time to go.

5.4.2 Central Density (ρ_{flat})

Figure 5.4 shows the variation in the model with changes in the central density for model cores viewed either at one freefall time or at 5×10^4 years. In the former case, we see that increasing the central density pushes the peaks of the profile

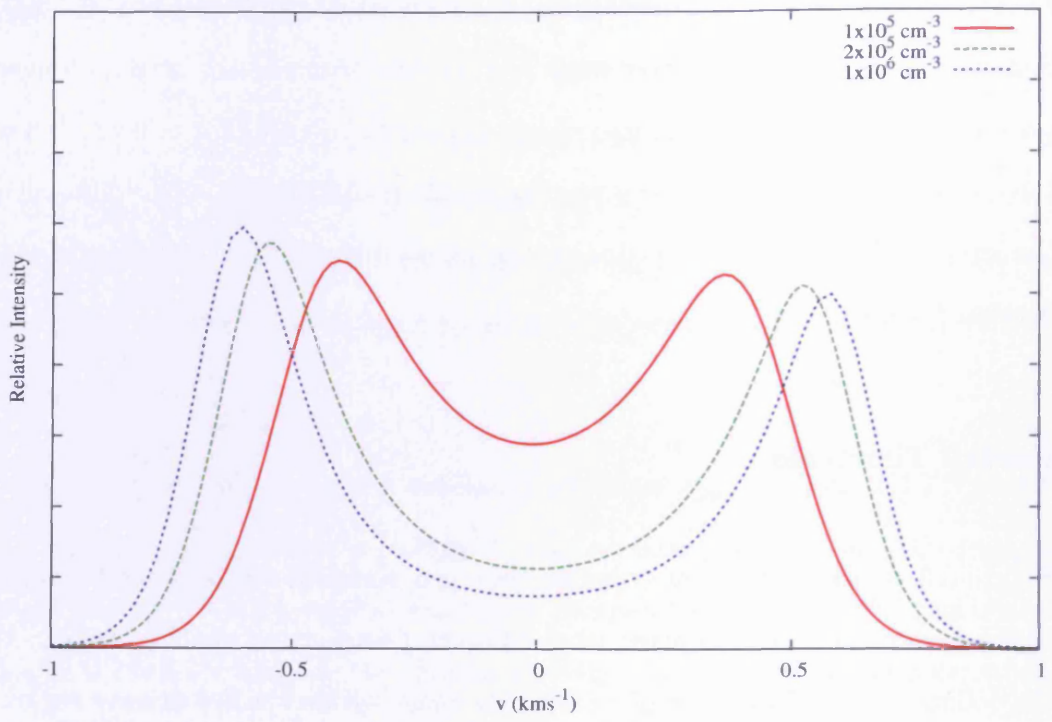

(a) Viewing at 1 freefall time (t_{ff})

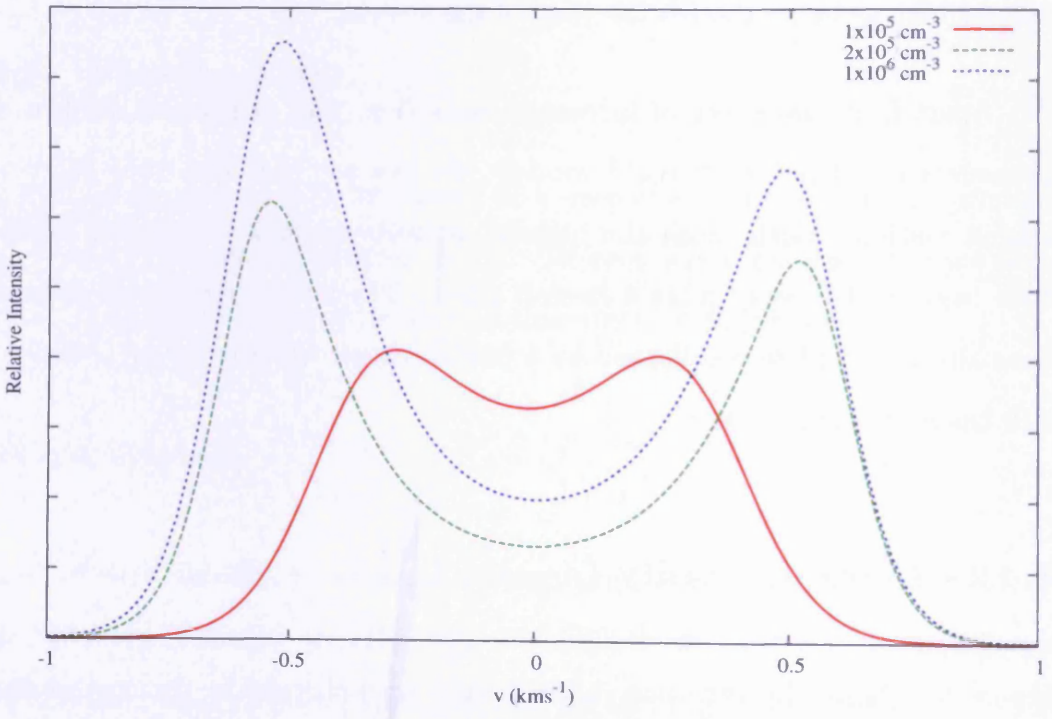

(b) Viewing at 5×10^4 years

Figure 5.4: Spectral line profiles for model cores of central densities 10^5, 5×10^5 and 1×10^6 cm^{-3}, viewed at 1 freefall time and 0.5×10^5 years.

apart, and increases the size of the absorption dip. The same trend is observed in the profiles viewed at 5×10^4 years.

The difference in the two plots is that for increasing central density, the freefall time of the system increases and so the relative heights of the profiles change, as seen in Figure 5.2 and Figure 5.3.

As the central density increases, the mass of the whole core increases and so do the rates of emission and absorption. Emission pushes the whole of the profile upward and the absorption brings the dip down further. The overall result is an apparent sideways drift of the peaks in the profile with increasing central density.

5.4.3 Central Core Size (r_{flat})

Figure 5.5 shows the profiles of cores as their central core size r_{flat} is varied. Two different examples, of different density and viewing time, are given. In both cases, increasing the central core size appears to lower the heights of the profiles, and increase the asymmetry between the two peaks. This is the result of an increased freefall time in the whole system. As the central mass increases, the whole system collapses faster and so the evolution of the object is accelerated until all the material is in the middle, and the profile has significantly reduced in intensity.

When the object has collapsed some way and is relatively dense in the middle, the effect of the temperature gradient becomes more obvious and so the two peaks appear to become more asymmetric. As the central core size goes up, the profile appears to skew more.

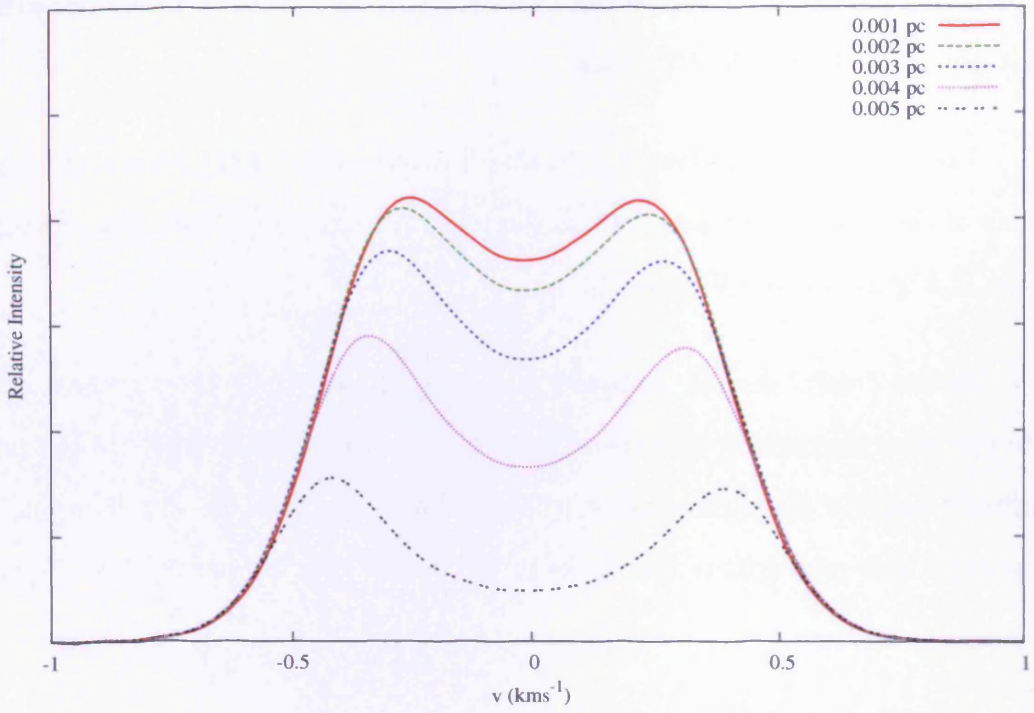

(a) $\rho_{flat} = 10^5$ cm^{-3}, viewing at 0.5 freefall times.

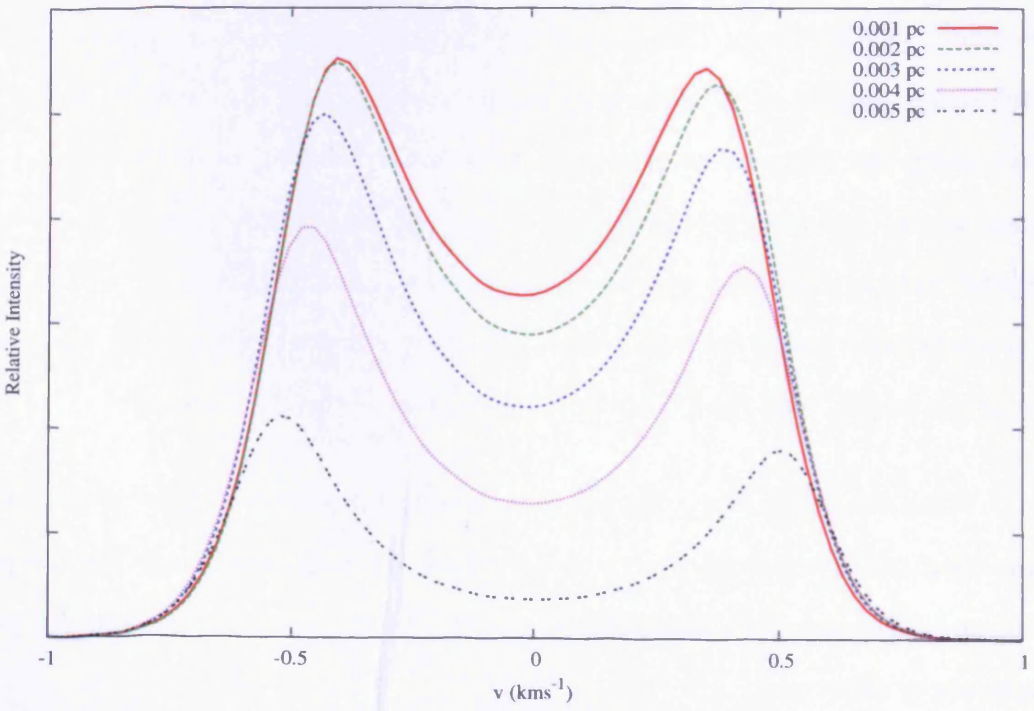

(b) $\rho_{flat} = 10^5$ cm^{-3}, viewing at 1 freefall time.

Figure 5.5: Spectral line profiles for model cores of central density 10^5 cm^{-3}, with central core sizes, r_{flat}, of 0.001, 0.002, 0.003, 0.004 and 0.005 pc.

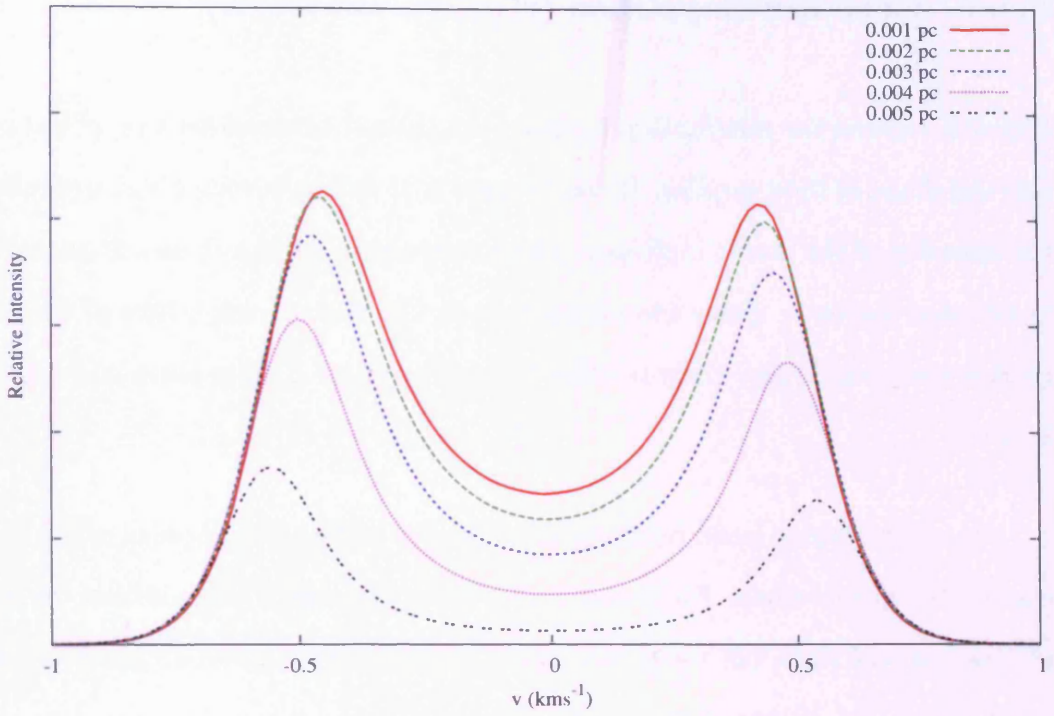

(a) $\rho_{flat} = 5{\times}10^5$ cm^{-3}, viewing at 0.5 freefall times.

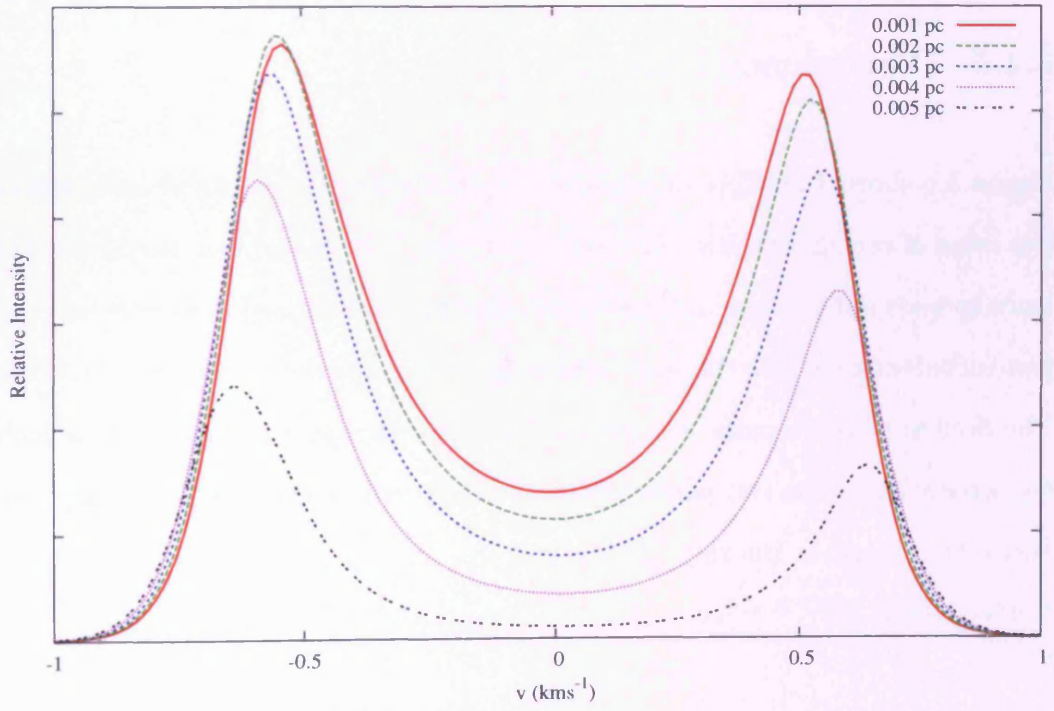

(b) $\rho_{flat} = 5{\times}10^5$ cm^{-3}, viewing at 1 freefall time.

Figure 5.6: Spectral line profiles for model cores of central density $5{\times}10^5$ cm^{-3}, with central core sizes, r_{flat}, of 0.001, 0.002, 0.003, 0.004 and 0.005 pc.

5.4.4 Core Envelope Size (r_{bdry})

Figure 5.7 shows the relationship between the extent, or envelope size, of the cores and the shape of their profiles. It can be seen that as the envelope size increases so the intensity of the profile increases. More material in an object means an increase in emission across it. Since the parameters in the more dense centre of the cloud remain unchanged, very little relative change in ratio of absorption and emission is seen.

No other obvious trend resulting from change in the envelope size of the object can be seen in this study. For this reason it is not a suitable diagnostic in the study of observational data and we cannot easily deduce the extent of an observed cloud using this model. Other observations are needed to tie down this parameter.

5.4.5 Turbulence (Δv_{turb})

Figure 5.8 shows the effect of small-scale turbulence on the model core profiles on two cores of central densities 10^5 and 5×10^5 cm^{-3}. In both plots, increasing turbulence spreads out the line and smoothes away the double-peak that is present in the non-turbulent case. As the lines spread out they appear to decrease in intensity. The double peak becomes less pronounced as turbulence increases. This increasing separation of the two peaks with increasing turbulence was previously seen by Ward-Thompson & Buckley (2001) and also by Ward-Thompson, Hartmann, & Nutter (2005).

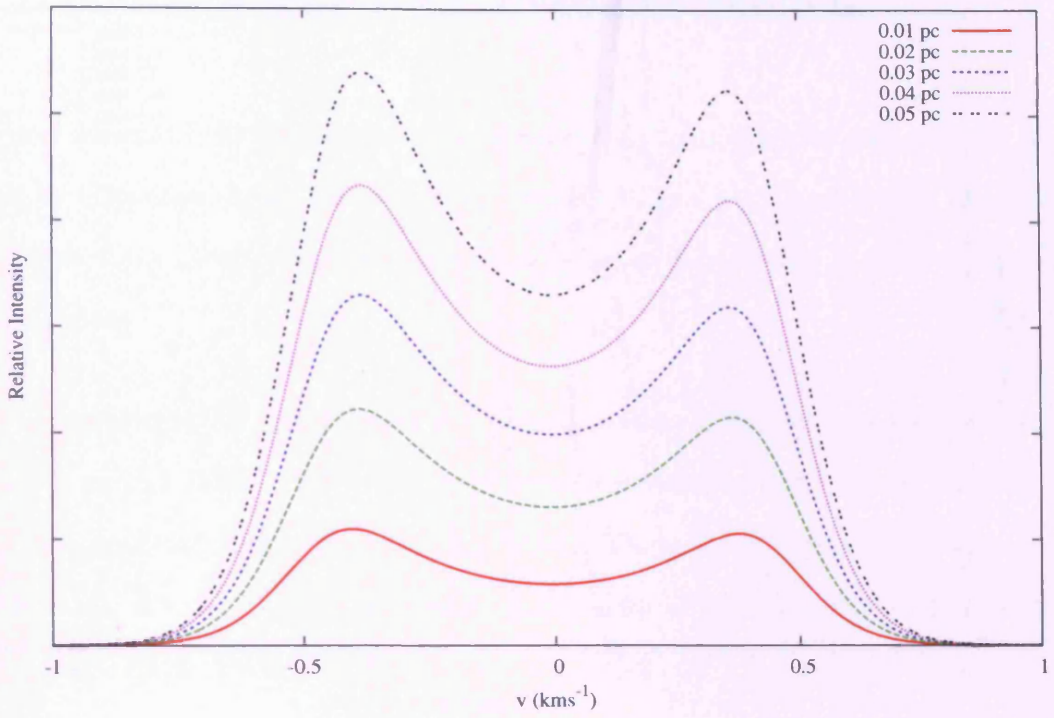

(a) $r_{flat} = 0.001$ pc

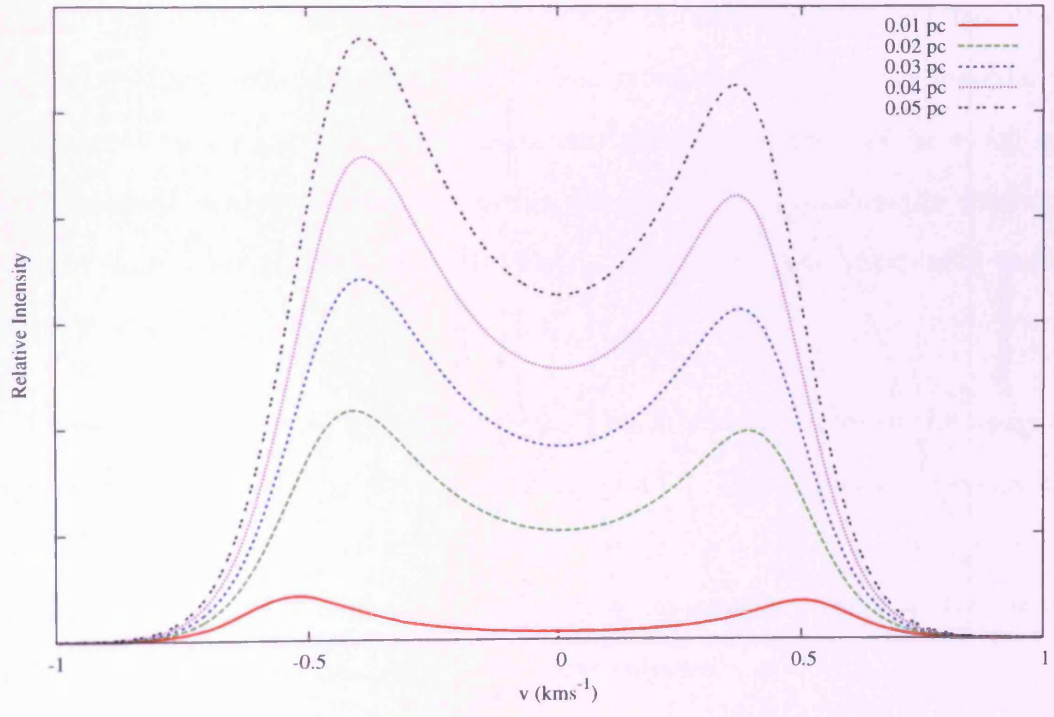

(b) $r_{flat} = 0.005$ pc

Figure 5.7: Spectral line profiles for model cores of central flat radius 0.002 and 0.005 pc, viewed at 1 freefall time for core envelope sizes of 0.01, 0.02, 0.03, 0.04 and 0.05 pc.

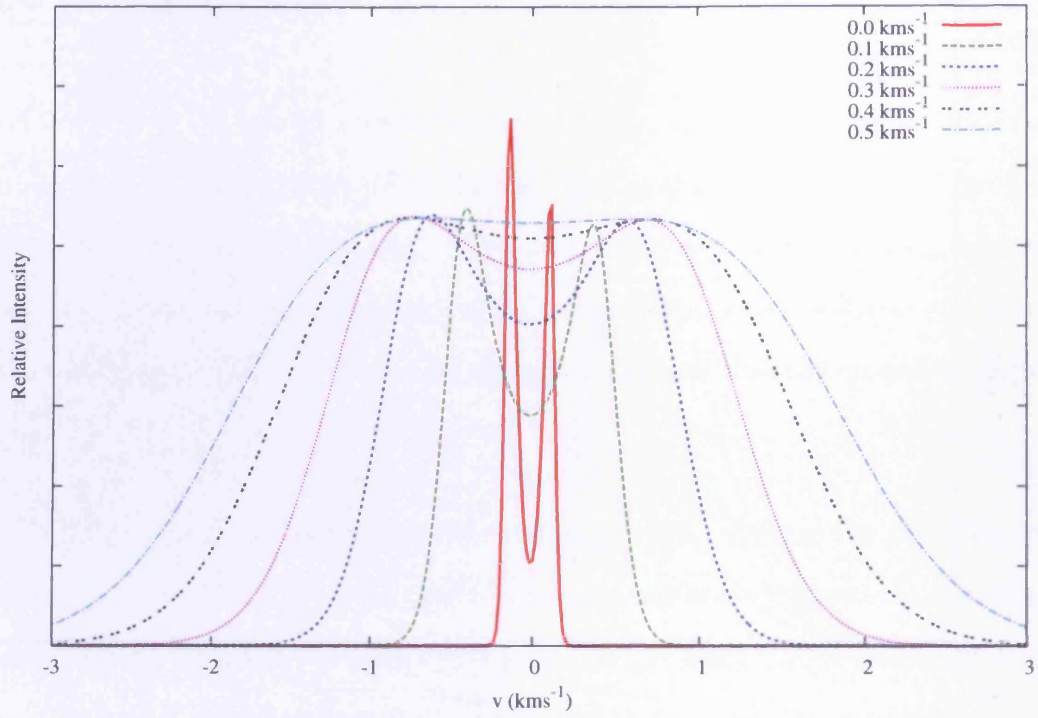

(a) $\rho_{flat} = 10^5$ cm^{-3}

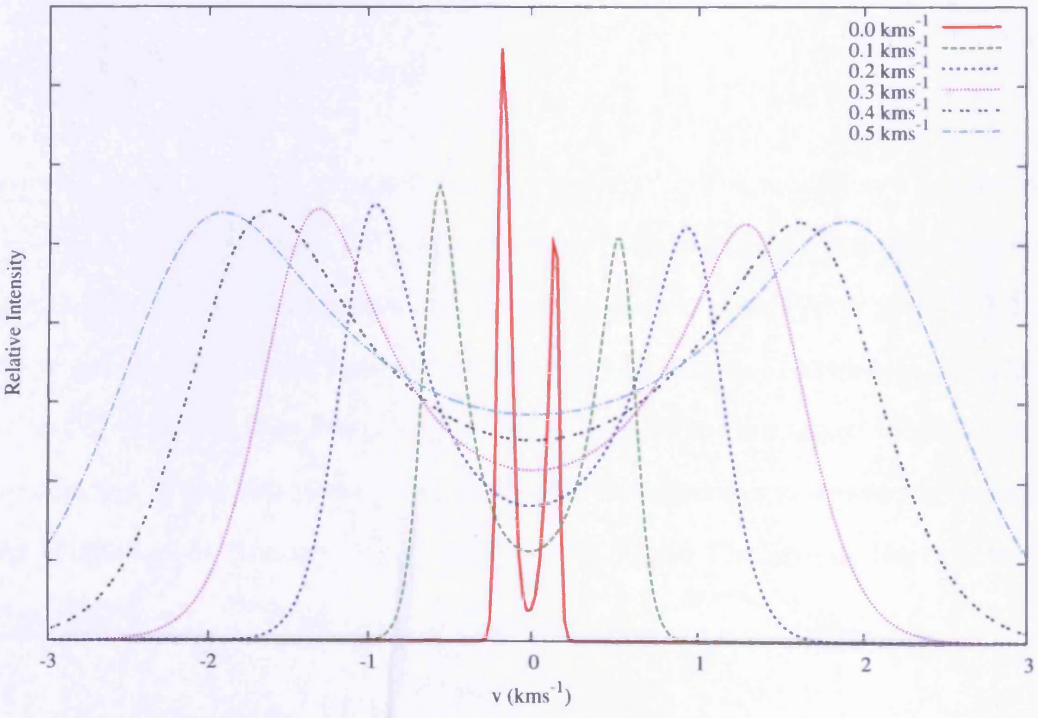

(b) $\rho_{flat} = 5{\times}10^5$ cm^{-3}

Figure 5.8: Spectral line profiles for model cores of central density $1{\times}10^5$ and $5{\times}10^5$ cm^{-3}, viewed at 0.5 freefall times for core turbulence values of 0, 0.1, 0.2, 0.3 and 0.4 km s^{-1}.

5.5 Comparison with Previous Models

Figures 5.9 and 5.10 shows a comparison between my model for collapse and that used by Gregersen et al. (1997). Both the HCO^+ (J=3→2) and HCO^+ (J=4→3) transitions are shown, and the time since collapse is indicated at the top of each pair of plots.

Gregersen et al. (1997) used the density and velocity fields of the inside-out collapse model (Shu, 1977) and a temperature distribution derived from scaling that used for B335 (Zhou et al., 1990). They use a constant abundance of $X(HCO^+) = 6 \times 10^{-9}$. I use a central core density of 5×10^5 cm^{-3} with an abundance of $X(HCO^+) = 6 \times 10^{-9}$.

The model they use is spherically symmetric and consists of 30 shells, 15 inside the infall radius and 15 outside the infall radius. At each stage of their evolution, they are effectively extending the infall radius outward, allowing more material to have fallen onto a central point. This is very different to the way in which my model proceeds, where all material within the central r_{flat} reaches the centre at the same time, after one freefall time. My r_{flat} parameter and their infall radius are not analogous.

I have used a value of $r_{flat} = 0.004$ pc. This is midway between the range of inner radius values used by Gregersen et al. (1997). This value, in combination with the chosen density, produces a collapse with a freefall time of $\simeq$43,000 years. This freefall timescale occurs early enough that material is present at the centre during much of the evolution, as it is for their collapse.

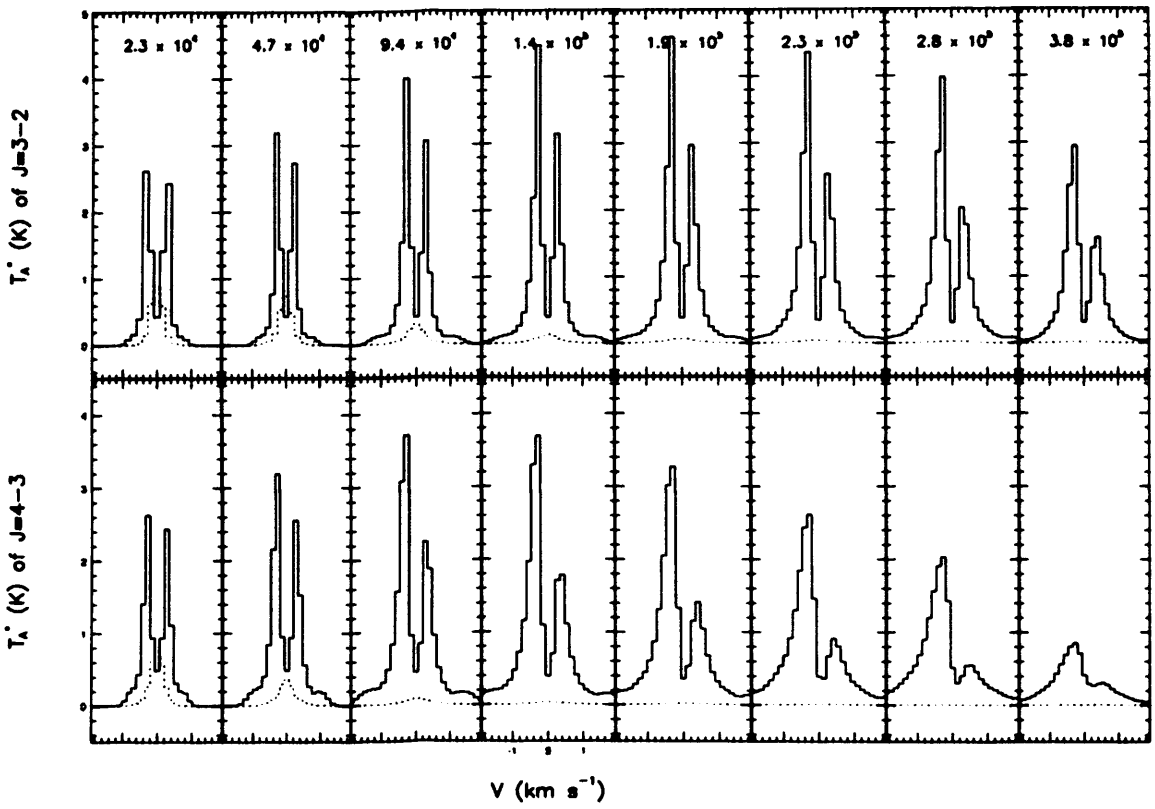

Figure 5.9: Temporal evolution of a modelled collapsing core from Gregersen et al. (1997). Spectral line profiles for HCO^+ (J=3→2) and HCO^+ (J=4→3) transitions shown on the upper, and lower rows respectively. The equivalent $H^{13}CO^+$ transition is shown below each plot as a dotted line – this is not dealt with here. Time since collapse began is shown at the top of each pair of plots. See text for details.

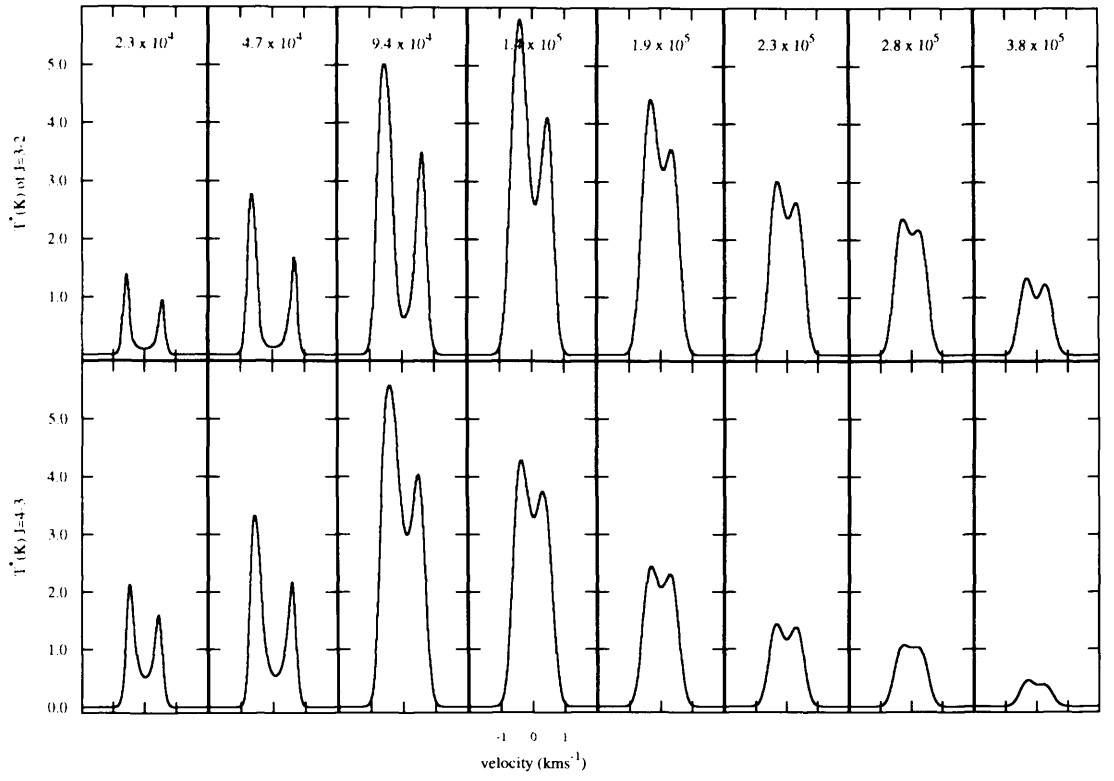

Figure 5.10: Temporal evolution of a modelled collapsing core from using my code. Spectral line profiles for HCO^+ (J=3→2) and HCO^+ (J=4→3) transitions shown on the upper, and lower rows respectively. Time since collapse began is shown at the top of each pair of plots. See text for details.

Their outer radius was 0.2 pc. This is the total radius of the core they are modelling, i.e. the outermost radius of the 30 shells. Changing the outer radius affects their line profiles very little (Gregersen et al., 1997). A similar result is seen using my code (see Section 5.4.4). My r_{bdry} parameter is very similar to their outer radius and so here, $r_{bdry} = 0.02$ pc.

All other values used to created my temporal evolution plot remain as they are for the canonical core described in Section 5.4.

Figures 5.9 and 5.10 are consistent. Both show a peak in asymmetry and temperature near the middle of the evolution. In the Gregersen et al. (1997) model this occurs at 1.9×10^5 years, in my model it is at 1.4×10^5 years. The main difference between the plots is in the nature of the central dip in the profiles. In my model, the surrounding material eventually collapses into the centre, but this does not happen during the Gregersen et al. (1997) evolution. In their model, all material beyond the infall radius does not collapse and so the absorption peak remains mostly unchanged.

Both models show that the HCO^+ (J=4$\rightarrow$3) transition is more dependent on density, as it drops more quickly than the HCO^+ (J=3$\rightarrow$2) transition. In both cases, the final HCO^+ (J=4$\rightarrow$3) plot shows that the profile has all but fallen away by 3.8×10^5 years, relative to the rest of the evolution.

I therefore believe that my model is as valid as the previously published model of Gregersen & Evans (2000) to compare with my data.

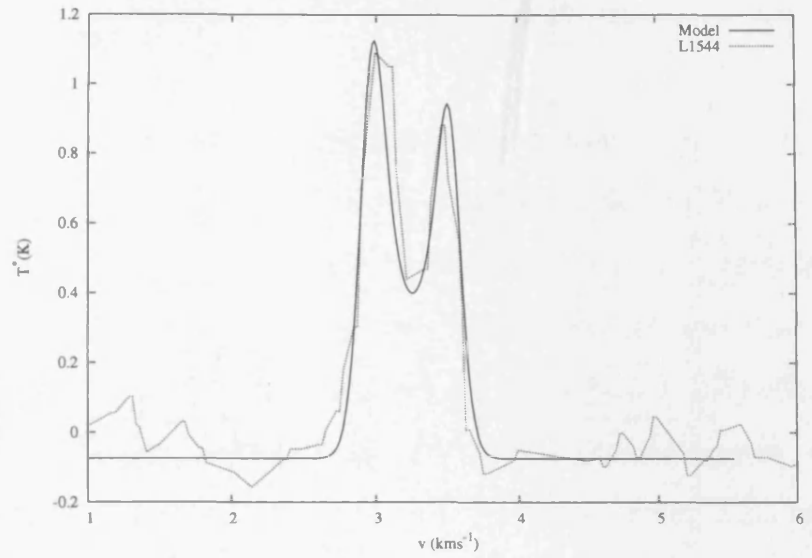

Figure 5.11: Comparison of HCO^+ (J=3→2) data of L1544, in Taurus, with the model. Observations are shown as a dotted line (Gregersen & Evans, 2000), the model is shown as a solid line. See text for details.

5.6 Comparison with Previous Observations

In this section I apply the model to HCO^+ (J=3→2) observations of three prestellar cores from Gregersen & Evans (2000). Figures 5.11 to 5.13 show my fits to the prestellar cores, and Table 5.1 summarises the best-fit parameters.

These fits were obtained manually, by visual inspection. The observed parameters were taken as a starting point, and then several iterations were made, varying the parameters around those values, to find a suitable fit. The results and more information about each core are given the following sections.

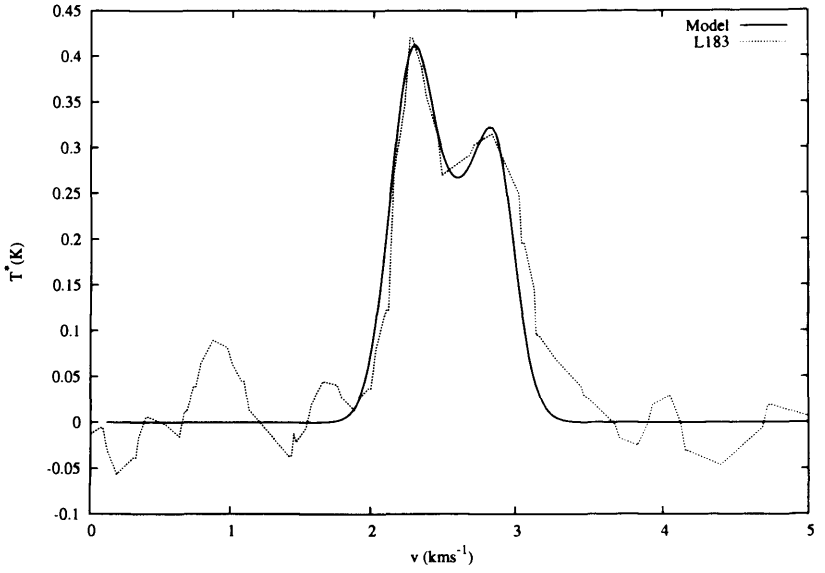

Figure 5.12: Comparison of HCO^+ (J=3→2) data of L183, with the model. Observations are shown as a dotted line (Gregersen & Evans, 2000), the model is shown as a solid line. See text for details.

5.6.1 L1544

The L1544 core (Figure 5.11) is located in the Eastern part of the Taurus cloud complex, at a distance of 140 pc. It is identified by Lynds (1962) and its spectral and continuum properties are explored by Tafalla et al. (1998).

I find good agreement to observation with a model of a low-density, young core (t_{ff}=1.7) with a low level of turbulence. The modelled initial r_{bdry} value of 0.03 pc is in close agreement with existing measurements (Jijina, Myers, & Adams, 1999). There is little discrepancy between the shape of the model and that of the observed data.

5.6.2 L183

Located at a distance of 150 pc (Gregersen & Evans, 2000), L183 (originally L134N, see Figure 5.12) is deemed a 'bright' submillimetre object by Kirk et al. (2005), who observed it at both 450μm and 850μm. Pagani et al. (2004) identify two peaks within L183: Peak 1, a large central condensation; and Peak 2, another condensation at the Northern end of L183. They find Peak 1, the bulk of the body of L183, to be a 2.5$M_{\odot}$ prestellar core. Peak two is deemed starless and possibly undergoing the very early stages of collapse. For further information see McGehee (2008) and references therein.

L183 can be modelled here as a small core (r_{flat} = 0.01 pc) which has been collapsing for 2.1×10^5 years. The model gives good agreement to the size (r_{bdry} = 0.04 pc) predicted by Jijina et al. (1999), and only a slightly lower value for turbulence.

5.6.3 L1689A

L1689A is located in Ophiuchus, at a distance of 139 pc (Nutter et al., 2006). It has been mapped in the far-infrared (Kirk, Ward-Thompson, & André, 2002) and the submillimetre (Kirk et al., 2005; Nutter et al., 2006). L1689A lies on the leading edge of the larger L1689 complex, near to the neighbouring Upper Scorpius OB association. Nutter et al. (2006) determine L1689A to be a 0.3$M_{\odot}$ prestellar core. Observations show that L1689A has a radius of 0.02–0.03 pc (Jijina et al., 1999; Nutter et al., 2006).

L1689A is modelled here as a comparatively dense core ($\rho_{flat} = 4\times10^5$ cm^{-3}),

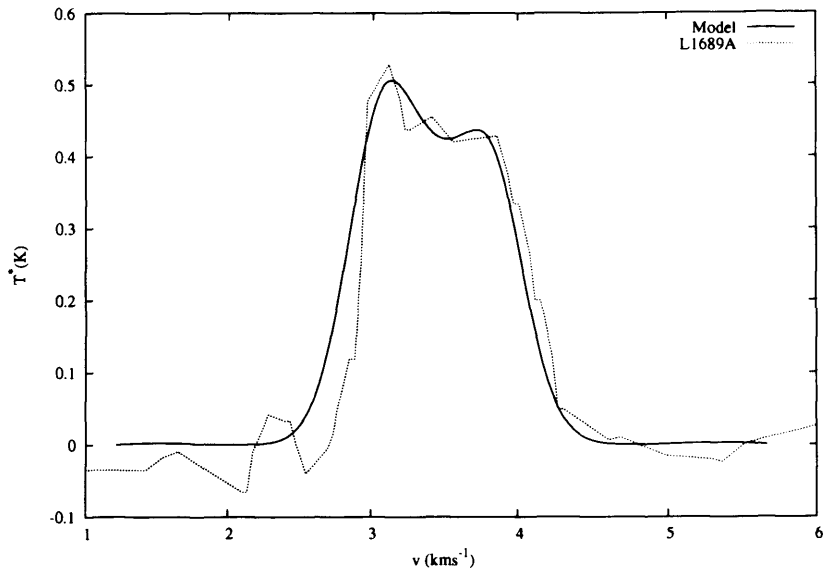

Figure 5.13: Comparison of HCO^+ (J=3→2) data of L1689A, in Ophiuchus, with the model. Observations are shown as a dotted line (Gregersen & Evans, 2000), the model is shown as a solid line. See text for details.

Table 5.1: Summary of results of model fitting for cores in Figures 5.11 to 5.13. For each core, the best-fit model's initial central density (ρ_{flat}), central core size (r_{flat}), envelope size (r_{bdry}), viewing time (t_{view}) and turbulence (Δv_{turb}) are given. The viewing time is given both in years and in terms of the freefall time of the system (t_{ff}).

Name	ρ_{flat} (cm^{-3})	r_{flat} (pc)	r_{bdry} (pc)	t_{view} (yrs)	t_{view} (t_{ff})	Δv_{turb} (km s^{-1})
L1544	1.0 x 10^5	0.004	0.03	160,000	1.7	0.07
L183	1.0 x 10^5	0.01	0.04	210,000	2.2	0.08
L1689A	4.0 x 10^5	0.005	0.03	140,000	3.0	0.14

undergoing collapse. The model gives good agreement to the size (r_{bdry} = 0.03 pc) measured observationally. Hence the model appears to be producing sensible results when compared to real data.

5.7 Comparison with my HARP Data

In this section I apply the model to HARP HCO^+ (J=4→3) observations of the Ophiuchus cores from Chapter 4. Model fits are made to these data to find the initial parameters of the cores. Since my model simulates only collapsing objects, the 20 cores displaying the characteristic blue-asymmetric double-peaked infall profile are used here. Figures 5.14 to 5.32 show the fits, and Table 5.2 summarises the best-fit parameters.

For these data, constraints from existing observations are available for the model. The extent of the cores, r_{bdry}, is given by the SCUBA data in Chapter 3. N_2H^+ observations in André et al. (2007) are used to limit the value for turbulence, Δv_{turb}. The temperature of the cores are taken from Nutter, Stamatellos, & Ward-Thompson (2009). With the above constraints, the only remaining free parameters are the central density, ρ_{flat}, the central core size, r_{flat}, and the viewing time, t_{view}.

The following model fits were obtained by visual inspection. First, a set of models were created for each core that kept the measured parameters fixed, but varied the central density, ρ_{flat}, the central core size, r_{flat}, and the viewing time, t_{view}, across a wide parameter space. The models that most closely fit the data were then used to constrain the free parameters and create more model profiles. This process was iterated until a best-fit result was obtained for each core. These plots also show the N_2H^+ line centres from André et al. (2007) as vertical dashed lines. These data are not available for all cores.

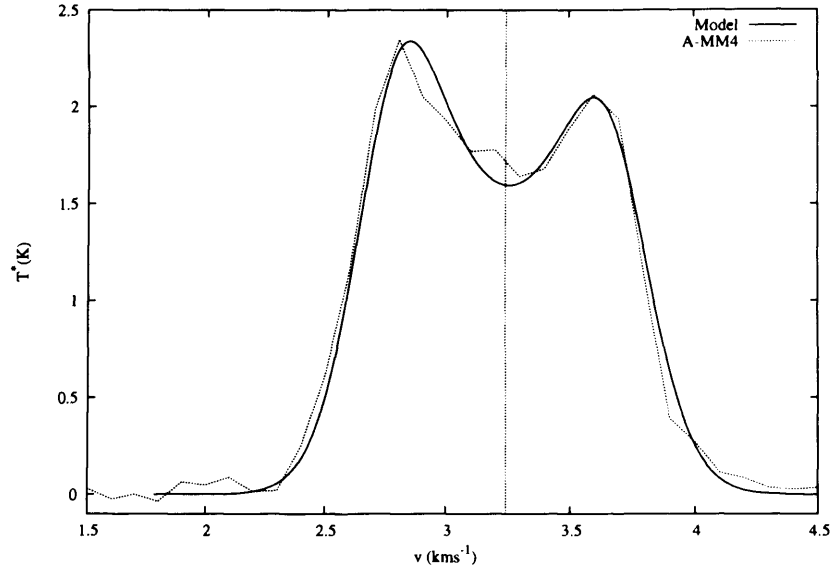

Figure 5.14: Comparison of HARP HCO^+ (J=4→3) data of A-MM4 with the model. Observations are shown as a dotted line, the model is shown as a solid line. See text for details.

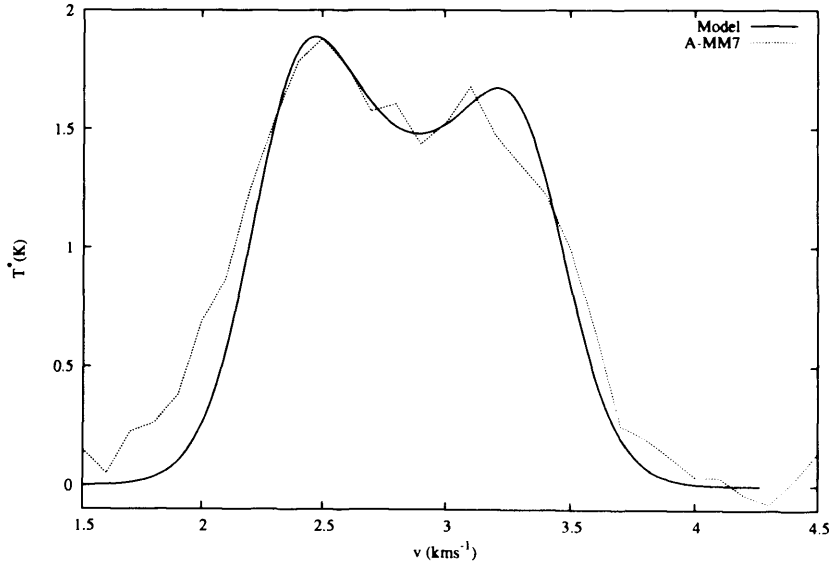

Figure 5.15: Comparison of HARP HCO^+ (J=4→3) data of A-MM7 with the model. Observations are shown as a dotted line, the model is shown as a solid line. See text for details.

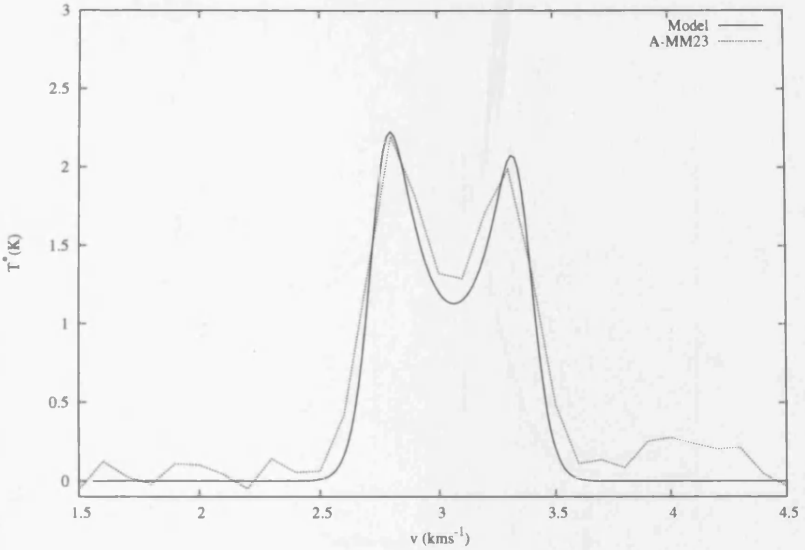

Figure 5.16: Comparison of HARP HCO^+ (J=4→3) data of A-MM23 with the model. Observations are shown as a dotted line, the model is shown as a solid line. See text for details.

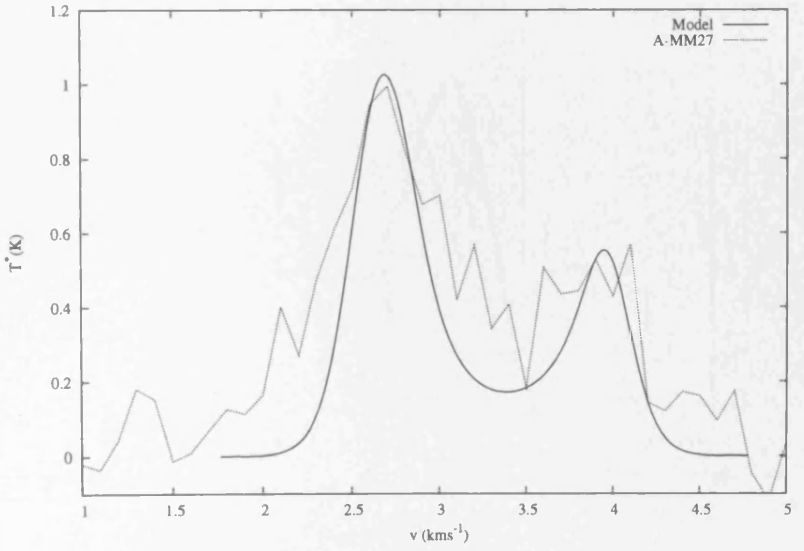

Figure 5.17: Comparison of HARP HCO^+ (J=4→3) data of A-MM27 with the model. Observations are shown as a dotted line, the model is shown as a solid line. See text for details.

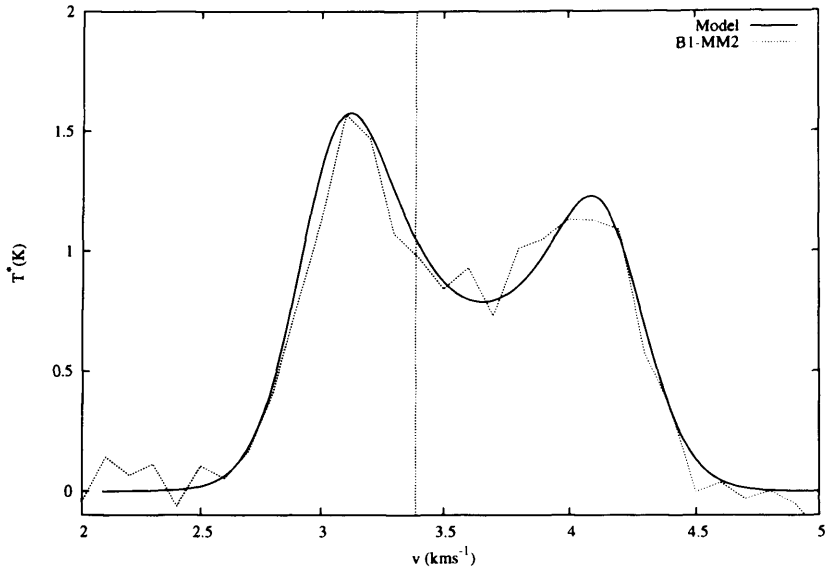

Figure 5.18: Comparison of HARP HCO^+ (J=4→3) data of B1-MM2 with the model. Observations are shown as a dotted line, the model is shown as a solid line. See text for details.

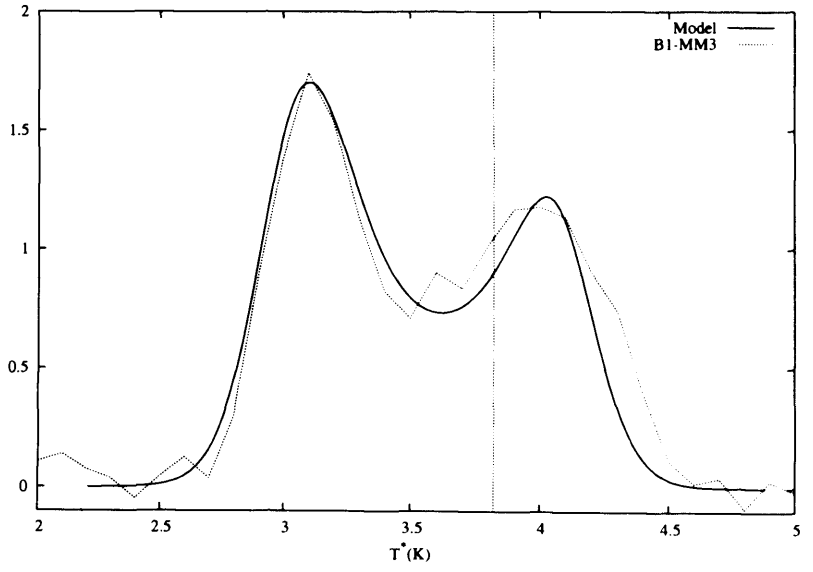

Figure 5.19: Comparison of HARP HCO^+ (J=4→3) data of B1-MM3 with the model. Observations are shown as a dotted line, the model is shown as a solid line. See text for details.

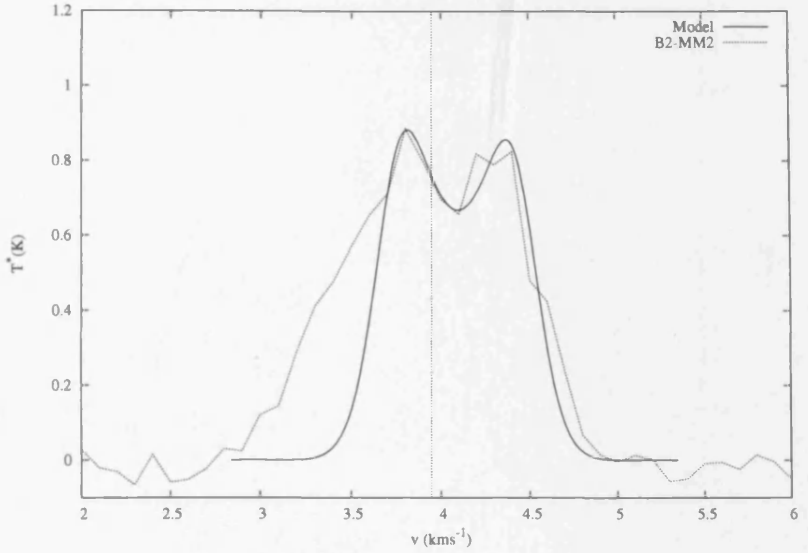

Figure 5.20: Comparison of HARP HCO^+ (J=4→3) data of B2-MM2 with the model. Observations are shown as a dotted line, the model is shown as a solid line. See text for details.

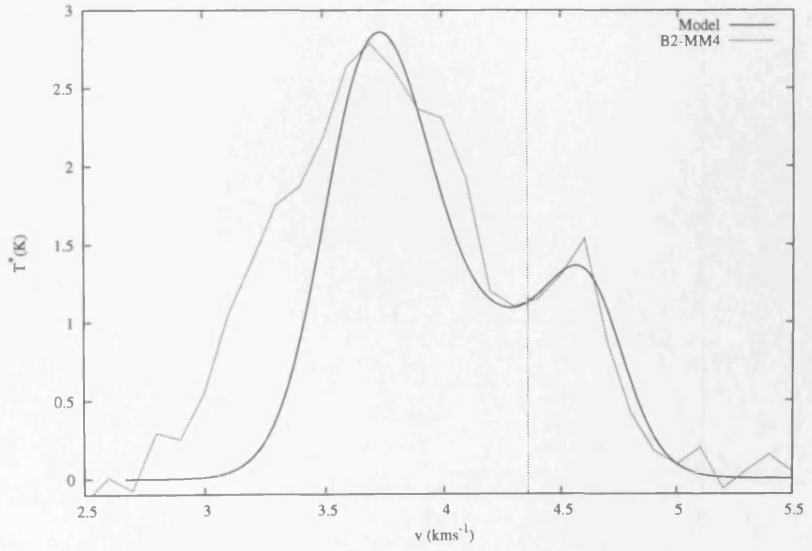

Figure 5.21: Comparison of HARP HCO^+ (J=4→3) data of B2-MM4 with the model. Observations are shown as a dotted line, the model is shown as a solid line. See text for details.

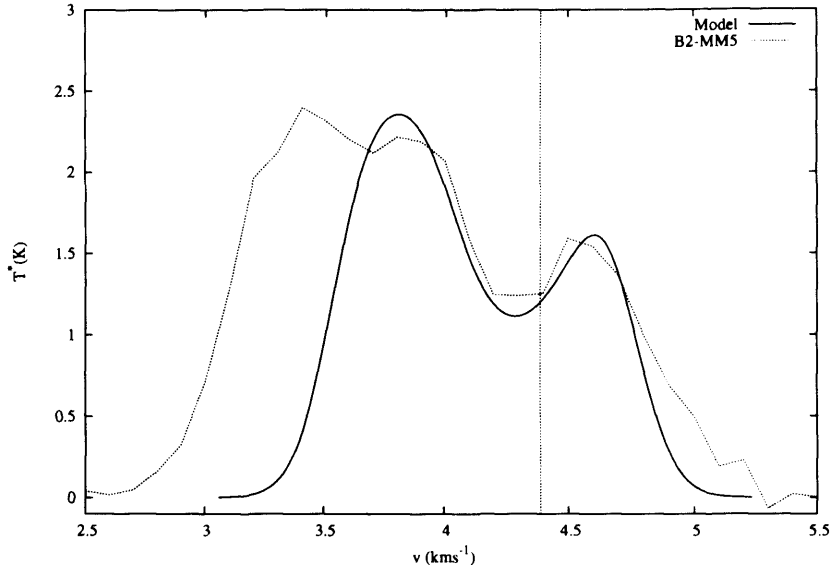

Figure 5.22: Comparison of HARP HCO^+ (J=4→3) data of B2-MM5 with the model. Observations are shown as a dotted line, the model is shown as a solid line. See text for details.

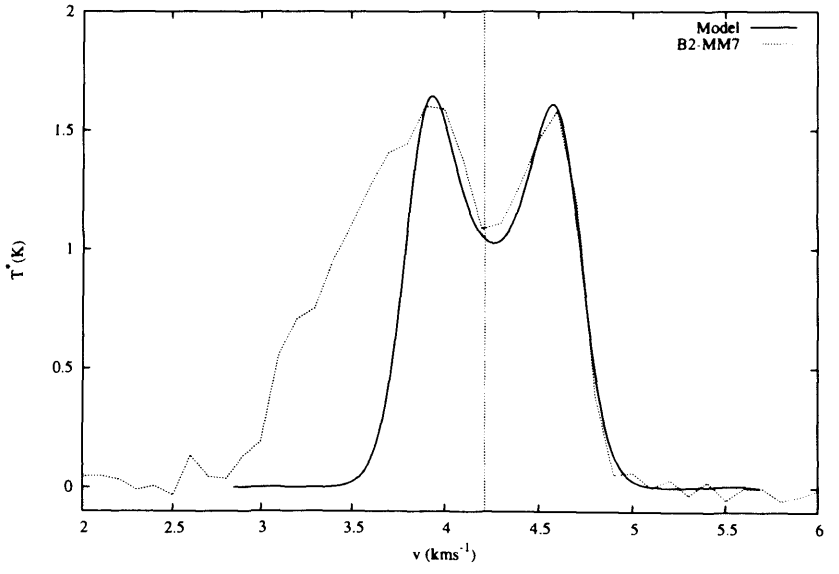

Figure 5.23: Comparison of HARP HCO^+ (J=4→3) data of B2-MM7 with the model. Observations are shown as a dotted line, the model is shown as a solid line. See text for details.

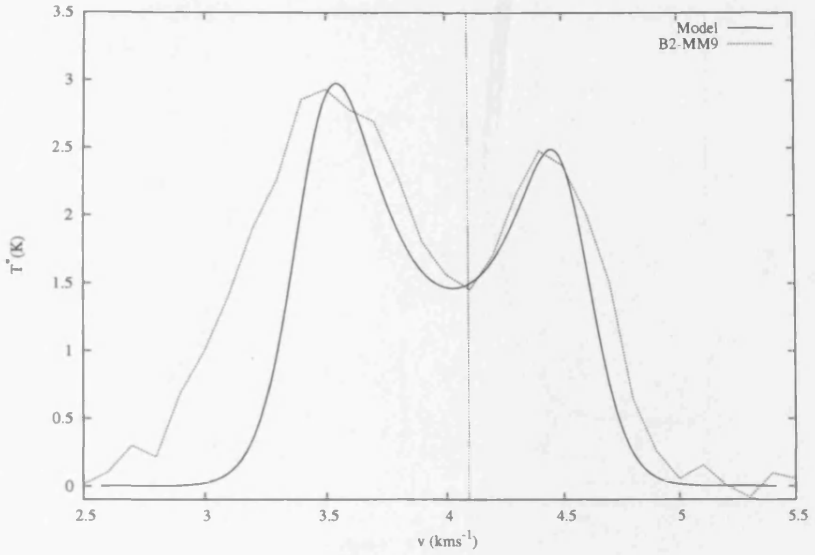

Figure 5.24: Comparison of HARP HCO^+ (J=4→3) data of B2-MM9 with the model. Observations are shown as a dotted line, the model is shown as a solid line. See text for details.

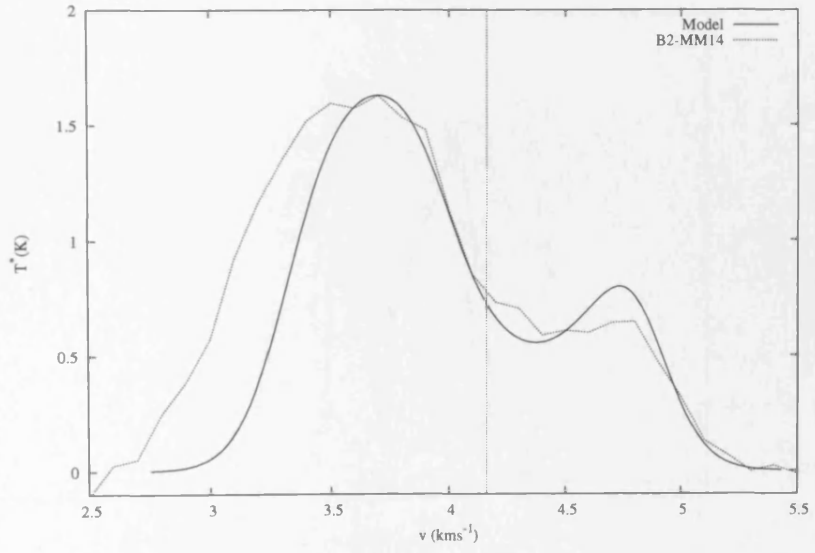

Figure 5.25: Comparison of HARP HCO^+ (J=4→3) data of B2-MM14 with the model. Observations are shown as a dotted line, the model is shown as a solid line. See text for details.

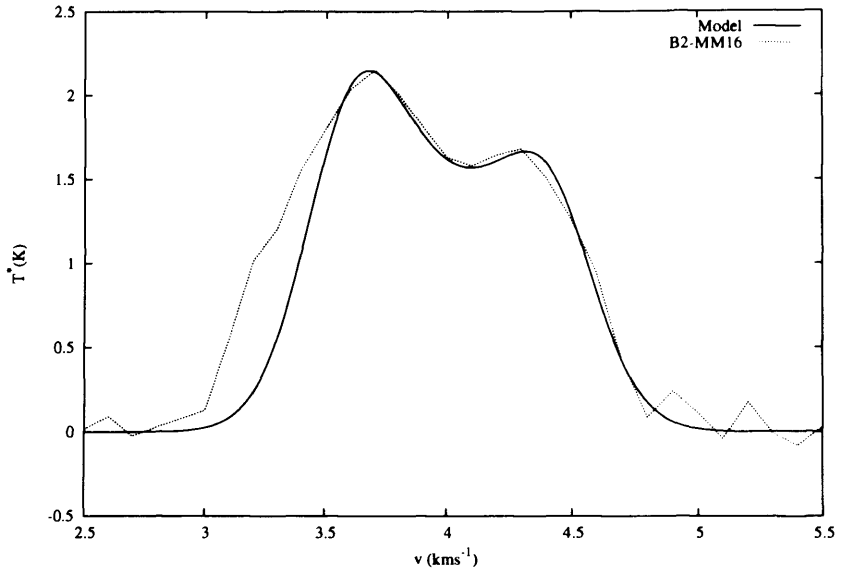

Figure 5.26: Comparison of HARP HCO^+ (J=4→3) data of B2-MM16 with the model. Observations are shown as a dotted line, the model is shown as a solid line. See text for details.

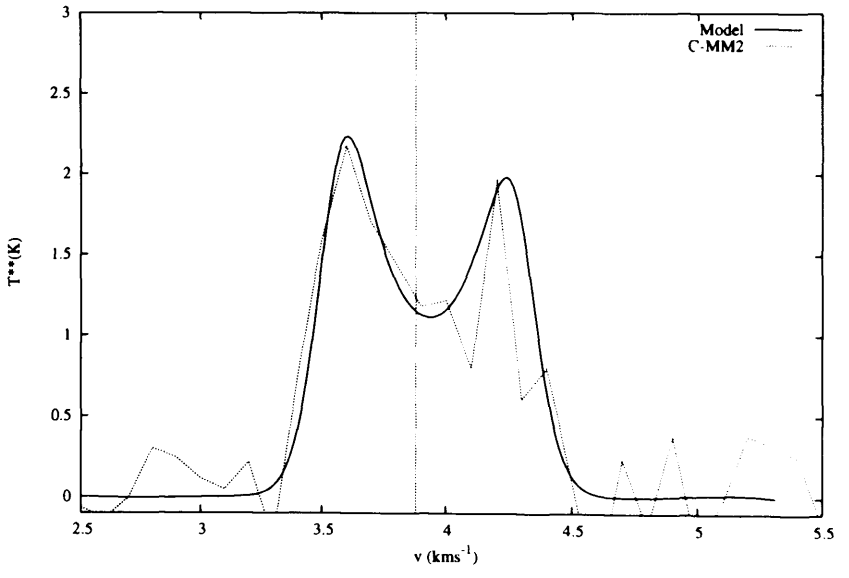

Figure 5.27: Comparison of HARP HCO^+ (J=4→3) data of C-MM2 with the model. Observations are shown as a dotted line, the model is shown as a solid line. See text for details.

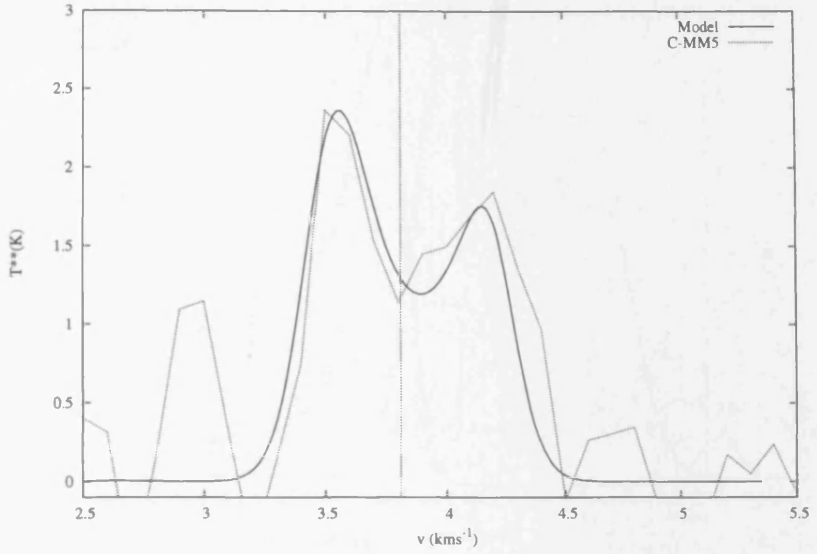

Figure 5.28: Comparison of HARP HCO^+ (J=4→3) data of C-MM5 with the model. Observations are shown as a dotted line, the model is shown as a solid line. See text for details.

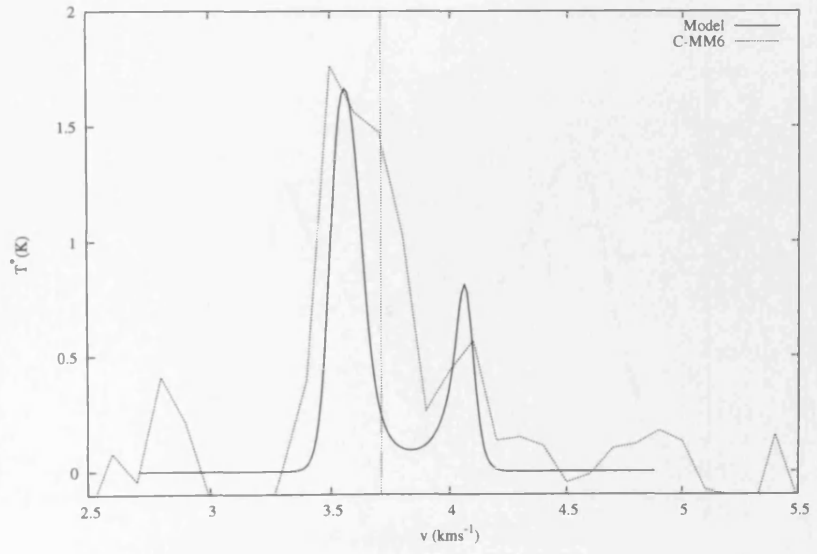

Figure 5.29: Comparison of HARP HCO^+ (J=4→3) data of C-MM6 with the model. Observations are shown as a dotted line, the model is shown as a solid line. See text for details.

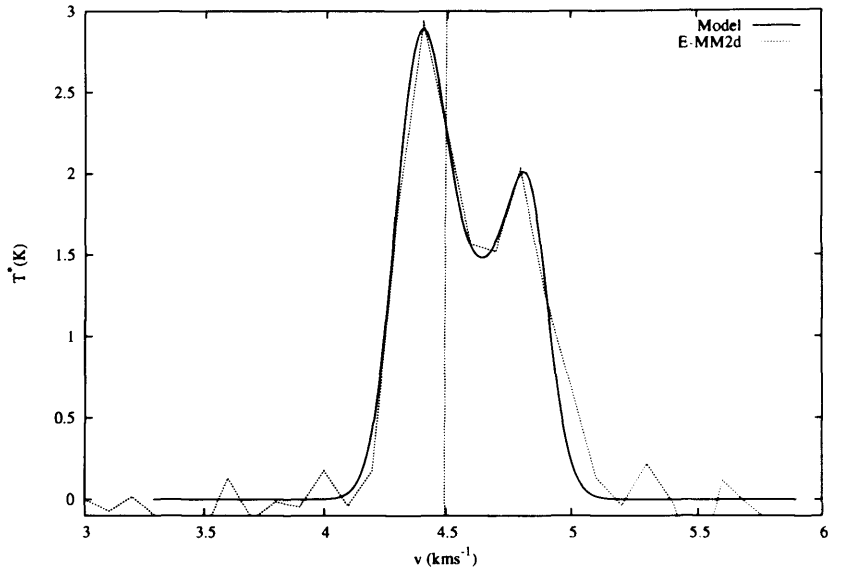

Figure 5.30: Comparison of HARP HCO^+ (J=4→3) data of E-MM2d with the model. Observations are shown as a dotted line, the model is shown as a solid line. See text for details.

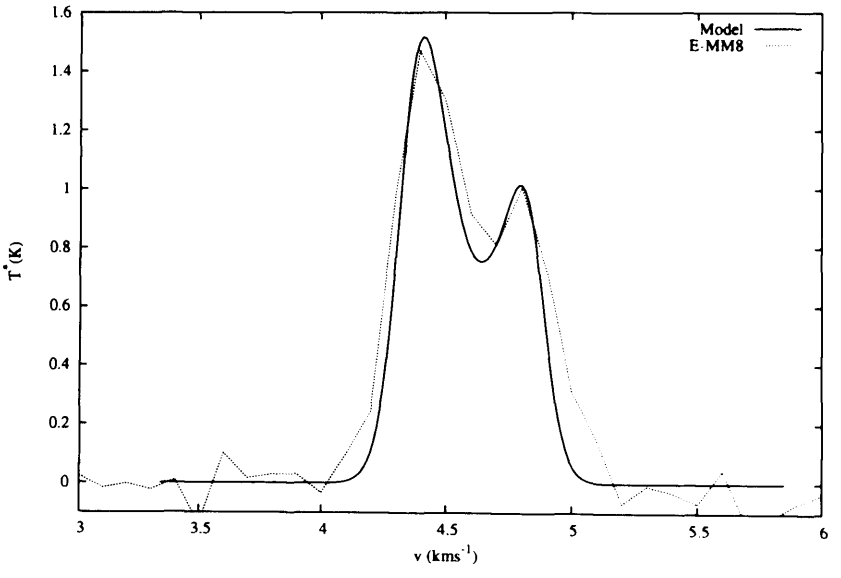

Figure 5.31: Comparison of HARP HCO^+ (J=4→3) data of E-MM8 with the model. Observations are shown as a dotted line, the model is shown as a solid line. See text for details.

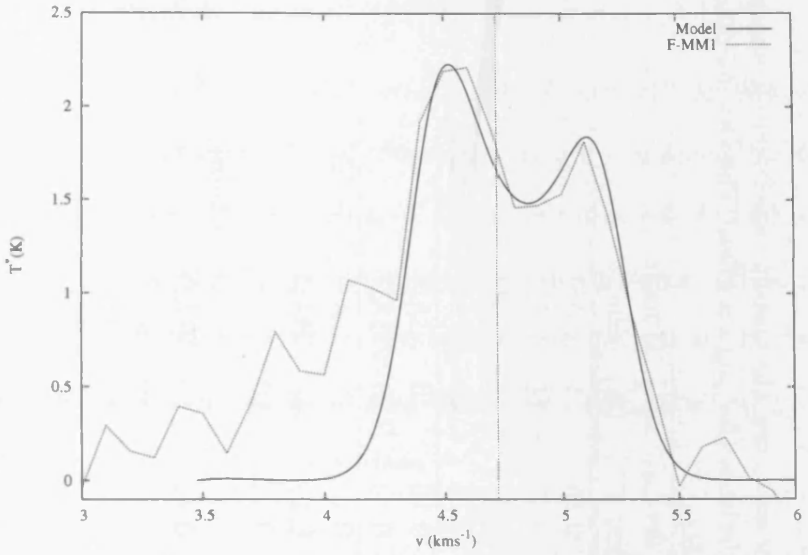

Figure 5.32: Comparison of HARP HCO^+ (J=4→3) data of F-MM1 with the model. Observations are shown as a dotted line, the model is shown as a solid line. See text for details.

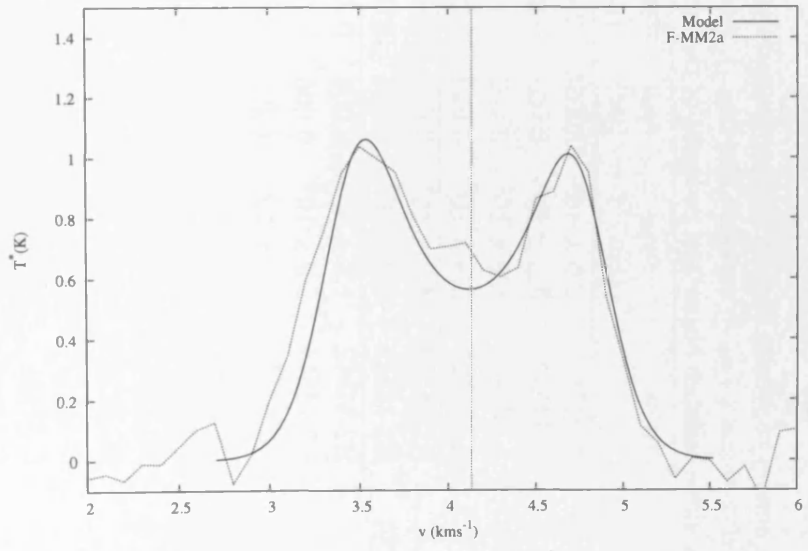

Figure 5.33: Comparison of HARP HCO^+ (J=4→3) data of F-MM2a with the model. Observations are shown as a dotted line, the model is shown as a solid line. See text for details.

Table 5.2: Summary of results of model fitting for cores in Figures 5.14 to 5.33. For each core, the best-fit model's initial central density (ρ_{flat}), central core size (r_{flat}), envelope size (r_{bdry}), viewing time (t_{view}) and turbulence (Δv_{turb}) are given. The viewing time is given both in years since collapse began and in terms of the freefall time of the system (t_{ff}).

Name	n_{flat} (cm^{-3})	r_{flat} (pc)	r_{bdry} (pc)	t_{view} (yrs)	t_{view} (t_{ff})	Δv_{turb} (km s^{-1})	T_0 (K)	Profile Shape
A-MM4	2.6 x 10^5	0.0035	0.01	107,315	1.8	0.15	11	BAD
A-MM7	3.5 x 10^5	0.004	0.015	97,632	1.9	0.17	11	BAD
A-MM23	1.2 x 10^5	0.002	0.022	105,389	1.2	0.07	11	BAD
A-MM27	3.5 x 10^5	0.013	0.025	71,940	1.4	0.15	11	BAD (Possible)
B1-MM2	4.0 x 10^5	0.005	0.015	86,520	1.8	0.15	10	BAD
B1-MM3	6.0 x 10^5	0.005	0.014	78,492	2.0	0.15	10	BAD
B2-MM2	1.0 x 10^5	0.006	0.015	38,453	0.4	0.14	10	BAD (Possible)
B2-MM4	7.0 x 10^5	0.003	0.006	98,104	2.7	0.14	10	BAD
B2-MM5	4.5 x 10^5	0.01	0.025	104,231	2.3	0.14	10	BAD
B2-MM7	2.0 x 10^5	0.005	0.02	13,595	0.2	0.12	10	BAD (Possible)
B2-MM9	4.0 x 10^5	0.004	0.019	76,907	1.6	0.14	10	BAD
B2-MM14	5.0 x 10^5	0.011	0.022	103,181	2.4	0.15	10	BAD
B2-MM16	4.0 x 10^5	0.005	0.012	110,553	2.3	0.16	10	BAD
C-MM2	1.9 x 10^5	0.003	0.01	115,560	1.6	0.1	10	BAD
C-MM5	6.0 x 10^5	0.003	0.01	90,226	2.3	0.09	10	BAD
C-MM6	2.0 x 10^5	0.015	0.03	61,179	0.9	0.06	10	BAD (Possible)
E-MM2d	2.7 x 10^5	0.005	0.015	122,860	2.1	0.07	10	BAD
E-MM8	1.0 x 10^5	0.007	0.015	182,653	1.9	0.07	10	BAD (Possible)
F-MM1	1.5 x 10^5	0.006	0.021	109,899	1.4	0.12	10	BAD
F-MM2a	3.5 x 10^5	0.005	0.02	25,693	0.5	0.2	10	BAD (Possible)

5.7.1 Summary

I have outlined the analytical model, created by Whitworth & Ward-Thompson (2001), describing the collapse of a starless core with a Plummer-like density profile. I have outlined how the inclusion of a simple radiative transfer code allows simulated spectral line profiles to be created for such cores. HCO^+ (J=3→2) spectral line observations, from three prestellar cores (Gregersen & Evans, 2000), are shown alongside best-fit models using this code. The parameters of these fits broadly match existing observational data.

I have also shown fits to 20 spectral line profiles from the HCO^+ (J=4→3) data outlined in Chapter 4. The best-fit parameters of these fits are shown in Table 5.2. In Chapter 6 I discuss the implications of these parameters, in the larger context of the evolution of the prestellar cores of Ophiuchus.

Chapter 6

Discussion

6.1 An Evolutionary Diagram for Prestellar Cores

The properties of the prestellar cores mapped in Chapters 3 and 4 are summarised in Table 4.2. They have been categorised based on their HCO^+ (J=4→3) spectral line profile shapes: cores with blue-asymmetric double-peaked profiles; cores with faint or only possible blue-asymmetric double-peaked profiles; cores with red-asymmetric double-peaked profiles; cores with single-peaked profiles and cores with unclear profile shapes. This can be used to begin to described their evolution.

Assuming that the prestellar cores are at a constant gas-kinetic temperature and are thermally supported (Johnstone et al., 2000, 2001; Kirk, Ward-Thompson, & André, 2007), they will have a radius-mass relationship determined by the external pressure on them. The exact solutions are given by Bonnor-Ebert spheres (Ebert, 1955; Bonnor, 1956). This is in contrast to the cloud at large, where densities are lower and turbulent motions are greater (Kirk et al., 2007).

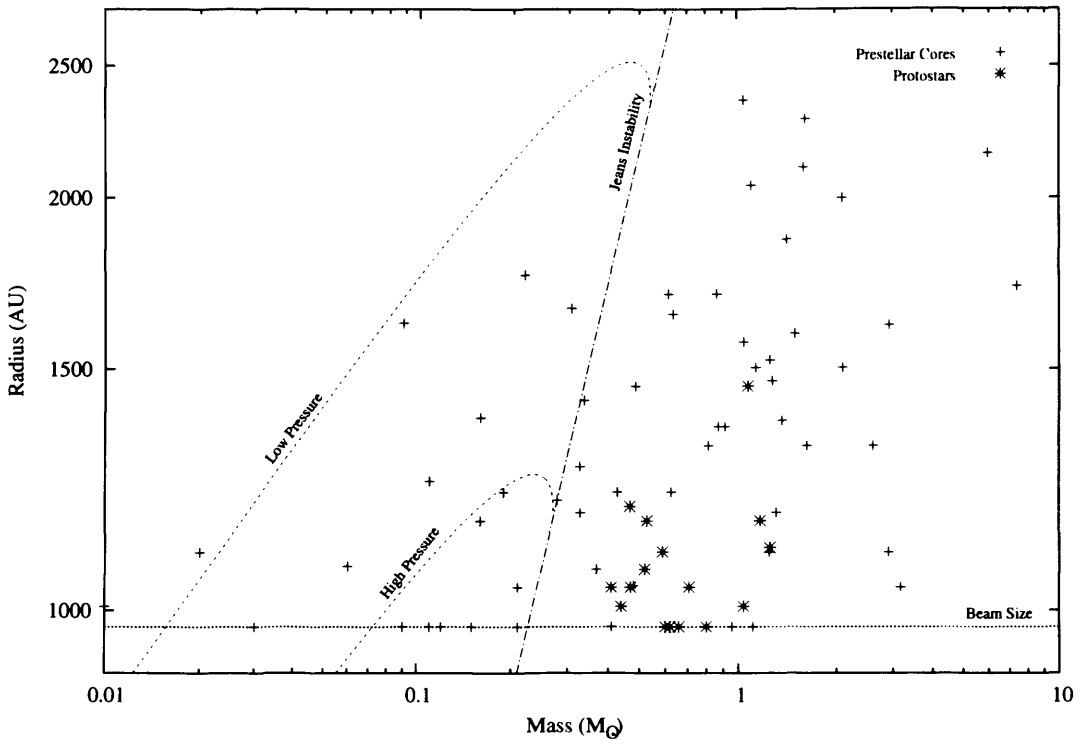

Figure 6.1: Prestellar and protostellar cores from Chapter 3 plotted in terms of radius against mass. Cold prestellar cores are indicated with crosses. Protostellar cores (i.e. cores with infrared associations) are marked with asterisks. See text for more details. For error bars, see Figure 6.2.

Assuming an approximately uniform and constant temperature for all the gas in the cloud allows us to calculate the Jeans Mass (Jeans, 1902). Below the Jeans Mass, the internal forces in the core are dominated by thermal pressure. When above the Jeans mass, the core becomes unstable and collapses under its own self-gravity.

Figure 6.1 shows the prestellar cores from Chapter 3 at 850μm with SCUBA, plotted in terms of radius versus mass (I define the radius of a core as the point at which its profile drops below the 3σ level of the SCUBA data – see Chapter 3). The crosses mark the prestellar cores.

The cores with associated infrared sources identified by Spitzer, as part of the

c2d survey (Enoch et al., 2008), are deemed to be protostellar and are marked with asterisks. I assume that these objects are Class 0 protostars (André et al., 1993), meaning that they have accreted less than half of their final mass. In order to account for the protostellar mass not detected by SCUBA, I use a mean IMF mass of $0.6M_{\odot}$ (Kroupa, 2002) and thus increase the masses of these objects by $0.3M_{\odot}$.

I propose the radius versus mass diagram shown in Figure 6.1 to be the equivalent of an HR diagram for prestellar cores. Cores evolve by accreting mass quasi-statically and maintaining Bonnor-Ebert equilibrium. Upon reaching the Jeans instability, cores collapse to form a protostar, moving downward on this diagram.

Protostellar cores lie beyond the Jeans limit, to the lower right on the graph, near the resolution limit of the observations. These cores have already accreted material and begun to collapse.

The hypothesis that this diagram illustrates the evolution of prestellar cores can be tested by looking at the position on this diagram occupied by collapsing prestellar cores. If this evolutionary picture is correct, then the blue-asymmetric double-peaked profiles should all lie on, or beyond, the Jeans instability.

Table 4.2 lists the masses and radii of those prestellar cores detected by SCUBA, which were also detected in HCO^+ (J=4→3) by HARP. Their profile shapes and positions are given. Figure 6.2 is the same as Figure 6.1 except that it shows only the cores listed in Table 4.2. This time they are plotted according to their spectral line profile shapes. Those cores with blue-asymmetric profiles, indicating collapse, are marked with dark boxes. Cores showing possible infall characteristics are marked with hollow boxes. All other cores are marked as crosses.

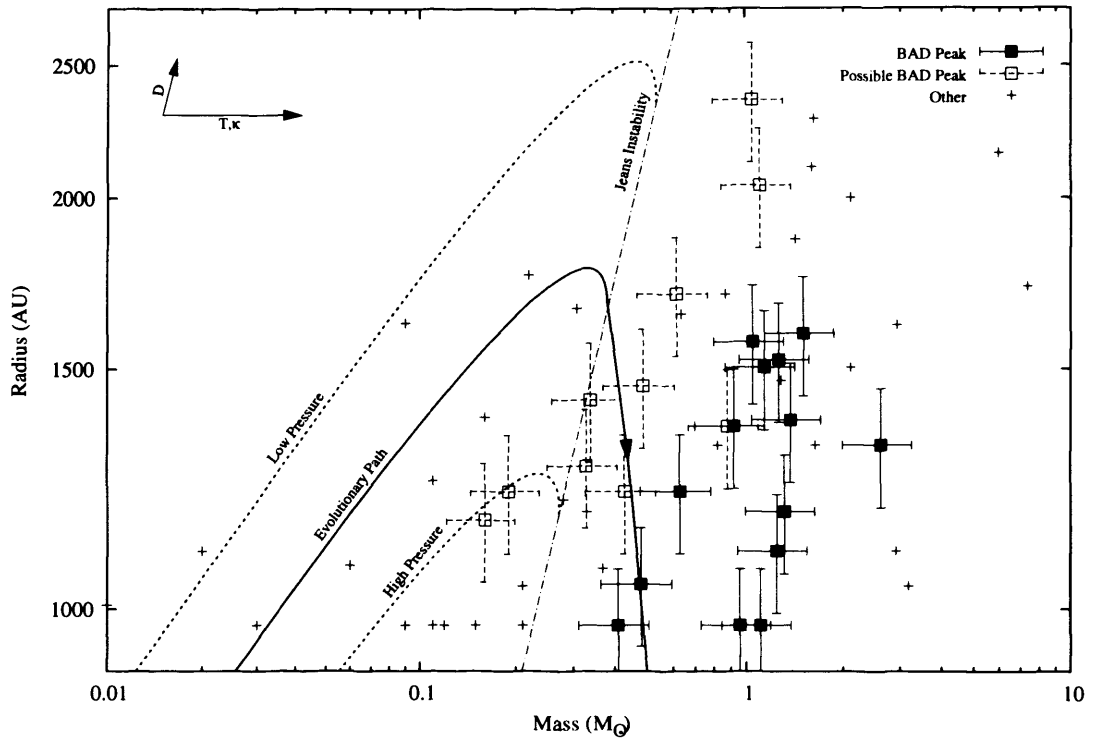

Figure 6.2: Same as Figure 6.1, excluding the protostellar cores. Prestellar cores showing definite blue-asymmetric double peaks in their spectral line profiles are shown as dark squares; cores with a possible blue-asymmetric double peak are shown as hollow squares; all other cores are shown as crosses. Error bars shown only for those cores where infall is detected. Systematic errors are shown in the top-left hand of the plot for distance to Ophiuchus, D, temperature of the cores, T and dust mass opacity, κ. I propose this as an evolutionary diagram for prestellar cores, and indicate the manner of this evolution with an arrow for a $\sim 0.5 M_{\odot}$ protostar.

Figure 6.2 displays mass and radius error bars for those cores showing infall characteristics in their profiles. The same errors could be shown for all the cores on the plot, however these have been omitted for clarity. Vectors in the top-left of the plot show the systematic errors for these data. Systematic errors consist of uncertainties in the distance to the cloud ($D = 139 \pm 6$ pc — Mamajek 2008); the dust mass opacity ($\kappa = 0.01 \pm 0.01$ cm^2 g^{-1} — Ossenkopf & Henning 1994; Motte et al. 1998); and the temperature, of the cores ($T = 10 \pm 5$ K — Motte et al. 1998; Johnstone et al. 2000; Stamatellos et al. 2007).

In Figures 6.1 and 6.2 the two dashed lines marked 'Low Pressure' and 'High Pressure' show the Bonnor-Ebert relations for external pressures of $P/k = 3 \times 10^6$ and 12×10^6 K cm^{-3} respectively (Johnstone et al., 2000; Jørgensen et al., 2008). The solid line in Figure 6.2 shows the proposed evolutionary track. This track initially follows a Bonnor-Ebert relation for an external pressure of $P/k = 6 \times 10^6$ K cm^{-3}. I assume a temperature for the cores in Ophiuchus of 10 K (Stamatellos et al., 2007).

The hypothesis that a radius-mass plot can serve as an evolutionary diagram for prestellar cores is supported by these results. In Figure 6.2, cores showing only weak signs of infall (hollow boxes) appear close to, or beyond, the Jeans mass line. Those cores that exhibit characteristic infall signatures (solid boxes) all appear beyond the Jeans mass line. This supports the conjecture that cores follow an evolutionary track in which they first move diagonally up the diagram, as they accrete material, and then move down it as they cross the Jeans mass limit and collapse.

Using this model, for any given prestellar core on this diagram, an approximate protostellar mass could be derived by following a Bonnor-Ebert track diagonally

upward to the Jeans mass line. From that point in the evolution, an efficiency for the collapse of the core needs to be assumed to reach an estimate of the final protostellar mass. If a core continues to accrete whilst collapsing, the gradient of its evolutionary track, after crossing the Jeans mass, will be shallow. If a core ceases to accrete after becoming Jeans unstable, the evolutionary track becomes vertical.

These data and, thus this evolutionary diagram, are subject to selection effects. Double-peaked infall profiles only occur for a narrow window of time during the evolution of prestellar cores. Although I find the location of such cores to be consistent with the proposed evolutionary diagram, I am only sensitive to pronounced, double-peaked profiles. Those cores shown on Figure 6.2 as crosses may simply have the wrong physical conditions to produce a detectable blue-asymmetric profile in HCO^+ (J=4$\rightarrow$3). There are likely to be infalling cores that lie beyond the scope of this study and the sensitivities of HARP.

Placing prestellar cores in the context of this evolutionary diagram shows how they can evolve into protostars inside molecular clouds. Future studies using instruments such as SCUBA-2 and Herschel may be able to probe further to the left on the diagram, and see how larger, lower-mass objects – such as CO cores – relate to the gravitationally bound prestellar cores already seen in the continuum. Such objects appear to follow different radius-mass relations to those explored in this study – see Figure 4 of Motte et al. (2001) and discussions by Johnstone et al. (2000, 2001).

6.2 Spectral Line Modelling

In Chapter 5, model fits were made to 20 of the HCO^+ (J=4→3) spectral line profiles described in Chapter 4. A summary of the parameters derived from these fits is given in Table 5.2. The locations of the 20 modelled cores are shown in Figure 6.3, on the RGB map originally shown as Figure 4.3.

6.2.1 Comparison with Observations

The model fits were shown in Section 5.7. The modelled spectral line profiles are, in general, very good approximations to the observational data. Notable exceptions to this are cores A-MM27 (Fig 5.17), B2-MM14 (Fig 5.25) and C-MM6 (Fig 5.29). The HARP spectrum of the centre of A-MM27 is very noisy and this makes the fit difficult. B2-MM14 (Fig 5.25) and C-MM6 (Fig 5.29) are both examples of the possible limit of the use of my model. They both present highly asymmetric profiles, which mean they are constrained to models of highly centrally condensed, high-density cores. The low signal-to-noise in the C-MM6 data is also difficult to fit.

All seven of the modelled cores from the Oph-B2 region show an extended blue-shifted wing, where the data cannot be modelled. This is not seen in the other cores, including the spectra from the neighbouring Oph-B1 region. This blue-shifted wing could be caused by some systematic bulk motion in the Oph-B2 region of L1688. The seven Oph-B2 cores can be seen in Figure 6.3, sitting along the middle axis of the region. A streamer of blue emission (2.0–3.0 kms^{-1}) is seen extending upward from the northern edge of the region. This may be related to the wings seen in the Oph-B2 spectra.

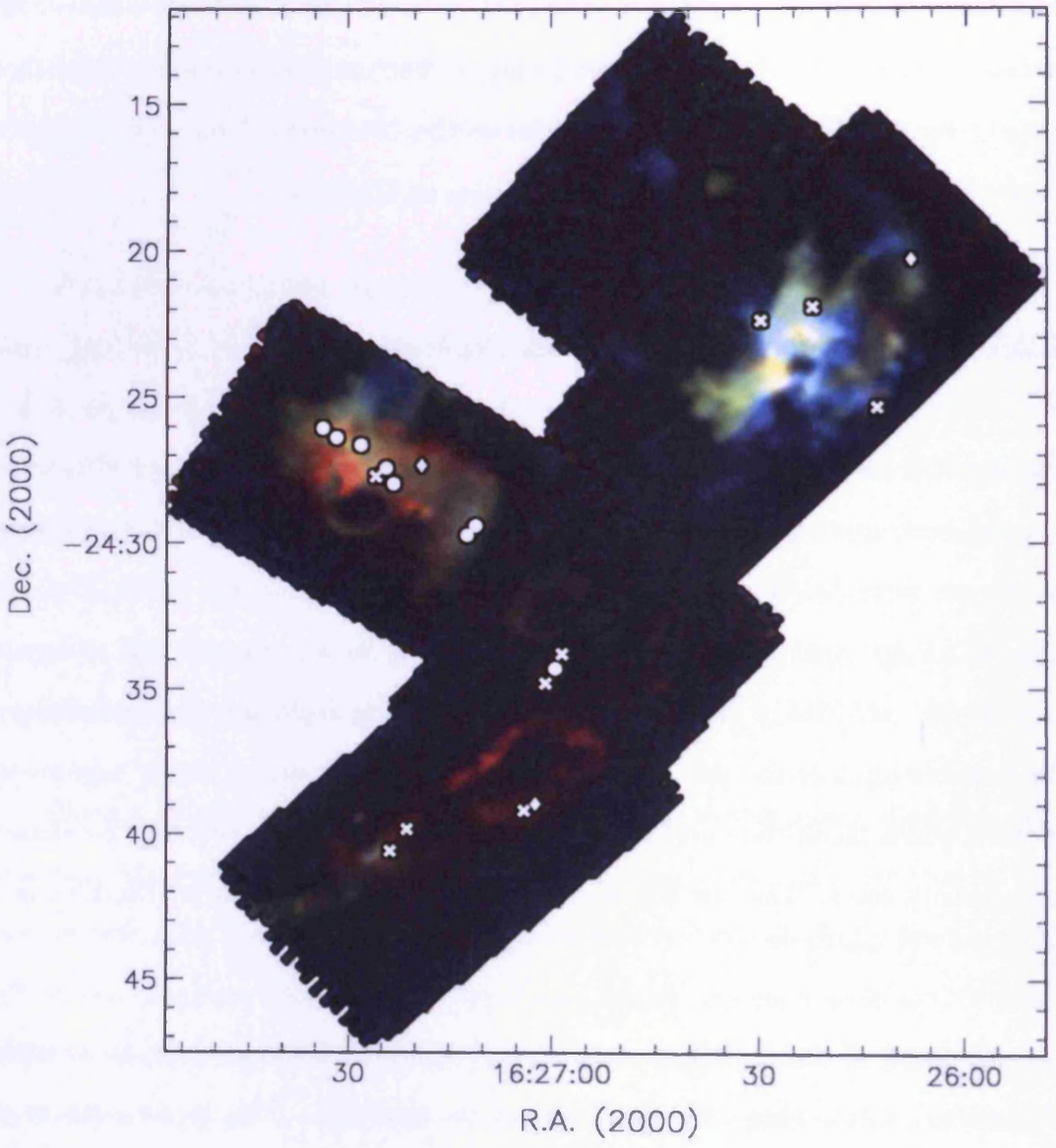

Figure 6.3: False colour image of HCO^+ (J=4→3) toward L1688 in red (4.0–5.0 kms^{-1}), green (3.0–4.0 kms^{-1}) and blue (2.0–3.0 kms^{-1}) velocity channels. The 20 modelled, collapsing cores are marked, indicating their modelled central core density, ρ_{flat}. Circles show $\rho_{flat} \geq 4.0 \times 10^5 cm^{-3}$. Crosses show $4.0 \times 10^5 cm^{-3} > \rho_{flat} > 1.0 \times 10^5 cm^{-3}$. Diamonds show $\rho_{flat} \leq 1.0 \times 10^5 cm^{-3}$.

6.2.2 Statistical Results

The model can only create meaningful spectral line profiles for cores which exhibit signs of infall in the form of an asymmetric peak. For this reason all my model fits give parameters either for collapsing prestellar cores, or for very early stage Class 0 protostars.

Some statistics can be extrapolated from the 20 modelled cores. There is a weak correlation (coefficient = 0.2) between turbulence in the core and the ratio of the inner, flat region to the total extent of the core (r_{flat}/r_{bdry}). This shows that greater turbulence leads to less centrally condense cores. This is to be expected. Greater turbulence means that material cannot coalesce easily into the centre of the core.

The modelled central density, ρ_{flat}, of the cores is shown, alongside their location in the cloud, in Figure 6.3. Seven of the eight most dense cores are in the Oph-B region. There are nine cores in Oph-B in total. All the model parameters are fits to the initial conditions of collapse, which means that this is not an age-related effect, but rather a property of the Oph-B region itself. Across the rest of L1688 no specific relationship between region and core density is seen. Figure 3.1 shows that Oph-A is the most dense region, with the highest 850μm continuum emission. The higher core densities in Oph-B could be a result of the lack of any evolved objects, such as SMM-1 and VLA1623. In Oph-A these bright, energetic cores could be disrupting the local environment and preventing high-density cores from forming.

There is an order of magnitude in age between the youngest core, B2-MM7 ($t_{view} \simeq 1.4 \times 10^4$ years), and the oldest core, E-MM8 ($t_{view} \simeq 1.8 \times 10^5$ years).

Table 6.1: Average core ages, in units of years and freefall times (t_{ff}), and number of standard deviations, σ, from the mean age, for different regions of L1688. Also shown are the fractions of collapsing cores, and protostellar infrared cores, in each region as a fraction of the whole population (see Table 3.3).

Region	Average Age (kyrs)	Average Age (t_{ff})	σ	Collapse Fraction	IR Fraction
Oph-A	96	1.6	0.15	11%	17%
Oph-B	79	1.7	0.30	33%	14%
Oph-C	87	1.5	0.08	30%	10%
Oph-E-F	112	1.6	0.60	20%	43%
All	90	1.6		21%	22%

Grouping L1688 into the regions described in Chapters 3 and 4, we can determine average core ages for different parts of the whole cloud. These average ages are given in Table 6.1.

6.3 Timeline for L1688

Tables 6.1 and 5.2, along with the data obtained in Chapters 3 and 4, allow an emerging picture of the L1688 cloud to be seen. This picture gives an approximate outline for the way star formation is proceeding in this cloud.

The cores in the southern, Oph-E and Oph-F regions began to collapse first, more than 100,000 years ago. Several early-stage protostars have since formed there, leading to a relative over-population of infrared sources in the regions. Oph-A followed, beginning collapse approximately 20,000 years later. Oph-A is also the densest part of the L1688 complex. Oph-B and Oph-C are the most recent clouds to collapse, as indicated by their relative lack of protostellar candidates and high fraction of collapsing cores.

As a whole, the population of infalling cores represent a full range of post-

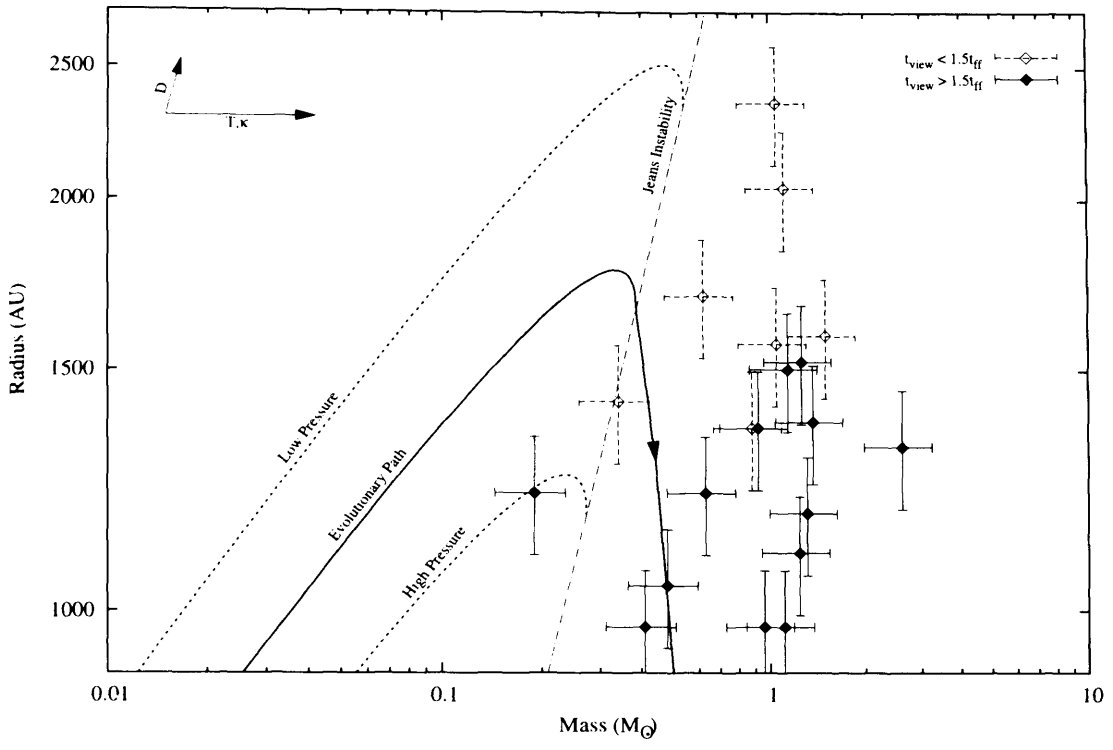

Figure 6.4: Same as Figure 6.2 but here only the 20 modelled HARP cores are plotted. Cores shown as white diamonds are those modelled as being viewed at less than $1.5t_{ff}$. Cores shown as black diamonds are those modelled as being viewed at greater than $1.5t_{ff}$. See text for more details.

collapse evolutionary states. The range of observed freefall timescales means that whilst some cores have only just begun to collapse, others are well on their way to forming protostars — many may even have deeply embedded early Class 0 objects at their centres.

In Figure 6.4 the 20 modelled cores have been placed onto the evolutionary diagram outlined in Section 6.1. Since these 20 cores are all collapsing, they appear beyond the Jeans instability on this radius-mass plot. The exception is the core E-MM8, which lies on the 'High Pressure' Bonnor-Ebert line, just before the Jeans instability. The cores have been divided into two types: those modelled as being viewed at less than $1.5t_{ff}$ and those which are older. The less-evolved cores are shown as white diamonds and the more-evolved cores are shown as black diamonds.

A clear distinction is seen between the two groups, showing cores that have had less time to collapse as being nearer to the point where collapse begins on this diagram, the Jeans instability.

This result shows that the evolutionary diagram hypothesis and the Plummer-like collapse model are consistent. The radiative transfer code used to model the spectral line profiles of the cores is simplistic. It is not a Λ-iteration code, but rather a simpler, non-iterative code, designed to run quickly (typically it takes ~2 seconds to generate one profile). This result, and the analysis in Chapter 5, show that this code can be a useful tool in guiding the understanding of prestellar cores and in determining trends in their evolution. Any one of the predictions could have been proved wrong by the observations or the modelling. However, all have come together and built up a consistent picture.

6.4 Summary

In this chapter I have discussed the evolution of the prestellar cores observed by HARP, as outlined in Chapters 4 and 5. The SCUBA data from Chapter 3 are used to place these cores in the context of the cloud at large, and within the sub-regions of L1688.

I have proposed an evolutionary diagram for prestellar cores in the form of a radius-mass plot. I hypothesise that a core is formed in the low-mass, low-radius region of the plot. It then accretes quasi-statically, increasing in both mass and radius. When it crosses the limit of gravitational instability it begins to collapse, decreasing in radius, towards the region of the diagram where protostellar cores are seen. This hypothesis is supported by the spectral line profiles measured using

HARP. Those cores displaying infall characteristics in their spectra appear on, or beyond, the Jeans instability on the radius-mass plot.

The modelled initial parameters fitted from the spectra of the 20 collapsing cores in Chapter 5 are discussed. These fits allow some statistical relationships to be examined in the population of collapsing cores in L1688. In conjunction with data from Chapters 3 and 4, these fits also allow the average ages of the regions of the L1688 cloud to be deduced and a potential timeline for the cloud to be established for the first time.

The ages of the modelled cores, in terms of their freefall timescales, are also outlined in this chapter. The cores are placed onto the proposed evolutionary diagram and are consistent with the proposed evolutionary track.

Chapter 7

Conclusions and Future Work

7.1 Conclusions

In this thesis I have presented an observational study of star formation. Star formation is a fundamental process at work in the Universe. It is not only a complex field in its own right, but it also has implications for many other aspects of astronomy.

In Chapter 1, I discussed our current understanding of the star formation process. The measured physical properties of molecular clouds, prestellar cores and protostars were outlined. I explained the basics of current models of cloud collapse and support. The universal stellar IMF and observed CMFs were outlined, along with the possible relation between them.

In Chapter 2, I reviewed the telescope and instruments used to obtain the data described in this thesis. The techniques and tools used to reduce those data were outlined in detail for both HARP and SCUBA. The atmosphere at the telescope,

and the strategies used to minimise its effect, were discussed.

In Chapter 3, I re-analysed the SCUBA archive data for L1688, incorporating all available scan-map and jiggle-map data. An updated form of the CMF in the L1688 cloud complex was presented using updated values for the distance to this region as well as new estimates for the temperatures of the cores.

I showed that the CMF for L1688 is consistent with a three part power-law fit with slopes the same as seen in the stellar IMF. The higher-mass end of the CMF declines as a power law, which is consistent with other studies of L1688 (MAN98; Johnstone et al., 2000; Stanke et al., 2006), as well as with studies of Orion (Nutter & Ward-Thompson, 2007; Motte et al., 2001; Johnstone et al., 2001, 2006).

The results are mostly in agreement with those found in earlier studies. But the deeper maps allowed the discovery of a turnover in the CMF at $0.3M_{\odot}$, which shows that the core mass function appears to mimic the stellar initial mass function. This agreement is indicative that the stellar IMF is determined at the prestellar core stage. It was shown that the relation between the CMF and IMF is not necessarily a simple 1:1 translation in the mass axis.

In Chapter 4, I presented HCO^+ (J=4$\rightarrow$3) spectral line observations from HARP on the JCMT. Data were presented for 59 of the prestellar cores mapped in Chapter 3. These cores were categorised according to their spectral line profile shapes and this was the basis for the analysis performed in Chapter 6.

In Chapter 5, I outlined the analytical model, created by Whitworth & Ward-Thompson (2001), describing the collapse of a starless core with a Plummer-like density profile. I explained how my addition of a radiative transfer code allows simulated spectral line profiles to be created for such cores. HCO^+ (J=3$\rightarrow$2)

spectral line observations from three prestellar cores (Gregersen & Evans, 2000), are shown alongside best-fit models using this code. The parameters of these fits broadly match existing observational data.

Chapter 5 also showed fits to 20 spectral line profiles from the HCO^+ (J=4→3) data outlined in Chapter 4. The best-fit parameters of these fits were used in the analysis in Chapter 6.

In Chapter 6, I outlined a proposed evolutionary diagram for prestellar cores in the form of a radius-mass plot. I hypothesised that a core is formed in the low-mass, low-radius region of the plot. It then accretes quasi-statically, increasing in both mass and radius. When it crosses the limit of gravitational instability it begins to collapse, decreasing in radius, towards the region of the diagram where protostellar cores are seen. This hypothesis was supported by the spectral line profiles measured using HARP.

The initial parameters resulting from fits to the 20 modelled spectra in Chapter 5 were also discussed. The 20 modelled cores were placed onto the proposed evolutionary diagram and were found to be consistent with the established evolutionary track. In conjunction with data from Chapters 3 and 4, these fits allowed a potential timeline for the L1688 cloud to be established for the first time.

Thus, all of the predictions of the evolutionary diagram were borne out by the observations and the modelling.

7.2 Future Work

The fact that my new CMF for L1688 is consistent with a three part power-law, the same as is seen in the stellar IMF, indicates that the IMF has its origins in the prestellar phase. This suggests that a star's final mass is determined by the fragmentation of a cloud, alongside some efficiency factor.

The spectral line model I have outlined in this thesis is based on a simplistic radiative transfer code. Future work would entail the addition of a Λ-iteration-style loop to my model. This would help to account for the radiation being emitted and absorbed between different parts of the collapsing core, which in turn could change the resultant simulated spectral lines. The compromise introduced by such a change would be a huge increase in the time taken to run the code. New server-based, cloud computing may hold the key to allowing this overhead to be reduced without the need for more high-performance computing facilities.

The combination of continuum mapping, spectral line observing and a simple computer model, allowed me to explore the evolutionary states of the prestellar cores of Ophicuhus. I was also able to outline a possible timeline for the L1688 region. Archive data exist for other, similar star formation regions, such as Serpens. This work could be repeated for these regions and the results compared.

At the time this thesis was being completed, SCUBA's successor, SCUBA-2, was performing its first science observations at the JCMT, during its shared-risk observing period. Less than a year earlier, Herschel was launched and began returning data. These new facilities will provide a plethora of data for star formation research in the coming years.

These data will be of unprecedented quality, and resolution, in the field of submillimetre astronomy. They will allow work, such as that performed for this thesis, to be taken much further. The solutions to many of the problems of star formation will perhaps be found, and many new questions will no doubt be raised.

Appendix A

Refereed Publications at 1^{st} February 2010

1. White G. J., et al., (34 co-authors, including **Simpson R. J.**), 2010, MNRAS, in prep, 'The JCMT legacy survey of the Gould Belt: a first look at Ophiuchus with HARP'

2. **Simpson R. J.,** Johnstone D., Nutter D., Ward-Thompson D., 2010, submitted, 'The initial conditions of isolated star formation – X. An evolutionary diagram for pre-stellar cores'

3. Graves S. F., et al., (34 co-authors, including **Simpson R. J.**), 2010, MNRAS, submitted, 'The JCMT legacy survey of the Gould Belt: a first look at Serpens with HARP'

4. Davis C. J., et al., (32 co-authors, including **Simpson R. J.**), 2010, MNRAS, in press, 'The JCMT legacy survey of the Gould Belt: a first look at Taurus with HARP', arXiv:1002.2020

5. Buckle J. V., et al., (32 co-authors, including **Simpson R. J.**), 2010, MNRAS, 401, 204, 'The JCMT legacy survey of the Gould Belt: a first look at Orion B with HARP'

6. **Simpson R. J.,** Nutter D. J., Ward-Thompson D., 2008, MNRAS, 391, 205, 'The initial conditions of star formation VIII: an observational study of the Ophiuchus cloud L1688 and implications for the prestellar core mass function'

7. Ward-Thompson D., et al., (61 co-authors, including **Simpson R. J.**), 2007, PASP, 119, 855, 'The James Clerk Maxwell Telescope legacy survey of nearby star-forming regions in the Gould Belt'

Appendix B

Cumulative Mass Function

If a mass function can be approximated to a power law, then the number of cores in the interval $\log M$ to $\log M + \mathrm{d}\log M$ is given by:

$$\frac{\mathrm{d}N}{\mathrm{d}\log M}\mathrm{d}\log M = kM^x \,\mathrm{d}\log M, \tag{B.1}$$

where k is a constant. Integrating Equation B.1 between $\log M$ and $\log M_{max}$ will give the number of stars with mass greater than M.

$$N(>M) = \int_{\log M}^{\log M_{max}} kM^x \mathrm{d}\log M. \tag{B.2}$$

Using the substituting $\mathrm{d}M/M = \mathrm{d}\log M$:

$$N(>M) = \int_{M}^{M_{max}} kM^x \frac{\mathrm{d}M}{M} = \int_{M}^{M_{max}} kM^{x-1}\mathrm{d}M. \tag{B.3}$$

Integrating this yields:

$$N(>M) = \left[\frac{kM^x}{x}\right]_{M}^{M_{max}} = \frac{k}{x}\left\{M_{max}^x - M^x\right\} \tag{B.4}$$

For negative values of x, the M_{max} term in Equation B.4 is negligible except when M approaches M_{max}.

Appendix C

Convolution theory

Two functions $f(t)$ and $g(t)$, have Fourier transforms ($\mathcal{FT}$) $F(\nu)$ and $G(\nu)$, given by:

$$F(\nu) = \mathcal{F}[f(t)](\nu) \int_{-\infty}^{\infty} f(t) e^{-2\pi i \nu t} \mathrm{d}t, \tag{C.1}$$

$$G(\nu) = \mathcal{F}[g(t)](\nu) \int_{-\infty}^{\infty} g(t) e^{-2\pi i \nu t} \mathrm{d}t. \tag{C.2}$$

The convolution, or degree of overlap of these functions is given by:

$$\begin{aligned}
f(t) \otimes g(t) &= \int_{-\infty}^{\infty} g(\tau) f(t-\tau) \mathrm{d}\tau, && \text{(C.3)} \\
&= \int_{-\infty}^{\infty} g(\tau) \left[\int_{-\infty}^{\infty} F(\nu) e^{2\pi i \nu (t-\tau)} \mathrm{d}\nu \right] \mathrm{d}\tau, && \text{(C.4)} \\
&= \int_{-\infty}^{\infty} g(\tau) \left[\int_{-\infty}^{\infty} F(\nu) e^{2\pi i \nu t} e^{-2\pi i \nu \tau} \mathrm{d}\nu \right] \mathrm{d}\tau, && \text{(C.5)} \\
&= \int_{-\infty}^{\infty} F(\nu) \left[\int_{-\infty}^{\infty} g(\tau) e^{-2\pi i \nu \tau} \mathrm{d}\tau \right] e^{2\pi i \nu t} \mathrm{d}\nu, && \text{(C.6)} \\
&= \int_{-\infty}^{\infty} F(\nu) G(\nu) e^{2\pi i \nu t} \mathrm{d}\nu, && \text{(C.7)} \\
&= \mathcal{F}^{-1}[F(\nu) G(\nu)]. && \text{(C.8)}
\end{aligned}$$

Taking the $\mathcal{FT}$ of both sides:

$$\mathcal{F}[f(t) \otimes g(t)] = F(\nu)\ G(\nu) = \mathcal{F}[f(t)]\ \mathcal{F}[g(t)], \tag{C.9}$$

we find that the $\mathcal{FT}$ of a convolution of two functions is equal to the product of the $\mathcal{FT}$s of the two functions.

Bibliography

Alves J. F., Lada C. J., Lada E. A., Internal structure of a cold dark molecular cloud inferred from the extinction of background starlight, 2001, Nature, 409, 159

Ambartsumian V. A., On the Problem of the Mechanism of the Origin of Stars in Stellar Associations, 1958, Reviews of Modern Physics, 30, 944

André P., Belloche A., Motte F., Peretto N., The initial conditions of star formation in the Ophiuchus main cloud: Kinematics of the protocluster condensations, 2007, A&A, 472, 519

André P., Deeney B. D., Phillips R. B., Lestrade J.-F., VLBI survey of Rho Ophiuchi - A population of magnetized, diskless young stellar objects, 1992, ApJ, 401, 667

André P., Montmerle T., From T Tauri stars to protostars: Circumstellar material and young stellar objects in the rho Ophiuchi cloud, 1994, ApJ, 420, 837

André P., Ward-Thompson D., Barsony M., Submillimeter continuum observations of Rho Ophiuchi A - The candidate protostar VLA 1623 and prestellar clumps, 1993, ApJ, 406, 122

André P., Ward-Thompson D., Barsony M., From Prestellar Cores to Protostars: the Initial Conditions of Star Formation, 2000, Protostars and Planets IV, Univ. Arizona Press, Tucson, 59

André P., Ward-Thompson D., Motte F., Probing the initial conditions of star formation: the structure of the prestellar core L 1689B., 1996, A&A, 314, 625

Archibald E. N., Jenness T., Holland W. S., Coulson I. M., Jessop N. E., Stevens J. A., Robson E. I., Tilanus R. P. J., Duncan W., Lightfoot J. F., On the atmospheric limitations of ground-based submillimetre astronomy using array receivers, 2002, MNRAS, 336, 1

Bachiller R., Bipolar Molecular Outflows from Young Stars and Protostars, 1996, Annual Review of Astronomy and Astrophysics, 34, 111

Bacmann A., André P., Puget J.-L., Abergel A., Bontemps S., Ward-Thompson D., An ISOCAM absorption survey of the structure of pre-stellar cloud cores, 2000, A&A, 361, 555

Ballesteros-Paredes J., Klessen R. S., Vázquez-Semadeni E., Dynamic Cores in Hydrostatic Disguise, 2003, ApJ, 592, 188

Barger A. J., Cowie L. L., Sanders D. B., Fulton E., Taniguchi Y., Sato Y., Kawara K., Okuda H., Submillimetre-wavelength detection of dusty star-forming galaxies at high redshift, 1998, Nature, 394, 248

Barsony M., Kenyon S. J., Lada E. A., Teuben P. J., A Near-Infrared Imaging Survey of the rho Ophiuchi Cloud Core, 1997, ApJS, 112, 109

Beichman C. A., Myers P. C., Emerson J. P., Harris S., Mathieu R., Benson P. J., Jennings R. E., Candidate solar-type protostars in nearby molecular cloud cores, 1986, ApJ, 307, 337

Berry D. S., CUPID User Manual, 2009, Starlink User Note 255.1, 1

Bonnell I. A., Bate M. R., Clarke C. J., Pringle J. E., Competitive accretion in embedded stellar clusters, 2001, MNRAS, 323, 785

Bonnor W. B., Boyle's Law and gravitational instability, 1956, MNRAS, 116, 351

Bontemps S., André P., Terebey S., Cabrit S., Evolution of outflow activity around low-mass embedded young stellar objects, 1996, A&A, 311, 858

Bouguer P., Essai d'Optique sur la gradation de la Lumiere, 1729, Paris

Buckle J. V. et al., HARP/ACSIS: a submillimetre spectral imaging system on the James Clerk Maxwell Telescope, 2009, MNRAS, 399, 1026

Chabrier G., The Galactic Disk Mass Budget. I. Stellar Mass Function and Density, 2001, ApJ, 554, 1274

Chabrier G., Galactic Stellar and Substellar Initial Mass Function, 2003, PASP, 115, 763

Chini R., Multicolour photometry of stars in the Ophiuchus dark cloud region, 1981, A&A, 99, 346

Cieza L. A., Padgett D. L., Stapelfeldt K. R., Augereau J.-C., Harvey P. M., Evans N. J., Merín B., Koerner D. W., Sargent A. I., van Dishoeck E. F., Allen L. E., Blake G. A., Brooke T. Y., Chapman N. L., Huard T. L., Lai S.-P., Mundy L. G., Myers P. C., Spiesman W. J., Wahhaj Z., The Spitzer c2d Survey of Weak-Line T Tauri Stars. II. New Constraints on the Timescale for Planet Building, 2007, ApJ, 667, 308

Cimatti A., Andreani P., Röttgering H., Tilanus R. P. J., Vigorous star formation hidden by dust in a galaxy at a redshift of 1.4, 1998, Nature, 392, 895

Currie M. J., Berry D. S., KAPPA - Kernel Application Package -User Manual, 2010, Starlink User Note 95.37, 1

Currie M. J., Draper P. W., Berry D. S., Jenness T., Cavanagh B., Economou F., Starlink Software Developments, 2008, Astronomical Data Analysis Software and Systems ASP Conference Series, 394, 650

Davis C. J., Matthews H., Ray T. P., Dent W. R. F., Richer J., A burst of outflows from the Serpens cloud core: wide-field submillimetre continuum, CO J=2-1 and optical observations, 1999, MNRAS, 309, 141

de Geus E. J., de Zeeuw P. T., Lub J., Physical parameters of stars in the Scorpio-Centaurus OB association, 1989, Astronomy and Astrophysics (ISSN 0004-6361), 216, 44

Dent W. R. F., Duncan W., Ellis M., Harris J., Lightfoot J. F., Wall R., Gibson H., Hills R. E., Richer J., Smith H., Withington S., Burgess T. A., Casorso R. V., Dewdney P. E., Hovey G. J., Redman R. O., Yeung K. K., Force B., Pain I., HARP and ACSIS on the JCMT, 2000, Imaging at Radio through Submillimeter Wavelengths, 217, 33

Draper P. W., Gray N., Berry D. S., Taylor M., GAIA - Graphical Astronomy and Image Analysis Tool - User Manual, 2009, Starlink User Note 214.38, 1

Draper P. W., Taylor M., SPLAT-VO - A VO-enabled Spectral Analysis Tool - User Manual, 2009, Starlink User Note 243.39, 1

Eales S., Lilly S., Gear W. K., Dunne L., Bond J. R., Hammer F., Févre O. L., Crampton D., The Canada-UK Deep Submillimeter Survey: First Submillimeter Images, the Source Counts, and Resolution of the Background, 1999, ApJ, 515, 518

Ebert R., Über die Verdichtung von H I-Gebieten. Mit 5 Textabbildungen, 1955, Zeitschrift für Astrophysik, 37, 217

Eisenhauer F., Quirrenbach A., Zinnecker H., Genzel R., Stellar Content of the Galactic Starburst Template NGC 3603 from Adaptive Optics Observations, 1998, ApJ, 498, 278

Emerson D. T., Approaches to Multi-beam Data Analysis, 1995, Astronomical Society of the Pacific Conference Series, 75, 309

Emerson D. T., Payne J. M., Multi-feed systems for radio telescopes, 1995, Astronomical Society of the Pacific Conference Series —vVol. 75+NRAO Work, 75

Enoch M. L., Evans N. J., Sargent A. I., Glenn J., Rosolowsky E., Myers P. C., The Mass Distribution and Lifetime of Prestellar Cores in Perseus, Serpens, and Ophiuchus, 2008, ApJ, 684, 1240

Evans N. J., Dunham M. M., Jørgensen J. K., Enoch M. L., Merín B., van Dishoeck E. F., Alcalá J. M., Myers P. C., Stapelfeldt K. R., Huard T. L., Allen L. E., Harvey P. M., van Kempen T., Blake G. A., Koerner D. W., Mundy L. G., Padgett D. L., Sargent A. I., The Spitzer c2d Legacy Results: Star-Formation Rates and Efficiencies; Evolution and Lifetimes, 2009, ApJS, 181, 321

Francesco J. D., André P., Myers P. C., Quiescent Dense Gas in Protostellar Clusters: The Ophiuchus A Core, 2004, ApJ, 617, 425

Francesco J. D., Evans N. J., Caselli P., Myers P. C., Shirley Y. L., Aikawa Y., Tafalla M., An Observational Perspective of Low-Mass Dense Cores I: Internal Physical and Chemical Properties, 2007, Protostars and Planets V, Univ. Arizona Press, Tucson, 17

Francesco J. D., Johnstone D., Kirk H., MacKenzie T., Ledwosinska E., The SCUBA Legacy Catalogues: Submillimeter-Continuum Objects Detected by SCUBA, 2008, ApJS, 175, 277

Friesen R., Johnstone D., Francesco J. D., Walsh A., Myers P. C., Dense gas and chemical variations in the Ophiuchus B core, 2005, Astrochemistry: Recent Successes and Current Challenges, 235, 325P

Glass I. S., An improved chopper for use in infrared photometry, 1972, The Observatory, 92, 140

Goodwin S. P., Nutter D., Kroupa P., Ward-Thompson D., Whitworth A. P., The relationship between the prestellar core mass function and the stellar initial mass function, 2008, A&A, 477, 823

Goodwin S. P., Whitworth A. P., Ward-Thompson D., An explanation for the unusual IMF in Taurus, 2004, A&A, 419, 543

Greaves J. S., Holland W. S., Moriarty-Schieven G., Jenness T., Dent W. R. F., Zuckerman B., McCarthy C., Webb R. A., Butner H. M., Gear W. K., Walker H. J., A Dust Ring around epsilon Eridani: Analog to the Young Solar System, 1998, ApJ, 506, L133

Greene T. P., Wilking B. A., André P., Young E. T., Lada C. J., Further mid-infrared study of the rho Ophiuchi cloud young stellar population: Luminosities and masses of pre-main-sequence stars, 1994, ApJ, 434, 614

Greene T. P., Young E. T., Near-infrared observations of young stellar objects in the Rho Ophiuchi dark cloud, 1992, ApJ, 395, 516

Gregersen E. M., Evans N. J., How to Identify Pre-Protostellar Cores, 2000, ApJ, 538, 260

Gregersen E. M., Evans N. J., Zhou S., Choi M., New Protostellar Collapse Candidates: an HCO + Survey of the Class 0 Sources, 1997, ApJ, 484, 256

Griffin M. J., Orton G. S., The near-millimeter brightness temperature spectra of Uranus and Neptune, 1993, Icarus, 105, 537

Hazell A. S., 1991, PhD thesis, 255

Hennebelle P., Chabrier G., Analytical Theory for the Initial Mass Function: CO Clumps and Prestellar Cores, 2008, ApJ, 684, 395

Herbig G. H., Radial velocities and spectral types of T Tauri stars, 1977, ApJ, 214, 747

Herbig G. H., Jones B. F., Large proper motions of the Herbig-Haro objects HH 1 and HH 2, 1981, AJ, 86, 1232

Hildebrand R. H., The Determination of Cloud Masses and Dust Characteristics from Submillimetre Thermal Emission, 1983, Royal Astronomical Society Quarterly Journal, 24, 267

Holland W. S., Greaves J. S., Zuckerman B., Webb R. A., McCarthy C., Coulson I. M., Walther D. M., Dent W. R. F., Gear W. K., Robson E. I., Submillimetre images of dusty debris around nearby stars, 1998, Nature, 392, 788

Holland W. S. et al., SCUBA-2: a 10,000-pixel submillimeter camera for the James Clerk Maxwell Telescope, 2006, Millimeter and Submillimeter Detectors and Instrumentation for Astronomy III. Edited by Zmuidzinas, 6275, 45

Holland W. S., Robson E. I., Gear W. K., Cunningham C. R., Lightfoot J. F., Jenness T., Ivison R. J., Stevens J. A., Ade P. A. R., Griffin M. J., Duncan W., Murphy J. A., Naylor D. A., SCUBA: a common-user submillimetre camera operating on the James Clerk Maxwell Telescope, 1999, MNRAS, 303, 659

Hovey G. J., Burgess T. A., Casorso R. V., Dent W. R. F., Dewdney P. E., Force B., Lightfoot J. F., Willis A. G., Yeung K. K., New spectral line multibeam correlator system for the James Clerk Maxwell Telescope, 2000, Proc. SPIE, 4015, 114

Hughes D. H., Serjeant S., Dunlop J., Rowan-Robinson M., Blain A., Mann R. G., Ivison R. J., Peacock J., Efstathiou A., Gear W. K., Oliver S., Lawrence A., Longair M., Goldschmidt P., Jenness T., High-redshift star formation in the Hubble Deep Field revealed by a submillimetre-wavelength survey, 1998, Nature, 394, 241

Ivison R. J., Dunlop J., Hughes D. H., Archibald E. N., Stevens J. A., Holland W. S., Robson E. I., Eales S., Rawlings S., Dey A., Gear W. K., Dust, Gas, and Evolutionary Status of the Radio Galaxy 8C 1435+635 at Z = 4.25, 1998, ApJ, 494, 211

Jeans J. H., The Stability of a Spherical Nebula, 1902, Philosophical Transactions of the Royal Society of London. Series A, 199, 1

Jeans J. H., The planetesimal hypothesis, 1929, The Observatory, 52, 172

Jenness T., Cavanagh B., Economou F., Berry D. S., JCMT Science Archive: Advanced Heterodyne Data Products Pipeline, 2008, Astronomical Data Analysis Software and Systems ASP Conference Series, 394, 565

Jenness T., Holland W. S., Chapin E., Lightfoot J. F., Duncan W., Dual-Beam Rastering and Deconvolution Techniques for SCUBA, 2000, Astronomical Data Analysis Software and Systems IX, 216, 559

Jenness T., Lightfoot J. F., SURF – SCUBA User Reduction Facility - User Manual, 2003, Starlink User Note 216.8, 1

Jenness T., Lightfoot J. F., Holland W. S., Removing sky contributions from SCUBA data, 1998, Proc. SPIE, 3357, 548

Jenness T., Stevens J. A., Archibald E. N., Economou F., Jessop N. E., Robson E. I., Towards the automated reduction and calibration of SCUBA data from the James Clerk Maxwell Telescope, 2002, MNRAS, 336, 14

Jessop N. E., Ward-Thompson D., A far-infrared survey of molecular cloud cores, 2000, MNRAS, 311, 63

Jessop N. E., Ward-Thompson D., The initial conditions of isolated star formation – IV. C18O observations and modelling of the pre-stellar core L1689B, 2001, MNRAS, 323, 1025

Jijina J., Myers P. C., Adams F. C., Dense Cores Mapped in Ammonia: A Database, 1999, ApJS, 125, 161

Johnstone D., Fich M., Mitchell G. F., Moriarty-Schieven G., Large Area Mapping at 850 Microns. III. Analysis of the Clump Distribution in the Orion B Molecular Cloud, 2001, ApJ, 559, 307

Johnstone D., Matthews H., Mitchell G. F., Large Area Mapping at 850 μm. IV. Analysis of the Clump Distribution in the Orion B South Molecular Cloud, 2006, ApJ, 639, 259

Johnstone D., Wilson C. D., Moriarty-Schieven G., Joncas G., Smith G., Gregersen E. M., Fich M., Large-Area Mapping at 850 Microns. II. Analysis of the Clump Distribution in the ρ Ophiuchi Molecular Cloud, 2000, ApJ, 545, 327

Jones B. F., Herbig G. H., Proper motions of T Tauri variables and other stars associated with the Taurus-Auriga dark clouds, 1979, AJ, 84, 1872

Jørgensen J. K., Johnstone D., Kirk H., Myers P. C., Allen L. E., Shirley Y. L., Current Star Formation in the Ophiuchus and Perseus Molecular Clouds: Constraints and Comparisons from Unbiased Submillimeter and Mid-Infrared Surveys. II., 2008, ApJ, 683, 822

Joy A. H., T Tauri Variable Stars., 1945, ApJ, 102, 168

Kenyon S. J., Hartmann L. W., Pre-Main-Sequence Evolution in the Taurus-Auriga Molecular Cloud, 1995, ApJS, 101, 117

Kirk J., Ward-Thompson D., André P., SCUBA Observations of Pre-Stellar Cores, 2002, EAS Publications Series, 4, 321

Kirk J., Ward-Thompson D., André P., The initial conditions of isolated star formation – VI. SCUBA mappingof pre-stellar cores, 2005, MNRAS, 360, 1506

Kirk J., Ward-Thompson D., André P., The initial conditions of isolated star formation – VII. Spitzer mapping of pre-stellar cores, 2007, MNRAS, 375, 843

Knude J., Hog E., Interstellar reddening from the HIPPARCOS and TYCHO catalogues. I. Distances to nearby molecular clouds and star forming regions, 1998, A&A, 338, 897

Kroupa P., On the variation of the initial mass function, 2001, MNRAS, 322, 231

Kroupa P., The Initial Mass Function of Stars: Evidence for Uniformity in Variable Systems, 2002, Science, 295, 82

Lada C. J., Star formation – From OB associations to protostars, 1987, IN: Star forming regions; Proceedings of the Symposium, 115, 1

Lada C. J., Wilking B. A., The nature of the embedded population in the Rho Ophiuchi dark cloud – Mid-infrared observations, 1984, ApJ, 287, 610

Larson R. B., Early star formation and the evolution of the stellar initial mass function in galaxies, 1998, MNRAS, 301, 569

Lee C. W., Myers P. C., Tafalla M., A Survey for Search of Infall Motions toward Starless Cores, 1999, Star Formation 1999, 177

Loren R. B., The cobwebs of Ophiuchus. I – Strands of (C-13)O - The mass distribution, 1989, ApJ, 338, 902

Low M.-M. M., Klessen R. S., Burkert A., Smith M. D., Kinetic Energy Decay Rates of Supersonic and Super-Alfvénic Turbulence in Star-Forming Clouds, 1998, Physical Review Letters, 80, 2754

Lynds B. T., Catalogue of Dark Nebulae., 1962, ApJS, 7, 1

Mamajek E. E., On the distance to the Ophiuchus star-forming region, 2008, Astronomische Nachrichten, 329, 10

Martín E. L., Brandner W., Bouvier J., Luhman K. L., Stauffer J., Basri G., Osorio M. R. Z., y Navascués D. B., Membership and Multiplicity among Very Low Mass Stars and Brown Dwarfs in the Pleiades Cluster, 2000, ApJ, 543, 299

Massey P., The Initial Mass Function of Massive Stars in the Local Group, 1998, The Stellar Initial Mass Function (38th Herstmonceux Conference) edited by Gary Gilmore and Debbie Howell. ASP Conference Series, 142, 17

Matthews H., Leech J., Friberg P., Guide to Spectral Line Observing at the JCMT, 2004, JAC Online Documentation, accessed 01 Jan 2010, 1

McGehee P. M., Star Formation and Molecular Clouds at High Galactic Latitude, 2008, Handbook of Star Forming Regions, 813

Mestel L., Spitzer L., Star formation in magnetic dust clouds, 1956, MNRAS, 116, 503

Montmerle T., Koch-Miramond L., Falgarone E., Grindlay J. E., Einstein observations of the Rho Ophiuchi dark cloud – an X-ray Christmas tree, 1983, ApJ, 269, 182

Motte F., André P., The circumstellar environment of low-mass protostars: A millimeter continuum mapping survey, 2001, A&A, 365, 440

Motte F., André P., Neri R., The initial conditions of star formation in the rho Ophiuchi main cloud: wide-field millimeter continuum mapping, 1998, A&A, 336, 150

Motte F., André P., Ward-Thompson D., Bontemps S., A SCUBA survey of the NGC 2068/2071 protoclusters, 2001, A&A, 372, L41

Mouschovias T. C., Nonhomologous contraction and equilibria of self-gravitating, magnetic interstellar clouds embedded in an intercloud medium: Star formation. II – Results, 1976, ApJ, 207, 141

Mouschovias T. C., Ciolek G. E., Magnetic Fields and Star Formation: A Theory Reaching Adulthood, 1999, The Origin of Stars and Planetary Systems. Edited by Charles J. Lada and Nikolaos D. Kylafis. Kluwer Academic Publishers, 305

Müller H. S. P., Schlöder F., Stutzki J., Winnewisser G., The Cologne Database for Molecular Spectroscopy, CDMS: a useful tool for astronomers and spectroscopists, 2005, Journal of Molecular Structure, 742, 215

Müller H. S. P., Thorwirth S., Roth D. A., Winnewisser G., The Cologne Database for Molecular Spectroscopy, CDMS, 2001, A&A, 370, L49

Myers P. C., Dense cores in dark clouds. III – Subsonic turbulence, 1983, ApJ, 270, 105

Myers P. C., Benson P. J., Dense cores in dark clouds. II – NH3 observations and star formation, 1983, ApJ, 266, 309

Myers P. C., Ladd E. F., Bolometric temperatures of young stellar objects, 1993, ApJ, 413, L47

Myers P. C., Linke R. A., Benson P. J., Dense cores in dark clouds. I – CO observations and column densities of high-extinction regions, 1983, ApJ, 264, 517

Neufeld D. A., Hollenbach D. J., Free-Free Emission from Accretion Shocks, 1996, ApJ Letters, 471, L45

Norman C. A., Ferrara A., The Turbulent Interstellar Medium: Generalizing to a Scale-dependent Phase Continuum, 1996, ApJ, 467, 280

Nutter D., Stamatellos D., Ward-Thompson D., The initial conditions of isolated star formation – IX. Akari mapping of an externally heated pre-stellar core, 2009, MNRAS, 396, 1851

Nutter D., Ward-Thompson D., A SCUBA survey of Orion – the low-mass end of the core mass function, 2007, MNRAS, 374, 1413

Nutter D., Ward-Thompson D., André P., A SCUBA survey of L1689 – the dog that didn't bark, 2006, MNRAS, 368, 1833

Onishi T., Mizuno A., Kawamura A., Tachihara K., Fukui Y., A Complete Search for Dense Cloud Cores in Taurus, 2002, ApJ, 575, 950

Ossenkopf V., Henning T., Dust opacities for protostellar cores, 1994, Astronomy and Astrophysics (ISSN 0004-6361), 291, 943

Pagani L., Bacmann A., Motte F., Cambrésy L., Fich M., Lagache G., Miville-Deschênes M.-A., Pardo J.-R., Apponi A. J., L183 (L134N) Revisited. II. The dust content, 2004, A&A, 417, 605

Papoular R., The processing of infrared sky noise by chopping, nodding and filtering, 1983, A&A, 117, 46

Plummer H. C., On the problem of distribution in globular star clusters, 1911, MNRAS, 71, 460

Preibisch T., Ossenkopf V., Yorke H. W., Henning T., The influence of ice-coated grains on protostellar spectra, 1993, Astronomy and Astrophysics (ISSN 0004-6361), 279, 577

Rawlings J. M. C., Hartquist T. W., Menten K. M., Williams D. A., Direct diagnosis of infall in collapsing protostars. I – The theoretical identification of molecular species with broad velocity distributions, 1992, MNRAS, 255, 471

Salpeter E. E., The Luminosity Function and Stellar Evolution., 1955, ApJ, 121, 161

Sandell G., Secondary calibrators at submillimetre wvelengths., 1994, MNRAS, 271, 75

Sandell G., Guide to SCUBA Calibration During Data Reduction, 2002, JAC Online Documentation, accessed 28 Nov 2009, 1

Sandell G., Jenness T., Jessop N. E., The SCUBA map reduction cookbook, 2001, Starlink Cookbook 11.2, 1

Shu F. H., Self-similar collapse of isothermal spheres and star formation, 1977, ApJ, 214, 488

Simpson R. J., Nutter D., Ward-Thompson D., The initial conditions of star formation – VIII. An observational study of the Ophiuchus cloud L1688 and implications for the pre-stellar core mass function, 2008, MNRAS, 391, 205

Smail I., Ivison R. J., Blain A., A Deep Sub-millimeter Survey of Lensing Clusters: A New Window on Galaxy Formation and Evolution, 1997, ApJ Letters, 490, L5

Smith H., Buckle J. V., Hills R. E., Bell G., Richer J., Curtis E. I., Withington S., Leech J., Williamson R., Dent W. R. F., Hastings P., Redman R. O., Wooff B., Yeung K. K., Friberg P., HARP: a submillimetre heterodyne array receiver operating on the James Clerk Maxwell Telescope, 2008, Millimeter and Submillimeter Detectors and Instrumentation for Astronomy IV. Edited by Duncan, 7020, 24

Smith H., Hills R. E., Withington S., Richer J., Leech J., Williamson R., Gibson H., Dace R., Ananthasubramanian P. G., Barker R. W., Baldwin R., Stevenson H., Doherty P., Molloy D., Quy V., Lush C., HARP-B: a 350-GHz 16-element focal plane array for the James Clerk Maxwell telescope, 2003, Millimeter and Submillimeter Detectors for Astronomy. Edited by Phillips, 4855, 338

Spezzi L., Alcalá J. M., Covino E., Frasca A., Gandolfi D., Oliveira I., Chapman N. L., Evans N. J., Huard T. L., Jørgensen J. K., Merín B., Stapelfeldt K. R., The Young Population of the Chamaeleon II Dark Cloud, 2008, ApJ, 680, 1295

Stamatellos D., Whitworth A. P., Ward-Thompson D., The dust temperatures of the pre-stellar cores in the ρ Oph main cloud and in other star-forming regions: consequences for the core mass function, 2007, MNRAS, 379, 1390

Stanke T., Smith M. D., Gredel R., Khanzadyan T., An unbiased search for the signatures of protostars in the ρ Ophiuchi molecular cloud . II. Millimetre continuum observations, 2006, A&A, 447, 609

Tafalla M., Mardones D., Myers P. C., Caselli P., Bachiller R., Benson P. J., L1544: A Starless Dense Core with Extended Inward Motions, 1998, ApJ, 504, 900

Testi L., Sargent A. I., Star Formation in Clusters: A Survey of Compact Millimeter-Wave Sources in the Serpens Core, 1998, ApJ, 508, L91

Thomson W., Is the Sun becoming Colder or Hotter?, 1892, Publications of the Astronomical Society of the Pacific, 4, 105

Tilanus R. P. J., Jenness T., Economou F., Cockayne S., The JCMT Telescope Management System, 1997, Astronomical Data Analysis Software and Systems VI, 125, 397

Tsamis Y. G., Rawlings J. M. C., Yates J. A., Viti S., Molecular line profiles as diagnostics of protostellar collapse: modelling the 'blue asymmetry' in inside-out infall, 2008, MNRAS, 388, 898

Vrba F. J., Role of magnetic fields in the evolution of five dark cloud complexes, 1977, AJ, 82, 198

Ward-Thompson D., André P., Crutcher R. M., Johnstone D., Onishi T., Wilson C. D., An Observational Perspective of Low-Mass Dense Cores II: Evolution Toward the Initial Mass Function, 2007, Protostars and Planets V, Univ. Arizona Press, Tucson, 33

Ward-Thompson D., André P., Kirk J., The initial conditions of isolated star formation – V. ISOPHOT imaging and the temperature and energy balance of pre-stellar cores, 2002, MNRAS, 329, 257

Ward-Thompson D., Buckley H. D., Modelling submillimetre spectra of the protostellar infall candidates NGC 1333-IRAS 2 and Serpens SMM4, 2001, MNRAS, 327, 955

Ward-Thompson D., Buckley H. D., Greaves J. S., Holland W. S., André P., Evidence for protostellar infall in NGC 1333-IRAS 2., 1996, MNRAS, 281, L53

Ward-Thompson D., Hartmann L. W., Nutter D., Turbulence in Class 0 and I protostellar envelopes, 2005, MNRAS, 357, 687

Ward-Thompson D., Motte F., André P., The initial conditions of isolated star formation – III. Millimetre continuum mapping of pre-stellar cores, 1999, MNRAS, 305, 143

Ward-Thompson D., Robson E. I., Whittet D. C. B., Gordon M. A., Walther D. M., Duncan W., Infrared and submillimetre observations of the Rho Ophiuchi dark cloud, 1989, MNRAS, 241, 119

Ward-Thompson D., Scott P. F., Hills R. E., André P., A Submillimetre Continuum Survey of Pre Protostellar Cores, 1994, MNRAS, 268, 276

Ward-Thompson D., Zylka R., Mezger P. G., Sievers A. W., Dust emission from star-forming regions. VI. The submillimetre YSO cluster in NGC 2264, 2000, A&A, 355, 1122

Whitney B. A., Wood K., Bjorkman J. E., Cohen M., Two-dimensional Radiative Transfer in Protostellar Envelopes. II. An Evolutionary Sequence, 2003, ApJ, 598, 1079

Whitworth A. P., Ward-Thompson D., An Empirical Model for Protostellar Collapse, 2001, ApJ, 547, 317

Wilking B. A., Blackwell J. H., Mundy L. G., Howe J. E., A millimeter-wave spectral-line and continuum survey of cold IRAS sources, 1989, ApJ, 345, 257

Wilking B. A., Lada C. J., The discovery of new embedded sources in the centrally condensed core of the Rho Ophiuchi dark cloud – The formation of a bound cluster, 1983, ApJ, 274, 698

Wilking B. A., Lada C. J., Young E. T., IRAS observations of the Rho Ophiuchi infrared cluster – Spectral energy distributions and luminosity function, 1989, ApJ, 340, 823

Williams J. P., Blitz L., McKee C. F., The Structure and Evolution of Molecular Clouds: from Clumps to Cores to the IMF, 2000, Protostars and Planets IV, Univ. Arizona Press, Tucson, 97

Zhou S., Evans N. J., Butner H. M., Kutner M. L., Leung C. M., Mundy L. G., Testing star formation theories – VLA observations of H2CO in the BOK globule B335, 1990, ApJ, 363, 168

Zhou S., Evans N. J., Koempe C., Walmsley C. M., Evidence for protostellar collapse in B335, 1993, ApJ, 404, 232

Zinnecker H., McCaughrean M. J., Wilking B. A., The initial stellar population, 1993, In: Protostars and planets III (A93-42937 17-90), 429